

東北医科薬科大学 分子生体膜研究所年報 2021年度 研究成果報告書

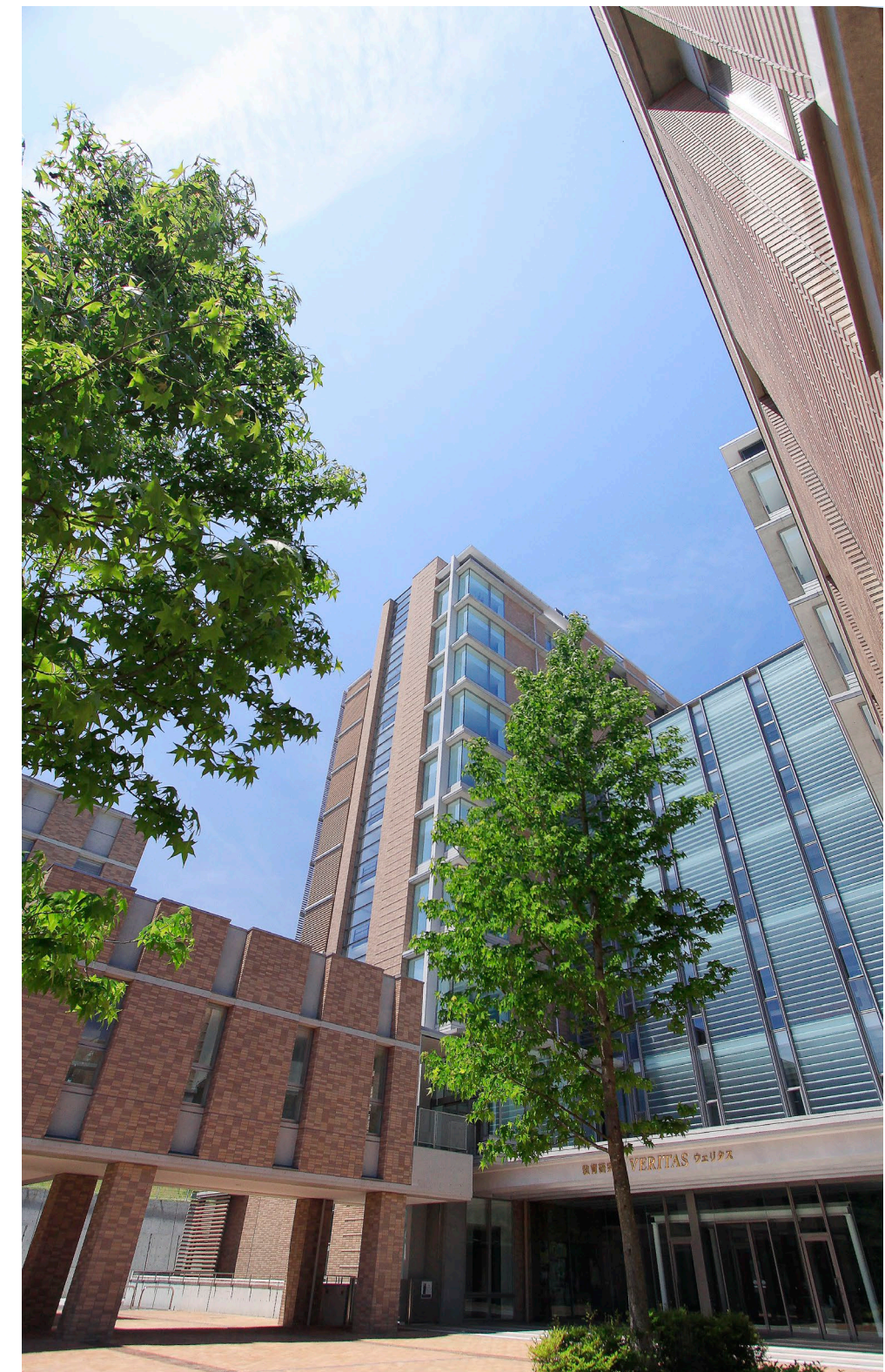
2021 Annual Report of
Institute of Molecular Biomembrane and Glycobiology



東北医科薬科大学
TOHOKU MEDICAL AND PHARMACEUTICAL UNIVERSITY

東北医科薬科大学
分子生体膜研究所年報

二〇二一年度〔令和3年度〕



目次

■ 所長挨拶	2
--------------	---

■ 箱守仙一郎賞	4
----------------	---

「箱守仙一郎賞」規約

第5回箱守仙一郎賞（2021年度）

奨励賞：ナマズ卵レクチンはヒト子宮頸がん由来 HeLa における

スニチニブの取り込みおよび排出に影響をおよぼす

菅原 栄紀（東北医科薬科大学 分子生体膜研究所 分子認識学・講師）

優秀論文賞： α 1,6-Fucosyltransferase contributes to cell migration and proliferation as well as
to cancer stemness features in pancreatic carcinoma.

梁 彩霞（Liang Caixia, 東北医科薬科大学・分子生体膜研究所・細胞制御学）

■ 研究報告	10
--------------	----

<機能病態分子部門>

「炎症・炎症性細胞死におけるスフィンゴ糖脂質 Gal2Cer の役割」

井ノ口仁一、稲森啓一郎、永福正和、狩野裕考、新田昂大

<分子認識部門>

「レクチンの抗腫瘍メカニズムの解明と糖脂質のかかわり 2021」

細野雅祐、菅原栄紀、立田岳生

<細胞制御学部門>

「糖鎖間の相互作用と糖鎖生合成の制御機構の解析」

顧 建国、福田 友彦、伊左治 知弥、黒田 喜幸

<糖鎖構造生物学部門>

「糖鎖構造解析のための技術基盤の構築」

山口 芳樹、真鍋 法義、大野 詩歩

ご挨拶

2021 年度は、新型コロナウイルス感染拡大の影響の 2 年目となり、1 年目の完全遠隔授業（オンライン）から 5 割対面と 5 割遠隔に切り替わりました。感染状況により緊急事態宣言が発出され、種々の行動制限が再び始まりました。賛否両論のあった、一年遅れの東京オリンピックが前代未聞の無観客下での開催となってことは、まだ記憶に新しい所であります。

一方で、驚異的な速さで開発された mRNA ワクチンの接種が日本でも本格的に進み始めていました。効果が 90%以上と言われたワクチンが広まれば、COVID-19 は 1、2 年の間に収束して行くのではないかと個人的には大きな期待を抱いていた時期がありました。ところが、非常に感染力の強いオミクロン株が主流となって更に大きな感染の波になってしまいました。幸いなことに、重症化したり死亡したりするリスクは、昨年猛威を振るったデルタ株よりは世界的に見ても低下しているようです。そのため世界の多くの国ではコロナ前の日常を取り戻すべく、経済活動とコロナを両立させるウイズコロナに舵を切った国が多く、日本でも従来のような厳しい行動制限はかなり緩和されました。これまでに水際対策として新規留学生の入国が難しくしていた措置も 2021 年 12 月から大きく緩和され、本来 2021 年 4 月から入学する留学生達が 1 年遅れて 2022 年 4 月に入学できるようになりました。

この 1 年間、多くの学会は Web 開催かハイブリッド形式での開催でした。皆さんも対面で人と接する大切さを再確認されたのではないのでしょうか。対面がかなわない状況で、オンライン講義・会議、テレワークなどの活用は、その不便さをある程度補ってくれました。しかしながら、研究活動や教育あるいは仕事を進める上で不可欠な人との信頼関係や共感を、リモートの環境だけで醸成するのは難しいことも実感しました。来年度からは全面的に対面で活動できるようになることを切に願っています。

研究面については、長年の蓄積と実績のある糖鎖構造と機能解析に関して、糖鎖科学を牽引する研究拠点を目指します。上述のような厳しい状況下において、コロナ感染対策を取り対面講義をこなしながら学問への情熱を持ち続け教員と、研究を続けた大学院生のみなさんの熱意と努力により、分子生体膜研究所（分生研）は研究教育活動を活発に行うことができました。その結果、第 40 回日本糖質学会でポスター賞（宋 万里, D3）、第 15 回東北糖鎖研究会でみちのく糖鎖ポスター賞（宋 万里, D3）、第 5 回箱守奨励賞（菅原 栄紀, 講師）と優秀論文賞（梁 彩霞, D3）（上図, 左から梁さん、顧と菅原先生）などが受賞さ



れました。また、細胞制御学に所属する黒田助教は、来年度から古巣の愛知県立大学の講師として栄転することになっています。おめでとうございます！

今年度から分生研 journal club & progress report を4教室の持ち回りの隔週開催でスタートさせました。教室間の交流のみならず、英語で発表することで若手教員や大学院生が国際学会で発表する機会にも繋がると信じています。また、8月には、研究所全体で科研費申請内容に対する意見交換を行い、採択率の向上を目指しています。来年度はこれまで国内で例がない大型国家プロジェクトである「ヒューマングライコームプロジェクト」が始まります。今年度は準備組織であるネットワーク拠点から、日本における独創的専門技術を有する糖鎖研究者として、当研究所の4名の教授が Collaborative Fellow (CF 相談役)に任命されました。今後、本プロジェクトに積極的に参画していきたいと考えています。

今回の年報では、各研究部門の研究活動報告および第5回箱守仙一郎賞の奨励賞および優秀論文賞をご紹介します。

皆様からのご指導ご鞭撻のほど心よりお願い申し上げます。

令和4年3月

東北医科薬科大学分子生体膜研究所・所長

顧 建国

東北医科薬科大学分子生体膜研究所
「箱守仙一郎賞」(Sen-itiroh Hakomori Glycoscience Award) 規約

令和 2 年 4 月
東北医科薬科大学分子生体膜研究所
顧 建国

名称	箱守仙一郎賞
授与機関	東北医科薬科大学分子生体膜研究所
目的	生物系化学系を問わず広く糖鎖科学を専攻し、日夜努力を続けている東北エリアの研究者を顕彰することにより、日本の糖鎖科学研究の増進を図る。
賞の種別	奨励賞 1～2 名 顕彰楯および副賞 優秀論文賞 1～2 名 顕彰楯および副賞
対象	(1) 奨励賞：東北エリア（新潟県および群馬県を含む）で研究に従事する応募時 45 歳までの研究者 (2) 優秀論文賞：同地域で研究に従事し、申請時点で大学院生もしくは博士研究員である者 ＊ いずれも指定された期間内(各年度内)に発表（accepted でも可）された学術原著論文に対して審査・授与する。
選考方法	自薦および他薦によるものとし、東北糖鎖研究会世話人が審査する。評価を点数化（次項参照）して決する。
授賞方法	東北糖鎖研究会開催時に授賞および受賞講演を行う。
運用方法	顕彰楯および副賞の購入費は、箱守賞基金を原資とし、分子生体膜研究所がこれを支弁する。
その他	事務局は分子生体膜研究所内に置く。

応募と審査方法

(1) 応募資格および応募方法

東北 6 県、新潟県および群馬県（東北糖鎖研究会エリア）で研究を行っている 45 歳以下の糖鎖科学研究者（大学院生、博士研究員は自動的に優秀論文賞へのノミネートとなる）。対象論文は、その年度内に Impact factor が付与されている英文学術雑誌（査読有）に出版、または掲載が決定されている原著論文（accepted でも可）とし、応募者が筆頭著者となっているものとする。要旨和訳と論文 PDF を添えて既定のエントリーフォームに記入してメールにて応募する。化学系・生物系は問わない。自薦および他薦どちらでも受け付ける。応募期間等についてはその都度決定し、周知する。

書類送付先：東北医科薬科大学 分子生体膜研究所 所長 顧 建国

メールアドレス：jgu@tohoku-mpu.ac.jp； 応募締め切り：5 月 31 日

(2) エントリーフォーム（別添）

(3) 審査委員および審査方法

- 1) 分子生体膜研究所所長が審査員長を務める。
- 2) 東北糖鎖研究会世話人が審査員となる。ただし、世話人が推薦者または自薦者の所属責任者あるいは論文の共著者である場合は審査に参加しない。
- 3) 期限内に提出された論文について事務局が一次審査（下記基礎点と推薦者の評価点の合計による）を行い、奨励賞および優秀論文賞それぞれ上位 3 報を選定する。
- 4) 上位 3 報について審査員が下記評価項目を採点し、全員（その都度人数は異なる）の評価平均点＋基礎点＋推薦者の評価点から上位者を受賞者として決定する。
- 5) 最高点が複数出た場合は審査員長の判断に委ねる。

基礎点

Impact factor (IF): IF×5 点

推薦者（自薦または他薦）の評価点（推薦書に記入、最高点 10 点）

共同研究者の貢献を考慮し、以下の項目を参考して該当研究に対する応募者の貢献度を客観的にみて公正に評価する。

- 1) 研究の考案（最高点 2 点）
- 2) 実験の実行（最高点 5 点）
- 3) 論文作成（最高点 3 点）

評価最高点

独創性	10 点
インパクト（重要性）	10 点
論文構成	10 点
将来性	10 点

第5回箱守仙一郎賞（2021年度）

奨励賞

ナマズ卵レクチンはヒト子宮頸がん由来 HeLa における
スニチニブの取り込みおよび排出に影響をおよぼす

**Catfish egg lectin affects influx and efflux rates of sunitinib in human
cervical carcinoma HeLa cells**

菅原 栄紀（東北医科薬科大学 分子生体膜研究所 分子認識学・講師）

ナマズ卵由来レクチン（SAL）は、グロボトリアオシルセラミド（Gb3）の糖鎖を介してバーキットリンパ腫細胞株 Raji に結合し、ヨウ化プロピジウム（PI）およびドキシソルビシンの細胞内取り込み量を増加させて細胞生存率を著しく減少させることを報告している。本研究では、SAL が Gb3 を発現している HeLa において分子標的薬であるスニチニブ（スーテント，SU）の細胞毒性作用を増強するか否かを検討した。SAL を前処理することにより SU による HeLa の生存率が有意に減少し、この時の SU の取り込みは、30 分後で有意に増加していた。次に、培地から薬剤を除去し細胞内の SU の残存量を観察したところ、SAL 未処理細胞では3時間後に大部分の SU が排出されているが、処理細胞では24時間経過しても多くの SU が細胞内に残存していた。また、Gb3 欠損 HeLa では、SAL 処理による SU の取り込み促進および排出抑制のどちらも認められなかった。次に、SU の集積する部位を、共焦点レーザー顕微鏡を用いて調べた結果、SU は SAL 処理細胞内に形成される油滴状の膜構造物の周囲に集まる像が確認された。さらに、この構造物の帰属を明らかにするために、リソソームのマーカーである LAMP1 と RFP の融合タンパク質を HeLa に強制発現させた後、SAL 処理した細胞に SU を取り込ませたところ、SU と LAMP1 は共局在していることが明らかとなった。以上の結果から、SAL は HeLa 細胞内にリソソーム様の構造物形成を促進し、細胞内に取り込まれた SU はこの構造物にトラップされ細胞内に蓄積し、HeLa に対する細胞毒性を増加させている可能性が示唆された（1）。

- (1) Sugawara S, Takayanagi M, Honda S, Tatsuta T, Fujii Y, Ozeki Y, Ito J, Sato M, Hosono M. Catfish egg lectin affects influx and efflux rates of sunitinib in human cervical carcinoma HeLa cells. *Glycobiology*, 30, 802-816 (2020).

【経歴】

2000 年：東北薬科大学薬学部卒業

2002 年：東北大学大学院薬学研究科 博士課程前期課程修了

（自然免疫におけるペプチドグリカン認識タンパク質の機能解析に従事）

2005 年：東北薬科大学大学院薬学研究科 博士課程後期課程修了

（糖鎖あるいは DNA を認識する魚卵由来タンパク質の生化学的解析に従事）

2005 年：東北薬科大学附属癌研究所第一部 助手

2007 年：東北薬科大学 分子生体膜研究所 分子認識学教室 助教

2017 年～現在：東北医科薬科大学 分子生体膜研究所 分子認識学教室 講師

（ナマズ卵レクチンを利用した新規がん治療法の開発に従事）

【受賞の御礼ならびに抱負】

この度は、第 5 回箱守仙一郎賞奨励賞を賜りましたこと、大変光栄に存じますとともに箱守仙一郎賞審査員長の顧 建国先生ならびに審査員の先生方に厚く御礼申し上げます。仙台の地で糖鎖研究を行う一研究者として箱守仙一郎先生のお名前が冠された賞を受賞することは私の目標でもありました。これからは頂いた賞に恥じぬように、これまで以上に糖鎖科学の発展に努めていきたいと思っております。

私の研究テーマは、大学院博士後期課程入学時から一貫して、ナマズ卵レクチン（SAL）のがん治療への応用を目指した基礎研究であります。中でも、糖脂質の一種であるグロボトリアオシルセラミド（Gb3）を高発現しているがん細胞に対する効果的な治療法の開発を思考して研究に取り組み、これまでに 1）Gb3 を発現しているバーキットリンパ腫細胞はナマズ卵レクチン処理により初期アポトーシス初期状態に変化する、2）ナマズ卵レクチンはバーキットリンパ腫細胞 Raji の増殖を抑制するなどの成果を報告してきました。研究生活の中で様々な難題にあたり困難を極めたこともありましたが、箱守先生が来学された際に行われる研究報告会では、いいデータは褒めていただき、研究に足りないところは文献や研究方法などを含めて詳細にお話しいただき、これからの研究に光がさしたような感じがしてとても有り難かったです。受賞論文では、Gb3 を発現している子宮頸がん由来細胞株 HeLa おいて抗がん剤と SAL を併用することにより薬剤の濃度を下げても高濃度と同じ効果が得られ、この時、細胞内への薬剤の取り込み量が増加していることを明らかにしました。抗がん剤治療で最も問題となるのは副作用の発現であります。SAL は、がん細胞の薬剤感受性を高める効果を発揮することでこの問題を解決でき、また Gb3 を発現しているがん細胞であれば、SAL は併用する抗がん剤の用量低減に貢献できる可能性も有すると考えております。しかしながら、SAL 処理による薬剤の取り込み促進の分子メカニズム

など不明な点は残されているので、これらのことを少しずつ明らかにしてレクチンによるがん治療実現に向けて研究を進めていきたいと考えております。

最後に、研究のご指導を頂きました細野雅祐教授をはじめ本研究にご協力いただきました先生方、研究室員の皆様に深く感謝申し上げます。これからも日々の努力を怠らず仙台の地から糖鎖科学に関する新しい知見を多く発信できるように精進していきたいと存じます。今後ともご指導ご鞭撻のほどよろしくお願い申し上げます。

優秀論文賞

α 1,6-Fucosyltransferase contributes to cell migration and proliferation as well as to cancer stemness features in pancreatic carcinoma.

Liang C., Fukuda, T., Isaji, T., Duan, C., Song, W., Wang, Y. and Gu, J.

Biochim Biophys Acta Gen Subj., 1865, 3239-3252, 2021

梁 彩霞 (Liang Caixia, 東北医科薬科大学・分子生体膜研究所・細胞制御学)

論文要旨

膵がんでは FUT8 の発現が上昇するが、膵がんの特徴である浸潤・転移しやすさとコアフコシル化の関係は未解明である。膵がんの予後不良に対する FUT8 の役割を明らかにするため、膵がんの研究に広く用いられている MIA PaCa-2 や PANC-1 細胞株に CRISPR/Cas9 を用いて FUT8 を欠損させた細胞を作成し、膵がんにおける FUT8 の機能を明らかにした。細胞遊走能を検討したところ、FUT8 欠損 MIA PaCa-2 細胞は野生型に比べて、約 80%と顕著な遊走能の阻害が認められた。また、MTT およびコロニー形成による細胞増能を検討したところ、いずれの方法でも FUT8 欠損細胞は 50%以下に減少し、細胞表面における増殖因子受容体数も減少していた。さらに、フコース誘導体(2FF)の添加によりコアフコシル化を阻害しても、FUT8 欠損細胞と同様に、増殖・遊走に対する抑制が確認された。FUT8 欠損により、腫瘍増殖抑制作用が期待されたため、免疫不全マウス皮下に作成した細胞を移植したところ、生着・増殖は認められものの、有意な腫瘍増殖抑制作用が認められた。そこで、再発・転移に重要な役割を果たすと考えられているがん幹細胞性に与える影響を検討した。まず、がん幹細

胞マーカーの発現を検討したところ、FUT8 欠損細胞では、CD133, CXCR4, C-Met, EpCAM などの発現が減少していた。次に、がん細胞同士の相互作用を検討するため、スフェロイドを形成させたところ、FUT8 欠損細胞では細胞間の凝集が弱く不安定であることが分かった。さらに、がん幹細胞の特徴の一つである薬物耐性に対しても検討した。その結果、FUT8 の欠失は、膵がんの治療薬である Gemcitabine に対する応答性を高めた。これらの結果は、FUT8 の発現が無くなると、幹細胞性が失われることを示唆している。実験的ではあるものの、2FF の投与でも FUT8 欠損細胞と同様の効果が得られたことは、フコース誘導体をもちいて FUT8 の機能制御を介して、膵がん幹細胞を標的とした治療などの可能性が示された。

受賞の御礼ならびに抱負

I am both excited and deep humbled when I was informed by Prof. Gu that I have received the Sen-itiroh Hakomori glycoscience award. I couldn't believe my ears, I was not so sure if I really deserved this honor, because I knew many of researchers in the field even worked more harder than I did. It is a great honor for me to receive the award, which is not only a recognition of my existing work, but also an encouragement for the following research work. I am sure that this achievement couldn't be received without a wonderful and strong productive research team. I'd like to express my sincere appreciation to all members of Institute of Molecular Biomembrane and Glycobiology, Tohoku Medical and Pharmaceutical University.

I'd like also to express my sincere appreciation to the prize committee members. Prof. Hakomori was an outstanding scientist in the field of glycobiology. His academic reports and passion for scientific research are a deep inspiration to our younger generation. The Fall of the Star brings regret and deep pain to us, but it is more about nostalgia and admiration. His hard work, boundless love and dedication to science will always inspire us to move forward.

The three years of doctoral life were very important and memorable experiences for me. I owe my sincerely gratitude to President Motoaki Takayanagi for providing the opportunity to study at Tohoku Medical and Pharmaceutical University and provide financial assistance. Thanks to my mentor, Prof. Gu, who gave me great guidance and help in my studies and life. What is more, I would like to thank Dr. Tomohiko Fukuda and Dr. Isaji Tomoya for their consultation and technical support, and Ms. Yan Hao as well as other members of the laboratory. Thank you for taking me on the most enjoyable journey of my life.

During the three years of studying in Japan, many kind people gave me great support, encouragement and help. I want to take this opportunity to thank them all. Thank you very much! Now, I was already graduated from Tohoku medical and pharmaceutical university and worked in the clinical medical research center of The Second Affiliated Hospital of Nantong University. I am still engaged in basic research on glycobiology. I will continue to do my best to contribute to the glycobiology society.

Thank you very much!

梁彩霞 (Liang Caixia)

研究報告

＜機能病態分子部門＞

特任教授 井ノ口仁一

准教授 稲森啓一郎

講師 永福正和

助教 狩野裕考

博士研究員 新田昂大

炎症・炎症性細胞死におけるスフィンゴ糖脂質 Gal2Cer の役割

糖尿病性腎症は、いまだ根治を可能とする治療法・治療薬が存在しない疾患であり、詳細な発症・増悪メカニズムの解明ならびに治療ターゲットとなる分子の同定が求められている。

細胞膜構成成分のひとつであるスフィンゴ糖脂質は、糖尿病性腎症において病態に関連した腎臓での発現変化が観察されることは、すでに知られていたが、その病態生理学的な役割については、ほとんど分かっていなかった。我々は、2型糖尿病性腎症病態で、グロボ系スフィンゴ糖脂質の腎発現が変化することに加え、炎症促進に関与していることを明らかにし、2019年に報告した(*Glycobiology*, 29: 260-268, 2019)。最近、1型糖尿病性腎症においても、特徴的なスフィンゴ糖脂質の腎発現が変化していること、そして、その糖脂質がマクロファージにおける炎症・炎症性細胞死(パイロトーシス)に関与することを新たに見出した。

【1型糖尿病性腎症病態における腎スフィンゴ糖脂質の発現変化】

薬剤(Streptozotocin)誘導性マウスモデルならびに、自然発症マウスモデル(Akita)を用いて、腎臓のスフィンゴ糖脂質発現を薄層クロマトグラフィー(TLC)にて解析を行った。これまで行ってきた2型糖尿病性腎症モデルマウスの解析では、グロボ系スフィンゴ糖脂質の発現が顕著に増加していたが、上記の1型のモデルマウスにおいては、グロボ系の発現は減少しており、それとは異なる糖脂質の発現増加が認められた。レクチン(PA-1L)を用いたさらなる解析によって、この増加していた糖脂質はガラビオシルセラミド(Gal2Cer)であることが明らかとなった(図1)。

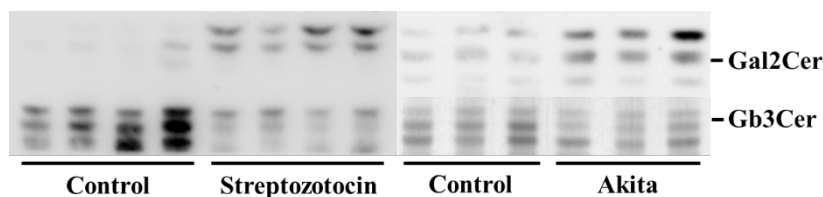


図1 1型糖尿病性腎症モデル。マウスの腎糖脂質発現変化

【GalCerの持つ炎症ならびに炎症性細胞死の促進活性】

当研究室では、これまでにスフィンゴ糖脂質 Gb3Cer、Gb4Cer ならびにガングリオシド GM3 が、Toll-like receptor 4(TLR4)を介したマクロファージの活性化促進能を有することを明らかにしてきた。(EMBO J, 39: e101732, 2020)。Gal2Cer についても、上記と同様にマクロファージ(BMDMs)の活性化を促進するかどうかを今回検討した。TLR4 リガンドであるリポ多糖(LPS)と Gal2Cer でマクロファージを共刺激し、培養上清中の炎症性サイトカイン(TNF α)を ELISA にて定量した。その結果、LPS 単独よりも Gal2Cer との共刺激の方が、より TNF α の検出量が高値であった(図 2A)。これは、Gal2Cer においても炎症を促進する活性があることを示唆しており、マクロファージ活性化に寄与していることが明らかとなった。

また、近年注目集めている炎症性細胞死(パイロトーシス)についても Gal2Cer の関与を検討した。パイロトーシスの誘導経路には、TLR4 を介したメカニズムが報告されており、TLR4 を介した炎症促進に関与していた Gal2Cer が、パイロトーシスの誘導促進に寄与する可能性は高いと考えられた。評価方法については、上記と同様にマクロファージを共刺激し、培養上清中に分泌されるパイロトーシスの指標である IL-1(α , β)の量を ELSIA にて定量した。その結果、IL-1 の検出量は LPS 単独と比較して共刺激の方が高かった(図 2B)ことから、Gal2Cer にはパイロトーシス誘導促進活性が存在することが示唆された。興味深いことに、Gal2Cer 単独でのパイロトーシス惹起は誘導されないことから(図 2B)、これまで知られている誘導メカニズムとは異なる可能性が考えられる。したがって、今後はその詳細な機序について明らかにし、パイロトーシスの関与する疾患における治療法・予防法の開発につなげたい。

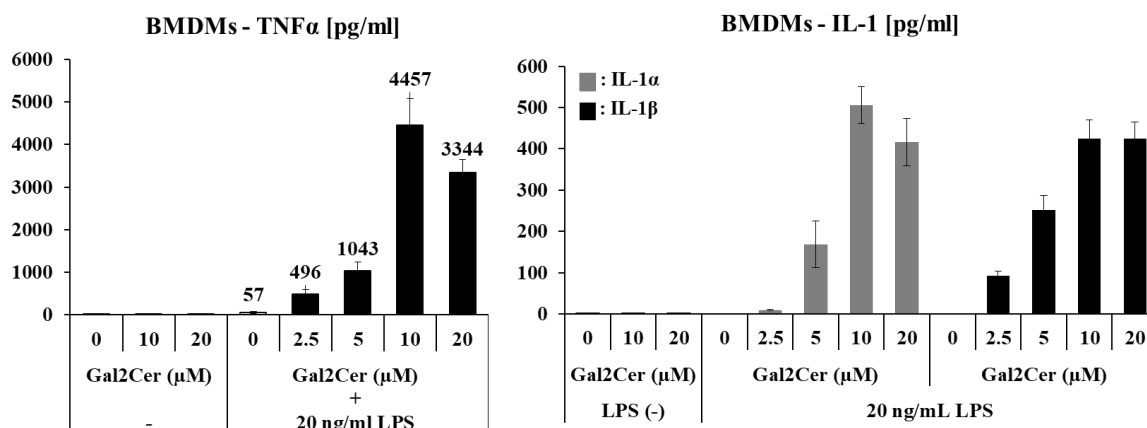


図2 A: マウス骨髄由来マクロファージ(BMDMs)を LPS/Gal2Cer で刺激。48 時間後、培養上清中の TNFα 量を ELSIA にて定量。 B: マウス骨髄由来マクロファージ(BMDMs)を LPS/Gal2Cer で刺激。48 時間後、培養上清中の IL(α, β)量を ELSIA にて定量。

< 発表論文 >

1. Homeostatic and pathogenic roles of the GM3 ganglioside

Jin-ichi Inokuchi, Hiroataka Kanoh, Kei-ichiro Inamori, Masakazu Nagafuku, Takahiro Nitta, and Koichi Fukase ^a

(Department of Chemistry, Graduate School of Science, Osaka University ^a)

The FEBS Journal (2021) PMID: 34125497 DOI: 10.1111/febs.16076

2. GRASP55 regulates intra-Golgi localization of glycosylation enzymes to control glycosphingolipid biosynthesis

Prathyush Pothukuchi ^a, Ilenia Agliarulo ^a, Marinella Pirozzi ^a, Riccardo Rizzo ^a, Domenico Russo ^a, Gabriele Turacchio ^a, Julian Nüchel ^b, Jia-Shu Yang ^c, Charlotte Gehin ^d, Laura Capolupo ^d, Maria Jose Hernandez-Corbacho ^e, Ansuman Biswas ^f, Giovanna Vanacore ^a, Nina Dathan ^a, Takahiro Nitta, Petra Henklein ^g, Mukund Thattai ^f, Jin-Ichi Inokuchi, Victor W Hsu ^c, Markus Plomann ^b, Lina M Obeid ^e, Yusuf A Hannun ^e, Alberto Luini ^a, Giovanni D'Angelo ^{a,d}, Seetharaman Parashuraman ^a

(Institute of Biochemistry and Cell Biology, National Research Council of Italy, Rome Italy ^a, Medical Faculty, Center for Biochemistry, University of Cologne, Cologne Germany ^b, Division of Rheumatology, Inflammation and Immunity, Department of Medicine, Brigham and Women's Hospital Harvard Medical School, Boston MA, USA ^c, École Polytechnique Fédérale de

Lausanne (EPFL), Lausanne Switzerland ^d, Stony Brook University Medical Center, Stony Brook NY, USA ^e, National Center of Biological Sciences, Bengaluru India ^f,
Universitätsmedizin Berlin Institut für Biochemie Charité CrossOver Charitéplatz 1 / Sitz,
Berlin Germany ^g)
EMBO J (2021) PMID: **34516001** DOI: [10.15252/embj.2021107766](https://doi.org/10.15252/embj.2021107766)

<学会発表>

・ **Glycosphingolipids in central and peripheral leptin signaling**

Kei-ichiro Inamori

日本薬学会第 141 年会, Web 開催, 2021 年 3 月, S44-3

・ **Homeostatic and Pathogenic Balance Regulated by Ganglioside GM3**

Jin-ichi Inokuchi

3rd Australasian Glycoscience Symposium

June 3-4, 2021, Web 開催

・ **1 型糖尿病性腎症における糖脂質発現変化**

新田昂大、狩野裕考、稲森啓一郎、鈴木明身、井ノ口仁一

第 63 回日本脂質生化学会 Web 開催 2021 年 6 月 要旨集 P100-101

・ **潰瘍性大腸炎におけるスフィンゴ糖脂質の発現変化**

稲森啓一郎, 小川仁 ^a, 新田昂大, 大川光, 狩野裕考, 遠藤克哉 ^b, 佐藤賢一 ^b, 中村保宏 ^c, 柴田近 ^a, 鈴木明身, 井ノ口仁一 (東北医薬大・医・外科学第一 (消化器外科) ^a、東北医薬大・医・内科学第二 (消化器内科) ^b、東北医薬大・医・病理学 ^c)

第 15 回東北糖鎖研究会, Web 開催, 2021 年 9 月, 要旨集 14-15

・ **潰瘍性大腸炎におけるスフィンゴ糖脂質の発現変化**










稲森啓一郎, 小川仁 ^a, 新田昂大, 大川光, 狩野裕考, 遠藤克哉 ^b, 佐藤賢一 ^b, 中村保宏 ^c, 柴田近 ^a, 鈴木明身, 井ノ口仁一 (東北医薬大・医・外科学第一 (消化器外科) ^a、東北医薬大・医・内科学第二 (消化器内科) ^b、東北医薬大・医・病理学 ^c)

第 14 回セラミド研究会学術集会, ハイブリッド開催, 2021 年 10 月,
要旨集 23

- 糖尿病性腎症におけるスフィンゴ糖脂質の発現変化解析**
 新田昂大, 狩野裕考, 稲森啓一郎, 鈴木明身, 井ノ口仁一
 第 14 回セラミド研究会学術集会 Web 開催 2021 年 10 月 要旨集 P17
- 新規ミスセンス変異を認めた本邦初の B4GALNT1 関連神経変性症の 1 例**
 中村勝哉 ^{a,b}, 土田奈緒美 ^c, 井ノ口仁一, 小島朋美 ^a, 池田淳司 ^b,
 小平農 ^b, 稲森啓一郎, 永福正和, 新田昂大, 真鍋法義, 大野詩歩 ^d,
 山口芳樹 ^d, 下畑享良 ^e, 松本直通 ^e, 古庄知己 ^{a,f}, 関島良樹 ^b
 (信州大学医学部附属病院遺伝子医療研究センター ^a, 同 脳神経内科 ^b リウマチ・膠原病内科、横浜市立大学大学院医学研究科遺伝学 ^c, 東北医科薬科大学分子生体膜研究所糖鎖構造生物学 ^d, 岐阜大学大学院医学系研究科脳神経内科学分野 ^e, 信州大学医学部遺伝医学教室 ^f)
 日本人類遺伝学会第 66 回大会 2021 年 10 月 WEB 開催
- 全ヒト糖鎖関連遺伝子 Variant の網羅的抽出と解析**
 西原祥子 ^a, 木下聖子 ^a, 梶谷内晶 ^a, 細田正恵 ^a, 伊藤和義 ^a, 山口芳樹 ^b, 真鍋法義 ^b, 大野詩歩 ^b, 稲森啓一郎, 井ノ口仁一, 灘中里美 ^c, 北川裕之 ^c, 城田松之 ^d, 木下賢吾 ^d
 (創価大学 糖鎖生命システム融合研究所 ^a, 東北医科薬科大学 分子生体膜研究所 ^b, 神戸薬科大学 ^c, 東北大学 東北メディカル・メガバンク機構 ^d)
 第 40 回日本糖質学会年会 (2021 年 10 月 27~29 日、鹿児島) 口頭発表
 要旨集 120
- 潰瘍性大腸炎患者におけるスフィンゴ糖脂質の発現変化**
 稲森啓一郎, 小川仁 ^a, 新田昂大, 大川光, 狩野裕考, 遠藤克哉 ^b, 佐藤賢一 ^b, 中村保宏 ^c, 柴田近 ^a, 高橋伸一郎 ^d, 鈴木明身, 井ノ口仁一 (東北医薬大・医・外科学第一 (消化器外科) ^a, 東北医薬大・医・内科学第二 (消化器内科) ^b, 東北医薬大・医・病理学 ^c, 東北医薬大・医・臨床検査医学 ^d)
 第 15 回スフィンゴセラピー研究会, Web 開催, 2021 年 11 月, 要旨集 15
- GM3 Ganglioside in Insulin Resistance and Inflammation**
 Jin-ichi Inokuchi
 16th Meeting of the International Endotoxin and Innate Immunity Society (IEIIS) Oct 12-15, 2021 Kobe Japan Invited Oral presentation

- ・ **1 型と 2 型糖尿病性腎症における腎スフィンゴ糖脂質発現変化の比較**
 新田昂大、狩野裕考、稲森啓一郎、鈴木明身、井ノ口仁一
 第 94 回 日本生化学会大会 Web 開催 2021 年 11 月 プログラム集 P86
- ・ **細胞膜スフィンゴミエリンによる CD8T 細胞の分化・機能制御機構の解明**
 豊島 かおる^a, 井ノ口 仁一, 大野 勲^a
 (東北医薬大・医・医学教育推進センター^a)
 第 44 回 日本分子生物学会年会 Web 開催, 2021 年 12 月
- ・ **TLR リガンドの機能評価**
 ～レポーターアッセイとイメージングによる解析～
 大垣 仁之^a、樺山 一哉^{a,b}、内藤 ひかり^a、下山 敦史^{a,b}、狩野 裕考、井ノ口 仁一、深瀬 浩一^{a,b} (阪大・院理・化学^a, 阪大・院理・PRC^b)
 第 44 回 日本分子生物学会年会 Web 開催, 2021 年 12 月

GRASP55 regulates intra-Golgi localization of glycosylation enzymes to control glycosphingolipid biosynthesis

Prathyush Pothukuchi¹ , Ilenia Agliarulo^{1,†}, Marinella Pirozzi^{1,‡}, Riccardo Rizzo^{1,§}, Domenico Russo¹, Gabriele Turacchio¹, Julian Nüchel² , Jia-Shu Yang³, Charlotte Gehin⁴ , Laura Capolupo⁴, Maria Jose Hernandez-Corbacho⁵, Ansuman Biswas⁶, Giovanna Vanacore¹, Nina Dathan¹, Takahiro Nitta⁷, Petra Henklein⁸, Mukund Thattai⁶, Jin-Ichi Inokuchi⁷ , Victor W Hsu³ , Markus Plomann² , Lina M Obeid^{5,†} , Yusuf A Hannun⁵, Alberto Luini¹, Giovanni D'Angelo^{1,4}  & Seetharaman Parashuraman^{1,*} 

Abstract

The Golgi apparatus, the main glycosylation station of the cell, consists of a stack of discontinuous cisternae. Glycosylation enzymes are usually concentrated in one or two specific cisternae along the *cis-trans* axis of the organelle. How such compartmentalized localization of enzymes is achieved and how it contributes to glycosylation are not clear. Here, we show that the Golgi matrix protein GRASP55 directs the compartmentalized localization of key enzymes involved in glycosphingolipid (GSL) biosynthesis. GRASP55 binds to these enzymes and prevents their entry into COPI-based retrograde transport vesicles, thus concentrating them in the *trans*-Golgi. In genome-edited cells lacking GRASP55, or in cells expressing mutant enzymes without GRASP55 binding sites, these enzymes relocate to the *cis*-Golgi, which affects glycosphingolipid biosynthesis by changing flux across metabolic branch points. These findings reveal a mechanism by which a matrix protein regulates polarized localization of glycosylation enzymes in the Golgi and controls competition in glycan biosynthesis.

Keywords glucosylceramide synthase; glycosphingolipids; glycosylation; Golgi apparatus; GRASP55

Subject Categories Membranes & Trafficking; Metabolism

DOI 10.15252/emboj.2021107766 | Received 18 January 2021 | Revised 26 July 2021 | Accepted 6 August 2021 | Published online 13 September 2021

The EMBO Journal (2021) 40: e107766

Introduction

Glycans are one of the fundamental building blocks of the cell and play key roles in development and physiology (Bishop *et al*, 2007; Kohyama-Koganeya *et al*, 2011; Ryczko *et al*, 2016; Varki, 2017; Akintayo & Stanley, 2019). Cellular glycan profiles are sensitive to changes in cell state and/or differentiation and are also important contributors to the process (Russo *et al*, 2018b). Indeed, several developmental disorders are associated with impaired production of glycans (Chang *et al*, 2018). Thus, how the glycan biosynthesis is regulated to achieve specific cellular glycan profiles is an important biological problem. In eukaryotes, glycans are assembled mainly by the Golgi apparatus on cargo proteins and lipids that traverse the organelle (Stanley, 2011). Glycan biosynthesis happens in a template-independent fashion (Varki & Kornfeld, 2015), yet the products are not random polymers of sugars but a defined distribution of glycans that is cell-type and cargo-specific (Rudd *et al*, 2015; Varki & Kornfeld, 2015). This suggests that their biosynthesis is guided by regulated program(s). Transcriptional programs have been identified that contribute to defining the glycome of a cell, but they only partially account for it (Nairn *et al*, 2008, 2012; Varki & Kornfeld, 2015). An obviously important but unexplored factor that

¹ Institute of Biochemistry and Cell Biology, National Research Council of Italy, Rome, Italy

² Medical Faculty, Center for Biochemistry, University of Cologne, Cologne, Germany

³ Division of Rheumatology, Inflammation and Immunity, Department of Medicine, Brigham and Women's Hospital, Harvard Medical School, Boston, MA, USA

⁴ École Polytechnique Fédérale de Lausanne (EPFL), Lausanne, Switzerland

⁵ Stony Brook University Medical Center, Stony Brook, NY, USA

⁶ National Center of Biological Sciences, Bengaluru, India

⁷ Division of Glycopathology, Institute of Molecular Biomembrane and Glycobiology, Tohoku Medical and Pharmaceutical University, Sendai, Japan

⁸ Universitätsmedizin Berlin Institut für Biochemie Charité CrossOver Charitéplatz 1 / Sitz, Berlin, Germany

*Corresponding author. Tel: +39-081-6132283; E-mail: raman@ibbc.cnr.it

[†]Deceased.

[‡]These authors contributed equally to this work

[§]Present address: Institute of Nanotechnology, National Research Council (CNR-NANOTEC), Lecce, Italy

influences glycosylation is the Golgi apparatus itself (Varki, 1998; Maccioni *et al*, 2002).

The Golgi apparatus is a central organelle of the secretory pathway that processes newly synthesized cargoes coming from the endoplasmic reticulum (ER), primarily by glycosylation, before sorting them toward their correct destination in the cell. It consists of a stack of 4–11 cisternae (Klumperman, 2011), populated by enzymes and accessory proteins that maintain a suitable milieu for the enzymes to act on biosynthetic cargoes. The stack is polarized with a *cis*-side where cargoes arrive and a *trans*-side from where they leave. The enzymes are not homogeneously distributed across the Golgi stack but are restricted or compartmentalized to 1–3 specific cisternae. The cisternal maturation model provides a conceptual framework for understanding Golgi enzyme compartmentalization (Nakano & Luini, 2010; Glick & Luini, 2011). According to the model, secretory cargoes are transported forward by the anterograde flux mediated by cisternal progression, which consists of constant formation and consumption of *cis* and *trans* cisternae, respectively. The retention of Golgi glycosylation enzymes in the face of this continuous forward flux is mediated by their retrograde transport that acts as counterbalance for the forward transport. The retrograde transport is promoted by coat protein complex I (COPI) machinery (Rabouille & Klumperman, 2005; Popoff *et al*, 2011; Papanikou *et al*, 2015; Ishii *et al*, 2016; Liu *et al*, 2018) and is assisted in this process by adaptor molecules like GOLPH3 (Tu *et al*, 2008, 2012; preprint: Rizzo *et al*, 2019), conserved oligomeric complex (COG) proteins, and Golgi matrix proteins especially Golgins (Eckert *et al*, 2014; Wong & Munro, 2014; Blackburn *et al*, 2019). However, the specific molecular mechanisms and processes by which the same retrograde transport pathway promotes localization of enzymes to distinct cisternae remain unknown.

The compartmentalized localization of enzymes has been suggested to influence both sequential as well as competing glycosylation reactions. The localization of enzymes along the *cis-trans* axis reflecting their order of action (Dunphy & Rothman, 1985) has been suggested to influence the efficiency of sequential processing reactions (Fisher *et al*, 2019). On the other hand, the promiscuity of glycosylation enzymes (Biswas & Thattai, 2020) makes compartmentalized localization of competing enzymes a critical factor in determining the specificity in glycan output (i.e., the type and quantity of glycans produced) (Dunphy & Rothman, 1985; Pothukuchi *et al*, 2019; Jaiman & Thattai, 2020). When two or more enzymes compete for a substrate, the order in which they get access to it can substantially influence the glycans produced and subsequently the physiological outcomes. Competing reactions are frequent in glycosylation pathways, and all known glycosylation pathways have one or more competing glycosylation steps. Nevertheless, how the compartmentalized localization of competing enzymes is achieved, how it is regulated to influence glycosylation reactions, and what the physiological relevance of this regulation is remain unexplored.

To evaluate and understand the contribution of Golgi compartmentalization in regulating glycosylation, we have focused our study on sphingolipid (SL) glycosylation. We chose this model system for several reasons: a. It is well characterized from both biochemical and transcriptional perspectives (Halter *et al*, 2007; D'Angelo *et al*, 2013; Russo *et al*, 2018b); b. the glycosylation reaction is less influenced by the cargo structure in contrast to protein glycosylation and thus is a *cleaner* system to study effects of Golgi

processes on glycosylation; c. there are simple biochemical methods available to analyze SL glycosylation (D'Angelo *et al*, 2013); and d. finally, SLs have important roles in physiology and development (Hannun & Obeid, 2018; Russo *et al*, 2018a). The SL glycosylation pathway exhibits the essential features of glycosylation pathways like localization of enzymes reflecting their order of action and also at least two competing reaction steps that are important in determining the metabolic outcome of the pathway (see below). Further, while enzymes of the pathway are well characterized, molecular players regulating their sub-Golgi compartmentalization are unknown. By studying SL glycosylation, we identify GRASP55 as an important factor that compartmentalizes two enzymes catalyzing critical branch points of the SL glycosylation pathway. GRASP55 binds to and prevents the entry of these enzymes into retrograde transport carriers. This *retaining* action of GRASP55 is essential for dynamic compartmentalization of these enzymes in the Golgi stack. The competing enzymes thus positioned at appropriate levels in the Golgi stack regulate cargo flux across competing reactions of the pathway and determine the metabolic outcome *viz.* sphingolipid produced by the cell. These results delineate a molecular mechanism of enzyme compartmentalization and how it controls cell surface glycan profile.

Results

Disruption of Golgi organization alters SL biosynthesis

SL biosynthesis starts with the production of ceramide (Cer) in the ER, which is then processed in the Golgi to sphingomyelin (SM) or glycosphingolipids (GSLs). The model cell system we use, HeLa cells, produces two species of GSLs—globosides (Gb3) and gangliosides (GM1 and GM3) (Halter *et al*, 2007; D'Angelo *et al*, 2013; Russo *et al*, 2018b) (See Fig 1A for schematic of the SL system in HeLa cells). This SL pathway includes sequential processing of Cer to complex GSLs as well as two bifurcating steps where the substrates get differentially channeled. The first is the bifurcation between SM and glucosylceramide (GlcCer) biosynthesis, where the substrate Cer is channeled into either of the pathways. The second is the biosynthesis of Gb3 or GM3 from lactosylceramide (LacCer). These two critical steps determine the amount and type of SLs produced by the cell. We first examined the localization of SL biosynthetic enzymes and found that they localize to three distinct zones in the secretory pathway (Fig 1B, Appendix Fig S1): (i) the early secretory pathway including the ER and the *cis/medial*-Golgi (C1, C2 cisternae), where Cer biosynthetic enzymes are localized (33), have little if any SL biosynthetic enzymes except for a slightly elevated amount of GM3S and GlcCer synthase (GCS) in the *cis/medial*-Golgi compared with other GSL biosynthetic enzymes; (ii) *medial/trans*-Golgi (C3, C4 cisternae) where most of the GSL biosynthetic enzymes are present alongside substantial amounts of Sphingomyelin synthase 1 (SMS1) and (iii) *trans*-Golgi network (TGN), where SMS1 predominates. While all the GSL biosynthetic enzymes show a gradient of increasing concentration from *cis*- to *trans*-Golgi, the gradient is much sharper in the case of GB3S and LacCer synthase (LCS) compared with GCS and GM3S (Appendix Fig S1). Thus, the SL biosynthetic enzymes are distributed reflecting their order of action with precursor (Cer) producing

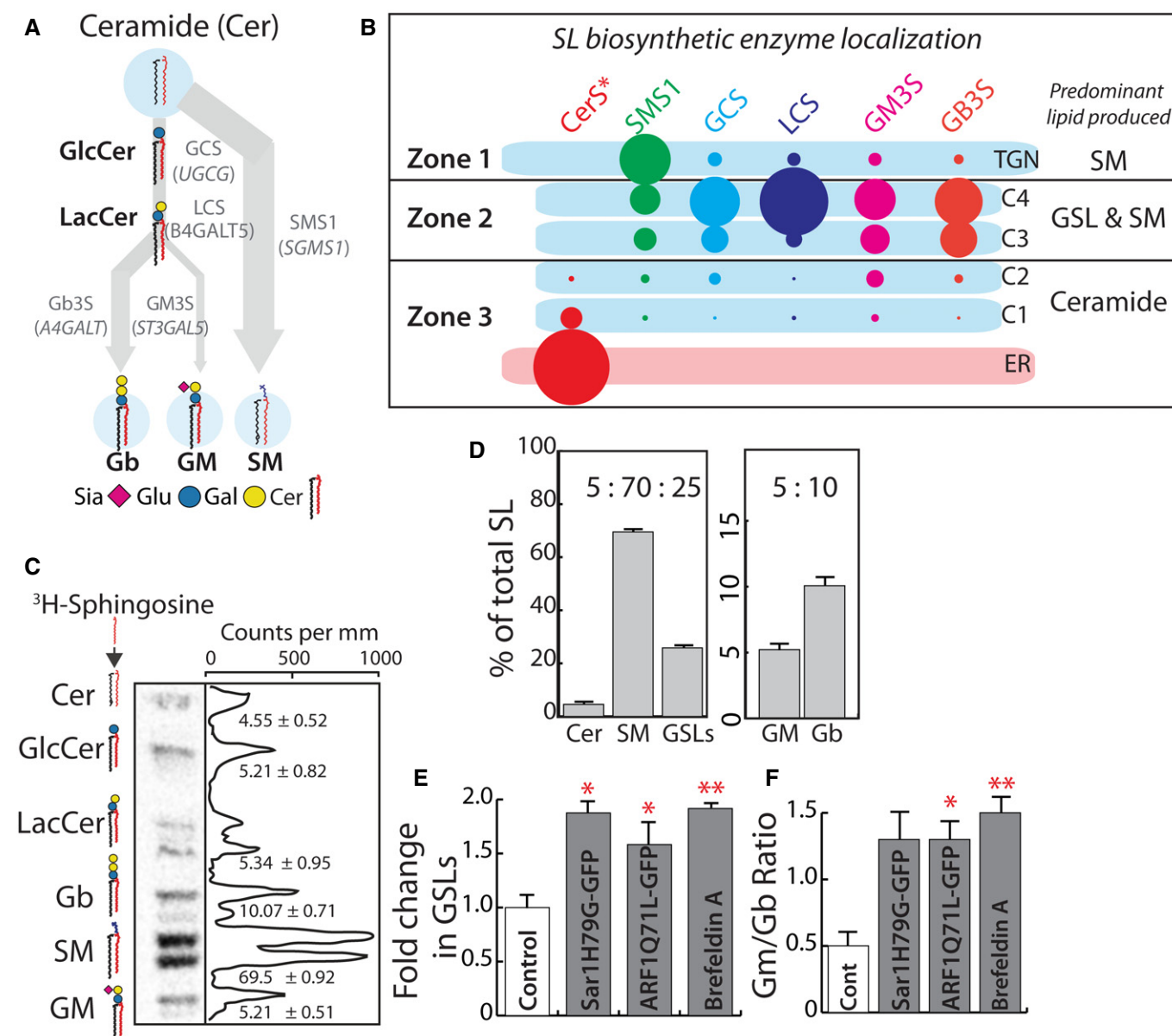


Figure 1. Disruption of SL biosynthetic machinery organization alters SL output.

A Schematic representation of GSL biosynthetic pathway in HeLa cells (Glu, glucose; Gal, galactose; Sia, N-acetylneuraminic acid; Cer, ceramide). Products of biosynthesis are represented in bold and enzymes that catalyze the reactions in gray. The arrows represent the SL metabolic flux from ceramide.

B Schematic representation of GSL biosynthetic zones in HeLa, SM biosynthesis predominates in TGN, whereas GSL and SM productions happen in *medial/trans*-Golgi (C3 and C4 cisternae). *Cis*-Golgi/ER is where Ceramide biosynthesis happens with little, if any, SL production. CerS* refers to the group of Ceramide synthases localized to the ER. The size of the lipid label arbitrarily represents the proportion of the lipid expected to be synthesized in the compartment based on the localization of corresponding enzymes.

C High-performance thin-layer chromatography (HPTLC) profile of HeLa cells pulsed for 2 h with [³H]-sphingosine and chased for 24 h. The peaks corresponding to each SL species are indicated, and numbers represent each SL species as percentage of total SL.

D The total radioactivity associated with Cer, SM, and GSLs (GluCer, LacCer, Gb, and GM), or GM and Gb were quantified and presented as percentages relative to total. Data represented as means ± SD of three independent experiments.

E, F Biosynthesis of SL in HeLa cells expressing GTP-locked mutants of Sar1 or ARF1 or treated with Brefeldin A (BFA; 5 µg/ml) was measured by [³H]-sphingosine pulse-chase assay. Radioactivity associated with GSLs was quantified and represented as fold change with respect to control. (E) For BFA-treated cells, the SL output was measured 8 h after pulse. Data represented as means ± SD of two independent experiments. **P* < 0.05, ***P* < 0.01 (Student's *t*-test). (F) The ratio of GM/Gb is represented. Data represented as means ± SD of two independent experiments. **P* < 0.05, ***P* < 0.01 (Student's *t*-test).

enzymes in the early secretory pathway and the Cer processing enzymes in late secretory pathway, which is in turn divided into two distinct zones where GSL and SM biosynthesis predominate. Of

note, we expressed HA-tagged enzymes (see Materials and Methods) for our studies since the endogenous enzymes were barely detectable and efficient antibodies for EM studies of endogenous

enzymes were not available. Nevertheless, the localization mostly reflects expected localization based on enzyme activity and previously published evidence (Parashuraman & D'Angelo, 2019). A notable exception is the localization of GCS that was shown to be on the *cis*-side of the Golgi (Halter *et al*, 2007) contrary to what we report here. This is because the earlier studies had used a construct with a tag that blocks the signal for intra-Golgi localization that we identify and describe here. When this signal is blocked, localization of GCS is altered resulting in localization to *cis*-Golgi (see below).

Next, SL output of this system was measured by metabolic labeling with ^3H -sphingosine, a precursor of ceramide. This revealed the following distribution of products at *quasi steady state* i.e., 24 h after labeling: SM (70%), globosides (10%), and gangliosides (5%) and rest remaining as precursors (Cer, GlcCer or LacCer; 15%) (Fig 1C and D). The GSLs (globosides, gangliosides, and GSL precursors GlcCer and LacCer) together constituted 25% of total SLs produced. We will refer to the ratio of GSL:SM::25:70 as SL output and the ratio of gangliosides (GM) to Globosides (Gb), GM:Gb::5:10 as GSL output (Fig 1D). For simplicity, the SL output will be represented as GSL fraction since a change in GSLs is always associated with a proportional change in SM in the opposite direction. For GSL output, the situation is complex since a substantial portion of signal remains as precursors (GlcCer and LacCer), and so GSL output will be represented as a GM/Gb ratio which under the control conditions corresponds to 0.5 (GM:Gb::5:10). To summarize, the SL machinery has a compartmentalized localization across the Golgi in HeLa cells and produces a SL output such that 70% of the Cer is directed toward the production of SM and 25% toward the production of GSLs. Within this 25, 5% is directed toward the production of gangliosides and 10% toward the production of globosides.

This distribution of glycoforms produced by the Golgi apparatus has largely been ascribed to the expression of the corresponding glycosylation enzymes (Maccioni *et al*, 2002; Nairn *et al*, 2008, 2012). To assess the contribution of enzyme compartmentalization to this, we monitored SL output after disrupting the spatial organization of SL biosynthetic enzymes by a) overexpressing GTP-locked mutants of monomeric GTPases—secretion-associated Ras-related GTPase (Sar1 H79G) and ADP ribosylation factor 1 (ARF1 Q71L) that are well known to disorganize the secretory pathway (Zhang *et al*, 1994; Aridor *et al*, 1995) and b) by treating the cells with Brefeldin A, which causes relocation of Golgi enzymes back to the ER. Overexpression of Sar1 H79G led to collapse of the Golgi apparatus into the ER with SL biosynthetic enzymes showing a reticular ER pattern (Appendix Fig S2A). On the other hand, overexpression

of ARF1 Q71L mutant led to disruption of stacked cisternal structure of the Golgi, which was replaced by tubulo-vesicular clusters (Appendix Fig S2B), with no separation between *cis*- and *trans*-Golgi markers (Appendix Fig S2C) (List of recombinant DNA used in this study are listed in Appendix Table S2). The treatment with Brefeldin A led to the translocation of the enzymes back into the ER as expected, apart from SMS1 which while present in the ER also displayed presence in some punctate structures (Appendix Fig S2A). The SL output was altered in these cells, and consistently, in all three conditions there was an increased production of GSLs over SM and gangliosides over globosides (Appendix Fig S2D and E). The SL output represented as fold change in GSL fraction showed that GSL production in these cells increased by 1.5–1.9 fold over control cells (Fig 1E). Similarly, GSL output measured as GM/Gb ratio changed from 0.5 in control cells to 1.3–1.5 in treated cells (Fig 1F). These data suggest that impaired spatial organization of enzymes correlates with altered SL output, and especially, the output from steps involving competing reactions is sensitive to disorganization of the Golgi. The contribution of enzyme expression to determination of glycosylation is well established (Nairn *et al*, 2012) but the contribution of the Golgi organization and its importance to this process was not clear. These results underscore a significant and substantive role played by the Golgi apparatus in determining the glycan output of a cell.

GRASP55 regulates SL output by controlling substrate flux between competing glycosylation pathways

Given the importance of the organization of the Golgi apparatus, and likely of the SL biosynthetic machinery localized to the organelle, to determine SL output, we wanted to identify the molecular players involved in this process. Retention of enzymes in the Golgi depends on their COPI-dependent retrograde transport. Golgi matrix proteins especially Golgins contribute to specificity in this process (Wong & Munro, 2014) and thus to compartmentalization of enzymes. So, to identify specific regulators of compartmentalization of SL biosynthetic enzymes, we systematically silenced Golgi matrix proteins and studied the effect on SL production. Among the 14 matrix proteins tested by depletion, downregulation of GRASP55 significantly increased the production of GSLs (a 40% increase in GSLs compared with control) while downregulation of GOPC and GCC2 led to a decrease in GSL levels (Fig 2A) (siRNA sequences used in this study to downregulate indicated human gene expression are listed in Appendix Table S3). We followed up on GRASP55 since

Figure 2. GRASP55 regulates SL biosynthesis.

- A HeLa cells were treated with control or indicated siRNA (pool of 4 or 2 as indicated in methods) for 72 h and SL biosynthesis measured by ^3H -sphingosine pulse-chase assay. GSL levels are expressed as fold changes with respect to control. CERT and FAPP2 knockdowns (blue bars) were used as controls. Data represented are mean \pm SD of three independent experiments $**P < 0.01$ (Student's *t*-test).
- B, C Effect of GRASP55 depletion on SL biosynthesis monitored by ^3H -sphingosine pulse-chase assay in GRASP55 KO cells or cells treated with GRASP55 siRNA or following expression of GRASP55-GFP in GRASP55 depleted cells. GSL levels are expressed as fold changes with respect to control. Data represented are mean \pm SD of three independent experiments $*P < 0.05$, $**P < 0.01$, $***P < 0.001$ (Student's *t*-test). (C) The levels of GM and Gb were quantified and represented as GM/Gb ratio. Data represented are mean \pm SD of three independent experiments $*P < 0.05$, $***P < 0.001$ (Student's *t*-test).
- D Control and GRASP55KO cells were processed for Cy3-conjugated Shiga Toxin (ShTxB) and Alexa488-conjugated Cholera Toxin (ChTxB) staining followed by flow cytometry analysis. Mean fluorescence intensity was measured and represented. Data represented are mean \pm SD of three independent experiments $*P < 0.05$, $***P < 0.001$ (Student's *t*-test). Scale bar: 10 μm .
- E, F SL levels as assessed by LC/MS or MALDI-MS (Gb3) in control and GRASP55 KO (#2) cells. Data represented are mean \pm SD of three independent experiments $*P < 0.05$, $***P < 0.001$ (Student's *t*-test).

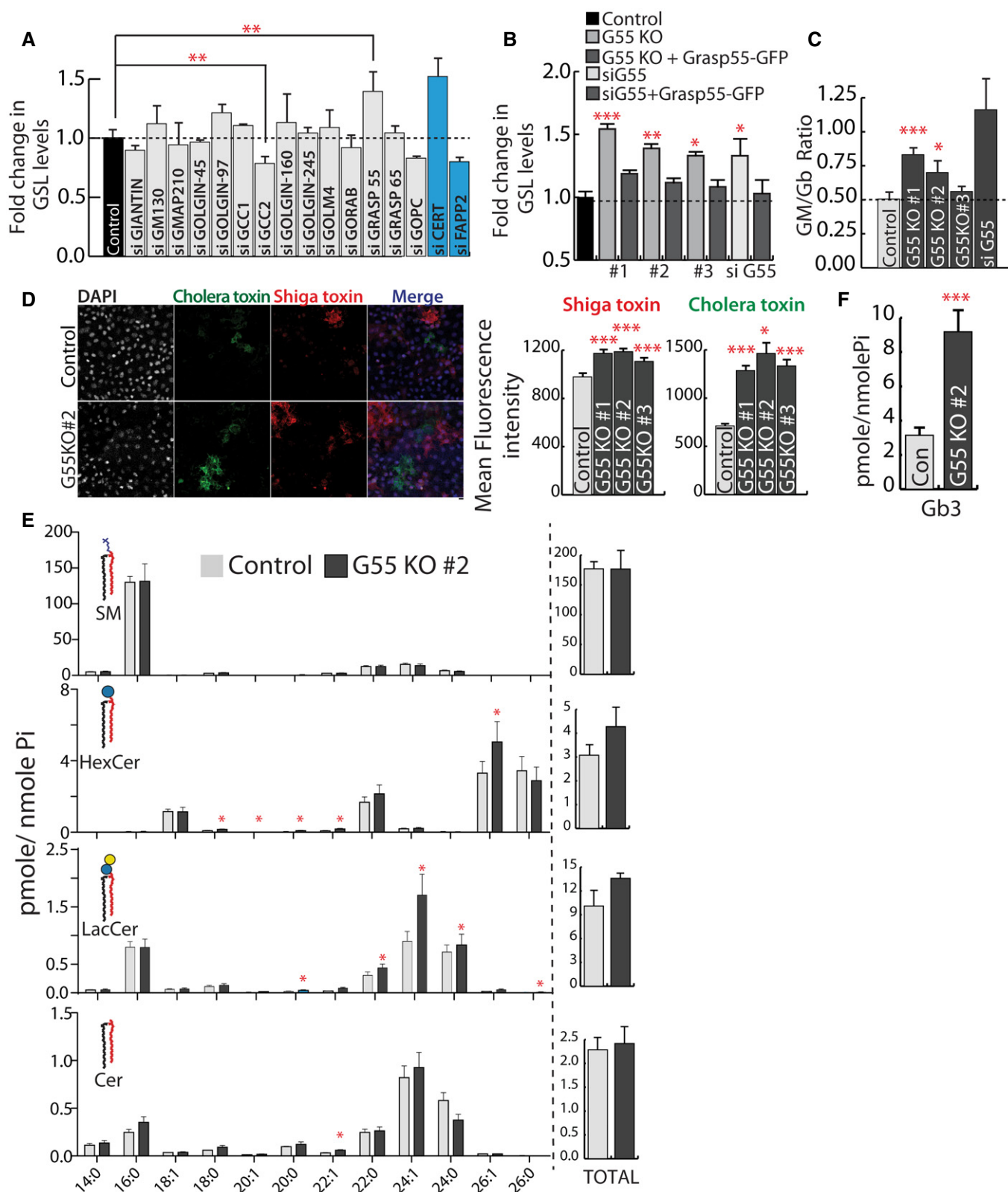


Figure 2.

its depletion altered SL output similar to that obtained by disorganization of the Golgi apparatus (Fig 1E).

GRASP55 was originally identified as a Golgi stacking *protein* using *in vitro* studies (Shorter *et al*, 1999; Xiang & Wang, 2010), but recent studies with knockout (KO) animals and acute protein degradation have demonstrated that removing Grasp proteins does not affect stacking of Golgi (Grond *et al*, 2020; Zhang & Seemann, 2021). Other studies have shown that it plays a role in secretion (both conventional and unconventional) (D'Angelo *et al*, 2009; Kim *et al*, 2016; Chiritoiu *et al*, 2019) and glycosylation (Xiang *et al*, 2013; Jarvela & Linstedt, 2014). So, the function of GRASP55 at the Golgi apparatus and the mechanistic details remains unclear. We generated GRASP55 KO HeLa cells (3 independent clones) using clustered regularly interspaced short palindromic repeat (CRISPR)/CRISPR-associated protein 9 (Cas9) technique (Appendix Fig S3A) (gRNAs used in this study to generate GRASP55 knockout cell lines are listed in Appendix Table S1) (see Materials and Methods). Western blotting and immunofluorescence confirmed the complete abolishment of GRASP55 expression in these KO clones (Appendix Fig S3B and C) while expression levels of other Golgi matrix proteins were not altered (Appendix Fig S3D) (antibodies used in this study are listed in Appendix Table S4). Fragmentation of Golgi ribbon architecture was confirmed using both *cis*- and *trans*-Golgi markers (Appendix Fig S4A–C). The Golgi stack itself did not reveal any obvious alterations with the length of the cisterna, the number of peri-Golgi vesicles, or the fraction of membrane in vesicles and cisternae (Appendix Fig S4D–G). Metabolic labeling experiments showed that biosynthesis of GSLs significantly increased in all three clones (by 30–50%) with a corresponding decrease in SM (Fig 2B, Appendix Fig S5A and B) suggesting a bias toward GSL production in the absence of GRASP55. The total levels of complex GSLs (GM and Gb) also increased and GM/Gb ratio was altered favoring ganglioside production in 2 out of 3 clones, with a strong effect observed only in one clone (G55KO #1) and GRASP55 siRNA-treated cells (Fig 2C). We also analyzed the kinetics of GSL production in GRASP55KO cells (G55 KO#2). SM was produced at similar but faster rate than GSLs in both control and GRASP55 KO cells (Appendix Fig S5A and B) likely because of faster CERT-mediated transport of ceramide for SM biosynthesis (Hanada *et al*, 2003). We also observed differences in the rate of Gb and GM biosynthesis between control and GRASP55 KO cells (Appendix Fig S5A and B). While amounts of Gb were consistently more in GRASP55 KO cells across all time points, a large increase in GM in GRASP55 KO cells compared with control was observed only at the final time point (Appendix Fig S5A and B). Given the very low levels of GM in HeLa cells, the difference between control and GRASP55 KO cells is likely seen only after 24 h of chase. Next, we sought to confirm the increased levels of GSLs in GRASP55 KO cells by complementary methods. GRASP55 KO cells showed increased binding to bacterial toxins (Shiga and cholera toxins that bind Gb3 and GM1 respectively) compared with control cells (Fig 2D, Appendix Fig S5D) (all the Software used for analysis and figure preparation are listed in Appendix Table S8). Mass spectrometry analysis showed that there was an increase in the levels of several species of GlcCer, LacCer, and globosides in GRASP55 KO cell line (Fig 2E and F). A similar increase in GSLs was also observed in GRASP55 KO human fibroblast cell line (Wi-26) (Appendix Figs S3E and S5C). Finally, the change in SL output

associated with GRASP55 abolition was rescued by re-expressing GRASP55-GFP in these cell lines (Fig 2B, Appendix Fig S3C) suggesting that the observed changes in GSLs were specific. We conclude that GRASP55 acts as a regulator of substrate (Cer and LacCer) flux at the two steps that involve competing reactions—SM versus GSLs and gangliosides versus globosides in the SL biosynthetic pathway.

GRASP55 regulates the intra-Golgi localization of GSL biosynthetic enzymes functioning at metabolic branch points

GRASP55 has been proposed to regulate glycosylation by regulating the kinetics of intra-Golgi transport (Xiang *et al*, 2013) and/or ribbon formation (Jarvela & Linstedt, 2014). For GRASP55-mediated regulation of GSL biosynthesis, neither is a likely explanation since the kinetics of GSL biosynthesis (Appendix Fig S5A) is very different from that of protein glycosylation (Xiang *et al*, 2013) and downregulation of several matrix proteins known to fragment Golgi ribbon does not affect GSL biosynthesis (Fig 2A). So, to understand how GRASP55 regulates GSL biosynthesis we first studied the consequences of GRASP55 deletion on the SM biosynthetic machinery (ceramide transfer protein—CERT and SMS1). GRASP55 deletion did not reduce the levels of CERT, and there was surprisingly a consistent increase in SMS1 transcript levels in all 3 clones (Appendix Fig S6A and B). GRASP55 deletion also did not alter their localization to Golgi (Appendix Fig S6C and D) or change the dynamics of CERT (Appendix Fig S6D and E). The kinetics of ceramide transport to the Golgi also remained unaltered (Appendix Fig S6F). These data suggest that SM biosynthesis is not directly affected by GRASP55 deletion.

We next examined the effect of GRASP55 deletion on enzymes of the GSL biosynthetic branch (primers used in this study to determine mRNA levels of indicated gene are listed in Appendix Table S6). There were no consistent changes in their levels (Appendix Fig S7A) or their presence in the Golgi (Appendix Fig S7B) in GRASP55 KO cells (all the commercial kits used for cDNA extraction and mRNA analysis are listed in Appendix Table S7). Their intra-Golgi localization was then examined in nocodazole-induced ministacks with GM130 as a marker for *cis*-Golgi/ *cis*-Golgi network (CGN) compartment and TGN46 as a marker for TGN. Nocodazole-induced ministacks were used since they show a clearer separation of *cis*- and *trans*-Golgi markers and facilitate the intra-Golgi localization of proteins (Rizzo *et al*, 2013; Beznoussenko *et al*, 2014). The peak localization of GSL biosynthetic enzymes was found in the *medial/trans* part of the Golgi in control cells (Appendix Fig S8). When GRASP55 was deleted, the intra-Golgi localizations of GlcCer synthase (GCS) and LacCer synthase (LCS) were shifted in the direction of *cis*-Golgi (Fig 3A and B, Appendix Fig S8A and B) while the localizations of SMS1, Gb3 synthase (Gb3S), and GM3 synthase (GM3S) were not altered (Appendix Fig S8C–E).

The shift toward the *cis*-Golgi was also confirmed by electron microscopy. GCS which is localized mostly to *medial/trans*-Golgi (C3, C4 cisterna) with peak localization in C4 cisterna became evenly distributed across the stack in GRASP55 KO conditions (Fig 3C and D). The *cis*-most cisterna (C1) which had minimal amount of GCS in control cells showed increased levels of GCS in GRASP55 KO cells, where it reached almost the same level as in

other cisternae and in one clone (#2) even resulted in having the peak amount of enzyme (Fig 3D).

In case of LCS, there was a redistribution of the enzyme from *trans*-Golgi (C4 cisterna) to medial-Golgi (C2-C3 cisternae) in GRASP55 KO cells (Fig 3C and E). Unlike GCS, LCS levels in the C1 cisterna did not change significantly (Fig 3E), and thus, the shift in intra-Golgi localization was less pronounced in case of LCS. As a control, the localization of SMS1 was not altered under the same conditions (Appendix Fig S8F). To conclude, GRASP55 deletion changed the intra-Golgi localization of two core enzymes of the GSL biosynthetic pathway involved in metabolic branching steps *viz.* GCS and LCS, shifting them from their mainly *trans*-Golgi localization to more *cis/medial*-Golgi localization. These observations raise the following questions: a. What is the mechanism by which the depletion of GRASP55 causes the shift in localization of GCS and LCS? and b. Is the displacement of enzymes responsible for metabolic effects observed after GRASP55 depletion?

GRASP55 interacts directly with GCS to promote its intra-Golgi localization

To understand how GRASP55 regulates the localization of enzymes, we first studied whether GRASP55 interacts with enzymes of the GSL biosynthetic pathway. We expressed GRASP55-GFP and HA-tagged versions of GSL biosynthetic enzymes in HeLa cells, immunoprecipitated GRASP55-GFP and analyzed for co-immunoprecipitation of HA-tagged enzymes by Western blotting. We found that both GCS and LCS co-immunoprecipitated with GRASP55-GFP while GM3S and Gb3S do not interact (Fig 4A). The interaction of GCS and LCS with endogenous GRASP55 was also observed in human fibroblast cells (Fig 4B). Surprisingly, in spite of significant homology between GRASP55 and GRASP65 proteins (Shorter *et al*, 1999), the enzymes do not interact with GRASP65, underscoring the specificity of the interaction (Fig 4B).

GRASP55 is a peripheral membrane protein that is anchored to the Golgi membrane through its myristoylated N-terminus. So, interaction with GRASP55 is likely mediated by cytosolically exposed portions of the enzymes. Many Golgi glycosylation enzymes are type II membrane proteins with a short N-terminal cytosolic tail, a transmembrane domain, and the luminal enzymatic domain. Thus, the likely part to interact with GRASP55 is the short N-terminal tail. GCS is an exception to this rule and is a multi-transmembrane protein with both N- and C-terminal cytosolic tails and a large catalytic portion facing the cytosol. We noticed that the C-terminal tail of GCS ends with a consensus class II PDZ domain interacting motif (Φ -X- Φ -COOH, where Φ refers to hydrophobic amino acids and X to any amino acid) that can potentially bind to the N-terminal tandem PDZ domains of GRASP55. We chemically synthesized the C-terminal cytosolic tail of GCS and N-terminal cytosolic tails of other GSL biosynthetic enzymes and studied their interaction with GRASP55 present in cell lysates as well as purified His-tagged protein (list of cytosolic peptides used in this study for immunoprecipitation assays are listed in Appendix Table S5).

We found that GCS tail strongly bound to GRASP55 from both cell lysates and the purified protein unlike the tails of other GSL biosynthetic enzymes (Gb3S or GM3S) or the tail of B4GALT1 (see below for description of LCS binding) (Fig 4C and D). We used B4GALT1 a galactosyltransferase involved in protein glycosylation

since it was unrelated to the GSL biosynthetic pathway. GRASP55 consists of two domains—N-terminal tandem PDZ domains (GRASP domain) followed by a serine proline-rich (SPR) region (30). The cytosolic tail of GCS interacted with the GST-tagged GRASP domain of GRASP55 but not with GST-tagged SPR region (Fig 4E). Deleting the Φ -X- Φ -COOH motif in GCS cytosolic tail (GCS- Δ 3C tail) impaired its interaction with GST-tagged GRASP domain of GRASP55 (Fig 4E). Further, deleting this motif also impaired the interaction of full-length GCS (GCS- Δ 3C) with GRASP55 in cells as evidenced by co-immunoprecipitation analysis (Fig 4B). Next to gain further insights into this interaction, we studied it by using isothermal titration calorimetry (ITC). By ITC, we found that the cytosolic tail of GCS interacts strongly with the GRASP domain of GRASP55 with a K_d value of 2 μ M (Fig 4F). Of note, the K_d values of interaction between GRASP55 and the Golgin-45 tail were approx. 0.27 μ M (Zhao *et al*, 2017) and that of the LCS tail and GOLPH3 (another Golgi matrix protein that interacts with Golgi enzymes) were approx. 60 μ M (preprint: Rizzo *et al*, 2019). There was no significant interaction of the GRASP domain of GRASP55 with the GCS tail deleted of Φ -X- Φ -COOH motif or B4GALT1 tail (Fig 4F). These studies in sum suggest that the GCS C-terminal tail directly and specifically interacts with the GRASP domain of GRASP55.

To identify the amino acid residues in GRASP55 that are critical for this interaction, we resorted to modeling. The crystal structure of the GRASP domain of GRASP55 bound to Golgin45 C-terminal region (which contains a hydrophobic amino acid similar to GCS) showed that the peptide binds to a cleft between the PDZ1 and PDZ2 domains of the proteins (Zhao *et al*, 2017). A conserved pocket in the GRASP domain consisting of 95 LLGV 98 corresponding to the X- Φ 1-G- Φ 2 motif (X: any amino acid, Φ : hydrophobic amino acid, G: glycine) acts as a binding site for the C-terminal end of the interacting peptide forming hydrogen bonds with the last four residues of Golgin-45 peptide. The X- Φ 1-G- Φ 2 peptide has a strained left-handed helix conformation, which is usually populated by glycine residues in the Ramachandran plot (Lee & Zheng, 2010). B-factor analysis of the crystal structure of the GRASP55:Golgin-45 complex revealed that the X- Φ 1-G- Φ 2 motif forms a rigid loop (Appendix Fig S9A) where usually Gly is favored over Asp. Indeed, substitution of Gly to Asp abolished the GRASP55-Golgin-45 peptide interaction (Zhao *et al*, 2017). A model of the GCS peptide was first built using the backbone conformation of the Golgin-45 peptide as a template and docked onto the cleft between PDZ1 and PDZ2 domains. The lowest energy model generated was analyzed to probe the protein:peptide interaction. The structural analysis also indicated the important contribution of the 95 LLGV 98 pocket to binding with the C-terminal amino acids of the GCS peptide (Fig 4G). The predicted binding affinity (Δ G) between protein and peptide was -13.1 kcal/mol, indicating a favorable interaction, and when “LDV” was removed from the peptide, the binding affinity was reduced ($\Delta\Delta$ G = -1.5 kcal/mol) indicating the importance of the backbone-mediated conserved hydrogen bonds in peptide binding. Given the overall similarity between the GRASP55-Golgin-45 peptide and GRASP55-GCS peptide interactions, we tested whether the interactions show similar sensitivities to mutations. As mentioned before, the GRASP55-Golgin-45 peptide interaction is sensitive to the substitution of Gly 97 to Asp (Zhao *et al*, 2017) and so we introduced the corresponding G97D mutation in the GRASP55 PDZ domain to examine its effect on the interaction with the GCS tail. The

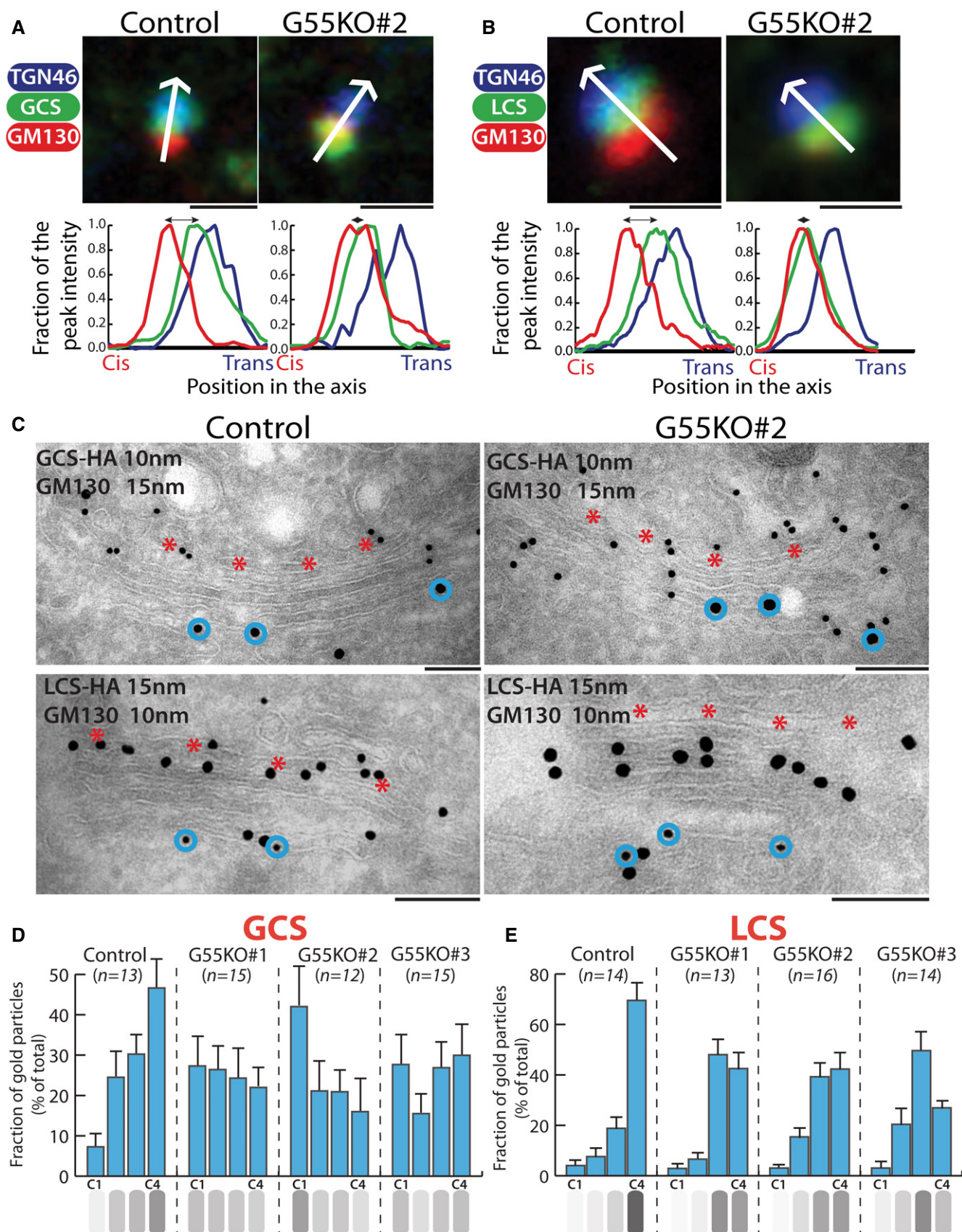


Figure 3.

Figure 3. GRASP55 regulates the intra-Golgi localization of GSL biosynthetic enzymes.

- A, B Control and GRASP55 KO clones were transfected with HA-tagged GSL biosynthetic enzymes, treated with nocodazole (33 μ M) for 3 h, and processed for immunofluorescence with anti-HA (green), anti-GM130 (red), and anti-TGN46 (blue) antibodies. The relative position of HA-tagged enzymes with respect to GM130 and TGN46 was measured by line scanning and expressed as normalized positions of the peak intensity with the start of GM130 peak indicated as *Cis* and the end of TGN46 peak indicated as *trans* in the graph. The double-headed arrows show the distance between the peak localization of GM130 and the enzymes. Scale bar 1 μ m.
- C Control and GRASP55 KO cells were transfected for 16 h with GCS-HA or LCS-HA and processed for cryoimmunolabeling with anti-HA antibody (10-nm gold particles) and anti-GM130 antibody (15-nm gold particles) in case of GCS-HA and anti-HA antibody (15-nm gold particles) and anti-GM130 antibody (10-nm gold particles) in case of LCS-HA. Representative images of the distribution of GCS-HA and LCS-HA are shown. Scale bar 200 nm. Red asterisk marks C4 cisterna and blue circles indicate GM130 labeling.
- D, E Distribution of indicated enzymes across the Golgi stack was quantified and represented as fraction of Gold particles in each cisternae for GCS-HA (D) and LCS-HA (E) (*n* indicated in the graph; data are Mean \pm SEM).

interaction of the mutant protein GCS C-terminal tail was greatly diminished (Fig 4H). Thus, the interaction between GCS and GRASP55 is likely mediated by the C-terminal LDV motif of GCS interacting with the ⁹⁵LLGV⁹⁸ pocket in the GRASP domain of GRASP55 with Gly97 playing a critical role in the process (Fig 4H). Next, we examined whether binding to GRASP55 is essential for intra-Golgi localization of GCS. The last 3 C-terminal amino acids of GCS were deleted (GCS- Δ 3C) and the localization of the mutant protein was studied. The intra-Golgi localization of GCS- Δ 3C was altered, with it displaying a more *cis*-Golgi localization compared with the WT enzyme (Fig 4I and J). Thus, direct interaction with GRASP55 is essential for the correct sub-compartmentalization of GCS.

Compared with GCS, the LCS tail showed a qualitatively weaker interaction with GRASP55 both for endogenous and recombinant protein (Fig 4C). Nevertheless, it was significantly above that of other GSL biosynthetic enzymes (GM3S or GB3S) and that of B4GALT1. This weak interaction was mediated by the GRASP domain of GRASP55 (Appendix Fig S9B). Nevertheless, ITC studies did not show a significant interaction between purified LCS cytosolic tail and the GRASP domain of GRASP55 (Appendix Fig S9C). Thus, in the case of LCS, while the full-length enzyme co-immunoprecipitated with GRASP55, the cytosolic tail of the enzyme itself shows only a weak or no interaction with the protein suggesting that the interaction between LCS and GRASP55 is likely to be indirect. The change in localization of LCS in the absence of GRASP55 correlates with the observed interaction with GRASP55 (Fig 4A and B). In summary, we conclude that GCS and LCS interact with GRASP55, and in the case of GCS, this interaction is direct and is essential for its intra-Golgi localization.

GRASP55 compartmentalizes the enzymes by preventing their entry into retrograde carriers

According to the cisternal maturation model, the retention of resident proteins in the Golgi is due to their continuous retrograde transport mediated by COPI in the face of anterograde flux of cargoes (Nakano & Luini, 2010; Glick & Luini, 2011). In the framework of this model, compartmentalization of enzymes to specific cisternae of the Golgi is achieved by a balance between the anterograde and retrograde flux of enzymes. Indeed, impairing the retrograde transport of enzymes promotes their forward transport leading to their localization to post-Golgi compartments (Rizzo *et al*, 2013). So, to understand how this balance is affected in GRASP55-depleted cells to change the steady-state localization of GCS and

LCS, we examined the distribution of GCS and LCS in peri-Golgi vesicles/carriers. These vesicles depend on COPI for their formation, and entry into these vesicles is essential for the intra-Golgi retrograde transport of proteins (Rizzo *et al*, 2013). In control HeLa cells, the distribution of enzymes in peri-Golgi vesicles varied. For instance, the density of LCS in peri-Golgi carriers was nearly the same as that of the cisterna while the density of GCS in vesicles was 1.8-fold more than that of the cisterna. Further SMS1, an enzyme unaffected by GRASP55 depletion was depleted in peri-Golgi vesicles compared with cisterna (density in vesicles was 0.3-fold that of the cisterna) (Fig 5A–C). These differences in density of enzymes in vesicles correlate well with their observed distribution in the Golgi at steady state, *i.e.*, an increased presence in peri-Golgi vesicles correlates with increased *cis*/medial-Golgi localization. For instance, GCS with higher relative density in peri-Golgi vesicles also has a higher *cis*-Golgi to TGN ratio than SMS1, which has a lower relative density in peri-Golgi vesicles (Appendix Fig S1). This suggests that the presence of proteins in retrograde transport carriers could be a reliable indicator of intra-Golgi distribution of proteins. Next, we studied the density of enzymes in peri-Golgi vesicles in the absence of GRASP55. We found that the density of GCS in vesicles increased to 2.5-fold compared with that present in the cisterna and that of LCS increased to twofold over that of the cisterna, while that of SMS1 was unaltered (Fig 5A–C). Thus, GCS and LCS that show an increased localization to *cis*/medial-Golgi in the absence of GRASP55 also show an increased presence in vesicles in GRASP55 KO cells compared with control, while vesicle distribution of SMS1, whose intra-Golgi localization is unaltered by the absence of GRASP55, remains unchanged. To further validate the increased entry of GCS and LCS into peri-Golgi carriers in the absence of GRASP55, we resorted to *in vitro* budding assays to purify COPI-coated vesicles from Golgi membranes using well-established methods (Yang *et al*, 2002). The Golgi apparatus was purified from control and GRASP55 KO (#2) cells and was incubated with purified coatomer, myristoylated ARF1, and BARS (Brefeldin A ADP ribosylation substrate) to promote budding of COPI retrograde carriers from the Golgi. The budded vesicles were then separated from the Golgi apparatus by centrifugation. The Golgi apparatus was recovered in the pellet fraction while purified COPI vesicles remained in the supernatant fraction (Appendix Fig S10A). We then analyzed the presence of LCS and GCS in the supernatant fractions by Western blotting. We found that there were increased amounts of LCS and GCS in COPI vesicles that budded from the Golgi apparatus purified from GRASP55 KO cells as compared to control cells

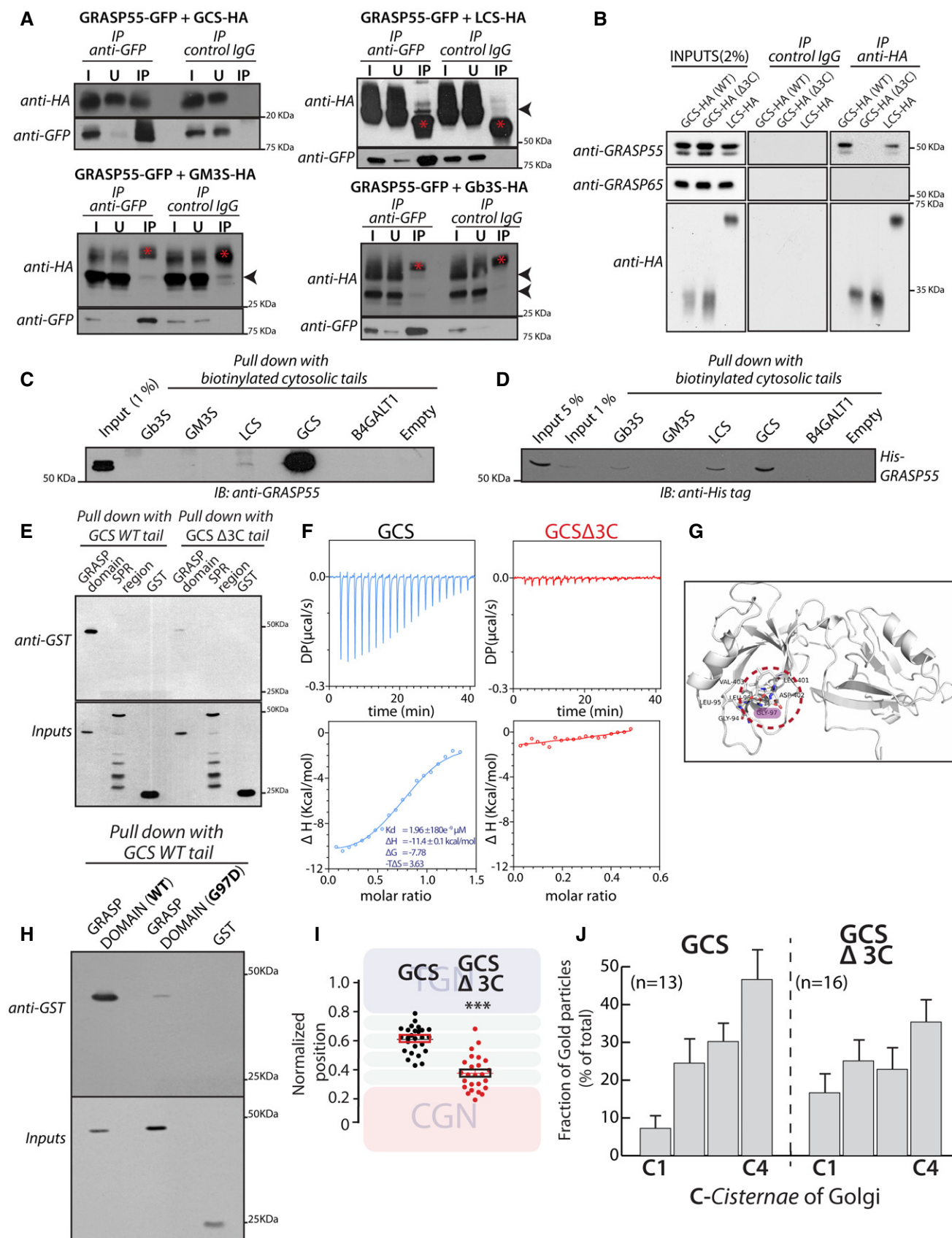


Figure 4.

Figure 4. GRASP55 interacts with GCS and LCS.

- A HeLa cells co-transfected with indicated HA-tagged enzymes (GCS, LCS, GM3S, and Gb3S) and GRASP55-GFP were lysed, immunoprecipitated with anti-GFP antibody or control IgG, and were analyzed by Western blotting for interaction by immunoblotting (IB) with anti-HA antibody. I represents 5% on the input lysate, U 5% of the unbound fraction, and IP the immunoprecipitate. Red asterisks indicate IgG bands, and arrow heads indicate the expected position of HA-tagged enzymes
- B WI-26 fibroblasts transfected with the indicated HA-tagged enzymes were lysed, immunoprecipitated with anti-HA antibody or control IgG, and were analyzed by Western blotting for interaction by immunoblotting with the indicated antibodies.
- C Chemically synthesized biotinylated peptides corresponding to cytosolic portions of glycosylation enzymes were bound to avidin beads and were used to pull down interactors from HeLa cell lysates and subjected to immunoblotting with anti-GRASP55 antibody.
- D The interaction of chemically synthesized biotinylated peptides, corresponding to cytosolic portions of glycosylation enzymes, with purified His-tagged full-length GRASP55 and their interaction was monitored by pulling down the biotinylated peptides bound to avidin beads followed by Western blotting with anti-His tag antibody.
- E Chemically synthesized biotinylated peptides corresponding to cytosolic portions of GCS (WT and $\Delta 3C$) and indicated purified GST-tagged GRASP domain or SPR region of GRASP55 were incubated together, and their interaction was monitored by pulling down the biotinylated peptides with avidin beads followed by Western blotting with an anti-GST tag antibody.
- F ITC profile, representative of at least two independent experiments, for biotinylated GCS and GCS $\Delta 3C$ cytosolic tails with recombinant GRASP55.
- G The molecular basis of interaction between GRASP55 and ceramide glucosyltransferase C-terminal peptide is studied by building a model of GRASP55:GCS peptide structure in the absence of the complex crystal structure. The carboxylate group of Leu of "LDV" motif retains conserved hydrogen bonds with the backbone of 95LLGV98 motif of GRASP55. Gly97 residue which crucial to GRASP:GCS interaction is highlighted (pink).
- H The interactions of chemically synthesized biotinylated peptides corresponding to cytosolic portions of GCS (WT) with the indicated purified GST-tagged GRASP domain (WT) or GRASP domain (G97D) were monitored by pulling down the biotinylated peptides with avidin beads followed by Western blotting with an anti-GST tag antibody.
- I HeLa cells were transfected with either WT GCS or GCS $\Delta 3C$, treated with nocodazole (33 μ M) for 3 h and labeled for enzymes, GM130, and TGN46 (to mark CGN and TGN respectively). Line scan analysis was performed as in Fig 3A and B, and the relative position of enzymes was quantitated and plotted. The data are mean \pm SD ($n = 30$) representative of two experiments. ** $P < 0.01$, *** $P < 0.001$ (Student's *t*-test) and *ns* signifies not statistically significant.
- J HeLa cells were transfected with either WT GCS or GCS $\Delta 3C$ for 16 h and processed for cryoimmunolabeling. Distribution of indicated enzymes across the Golgi stack was quantified and represented as fraction of Gold particles in each cisterna (n indicated in the graph; data are Mean \pm SEM).

Source data are available online for this figure.

(Fig 5D and E), thus confirming our EM observations. The formation of these COPI vesicles depended on the presence of ARF1, ARFGAP, and BARS and did not contain transferrin receptor (a cargo that does not enter COPI vesicles) suggesting that the vesicles purified were indeed genuine COPI vesicles (Fig 5D, Appendix Fig S10A). This specific increase in amounts of GCS and LCS in the peri-Golgi carriers in the absence of GRASP55 is consistent with the hypothesis that GRASP55 limits the retrograde transport of these enzymes.

If absence of GRASP55 alters the distribution of the protein, does an increase in GRASP55 levels also influence their distribution? To test this, we overexpressed GRASP55-GFP in cells along with GSL biosynthetic enzymes LCS and GCS. In the case of LCS, when GRASP55 was overexpressed, there was a change in localization of the enzyme, which was now present in endosome-like structures along with the Golgi (Appendix Fig S10C). These structures were similar to those to which LCS localizes in the absence of GOLPH3, an adaptor that links LCS to COPI and thus promoting its retrograde transport through peri-Golgi vesicles (46). This suggests that overexpression of GRASP55 likely inhibits retrograde transport in a way that is similar to the absence of GOLPH3. On the other hand, overexpression of GRASP55 did not shift GCS to a post-Golgi localization (Appendix Fig S10B) but GCS was increasingly found in the TGN under these conditions (Fig 5F). This suggests that GCS behaves similar to LCS upon GRASP55 overexpression, *i.e.*, its localization shifts to a forward position along the secretory pathway. This distribution of enzymes to TGN or post-Golgi compartment caused by GRASP55 overexpression is consistent with an impairment of their retrograde transport. Thus, GRASP55 likely acts to inhibit retrograde transport of LCS and GCS, such that in its absence the enzymes shift to a *cis*/medial-Golgi localization and when GRASP55 levels are increased, they shift to a TGN/post-Golgi localization.

These observations suggest that GRASP55 prevents retrograde transport of GCS and LCS. In case of LCS, it is known that GOLPH3 promotes its retrograde transport. So we studied what happens to LCS when both GRASP55 and GOLPH3 are removed. GOLPH3KD led to the localization of LCS in endosomal structures (Appendix Fig S10C) as reported earlier (Rizzo *et al*, 2021). Double knockdown of GRASP55 and GOLPH3 also led to a similar phenotype (Appendix Fig S10C) suggesting that GOLPH3 likely acts downstream of GRASP55 such that the effect of GOLPH3 KD dominates over the effect of GRASP55 reduction.

We propose that GRASP55 inhibits retrograde transport of LCS and GCS by acting as a "retainer" that binds to and prevents their entry into retrograde transport carriers. While the action of adaptors, exemplified by GOLPH3, that promote entry into retrograde transport vesicles is well accepted, a *retainer* action in the Golgi apparatus has not been hypothesized before. A retainer molecule that prevents the entry of its interactors into peri-Golgi vesicles can be expected to be absent from the peri-Golgi vesicles unlike adaptor molecules (GOLPH3) that promote the sorting of their interactors into peri-Golgi vesicles (Eckert *et al*, 2014). So, we analyzed the distribution of GRASP55 on the cisterna and on peri-Golgi vesicles. We find that while nearly half of the Golgi-localized GOLPH3 was found in peri-Golgi carriers, only about 8% of the Golgi-associated staining of GRASP55 is associated with peri-Golgi vesicles, suggesting that GRASP55 is likely excluded from peri-Golgi vesicles (Appendix Fig S10D).

Rationalizing these observations into a model, we propose that recycling adaptors and retainers act in an opposing manner to promote compartmentalization of enzymes in the Golgi apparatus. The binding to COPI either directly (Liu *et al*, 2018) or through recycling adaptors like GOLPH3 (Tu *et al*, 2008, 2012) promotes the retrograde transport of enzymes thus preventing their exit from the

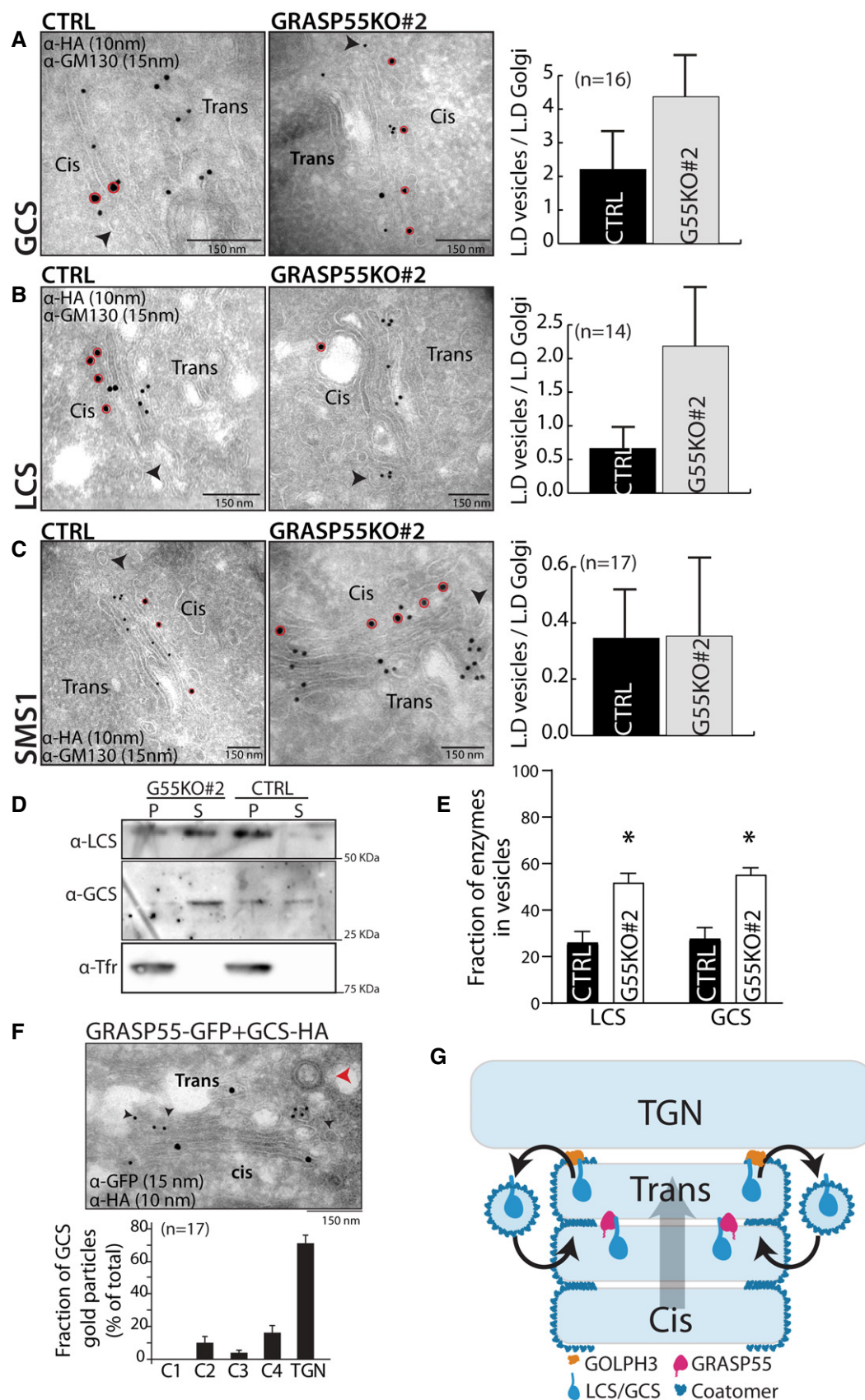


Figure 5.

Figure 5. GRASP55 compartmentalizes the enzymes by preventing their entry into retrograde carriers.

- A–C Control and GRASP55 KO (#2) cells were transfected for 16 h with the indicated HA-tagged enzymes and processed for cryoimmunolabeling with anti-HA antibody (10-nm gold particles) and anti-GM130 antibody (15-nm gold particles). Representative images of the distribution of HA-tagged enzymes are shown. Red circles indicate GM130 labeling. Arrow heads represent the peri-Golgi vesicles. Scale bar 150 nm. Quantification of the distribution of enzymes in vesicles represented as normalized linear density (n indicated in the graph; data are Mean \pm SEM).
- D COPI vesicles were reconstituted using the two-stage incubation system (detailed in the Methods section). After the second-stage incubation, samples were centrifuged to obtain the pellet fraction that contains Golgi membranes and the supernatant fraction that contains reconstituted COPI vesicles. Both fractions were immunoblotted for LCS, GCS, and transferrin receptor (Tfr) to show their relative distributions on Golgi membranes and in COPI vesicles.
- E The COPI vesicle reconstitution system was performed as described above (in D), and then the fraction of LCS and GCS in COPI vesicles versus their total distribution (on Golgi membranes and in COPI vesicles) was calculated. The mean and standard error from three independent experiments are shown, * $P < 0.05$, Student's t -test.
- F HeLa cells co-transfected with HA-tagged GCS and GRASP55-GFP were incubated for 16 h and were processed for cryoimmunolabeling with anti-HA antibody (10-nm gold particles) and anti-GFP antibody (15-nm gold particles). Representative images of the distribution of GCS and GRASP55-GFP are shown. Red arrowhead indicates the clathrin-coated vesicle that marks the TGN area, and black arrowheads indicate the presence of GCS-HA in TGN. Scale bar 150 nm. Distribution of GCS across the Golgi stack and TGN was quantified and represented as fraction of gold particles (n indicated in the graph; data are Mean \pm SEM).
- G Model represents GRASP55-mediated compartmentalization of GCS and LCS. A cyclical and balanced activity of GRASP55 and GOLPH3 compartmentalizes LCS/GCS to the trans-Golgi. The anterograde transport of enzymes (forward direction arrow; cis to trans direction) counterbalances their retrograde transport (reverse direction arrow; trans to cis direction) resulting in the compartmentalization of these enzymes.

Source data are available online for this figure.

Golgi. On the other hand, retainers bind to their client molecules to prevent their entry into retrograde transport carriers and thus indirectly promote their anterograde transport by cisternal progression (Fig 5G). Thus, a cyclical and balanced transport of enzymes—in the retrograde direction by COPI machinery assisted by recycling adaptors and in the anterograde direction by cisternal flow assisted by retainers—compartmentalizes them to specific cisterna of the Golgi apparatus. Of note, this model explains how distinct molecular compositions of cisternae are achieved within the Golgi stack, which includes *cis*- to *trans*-Golgi cisterna where COPI operates (Oprins *et al*, 1993) and not TGN where COPI coat is absent (Ladinsky *et al*, 1999) (Fig 5G).

Change in intra-Golgi localization of GSL biosynthetic enzymes changes GSL output

We then examined whether the change in localization of enzymes following reduction in GRASP55 levels contributes to the associated changes in GSL biosynthesis. When GSL biosynthesis was examined in Brefeldin-A-treated cells, the increased GSL production in GRASP55 KO cells and the increased GM/Gb ratio were not observed (Fig 6A and B), suggesting that compartmentalized localization of enzymes is essential to manifest GRASP55-deletion-induced alteration in GSL production. Of note, while data in Fig 2B suggested that the Gm/Gb ratio was strongly increased only in one clone (G55KO#1), here we observed an apparent increase of GM/Gb ratio in all three clones. This is probably due to the differences in time of chase. While data in Fig 2B were obtained after 24 h of chase, the data in Fig 6B were obtained after 8 h chase (toxicity of BFA prevented longer chase periods). Nevertheless, in both cases the GM/Gb ratio showed similar tendency with G55KO #1 > G55KO #2 > G55KO #3. Next, we examined GSL biosynthesis after expression of GCS and LCS mutants that have altered intra-Golgi localization. We expressed three GCS mutants: a. GCS- Δ 3C that shows more *cis*-Golgi presence than the WT enzyme (Fig 4J), b. GCS with a HA-tag at the C-terminus (GCS-HA_C) that is expected to block accessibility to the C-terminal valine. GCS-HA_C distributes across the stack with significant presence in *cis*-Golgi (30), and unlike GCS-

Δ 3C, it was also partially localized to the ER (Appendix Fig S11A) and c. GCS with a HA-tag in the N-terminal tail (GCS-HA_N), which localizes to ER (Appendix Fig S11A). Thus, they have distinct but overlapping distributions along the secretory pathway. Expression of the wild-type GCS construct in HeLa cells led to a 10% increase in the total GSLs produced compared with non-transfected cells suggesting that expression of the construct does not overwhelm the biosynthetic system. The expression of GCS- Δ 3C, which localizes to the *cis*-Golgi unlike wild-type GCS, led to a 30% increase in GSLs produced, a difference that is quantitatively similar to what is observed between control and GRASP55 KO cells. This suggests that the increased production of GSLs under GRASP55 KO conditions can be explained by the shift in localization of GCS. Interestingly, an increasing ER localization of GCS (GCS-HA_C and GCS-HA_N) led to a larger increase in GSL production (2.3- and 2.6-fold increase, respectively) (Fig 6C). The observed differences in GSL production are not due to differences in expression since addition of Brefeldin A neutralized these differences (Fig 6C), implying that changes in localization were indeed the cause for the observed increase in GSL production.

Next, we examined whether the next branch point in the SL metabolic pathway *viz* GB3-GM3 branch was also sensitive to enzyme localization. The key enzyme regulating this branch point is LCS, whose localization is again controlled by GRASP55. While we find that GRASP55 and LCS interact, there is no convincing evidence for their direct interaction so mutating key residues to decompartmentalize the protein similar to what was achieved for GCS is not possible. While studying the molecular basis of LCS localization, it was found that the 14 amino acid cytosolic tail of LCS contains the information needed to localize the protein in the Golgi (preprint: Rizzo *et al*, 2019). So, we performed alanine mutagenesis of most of the cytosolic tail of LCS (LCS9A) except for the membrane proximal 5 amino acid region essential for interaction with GOLPH3 and the subsequent retention of LCS in Golgi. We found that while LCS9A was still retained in the Golgi apparatus as expected, it localized in a de-compartmentalized manner with no clear trans-Golgi localization as observed with LCS-WT (Appendix Fig S11B). We do not know the reason why these mutations lead to a de-compartmentalized

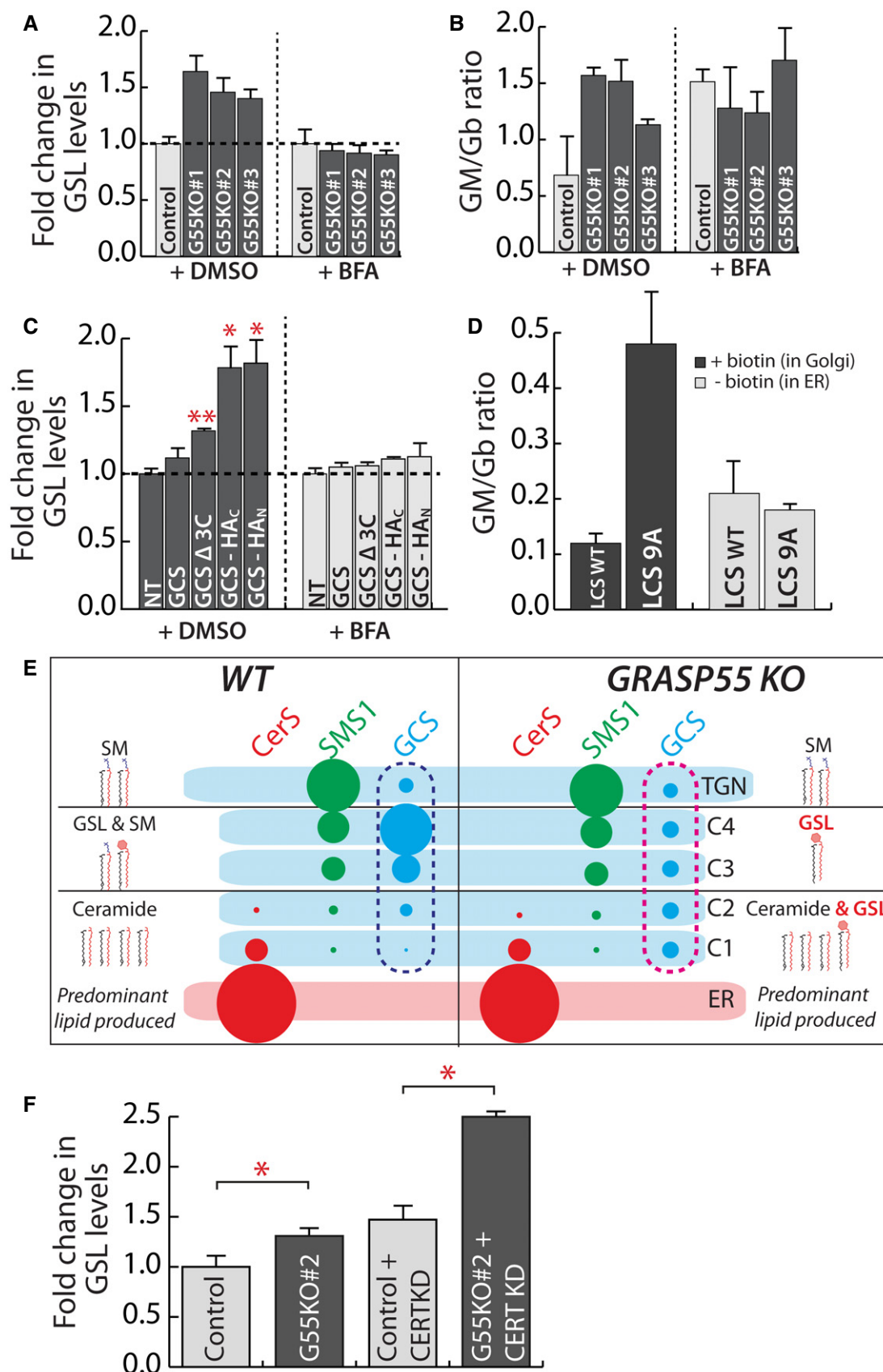


Figure 6.

Figure 6. Change in intra-Golgi localization of GSL biosynthetic enzymes changes GSL output.

- A, B Control and GRASP55 KO clones were pre-treated with DMSO or BFA (5 μ g/ml) for 30 min and SL output monitored by [3 H]-sphingosine pulse-chase assay (8 h chase). Total GSL levels were quantified and expressed as fold changes with respect to control (A). The GM/Gb ratio was calculated and represented (B). Data are mean \pm SD of two independent experiments.
- C HeLa cells were transfected with indicated GCS constructs for 16 h and SL output monitored by [3 H]-sphingosine pulse-chase assay (8 h chase) in the presence or absence of BFA (5 μ g/ml). Total GSL levels were quantified and expressed as fold changes with respect to control. NT refers to non-transfected cells. Data are mean \pm SD of two independent experiments. * P < 0.05, ** P < 0.01, (Student's t -test).
- D HeLa cells KO for LCS were transfected with indicated LCS RUSH constructs for 16 h, and expressed enzymes were retained in the ER (-biotin) or placed in the Golgi by the addition of biotin (40 μ M) (+biotin) and SL output monitored by [3 H]-sphingosine pulse-chase assay. The ratio of GM/Gb is represented. Data are mean \pm SD of two independent experiments.
- E Schematic representation of how the change in localization of GCS in GRASP55 KO with respect to control (pink dashed box versus blue dashed box) from trans- to cis-Golgi results in preferential access to ceramide and thus an increased production of GSLs.
- F CERT was silenced using siRNAs for 72 h in control and GRASP55 KO (#2) clone before subjecting to [3 H]-sphingosine pulse-chase assay. GSLs were quantified and represented as fold change with respect to control. Values are mean \pm SD (n = 3). * P < 0.05, (Student's t -test).

localization of LCS, but they provide an opportunity to test whether compartmentalization of LCS regulates the flux across Gb3-GM3 branches similar to what was observed with GCS. To this end, we analyzed the GSL output following the expression of LCS-WT and LCS9A constructs in LCS-KO HeLa cells (Yamaji & Hanada, 2014). We found that the expression of LCS9A in Golgi favored the production of gangliosides over globosides as compared to LCS-WT. Thus, the GM/Gb ratio of 0.12 that is observed in case of LCS-WT-expressing cells changed to 0.47 in case of LCS9A-expressing cells (Fig 6D). The differences were nullified when the enzymes were retained in the ER (Fig 6D) suggesting that the observed differences were likely due to an altered intra-Golgi localization of these enzymes. Thus, a change in LCS localization observed in GRASP55 KO conditions may contribute to the observed increase in GM/Gb ratio in these cells. From these data, we conclude that altered localization of key enzymes of the GSL pathway can reproduce the effects on SL biosynthesis following GRASP55 deletion and that localization of enzymes in the Golgi can control cargo flux across competing biosynthetic pathways.

To explain the effects of GRASP55 KO on GSL biosynthesis based on these results, we thus considered the localization of these respective enzymes. As discussed earlier, most of the GSL biosynthesis likely happens in the medial/trans-Golgi where along with the GSL enzymes, a substantial portion of SMS1 is also localized (Fig 1B). This likely leads to a competition between SMS1 and GCS for Cer that is transported by vesicular transport to the medial/trans-Golgi (Fig 6E). By moving GCS to the cis-Golgi, as happening in GRASP55 KO cells, the enzyme now gets preferential access to Cer and resulting in an increased production of GSLs (Fig 6E). Indeed, in CERT KD cells where the non-vesicular transport of Cer is blocked and Cer reaches the Golgi mostly by vesicular transport, the effect on GSL biosynthesis resulting from the absence of GRASP55 is further increased (Fig 6F) suggesting that GCS and SMS1 compete for Cer that is transported by vesicular transport to the Golgi. The effect of GRASP55 KO on GSL output can also be explained by a similar logic. While both GM3S and Gb3S are localized mainly to the medial/trans-Golgi, significant amounts of GM3S can also be seen in cis/medial-Golgi unlike Gb3S (Appendix Fig S1). Thus, when LCS is moved toward the cis/medial-Golgi, ganglioside biosynthesis by GM3S is favored over globoside biosynthesis likely due to preferential access of GM3S to the substrate LacCer.

Thus, these data provide a model of how compartmentalization of enzymes in the Golgi contributes to faithful glycan output. When

two enzymes compete for a common substrate and are localized in the same compartment, the product of a glycoenzyme with more affinity for substrate and/or increased expression dominates the glycan output. On the other hand, if one of the competing enzymes is present in an earlier part of the secretory pathway relative to the other, it gets preferential access to the substrate before its competitor and thus promotes flux across the pathway catalyzed by it resulting in a glycan output that has a bias toward the product of this enzyme. Thus, positioning of enzymes in the Golgi regulates the pattern of glycan distribution in the output.

Discussion

Here, we describe how GRASP55 compartmentalizes two key GSL biosynthetic enzymes—GCS and LCS by binding to these enzymes and preventing their entry into retrograde transport carriers. This action of GRASP55 opposes COPI-mediated retrograde transport of residents, and a balance between these two actions compartmentalizes the enzymes to trans-Golgi. Translocation of the enzymes to cis-Golgi in the absence of GRASP55 provides them a privileged access to cargoes thus favoring the reactions catalyzed by them. This is the first time a molecule that specifically regulates intra-Golgi localization of glycosylation enzymes is described and that acts by preventing the entry of cargoes into COPI carriers. This study has important implications for the cell biology of Golgi organization as well as glycobiology which we discuss below.

Mechanisms regulating Golgi compartmentalization

The retention of glycosylation enzymes in the Golgi apparatus is due to their continuous retrograde transport by the COPI machinery. How the same retrograde transport machinery achieves the compartmentalization of enzymes to different cisterna was not clear. The discovery of an enzyme adaptor—GOLPH3 acting at the trans-Golgi—suggested that trans- and cis-Golgi-localized enzymes may have differential modes of interacting with the COPI machinery. While the cis-Golgi-localized proteins interacted with COPI directly (Liu et al, 2018), the trans-Golgi residents may require an adaptor recruited specifically to the trans-Golgi, thus allowing the same COPI machinery to compartmentalize enzymes to two different sub-Golgi compartments. Our discovery of GRASP55 actively prevents entry of enzymes into COPI vesicles and shows this

process is more elaborate and with both retaining and recycling adaptors required for appropriate localization to the Golgi. Indeed, in the absence of GRASP55 and with only GOLPH3 present, the compartmentalization of LCS is altered. Thus, compartmentalization of Golgi residents is a dynamic process resulting from a balance between their anterograde and retrograde flux mediated by retaining and recycling adaptors, respectively (Fig 5G). Recently, GRASP proteins have been suggested to regulate COPI vesicle dynamics (Xiang *et al*, 2013; Grond *et al*, 2020). This activity of GRASP55 may further contribute to oppose the retrograde transport of residents. Of note, GRASP proteins have been linked to the Golgi localization of p24 (Barr *et al*, 2001) and the transport of cargoes through the Golgi (D'Angelo *et al*, 2009). To prove, whether these effects are also linked to the role of GRASP55-mediated sorting into COPI vesicles needs to be investigated. Given the well-known regulation of GRASP55 and GOLPH3 activities by phosphorylation in response to various stimuli, we expect that regulation of glycosylation by altering Golgi compartmentalization may turn out to be a regulated physiological phenomenon.

We also note that there are several other Golgi-resident proteins with canonical PDZ domain-binding motifs, which includes other enzymes and channels. Thus, GRASP55 (and possibly GRASP65) may play a wider role in the localization of several proteins in the Golgi.

Regulation of glycosylation by GRASP55

GRASP55 was originally discovered as Golgi stacking protein (Shorter *et al*, 1999; Xiang & Wang, 2010), but recent studies have unequivocally shown that absence of GRASP proteins does not affect Golgi stacking (Grond *et al*, 2020; Zhang & Seemann, 2021) leaving the role of this protein obscure. In this light, the contribution of GRASP55 to conventional as well as unconventional secretion (D'Angelo *et al*, 2009; Kim *et al*, 2016; Chiritoiu *et al*, 2019) and glycosylation (Xiang *et al*, 2013; Jarvela & Linstedt, 2014) become prominent areas to investigate. Its effect on glycosylation was proposed to be indirect through regulation of the kinetics of intra-Golgi transport of cargoes (Xiang *et al*, 2013) and/or ribbon formation (Jarvela & Linstedt, 2014). For GRASP55-mediated regulation of GSL biosynthesis, neither is a likely explanation since kinetics of GSL biosynthesis (Appendix Fig S5A) is very different from that of protein glycosylation and downregulation of several matrix proteins known to fragment Golgi ribbon does not affect GSL biosynthesis (Fig 2A). Instead, we show that absence of GRASP55 leads to a change in the localization of LCS and GCS (Fig 3). This alters SL production by providing a privileged early access of substrates to these enzymes and/or providing them a more permissive environment (Hayashi *et al*, 2018; Ishibashi *et al*, 2018) and thus increases GSL production (Fig 6E). Thus, our study here provides a mechanistic view of how GRASP55 regulates glycosylation and identifies an important role for this protein in the Golgi function.

It is well known that presence of two Grasp proteins is a feature of vertebrates while other organisms have only one Grasp protein and plants have none at all (Vinke *et al* 2011). Since this single Grasp protein is mostly localized in the cis-Golgi similar to GRASP65 (Vinke *et al* 2011), the medial-Golgi-localized GRASP55 is probably an evolutionary innovation of vertebrates. Analysis of GCS sequences showed that the C-terminal 3 amino acid PDZ domain-binding motif

is conserved only in vertebrates (Appendix Fig S9D) thus paralleling the evolution of GRASP55. This co-evolution of a protein and the interaction motif on its client suggests the evolution of a regulatory mechanism for GSL biosynthesis. The absence of classical PDZ binding motifs in other organisms may likely reflect the absence of such a regulation in these organisms.

Given the close link between GSL metabolism and cancers, we analyzed whether GRASP55 expression is altered in cancers. There were no significant alterations at the genomic level (mutations or copy number alterations) at the *GRASP55* loci, but expression levels of GRASP55 were moderately low in acute myeloid leukemia, kidney cancers, and thymoma compared with other cancer types (www.cbioportal.org). Acute myeloid leukemic cells are known to have increased levels of GSLs compared with non-transformed lymphocytes (Wang *et al*, 2012). Whether GRASP55 contributes to this phenomenon is worthy of exploration. Further, mouse insertional mutagenesis studies have found that inactivation of GRASP55 promotes tumorigenesis in liver and colorectal cancer models (Ref: Candidate Cancer Gene Database). Thus, studying the contribution of GRASP55 to cancer through its role in the regulation of GSL biosynthesis could be an interesting area to explore.

SL biosynthesis

SL biosynthesis depends on CERT-mediated transfer of ceramide from ER to TGN for SM biosynthesis (Hanada *et al*, 2003) and FAPP2-mediated transfer of GlcCer from *cis*-Golgi to TGN for Gb3 biosynthesis (D'Angelo *et al*, 2013). Earlier reports had shown that GCS and SMS1 are present in *cis*- and *trans*-Golgi respectively (Halter *et al*, 2007). Surprisingly, we observe that GCS is present in the *medial/trans*-Golgi. We ascribe the observed difference in localization of GCS to the use of constructs with a tag that blocks the C-terminus (important for interaction with PDZ domain of GRASP55) in the previous studies (Halter *et al*, 2007). This revised localization of GCS has implications for the model of SL biosynthesis: If GCS is localized to *trans*-side why is the activity of GCS not sensitive to CERT KD? While GCS is indeed present in the *trans*-Golgi, a large fraction of SMS1 is present in a distinct compartment, the TGN. CERT-mediated transfer of ceramide likely happens at the TGN, and thus, SMS1 depends on ceramide delivered by CERT unlike GCS.

To sum up, we identify a novel molecular pathway regulated by GRASP55 that compartmentalizes specific glycosylation enzymes and by this action modulates the competition between reactions to achieve a specific cellular glycan profile.

Materials and Methods

Reagents

All reagents and chemicals were molecular biology grade. Methanol (Cat # 9093) and chloroform (Cat # 9180) were purchased from JT Baker, USA. Silica-gel high-performance TLC (HPTLC) plates (Cat #1055830001) were purchased from Merck, Germany. Fatty acid-free Bovine Serum Albumin (Cat #A8806), HA Peptide (Cat #12149), and Brefeldin A (Cat #B7651) were purchased from Sigma-Aldrich, Germany. Protein A Sepharose CL-4B (Cat #17-0780-01) was purchased from GE Healthcare Life Sciences, USA. Anti-HA

magnetic beads (Cat #88836) were purchased from ThermoFisher Scientific, USA. Sphingosine, [3-³H]-, D-erythro > 97% (Cat #NET1072050UC) was purchased from PerkinElmer, USA. Lipofectamine 2000 (Cat #11668027) and Lipofectamine LTX with PLUS (Cat #15338100) were purchased from ThermoFisher Scientific, USA. TransIT-LT1 (Cat #MIR 2305) was purchased from Mirus, USA. RPMI 1640 (Cat #21875), DMEM (Cat #41965), DMEM/F-12 (Cat #11320033), and FBS (Cat #10437036) were purchased from Gibco/ThermoFisher Scientific, USA. BODIPY™ FL C5-Ceramide (Cat #D3521) was purchased from ThermoFisher Scientific, USA. Protein A gold 15 nm and Protein A gold 10 nm were acquired from Cell Microscopy Core, UMC Utrecht. Biotin (Cat #29129) was purchased from Pierce, USA. Bacterial strains *E. coli* (DH5 α) (Cat #18265017) and *E. coli* (BL-21-DE3) (Cat #C600003) were purchased from Thermo Fisher Scientific, USA. All the siRNAs and qPCR primers indicated in Appendix Tables S3 and S6 respectively were purchased from Sigma-Aldrich, Germany.

Cell lines

HeLa-M (human cervical cancer cells, female origin) was a kind gift from Prof. Paul Lehner, University of Cambridge. Wild-type and GRASP55 knockout Human Fibroblasts (WI-26) were a kind gift from Markus Plomann, Institute for Biochemistry, University of Cologne. TALEN LCS-KO HeLa cell line (human cervical cancer cells, female origin) was kind gift from Kentaro Hanada, National Institute of Infectious Diseases, Japan. HeLa-M and GRASP55 KO HeLa cell lines (see below) were cultured in RPMI-1640 supplemented with 10% FCS. TALEN LCS-KO cell lines were cultured in DMEM supplemented with 10% FCS. Wild-type and GRASP55 knockout Human Fibroblasts (WI-26) were cultured in DMEM: Nutrient Mixture F-12 (DMEM/F-12) supplemented with 10% FCS. All media were supplemented with 100 U/ml penicillin/streptomycin and 2 mM L-glutamine. All cells were grown in controlled atmosphere (5% CO₂ and 95% air) at 37°C. Mycoplasma contamination was not observed in cell cultures as observed by DAPI staining. Cell cultures between 3 and 15 passages were used for the experiments, and the cells were cultured to 80% confluence for the experiments unless indicated otherwise.

Generation of GRASP55 Knockout cell lines by CRISPR-CAS9

To generate HeLa-M cell lines in which GRASP55 expression was abolished, we performed genome editing using CRISPR/Cas9 system. We obtained a pool of three plasmids each encoding guide RNA (gRNA) sequence designed to target GRASP55 coding sequence and pSpCas9 ribonuclease (Cat # SC-401106; Santa Cruz Biotechnology, Inc.). The list of gRNA sequences are reported in Appendix Table S1. These plasmids also encoded EGFP allowing positive selection of transfected cells. HeLa-M cells were transfected with pooled plasmid for 48 h, EGFP-positive cells were isolated by FACS, and single cells were sorted into each well of 96 well plates. The single cells were maintained in optimal culture conditions for 10 days, by replenishing fresh media every 48 h. After 10 days, colonies formed from single cells were trypsinized and moved to 48 well plates and expanded to 6 well plates. Clones were collected, and protein lysates were subjected to SDS-PAGE analysis and Western blotting analysis using GRASP55-specific antibody to assess the presence of GRASP55 protein.

Generation of expression constructs

GCS-HA was generated by inserting 9aa HA- tag into the C-terminal cytoplasmic tail of GCS between the two indicated Gly residues DPTISWRTGRYRLRC**GG**TAAEILDV. The following oligonucleotide primers used:

F:5'/GCTGGAGAACTGGTCGCTACAGATTACGCTGTGGGTACCCA
TACGATGTTCCAGATTACGCTGGTACAGCAGAGGAAATCCTAGAT
GTATGATAAAGTCG-3'/R:5'/CGAGTTATCATACATCTAGGATTTCTCT
TGCTGTACCAGCGTAATCTGGAATATCGTATGGGTACCCACAGCG
TAATCTGTAGCGACCAAGTTCTCCAGC-3'

GCS Δ3C (del of three C-terminal amino acids) was obtained by PCR-amplifying GCS with the following primers to introduce a stop codon after the isoleucine residue at position -4 (DPTISWRT-GRYRLRCGGTAEEILDV):

F: 5'-CATCGCGGATCCATGGCGCTGCTGGACCTG-3' and

R: 5'-GATCCGCTCGAGTTATCAGATTTCCTCTGCTGTACCAGCG
TAATC-3'

The PCR-generated fragment for both constructs was digested with EcoRI and XhoI (New England Biolabs, USA) and cloned into pcDNA4b-3xHA expression vector. LCS9A Mutant (mutation of 9 amino acids to alanine in cytosolic tail of LCS) was generated by PCR amplification of LCS-WT-RUSH with following primers to introduce alanine into 9 amino acids (MAAAAAAAAAAPRRSLLA):

F: 5'-CACAACCCGGGAGGCGGCCATGGCAGCAGCAGCAGCAGCAGCAGCAGCA-3'

R: 5'- GCGAGCAGCGAGCGGCGGGTGTCTGCTGCTGCTGCTGCT
GCTGCTGC -3'. The PCR-generated megaprimer was then annealed
into LCS-WT-RUSH at 66°C and extension at 72°C for 25 cycles.

Plasmids and siRNA transfection

HeLa-M cells, Wi-26 cells, LCS-KO cells, and GRASP55 KO cells were transfected with plasmid vectors using TransIT-LT1 or Lipofectamine LTX reagents. A list of plasmids used in this study can be found in Appendix Table S2. Knockdown experiments for HeLa-M cells were carried out using a pool of 4 siRNAs or 2 siRNAs using Lipofectamine 2000 according to manufacturer's instructions (used at concentration of 100nM for the target gene). Expression or knockdown efficiencies (> 85%) were checked after every experiment either by indirect immunofluorescence or immunoblotting or by qPCR analysis. A list of siRNA sequences used in this study can be found in Appendix Table S3.

Cell lysis, Western blotting, and analysis

Cells were washed three times with ice-cold PBS and lysed immediately at 4°C in RIPA lysis buffer (0.1% Triton X-100, 20 mM Tris-HCl, pH 8.0, 0.1% SDS, 0.05% sodium deoxycholate, 150 mM NaCl, 10 mM Na₃VO₄, 40 mM β-glycerophosphate, and 10 mM NaF) and complete protease/phosphatases inhibitors (Roche). Cell lysates were clarified at 20,000 g for 10 min at 4°C to eliminate detergent-insoluble pellet. To visualize GCS on SDS-PAGE, the protein lysates prepared as described above were treated with 250 mM of DTT in sample buffer (62.5 mM Tris-HCl, pH 6.8, 2% SDS, 10% glycerol, 0.001% bromophenol, and 125 mM dithiothreitol) at 37°C for 30 min. The lysate was immediately processed for SDS-PAGE and immunoblotting with antibodies. A complete list of primary and

secondary antibodies are given in Appendix Table S4. The Western blots were then exposed to X-ray films, and exposure time was varied to obtain optimal signal.

Immunoprecipitation and peptide pull down assay

Total lysates were prepared using IP lysis buffer (150 mM NaCl, 25 mM Tris-HCl pH 7.5, 1% Triton X, 10 mM Na₃VO₄, 40 mM β -glycerophosphate, 10 mM NaF, and protease cocktail inhibitor from Roche). The protein concentrations were quantified using BCA Protein Assay kit (Pierce). 1 mg of protein was used for precipitation with antibodies conjugated to either Protein A sepharose or magnetic dynabeads or to monomeric avidin beads (Pierce) in case of cytosolic peptides, and incubated at 4°C overnight. The beads were then washed 5 times in IP lysis buffer, and bound proteins were subjected to SDS-PAGE and immunoblotted. The list of cytosolic peptides used in this study are reported in Appendix Table S5.

Reconstitution of COPI vesicle formation

A two-stage incubation system was performed essentially as previously described (Yang *et al*, 2005). In brief, the first stage involved incubating prewashed (3 M KCl) Golgi membrane (0.4 mg/ml) with coatamer (6 μ g/ml), ARF1 (6 μ g/ml), and 2 mM GTP in 500 μ l of assay buffer (25 mM Hepes-KOH, pH 7.2, 50 mM KCl, 2.5 mM Mg (OAc)₂, 1 mg/ml soybean trypsin inhibitor, and 200 mM sucrose) for 15 min at 37°C. Afterward, the Golgi membrane was pelleted (12,000 \times g at 4°C for 10 min) and then resuspended in 100 μ l of assay buffer for the second-stage incubation, which had ARFGAP1 (6 μ g/ml) and BARS (6 μ g/ml) added for 10 min at 37°C. Samples were then centrifuged for 10 min at 12,000 g and 4°C, with the pellet fraction containing the Golgi membrane and the supernatant fraction containing COPI vesicles.

Protein purification

Recombinant proteins were induced to express with 0.3 mM isopropyl β -D-thiogalactoside in BL21 (DE3) competent bacterial cells for 16 h at 22°C. Cells were harvested at 7,519 g for 30 min at 4°C, lysed in lysis buffer (cold PBS with 1 mM DTT, 1% triton X-100, phosphatase, and protease inhibitors), and purified with Glutathione Sepharose 4B beads (GE Healthcare, USA). Recombinant GST-tagged proteins were eluted in elution buffer (50 mM Tris, 100 mM NaCl, 50 mM reduced glutathione, and pH 8.0); purified recombinant proteins have been concentrated and the buffer has been exchanged by using Vivaspin TURBO 4 filters (Sartorius, UK) at 4°C and 4,000 \times g. The recombinant purified proteins were quantified by Bradford assay and were assessed for contaminants by SDS-PAGE.

Isothermal titration calorimetry (ITC)

ITC experiments were performed in a buffer containing 300 mM NaCl, 10 mM Bicine pH 8.5, and 1 mM DTT. Biotinylated peptides were synthesized and delivered as lyophilized powder with a biotin moiety located at the N or C-terminus (Charite Universitaetsmedizin Berlin, Germany). The peptides were dissolved in buffer, centrifuged at 14,000 \times g for 10 min, and only the supernatant was used. The dissolved peptide concentrations were calculated based upon their

absorbance at 280 nm and their corresponding molar extinction coefficient. Experiments consisted of titrations of 20 injections of 2 μ l of titrant (peptides) into the cell containing GRASP domain protein at a 25-fold lower concentration. Typical concentrations for the titrant were around 2.5 mM for experiments depending on the affinity. Experiments were performed at 25°C and a stirring speed of 1,000 rpm on a MicroCal PEAQ-ITC (Malvern Panalytic). All data were processed using MicroCal PEAQ-ITC Analysis Software and fit to a one-site binding model after background buffer subtraction.

GRASP55-GCS peptide modeling

Model of GCS peptide was first built using backbone conformation of Golgin45 peptide as a template and fit into the same cleft of GRASP55, where Golgin45 peptide is located using COOT (Emsley & Cowtan, 2004). This initial complex structure was further refined by the Docking2 module of Rosetta protocols through local docking search (Lyskov & Gray, 2008; Chaudhury *et al*, 2011; Lyskov *et al*, 2013). The lowest energy model generated by this protocol was analyzed to probe the protein:peptide interaction. PRODIGY software was used to calculate the protein-protein binding energy (Vangone & Bonvin, 2015; Xue *et al*, 2016).

Immunofluorescence and confocal microscopy

Indirect Immunofluorescence was performed as follows: cells were grown on 24 mm coverslips, washed with PBS, and fixed in 4% paraformaldehyde (Electron Microscopy Sciences, Hatfield, USA) for 30 min at room temperature (RT). The cells were then permeabilized and blocked in blocking buffer (0.05% saponin and 0.5% BSA in PBS) for 30 min at RT followed by incubation with specific primary antibodies (see Appendix Table S4) for 1 h at RT and washed with PBS. Cells were subsequently labeled with appropriate Alexa Fluor-conjugated secondary antibodies (Appendix Table S4). The coverslips were mounted using mowiol, and images are acquired using confocal microscope Zeiss LSM700.

Line scan analysis

The images were acquired with a pinhole set to 1 airy unit and under non-saturation conditions using a 63 \times objective (1.4 NA). Images were 8 bit with dimensions of 512 \times 512 pixels, and each pixel corresponded to an area of 132 \times 132 nm². The line scan analysis was performed as described previously (Rizzo *et al*, 2013) using the Zen software system (Carl Zeiss). In brief, images of stacks stained for GM130, TGN46, and enzyme of interest tagged with HA were acquired as described earlier. Only cells with a moderate level of expression were considered for the analysis. Golgi stacks with clearly separated GM130-stained and TGN46-stained zones were identified and used for the analysis. A line was drawn in the middle of the stacks along the cis-trans direction, and the fluorescence intensity of each stained marker along this line was plotted. At least 30 stacks were examined per treatment, and a representative data are shown for analysis. The normalization of the distances was carried out by considering the start of the GM130 peak as 0, and the end of the TGN peak as 1. The images of Golgi stacks were processed using the "Image with Zoom" function of Metamorph 7.7.3.0 (Universal Imaging), for presentation.

Cell profiler analysis

Control and GRASP55 KO cells were stained ShTxB-Cy3 and ChTxB-AlexaFluor 488 and images were acquired as described above using a 20× objective (NA 0.5). Images were 8 bit with dimensions of 512 × 512 pixels, and each pixel corresponded to an area of 623 × 623 nm². For quantification experiments, 10–15 random fields were imaged with the same microscope settings (i.e., laser power and detector gain). The integrated intensity of fluorescence of each cell was calculated for each channel after the cells were segmented by Cell Profiler (Carpenter *et al*, 2006). Since only a fraction of the cells were positive for staining, the normalized intensity analysis was performed by taking top 10% of total cells in all the conditions and normalized on the background intensity.

Flow cytometry analysis

Control and GRASP55 KO cells were subjected to trypsin digestion, fixed with 4% paraformaldehyde, washed, and resuspended with PBS. Cells were incubated with bacterial toxins for 1 h at 4°C. Then, cells were extensively washed with PBS and incubated with fluorescence-labeled secondary antibodies when required or directly analyzed by BD FACS ARIAIII cell sorter (BD Biosciences). Cells incubated with secondary antibody alone, or unlabeled cells, were used as a negative control. The cell surface expression of GSLs of selected cells was further analyzed in the gated region by BD FACS ARIAIII cell sorter (BD Biosciences). Bacterial toxins used are described in (Table S4).

Electron microscopy

Ultrastructural analysis of Golgi morphology

Briefly, control and GRASP55 knockout cells were grown in 35 mm plastic dishes to 80% confluence. Cells were then fixed with 1% Glutaraldehyde (Electron Microscopy Sciences) in 0.2 M HEPES pH 7.3 at RT for 1 h. The fixative was replaced with 1% BSA in PBS, and cells were carefully detached using a plastic cell scraper, collected into microfuge tubes, and centrifuged to obtain the pellet. All samples were then washed three times in 0.2 M HEPES pH 7.3 and post-fixed 30 min in 1% Osmium Tetroxide in the dark at 4°C in the same buffer. They were then washed three times in distilled water and post-fixed 25 min in 1% Osmium Tetroxide and 1.5% Potassium Ferrocyanide in the dark at room temperature in HEPES 0.2 M pH 7.3. After washing three times in distilled water, they were stained with 0.5% uranyl acetate over night at 4°C. The pellets were dehydrated in graded steps of ethanol (50, 70, 90, and 100%), 2 times with 100% of acetone, and embedded into Epon. Thin sections (60 nm) were cut on a Leica UC7 ultramicrotome and examined with 120 kV Philips Tecnai 12 Biotwin electron microscope (FEI, Eindhoven, The Netherlands) using a VELETA digital camera.

Cryo-immuno EM

Control or GRASP55 Knockout cells were transfected using indicated HA-tagged construct for 16 h. The cells were then fixed with 2% formaldehyde and 0.2% glutaraldehyde in PHEM buffer (0.1 M) pelleted by centrifugation, embedded in 12% gelatin, cooled on ice, and cut into 1-mm³ cubes at 4°C. The cubes were

immersed in 2.3 M sucrose at 4°C overnight and then frozen in liquid nitrogen. Fifty-nanometer sections were cut with a diamond knife on a UC7 Leica cryo-ultramicrotome. The sections were picked up in a mix of 2% methyl cellulose and 2.3 M sucrose (1:1), as previously described (Pulvirenti *et al*, 2008), and collected on grids covered with Formvar carbon supporting film (Electron Microscopy Sciences, PA, USA). The grids were first incubated with the rabbit anti-GM130 and/or mouse anti-HA polyclonal antibodies and then incubated with different sizes of Protein A gold (10 and 15 nm) to reveal antigen staining. After labeling, the sections were treated with 1% glutaraldehyde and embedded in methyl cellulose uranyl acetate for 10 min on ice. The excess of methyl cellulose uranyl acetate was removed, and the sections were dried at room temperature before their analysis at 120 kV in a Philips Tecnai 12 Biotwin electron microscope (FEI, Eindhoven, The Netherlands) using a VELETA digital camera. The polarity of the Golgi stacks was defined by compositional (cis-Golgi marker GM130) parameter. For quantitation (performed with ITEM image acquisition software), cis, medial, or trans-Golgi was defined as previously described (Rizzo *et al*, 2013). TGN was defined as the area in front of the trans cisterna up to a distance that equals the thickness of the Golgi stack. Vesicles were round profiles of 50–80 nm in diameter, present within 200 nm from the rims of the stack. The distribution of enzyme in the Golgi stack was expressed as the fraction of gold particles in each cisterna of the Golgi stack and TGN.

Lipid analysis

HPLC-Mass spectrometry

Sphingolipids of control and GRASP55 KO cells were analyzed by liquid chromatography–tandem mass spectrometry (LC-MS/MS) as described earlier (Bielawski *et al*, 2006). Briefly, cells were washed twice with ice-cold PBS, and lipids were extracted with 2 ml ethyl acetate/isopropyl alcohol/water (60:30:10%, v/v/v) solvent mixture (Bielawski *et al*, 2006). The lipid extracts were analyzed with a Quantum Ultra triple quadrupole mass spectrometer connected to an Accela HPLC and Accela autosampler using a solvent gradient at the Lipidomics Core at Stony Brook University. Ceramides were identified through MRM analysis with soft fragmentation. Calibration curves were generated for each lipid and used for quantitative analysis of lipids in the samples. Inorganic phosphate (Pi) released from total phospholipids was measured by using a colorimetric method. Briefly, following a lipid extraction by using the Bligh and Dyer method, samples were dried under a stream of nitrogen gas. Then, a mixture of sulfuric and hydrochloric acid was added to the sample to ash the organic content. Samples were heated overnight at 160°C. Then, water, ammonium molybdate, and ascorbic acid were subsequently added to samples and incubated for 30 min at 45°C. The absorbance was measured at 600 nm by using a Spectramax M5 plate reader. A calibration curve was created and utilized to quantify the inorganic lipid content for each sample and used as normalization for relative quantification of sphingolipids.

Radioactive pulse-chase assay to monitor SL biosynthesis

Radioactive pulse-chase assay was performed as described earlier (D'Angelo *et al*, 2013). Briefly, HeLa-M cells or human fibroblasts

wi-26 or GRASP55 KO cells were pulse labeled for 2 h with [^3H]-sphingosine (final concentration of 0.1 $\mu\text{Ci}/\text{ml}$; Perkin Elmer) in serum-free DMEM containing 1% fatty acid-free BSA followed by a chase for indicated times in complete media. Lipids were then extracted from the cells, resuspended in chloroform, spotted onto silica-gel high-performance TLC (HPTLC) plates (Merck, Germany), resolved using a mixture of chloroform, methanol, and water (65:25:4 v/v/v) and quantified using GINA® (Raytest, Germany) software analysis.

MALDI-MS

Total lipid extracts were prepared using a standard MTBE protocol followed by a methylamine treatment for sphingo- and glycosphingolipids analysis by mass spectrometry. Briefly, cell pellet was resuspended in 100 μl H_2O . 360 μl methanol and 1.2 ml of MTBE were added and samples were placed for 10 min on a vortex at 4°C followed by incubation for 1 h at room temperature on a shaker. Phase separation was induced by the addition of 200 μl of H_2O . After 10 min at room temperature, samples were centrifuged at 1,000 g for 10 min. The upper (organic) phase was transferred into a glass tube, and the lower phase was re-extracted with 400 μl artificial upper phase [MTBE/methanol/ H_2O (10:3:1.5, v/v/v)]. The combined organic phases were dried in a vacuum concentrator. Lipids were then resuspended in 500 μl of CHCl_3 and divided into two aliquots for a further methylamine treatment. 500 μl of freshly prepared monomethylamine reagent [methylamine/ H_2O /n-butanol/methanol (5:3:1:4, (v/v/v/v))] was added to the dried lipid extract and then incubated at 53°C for 1 h in a water bath. Lipids were cooled to room temperature and then dried. The dried lipid extract was then extracted by n-butanol extraction using 300 μl water-saturated n-butanol and 150 μl H_2O . The organic phase was collected, and the aqueous phase was re-extracted twice with 300 μl water-saturated n-butanol. The organic phases were pooled and dried in a vacuum concentrator. Lipids were then resuspended in 500 μl of CHCl_3 and analyzed by MALDI-MS. 30 mg/ml 2,5-DHB was freshly prepared in acetonitrile/water solution (50:50 v/v) with 0.1% TFA. An equivalent volume of sample solution (50 μl) was then mixed with matrix before deposition on the MALDI target. All mass spectrometry analysis for the identification of lipids (m/z 600–1,800) was obtained using an Applied Biosystems 4800 MALDI-TOF/TOF mass spectrometer equipped with a 200 Hz tripled frequency Nd:YAG pulsed laser with 355 nm wavelength. Measurements were performed in positive ion reflection mode at an accelerating potential of 20 kV. Each mass spectrum was obtained by applying a laser energy of 4,600 watts/ cm^2 , averaging 4,000 single laser shots/spectrum.

FRAP assay

Control and GRASP55 (#2) knockout cells were plated on 35-mm glass bottom microwell dishes (MatTech, USA) and transfected with CERT-YFP (1 μg) for 16 h. FRAP was performed using Zeiss LSM 710 confocal microscope equipped with an environmental control system set to 37°C and 5% CO_2 . FRAP experiments were performed by bleaching CERT-YFP in the Golgi area (50 bleaching iterations) followed by imaging every 7.5 s for 4 min (2% laser power). Recovery of fluorescence was calculated as ratio of Golgi intensity and that of total cell after background correction.

Ceramide transport assay

Control and GRASP55 knockout cells were grown on coverslips to 80% confluence. Cells were washed with DMEM-HEPES containing 10% FCS for three times and incubated with BODIPY ceramide (5 μM) in fatty acid-free BSA for 30 min on ice. After incubation, cells were washed with DMEM-HEPES for three times and followed by imaging. The laser conditions used were 488 nm (excitation) and 620 nm (emission), and fluorescence was recorded every 2 min for a period of 20 min. The fluorescence of bodipy Ceramide in the Golgi was determined followed by normalization to the maximum.

RNA extraction and Real-Time PCR

Total RNA was extracted from HeLa-M cells (Control and GRASP55 Knockout) using the RNeasy Mini Kit (Qiagen) according to manufacturer's instructions. The yield and the integrity of RNA were determined by spectrophotometer NanoDrop 2000c (Thermo Scientific) and by TAE agarose gel electrophoresis, respectively. RNA (1 μg) was reverse transcribed using QuantiTect Reverse Transcription Kit (Qiagen) according to the manufacturer's instructions and subjected to qPCR with gene-specific primers (Appendix Table S6) in the presence of LightCycler®480 SYBR Green I Master Mix (Roche, Switzerland) on a LightCycler®480 II detection system (Roche, Switzerland). Analyses were carried out on biological triplicate samples for each experiment, and they were processed separately. The thermal profile consisted of 10 min at 95°C pre-incubation, and 40 cycles at 10 s at 95°C, 10 s at 60°C, and 10 s at 72°C. The qPCR data were normalized to the average of the reference gene human hypoxanthine-guanine phosphoribosyltransferase 1 (HPRT1). The fold changes in the relative quantifications were calculated according to the $\Delta\Delta\text{Ct}$ method. All the commercial kits used are reported in (Appendix Table S7).

Experimental conditions for RUSH experiments

LCS-KO cells were transiently transfected with LCS or LCS9A constructs at 37°C in absence of biotin for 16 h, to localize the proteins to endoplasmic reticulum (ER). Their ER exit was promoted by the addition of biotin (40 μM) for 6 h. For pulse-chase assay experiments (Fig 4C), biotin was replaced every 3 h and maintained throughout chase period for a total of 24 h.

Statistics

Error bars correspond to either standard deviation (SD) or standard error of mean (SEM) as indicated in figure legends. All the statistical evaluations were done using GraphPad Prism built-in tests (unpaired two-tailed Student's *t*-tests), and as indicated, significance values are all marked as follows * $P < 0.05$, ** $P < 0.01$, and *** $P < 0.001$ (*ns*, not significant). All the measurements reported are from distinct samples.

Data availability

Source data are provided with the manuscript, and if not, they are available from the corresponding author upon reasonable request. Targeted lipidomics data from this study are available at

Metabolomics Workbench database (<https://www.metabolomicsworkbench.org/>) with the following ID=ST001877.

Expanded View for this article is available online.

Acknowledgements

We thank Antonella De Matteis for valuable discussions, Nina Dathan for help with cloning and construct preparation, and Francesco Russo for assistance with statistical analysis. We thank the Bioimaging Facility of the Institute of Biochemistry and Cell Biology and the joint FACS Facility of the Institute of Genetics and Biophysics (IGB-CNR, Naples) and IBBC-CNR for access to technologies and Pasquale Barba for assistance with FACS. PP thanks Samba Siva Rao. We thank Dr. Bruno Correia, EPFL, Switzerland, for help with the analysis of protein–protein interaction studies. We thank Drs. Ahamarshan, Corda, Colanzi, Grimaldi, Jung, Krishnamoorthy, Polishchuk, Qadri, and Roy for critical comments on the manuscript. We thank MEDINTECH, the Italian Node of Euro-Bioimaging (Preparatory Phase II –INFRADDEV), Italian Cystic Fibrosis Research Foundation (FFC #6-2019), POR Campania project 2014-2020 (C.I.R.O.), and CTC project for financial support. R.R. acknowledges financial support from Fondazione Italiana per la Ricerca sul Cancro (FIRC Fellowship 15111). A.L. acknowledges financial support from the AIRC (Projects IG 15767 and IG 20786), TERABIO, PON-IMPARA, and S.A.T.I.N. G.D.A. acknowledges financial support from EPFL institutional fund, Kristian Gerhard Jebsen Foundation, and from the Swiss National Science Foundation (SNSF) (grant number, 310030_184926).

Author contributions

PP contributed to development of the idea, conducted most of the experiments, analysis and interpretation of data, and contributed to writing the manuscript; IA conducted the experiments on peptide binding using purified proteins; MP was involved in labeling and acquisition of EM and confocal microscopy images; RR assisted in acquisition and analyses of electron micrographs; DR conducted mRNA analysis; GT was involved in EM sample preparation and acquisition of images; LC conducted MALDI-MS and lipidomics measurements; CG performed the ITC experiments; GV assisted PP in morphological analysis of Golgi; ND was involved in cloning and construct preparation; J-SY performed vesicle budding assay and was guided in this by VWH; PH was involved in synthesis of biotinylated peptides; JN provided the WT and GRASP55 KO fibroblasts, performed the protein–protein interaction studies, and was guided by MP; TN, J-II, MJH-C, LMO, and YAH contributed to MS analysis of lipids; AB performed *in silico* modeling of GRASP55-GCS peptide interaction and was guided by MT; AL contributed to development of the idea of how Golgi organization may play role in regulating glycosylation and the mode of action of GRASP55 in regulating enzyme compartmentalization, critical analysis of the data throughout the entire project and also provided inputs in manuscript preparation. GDA contributed to setting up the system to monitor SL biosynthesis, provided important inputs on the data to understand and interpret changes in lipid biosynthesis, and also provided critical inputs in manuscript preparation. SP developed the idea, designed and supervised the entire project, and wrote the manuscript.

Conflict of interest

The authors declare that they have no conflict of interest.

References

Akintayo A, Stanley P (2019) Roles for Golgi glycans in oogenesis and spermatogenesis. *Front Cell Dev Biol* 7: 98

- Aridor M, Bannykh SI, Rowe T, Balch WE (1995) Sequential coupling between COPII and COPI vesicle coats in endoplasmic reticulum to Golgi transport. *J Cell Biol* 131: 875–893
- Barr FA, Preisinger C, Kopajtich R, Korner R (2001) Golgi matrix proteins interact with p24 cargo receptors and aid their efficient retention in the Golgi apparatus. *J Cell Biol* 155: 885–891
- Beznoussenko GV, Parashuraman S, Rizzo R, Polishchuk R, Martella O, Di Giandomenico D, Fusella A, Spaar A, Sallese M, Capestrano MG *et al* (2014) Transport of soluble proteins through the Golgi occurs by diffusion via continuities across cisternae. *Elife* 3: e2009
- Bielawski J, Szulc ZM, Hannun YA, Bielawska A (2006) Simultaneous quantitative analysis of bioactive sphingolipids by high-performance liquid chromatography-tandem mass spectrometry. *Methods* 39: 82–91
- Bishop JR, Schuksz M, Esko JD (2007) Heparan sulphate proteoglycans fine-tune mammalian physiology. *Nature* 446: 1030–1037
- Biswas A, Thattai M (2020) Promiscuity and specificity of eukaryotic glycosyltransferases. *Biochem Soc Trans* 48: 891–900
- Blackburn JB, D'Souza Z, Lupashin VV (2019) Maintaining order: COG complex controls Golgi trafficking, processing, and sorting. *FEBS Lett* 593: 2466–2487
- Carpenter AE, Jones TR, Lamprecht MR, Clarke C, Kang IH, Friman O, Guertin DA, Chang JH, Lindquist RA, Moffat J *et al* (2006) Cell profiler: image analysis software for identifying and quantifying cell phenotypes. *Genome Biol* 7: R100
- Chang IJ, He M, Lam CT (2018) Congenital disorders of glycosylation. *Ann Transl Med* 6: 477
- Chaudhury S, Berrondo M, Weitzner BD, Muthu P, Bergman H, Gray JJ (2011) Benchmarking and analysis of protein docking performance in Rosetta v3.2. *PLoS One* 6: e22477
- Chiritoiu M, Brouwers N, Turacchio G, Pirozzi M, Malhotra V (2019) GRASP55 and UPR control interleukin-1 β aggregation and secretion. *Dev Cell* 49: 145–155 e4
- D'Angelo G, Uemura T, Chuang C-C, Polishchuk E, Santoro M, Ohvo-Rekilä H, Sato T, Di Tullio G, Varriale A, D'Auria S *et al* (2013) Vesicular and non-vesicular transport feed distinct glycosylation pathways in the Golgi. *Nature* 501: 116–120
- D'Angelo G, Prencipe L, Iodice L, Beznoussenko G, Savarese M, Marra P, Di Tullio G, Martire G, De Matteis MA, Bonatti S (2009) GRASP65 and GRASP55 sequentially promote the transport of C-terminal valine-bearing cargos to and through the Golgi complex. *J Biol Chem* 284: 34849–34860
- Dunphy WG, Rothman JE (1985) Compartmental organization of the Golgi stack. *Cell* 42: 13–21
- Eckert ES, Reckmann I, Hellwig A, Rohling S, El-Battari A, Wieland FT, Popoff V (2014) Golgi phosphoprotein 3 triggers signal-mediated incorporation of glycosyltransferases into coatamer-coated (COPI) vesicles. *J Biol Chem* 289: 31319–31329
- Emsley P, Cowtan K (2004) Coot: model-building tools for molecular graphics. *Acta Crystallogr D Biol Crystallogr* 60: 2126–2132
- Fisher P, Spencer H, Thomas-Oates J, Wood AJ, Ungar D (2019) Modeling Glycan processing reveals golgi-enzyme homeostasis upon trafficking defects and cellular differentiation. *Cell Rep* 27: 1231–1243.e6
- Glick BS, Luini A (2011) Models for Golgi traffic: a critical assessment. *Cold Spring Harb Perspect Biol* 3: a005215
- Grond R, Veenendaal T, Duran JM, Raote I, van Es JH, Corstjens S, Delfgou L, El Haddouti B, Malhotra V, Rabouille C (2020) The function of GORASPs in Golgi apparatus organization in vivo. *J Cell Biol* 219: e202004191
- Halter D, Neumann S, van Dijk SM, Wolthoorn J, de Maziere AM, Vieira OV, Mattjus P, Klumperman J, van Meer G, Sprong H (2007) Pre- and post-

- Golgi translocation of glucosylceramide in glycosphingolipid synthesis. *J Cell Biol* 179: 101–115
- Hanada K, Kumagai K, Yasuda S, Miura Y, Kawano M, Fukasawa M, Nishijima M (2003) Molecular machinery for non-vesicular trafficking of ceramide. *Nature* 426: 803–809
- Hannun YA, Obeid LM (2018) Sphingolipids and their metabolism in physiology and disease. *Nat Rev Mol Cell Biol* 19: 175–191
- Hayashi Y, Nemoto-Sasaki Y, Matsumoto N, Hama K, Tanikawa T, Oka S, Saeki T, Kumasaka T, Koizumi T, Arai S et al (2018) Complex formation of sphingomyelin synthase 1 with glucosylceramide synthase increases sphingomyelin and decreases glucosylceramide levels. *J Biol Chem* 293: 17505–17522
- Ishibashi Y, Ito M, Hirabayashi Y (2018) Regulation of glucosylceramide synthesis by Golgi-localized phosphoinositide. *Biochem Biophys Res Commun* 499: 1011–1018
- Ishii M, Suda Y, Kurokawa K, Nakano A (2016) COPI is essential for Golgi cisternal maturation and dynamics. *J Cell Sci* 129: 3251–3261
- Jaiman A, Thattai M (2020) Golgi compartments enable controlled biomolecular assembly using promiscuous enzymes. *Elife* 9: e49573
- Jarvela T, Linstedt AD (2014) Isoform-specific tethering links the Golgi ribbon to maintain compartmentalization. *Mol Biol Cell* 25: 133–144
- Kim J, Noh SH, Piao H, Kim DH, Kim K, Cha JS, Chung WY, Cho HS, Kim JY, Lee MG (2016) Monomerization and ER relocation of GRASP is a requisite for unconventional secretion of CFTR. *Traffic* 17: 733–753
- Klumperman J (2011) Architecture of the mammalian Golgi. *Cold Spring Harb Perspect Biol* 3: a005181
- Kohyama-Koganeya A, Nabetani T, Miura M, Hirabayashi Y (2011) Glucosylceramide synthase in the fat body controls energy metabolism in *Drosophila*. *J Lipid Res* 52: 1392–1399
- Ladinsky MS, Mastronarde DN, McIntosh JR, Howell KE, Staehelin LA (1999) Golgi structure in three dimensions: functional insights from the normal rat kidney cell. *J Cell Biol* 144: 1135–1149
- Lee HJ, Zheng JJ (2010) PDZ domains and their binding partners: structure, specificity, and modification. *Cell Commun Signal* 8: 8
- Liu L, Doray B, Kornfeld S (2018) Recycling of Golgi glycosyltransferases requires direct binding to coatamer. *Proc Natl Acad Sci USA* 115: 8984–8989
- Lyskov S, Chou FC, Conchuir SO, Der BS, Drew K, Kuroda D, Xu J, Weitzner BD, Renfrew PD, Sripakdeevong P et al (2013) Serverification of molecular modeling applications: the Rosetta Online Server that Includes Everyone (ROSIE). *PLoS One* 8: e63906
- Lyskov S, Gray JJ (2008) The RosettaDock server for local protein-protein docking. *Nucleic Acids Res* 36: W233–W238
- Maccioni HJ, Giraudo CG, Daniotti JL (2002) Understanding the stepwise synthesis of glycolipids. *Neurochem Res* 27: 629–636
- Nairn AV, Aoki K, dela Rosa M, Porterfield M, Lim J-M, Kulik M, Pierce J, Michael, Wells L, Dalton S, Tiemeyer M et al (2012) Regulation of glycan structures in murine embryonic stem cells: combined transcript profiling of glycan-related genes and glycan structural analysis. *J Biol Chem* 287: 37835–37856
- Nairn AV, York WS, Harris K, Hall EM, Pierce JM, Moremen KW (2008) Regulation of glycan structures in animal tissues: transcript profiling of glycan-related genes. *J Biol Chem* 283: 17298–17313
- Nakano A, Luini A (2010) Passage through the Golgi. *Curr Opin Cell Biol* 22: 471–478
- Oprins A, Duden R, Kreis TE, Geuze HJ, Slot JW (1993) Beta-COP localizes mainly to the cis-Golgi side in exocrine pancreas. *J Cell Biol* 121: 49–59
- Papanikou E, Day KJ, Austin J, Glick BS (2015) COPI selectively drives maturation of the early Golgi. *Elife* 4: e13232
- Parashuraman S, D'Angelo G (2019) Visualizing sphingolipid biosynthesis in cells. *Chem Phys Lipids* 218: 103–111
- Popoff V, Adolf F, Brugger B, Wieland F (2011) COPI budding within the Golgi stack. *Cold Spring Harb Perspect Biol* 3: a005231
- Pothukuchi P, Agliarulo I, Russo D, Rizzo R, Russo F, Parashuraman S (2019) Translation of genome to glycome: role of the Golgi apparatus. *FEBS Lett* 593: 2390–2411
- Pulvirenti T, Giannotta M, Capestrano M, Capitani M, Pisanu A, Polishchuk RS, San Pietro E, Beznoussenko GV, Mironov AA, Turacchio G et al (2008) A traffic-activated Golgi-based signalling circuit coordinates the secretory pathway. *Nat Cell Biol* 10: 912–922
- Rabouille C, Klumperman J (2005) Opinion: The maturing role of COPI vesicles in intra-Golgi transport. *Nat Rev Mol Cell Biol* 6: 812–817
- Rizzo R, Parashuraman S, Mirabelli P, Puri C, Lucocq J, Luini A (2013) The dynamics of engineered resident proteins in the mammalian Golgi complex relies on cisternal maturation. *J Cell Biol* 201: 1027–1036
- Rizzo R, Russo D, Kurokawa K, Sahu P, Lombardi B, Supino D, Zhukovsky M, Vocat A, Pothukuchi P, Kunnathully V et al (2019) The Glyco-enzyme adaptor GOLPH3 links intra-Golgi transport dynamics to glycosylation patterns and cell proliferation. *bioRxiv* <https://doi.org/10.1101/870477> [PREPRINT]
- Rizzo R, Russo D, Kurokawa K, Sahu P, Lombardi B, Supino D, Zhukovsky MA, Vocat A, Pothukuchi P, Kunnathully V et al (2021) Golgi maturation-dependent glycoenzyme recycling controls glycosphingolipid biosynthesis and cell growth via GOLPH3. *EMBO J* 40: e107238
- Rudd P, Karlsson NG, Khoo KH, Packer NH (2015) Glycomics and glycoproteomics. In Varki A, Cummings RD, Esko JD, Stanley P, Hart GW, Aebi M, Darvill AG, Kinoshita T, Packer NH, Prestegard JH, Schnaar RL, Seeberger PH (eds), *Essentials of glycobiology*, pp 653–666. New York: Cold Spring Harbor
- Russo D, Capolupo L, Loomba JS, Sticco L, D'Angelo G (2018a) Glycosphingolipid metabolism in cell fate specification. *J Cell Sci* 131: jcs219204
- Russo D, Della Ragione F, Rizzo R, Sugiyama E, Scalabri F, Hori K, Capasso S, Fioriniello Sticco LS, De Gregorio R, Granata I et al (2018b) Glycosphingolipid metabolic reprogramming drives neural differentiation. *EMBO J* 37: e97674
- Ryczko MC, Pawling J, Chen R, Abdel Rahman AM, Yau K, Copeland JK, Zhang C, Surendra A, Guttman DS, Figeys D et al (2016) Metabolic reprogramming by hexosamine biosynthetic and Golgi N-Glycan branching pathways. *Sci Rep* 6: 23043
- Shorter J, Watson R, Giannakou ME, Clarke M, Warren G, Barr FA (1999) GRASP55, a second mammalian GRASP protein involved in the stacking of Golgi cisternae in a cell-free system. *EMBO J* 18: 4949–4960
- Stanley P (2011) Golgi glycosylation. *Cold Spring Harb Perspect Biol* 3: a005199
- Tu L, Chen L, Banfield DK (2012) A conserved N-terminal arginine-motif in GOLPH3-family proteins mediates binding to coatamer. *Traffic* 13: 1496–1507
- Tu L, Tai WC, Chen L, Banfield DK (2008) Signal-mediated dynamic retention of glycosyltransferases in the Golgi. *Science* 321: 404–407
- Vangone A, Bonvin AM (2015) Contacts-based prediction of binding affinity in protein-protein complexes. *Elife* 4: e07454
- Varki A (1998) Factors controlling the glycosylation potential of the Golgi apparatus. *Trends Cell Biol* 8: 34–40
- Varki A (2017) Biological roles of glycans. *Glycobiology* 27: 3–49
- Varki A, Kornfeld S (2015) Historical background and overview. In Varki A, Cummings RD, Esko JD, Stanley P, Hart GW, Aebi M, Darvill AG, Kinoshita T, Packer NH, Prestegard JH, Schnaar RL, Seeberger PH (eds), *Essentials of glycobiology*, pp 1–18. New York: Cold Spring Harbor
- Vinke FP, Grieve AG, Rabouille C (2011) The multiple facets of the Golgi reassembly stacking proteins. *Biochem J* 433: 423–433


- Wang Z, Wen L, Ma X, Chen Z, Yu Y, Zhu J, Wang Y, Liu Z, Liu H, Wu D et al (2012) High expression of lactotriaosylceramide, a differentiation-associated glycosphingolipid, in the bone marrow of acute myeloid leukemia patients. *Glycobiology* 22: 930–938
- Wong M, Munro S (2014) Membrane trafficking. The specificity of vesicle traffic to the Golgi is encoded in the golgin coiled-coil proteins. *Science* 346: 1256898
- Xiang Y, Wang Y (2010) GRASP55 and GRASP65 play complementary and essential roles in Golgi cisternal stacking. *J Cell Biol* 188: 237–251
- Xiang Y, Zhang X, Nix DB, Katoh T, Aoki K, Tiemeyer M, Wang Y (2013) Regulation of protein glycosylation and sorting by the Golgi matrix proteins GRASP55/65. *Nat Commun* 4: 1659
- Xue LC, Rodrigues JP, Kastritis PL, Bonvin AM, Vangone A (2016) PRODIGY: a web server for predicting the binding affinity of protein-protein complexes. *Bioinformatics* 32: 3676–3678
- Yamaji T, Hanada K (2014) Establishment of HeLa cell mutants deficient in sphingolipid-related genes using TALENs. *PLoS One* 9: e88124
- Yang JS, Lee SY, Gao M, Bourgoin S, Randazzo PA, Premont RT, Hsu VW (2002) ARFGAP1 promotes the formation of COPI vesicles, suggesting function as a component of the coat. *J Cell Biol* 159: 69–78
- Yang JS, Lee SY, Spano S, Gad H, Zhang L, Nie Z, Bonazzi M, Corda D, Luini A, Hsu VW (2005) A role for BARS at the fission step of COPI vesicle formation from Golgi membrane. *EMBO J* 24: 4133–4143
- Zhang CJ, Rosenwald AG, Willingham MC, Skuntz S, Clark J, Kahn RA (1994) Expression of a dominant allele of human ARF1 inhibits membrane traffic in vivo. *J Cell Biol* 124: 289–300
- Zhang Y, Seemann J (2021) Rapid degradation of GRASP55 and GRASP65 reveals their immediate impact on the Golgi structure. *J Cell Biol* 220: e202007052
- Zhao J, Li B, Huang X, Morelli X, Shi N (2017) Structural basis for the interaction between Golgi reassembly-stacking protein GRASP55 and Golgin45. *J Biol Chem* 292: 2956–2965



License: This is an open access article under the terms of the Creative Commons Attribution-NonCommercial-NoDerivs 4.0 License, which permits use and distribution in any medium, provided the original work is properly cited, the use is non-commercial and no modifications or adaptations are made.

VIEWPOINT

Homeostatic and pathogenic roles of the GM3 ganglioside

Jin-ichi Inokuchi^{1,2} , Hirotaka Kanoh¹, Kei-ichiro Inamori¹, Masakazu Nagafuku¹, Takahiro Nitta¹ and Koichi Fukase^{2,3}

¹ Division of Glycopathology, Institute of Molecular Biomembrane and Glycobiology, Tohoku Medical and Pharmaceutical University, Sendai, Japan

² Core for Medicine and Science Collaborative Research and Education (MS-CORE), Project Research Center for Fundamental Sciences, Osaka University, Japan

³ Department of Chemistry, Graduate School of Science, Osaka University, Japan

Keywords

adipocytes; cholesterol transport; chronic inflammation; GM3 ganglioside; innate immunity; insulin resistance; leptin resistance; metabolic syndrome; NPC1L1; obesity; TLR4

Correspondence

J. Inokuchi, Division of Glycopathology, Institute of Molecular Biomembrane and Glycobiology, Tohoku Medical and Pharmaceutical University, 4-4-1 Komatsushima, Aoba-ku, Sendai 981-8558, Japan

Tel: +81 22 727 0117

E-mail: jin@tohoku-mpu.ac.jp

(Received 12 March 2021, revised 10 May 2021, accepted 14 June 2021)

doi:10.1111/febs.16076

Two decades ago, we achieved molecular cloning of ganglioside GM3 synthase (GM3S; ST3GAL5), the enzyme responsible for initiating biosynthesis of complex gangliosides. The efforts of our research group since then have been focused on clarifying the physiological and pathological roles of gangliosides, particularly GM3. This review summarizes our long-term studies on the roles of GM3 in insulin resistance and adipogenesis in adipose tissues, cholesterol uptake in intestine, and leptin resistance in hypothalamus. We hypothesized that GM3 plays a role in innate immune function of macrophages and demonstrated that molecular species of GM3 with differing acyl-chain structures and modifications functioned as pro- and anti-inflammatory endogenous Toll-like receptor 4 (TLR4) modulators in macrophages. Very-long-chain and α -hydroxy GM3 species enhanced TLR4 activation, whereas long-chain and unsaturated GM3 species counteracted this effect. Lipidomic analyses of serum and adipose tissues revealed that imbalances between such pro- and anti-inflammatory GM3 species promoted progression of metabolic disorders. GM3 thus functions as a physiological regulatory factor controlling the balance between homeostatic and pathological states. Ongoing studies based on these findings will clarify the mechanisms underlying ganglioside-dependent control of energy homeostasis and innate immune responses.

Introduction

Glycosphingolipids (GSLs), and their sialic acid-containing derivatives, gangliosides (Fig. 1A), are membrane lipid components having a lipid portion embedded in the plasma membrane outer leaflet and a sugar chain extending into the extracellular space. Structural features of GSLs affect membrane fluidity and facilitate microdomain formation, thus contributing to cell–cell interaction and receptor-mediated signal transduction. In cultured adipocytes with TNF α -

induced insulin resistance, elimination of GSLs by inhibition of glucosylceramide (GlcCer) synthase (D-PDMP) [1], the initial step in biosynthesis of all GlcCer-derived GSLs, results in nearly complete recovery of insulin receptor (IR) signaling [2]. Several metabolic diseases are characterized by elevated expression of GM3, the simplest ganglioside species synthesized by GM3 synthase (GM3S) (Fig. 1A), [2–5]. SAT-I, ST3GALIV, and ST3GAL5 are frequently used

Abbreviations

DAMPs, damage-associated molecular patterns; GSLs, glycosphingolipids; PAMPs, pathogen-associated molecular patterns; ST3GAL5, GM3 synthase; TLR4, Toll-like receptor 4.

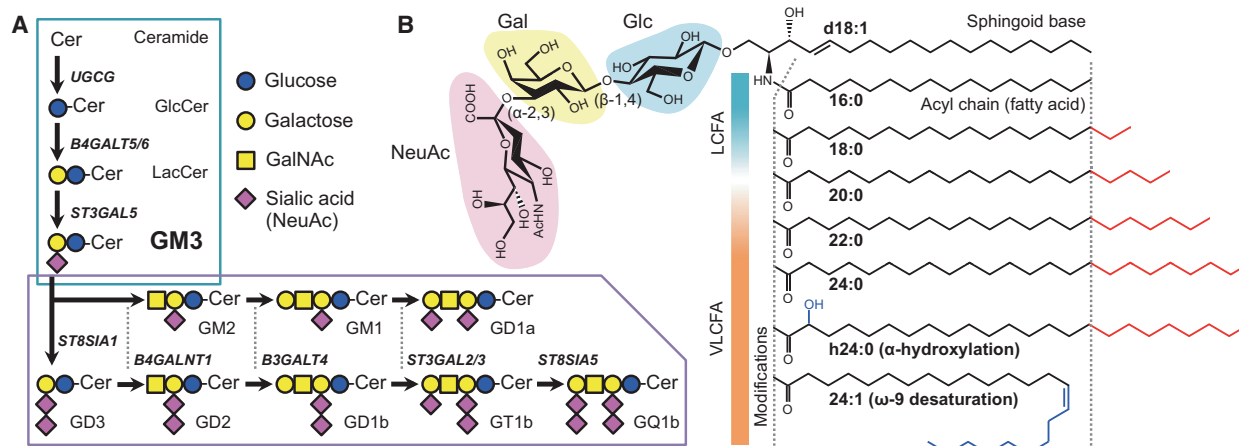


Fig. 1. Biosynthetic pathway of gangliosides and acyl-chain structures of GM3 molecular species. (A) Biosynthetic pathway (schematic) of GM3, from ceramide, and to complex gangliosides. (B) Detailed structures of GM3 species: sialyllactose head group, sphingoid base (d18:1), typical acyl-chain lengths (long-chain, very-long-chain), and acyl-chain modifications (α -hydroxylation, ω -9 desaturation).

abbreviations for this enzyme; *ST3GAL5* is recommended for common use [6]. *ST3GAL5* gene expression and GM3 content are upregulated in visceral adipose tissue in obese animal models [2,5]. We proposed a working hypothesis ‘Insulin resistance as a membrane microdomain disorder’ [7–9] based on findings that increase of membrane GM3 in adipocytes induced by inflammatory cytokine $\text{TNF}\alpha$ resulted in elimination of IR from caveolae [10,11] (Fig. 2).

Numerous molecular species of GM3 have been found that differ in acyl-chain length (16–24) and modifications (α -hydroxylation, ω -9 desaturation) (Fig. 1B). GM3 species are secreted abundantly into human serum and circulate to all parts of the body, including insulin-sensitive organs and major tissues (e.g., liver, muscle, adipose) [12]. Altered expression of various GM3 species has been observed in patients with metabolic disorders [4], but specific biological functions of these species are unclear. Our 2020 study demonstrated that GM3 species act as pro- and anti-inflammatory endogenous TLR4/MD-2 modulators, whose balance and acyl-chain structures affect progression of metabolic disorders starting at presymptomatic phase, and potentially serve as diagnostic and therapeutic targets of chronic inflammation in these disorders [12].

GM3 functions as a physiological regulator of insulin signaling and adipogenesis

Visceral adipose tissue, particularly mesenteric adipose tissue, is an important factor in the pathogenesis of

metabolic syndrome [13–21]. To elucidate the fundamental characteristics of mesenteric adipocytes, we established a physiologically relevant culture system for differentiation of rat mesenteric-stromal vascular cells (mSVC) into mesenteric-visceral adipocytes (mVAC) [22,23]. Insulin concentration was optimized at levels comparable to *in vivo* level ($0.85 \text{ ng}\cdot\text{mL}^{-1}$) by using physiological concentration ($200 \text{ ng}\cdot\text{mL}^{-1}$) of insulin-like growth factor (IGF-1). IGF-1 and insulin were found to act synergistically; IGF-1 alone was able to enhance CCAAT/enhancer binding protein alpha (C/EBP α) and adipocyte lipid-binding protein (aP2) mRNA expression, but did not induce lipid droplet accumulation associated with adipocyte maturation in the absence of insulin at physiological concentration.

We evaluated the contribution of resident macrophages in SVCs to adipogenesis using this culture system. Removal of resident macrophages led to increased adipogenesis of SVCs in mesenteric adipose tissues, accompanied by enhanced insulin signaling and reduced levels of GSLs (GlcCer, lactosylceramide [LacCer], GM3). Removal of macrophages also resulted in increases of IR and IR substrate 1 (IRS1) phosphorylation following insulin stimulation and of IR protein level in mSVCs [5]. Thus, levels of GSLs, particularly GM3, in adipocytes are precisely controlled by soluble factors secreted from resident macrophages that induce adipogenesis. Mouse embryonic fibroblasts (MEFs) prepared from *ST3Gal5*-null mice showed increased adipogenesis and insulin signaling [5]. These findings indicate that GM3 is directly involved in insulin signaling in adipose tissues and that

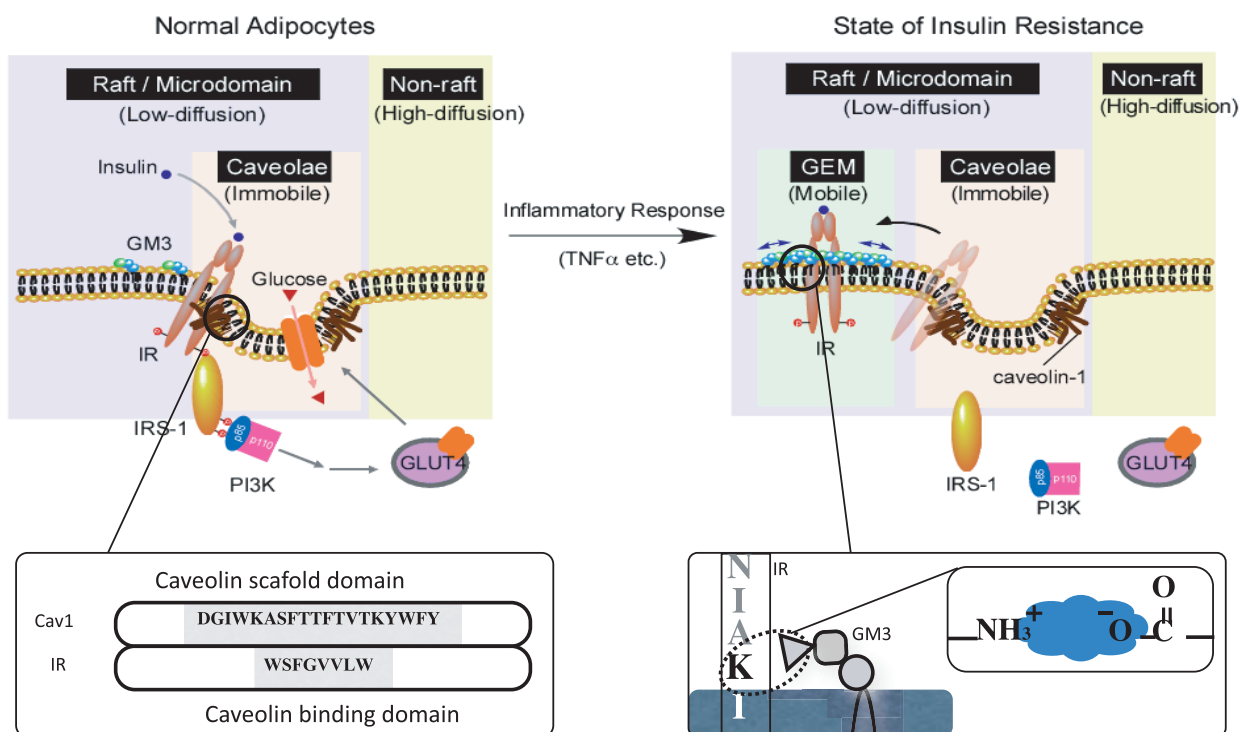


Fig. 2. Proposed mechanism underlying the shift of insulin receptors (IR) from the caveolae to the glycosphingolipid-enriched microdomains (GEM) in adipocytes during a state of insulin resistance. Caveolae and noncaveolar rafts (GEM) are shown in schematically. Caveolae and GEM reportedly can be separated by an anti-CAV1 antibody. IR may be constitutively resident in caveolae based on binding to CAV1 scaffolding domain through the caveolin-binding domain in its cytoplasmic region. Proper insulin metabolic signaling requires binding of IR and CAV1. In adipocytes, localization of IR in caveolae is disrupted by elevated levels of the endogenous GM3 during a state of insulin resistance induced by $\text{TNF}\alpha$ [10,11]. Our findings demonstrate that dissociation of the IR/CAV1 complex is results from interaction of a lysine residue at IR944, located just above the transmembrane domain, with increased GM3 clustered at the cell surface.

GM3 levels of preadipocytes and mature adipocytes maintain a degree of insulin signaling necessary for adipogenesis (Fig. 3).

GM3 membrane levels regulate hypercholesterolemia

Hypercholesterolemia is a key risk factor for the development of atherosclerosis and cardiovascular diseases. Prevention of these potentially fatal diseases depends on careful management of blood cholesterol levels, particularly low-density lipoprotein cholesterol (LDL-C) levels, to maintain them in a target range. Statins are commonly used to inhibit cholesterol biosynthesis through competitive inhibition of 3-hydroxy-3-methylglutaryl coenzyme A [24,25]. Another treatment option for the reduction in blood cholesterol levels is application of cholesterol absorption inhibitors in the intestine. LDL-C level was significantly reduced by

ezetimibe, the first of several new drugs that inhibit cholesterol absorption by enterocytes in the small intestine [26].

Several studies have addressed the mechanisms underlying cholesterol uptake by enterocytes and demonstrated that intestinal cholesterol absorption is mediated by transport proteins in these cells. Niemann–Pick C1-like protein 1 (NPC1L1), a polytopic transmembrane protein highly expressed on the apical membrane of enterocytes in the jejunum, acts as a cholesterol transporter [27]. NPC1L1 was identified as the molecular target of ezetimibe; this drug recognizes the extracellular loop of NPC1L1 protein and alters its conformation, thereby inhibiting cholesterol transport functions. Intestinal cholesterol absorption was ~ 67% lower in NPC1L1-null mice than in wild-type (WT) mice, although the null mice appeared healthy [28]. Degree of such reduction in ezetimibe-treated WT mice was similar to that in null mice. Cholesterol absorption

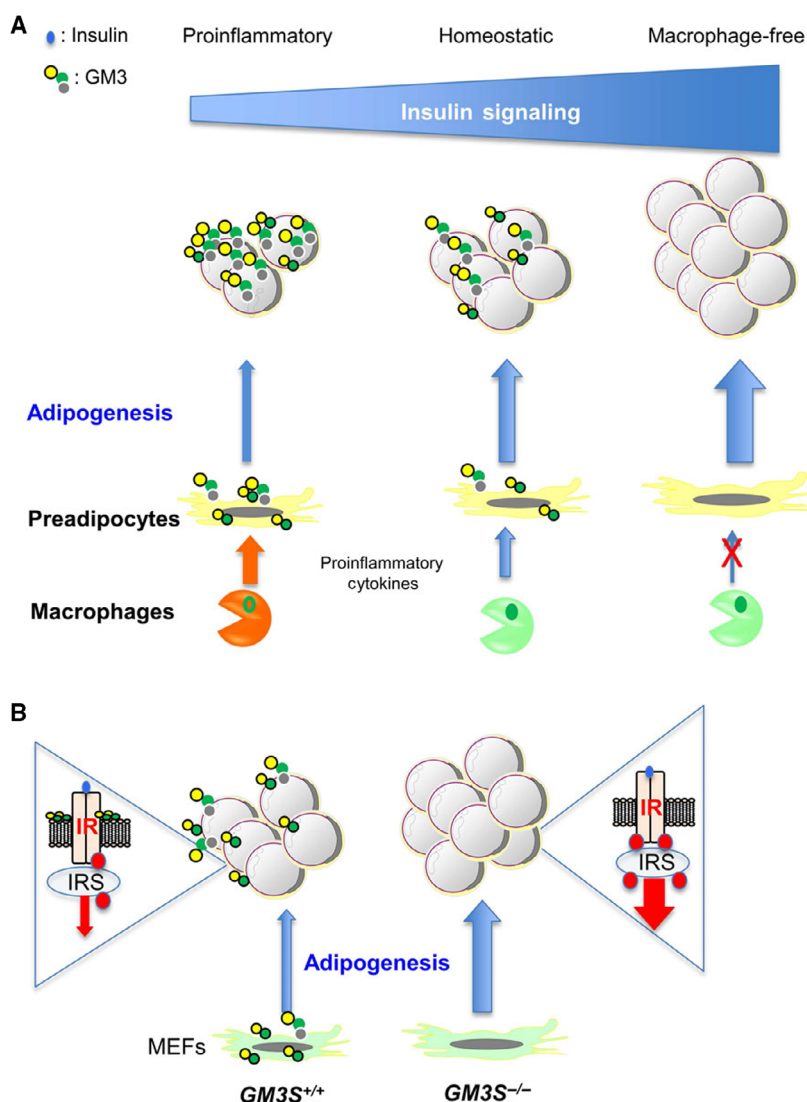


Fig. 3. Control of homeostatic and pathogenic balance in adipose tissue by GM3 [5]. (A) Enhanced adipogenesis of mesenteric preadipocytes following depletion of resident macrophages. Soluble factors secreted by resident macrophages maintain expression of GM3 and other GSLs in mesenteric preadipocytes and adipocytes, leading to normal adipogenesis. (B) *St3ga15* KO enhances IR signaling in MEFs and differentiated adipocytes.

in the null mice was not further reduced by ezetimibe treatment. Ezetimibe treatment was found to enhance apical cholesterol efflux to intestinal lumen in both human and mouse studies [29,30]. These findings indicate that NPC1L1 inhibition is an effective antihypercholesterolemia therapy.

The molecular pathways of cholesterol uptake by NPC1L1 involve clathrin-mediated endocytosis [31]. NPC1L1 protein contains three large extracellular domains and 13 transmembrane segments [32], and its extracellular N terminus binds cholesterol. A portion of the transmembrane segments termed sterol-sensing domain (SSD) detects cholesterol levels in the plasma membrane [33]. When the SSD senses increased cholesterol level, NPC1L1 attaches to a mixed micelle containing cholesterol and other hydrophobic lipids and internalizes it by clathrin-mediated endocytosis [34,35].

Cholesterol binding to NPC1L1 promotes formation in plasma membrane of cholesterol-enriched microdomains, also known as lipid rafts, by interacting with flotillin proteins preferentially localized in the microdomains [36]. Thus, these membrane microdomains function as a platform for cholesterol uptake into enterocytes.

Membrane microdomains are enriched in sphingomyelin and GSLs as well as cholesterol. Gangliosides (sialic acid-containing GSLs) are involved in cell–cell recognition, adhesion, and signal transduction within microdomains [37]. GM3 (NeuAc- α 2,3-Gal- β 1,4-Glc-ceramide), the simplest ganglioside, interacts with transmembrane receptors, such as the epidermal growth factor (EGF) receptor and IR, and regulates receptor functions by creating a specialized lipid environment [10,38]. Intestinal GM3S expression level is

high in neonatal mice and declines during the course of development in mice [39]. Our 2018 study demonstrated small, but significant, GM3 expression in young adult mice, based on TLC and LC-MS/MS analyses [40].

Membrane microdomain organization often involves close functional relationships between gangliosides and flotillins [39,41]. NPC1L1/flotillin interactions are mediated by gangliosides present on the apical surface of enterocytes. We observed reduction of NPC1L1-dependent cholesterol uptake in GM3S-deficient cells [40]. Cholesterol uptake was significantly lower in NPC1L1-expressing GM3S-null cells than in control cells, and cholesterol-dependent translocation of NPC1L1 from the plasma membrane to the intracellular region was impaired. GM3S-null mice, consistently with these findings, showed reduced cholesterol uptake and cholesterol-dependent translocation of NPC1L1 in intestinal enterocytes.

GM3 deficiency was associated with reduction of both genetic hypercholesterolemia in Apo E mutation and diet-induced hypercholesterolemia. On the other hand, GM3S-null mice fed a normal diet had plasma cholesterol levels similar to those of WT mice. These findings indicate involvement of GM3 in the exogenous pathways of cholesterol metabolism, including intestinal NPC1L1 activity.

Developmental changes in intestinal GSL composition are synchronized with expression levels of intestinal nutrient transporters [42]. KO of intestinal GlcCer synthase in a mouse model resulted in retarded growth and early death because of defects in intestinal intracellular vesicular transport [43]. These studies indicated the physiological importance of GSLs in intestinal nutrient absorption, but did not address role of GSLs in the NPC1L1 pathway. Function of NPC1L1 as a cholesterol transporter requires a cholesterol-enriched membrane microdomain [35,36,44]; however, the detailed mechanisms underlying function of GM3 and related gangliosides in NPC1L1-mediated cholesterol absorption remain unclear.

Gangliosides, particularly GM3, and its synthesizing enzyme, GM3S, are potential targets for hypercholesterolemia therapy. Genetic variation in NPC1L1 is closely associated with interindividual variation in response to ezetimibe [45], and studies have revealed loss of ezetimibe-binding mutations in the extracellular loop of NPC1L1 [46]. Thus, mutations in this region may result in loss of response to ezetimibe treatment. Membrane lipid modification, *that is*, through GM3S inhibition, is applicable regardless of binding affinity of compounds to NPC1L1 and may provide an alternative therapeutic approach for nonresponsive individuals.

GM3-related gangliosides regulate hypothalamic leptin signaling

Recent studies by our group and others have demonstrated essential roles of neural gangliosides in central control of energy homeostasis through regulation of leptin signaling. Leptin, an adipocyte hormone produced in proportion to body fat mass, serves as an adiposity signal and helps maintain body weight homeostasis and energy balance through binding to its cognate receptor, LepR [47, 48]. Several LepR isoforms (six in mice and five in humans) have been identified to date, and only the longest isoform, LepRb, has a crucial cytoplasmic region necessary for efficient leptin signaling in central neurons that control feeding and energy expenditure [49].

Leptins carry information on adiposity status to the brain, specifically to various hypothalamic nuclei: arcuate nucleus (ARC), paraventricular nucleus (PVN), ventromedial hypothalamus (VMH), and lateral hypothalamic area (LH). ARC, the primary target of leptin activity, contains two interconnected groups of LepRb-expressing neurons: anorexigenic POMC (proopiomelanocortin) neurons and orexigenic AgRP/ NPY (agouti-related peptide/neuropeptide Y) neurons [50]. These two types of neurons regulate melanocortin signaling in a coordinated manner to maintain energy balance.

Mice lacking functional leptin (*ob/ob*) or LepRb (*db/db*) are hyperphagic and display severe early-onset obesity [51]. Leptin binding to LepRb leads to phosphorylation of Janus kinase 2 (JAK2), which subsequently phosphorylates three conserved Tyr residues in LepRb (Tyr⁹⁸⁵, Tyr¹⁰⁷⁷, Tyr¹¹³⁸). Each of the resulting phospho-Tyr (p-Tyr) residues recruits specific Src homology 2 (SH2) domain-containing proteins to the LepRb-JAK2 complex (Fig. 4) [52]. p-Tyr¹¹³⁸ is the binding site for the SH2 domain of signal transducer and activator of transcription 3 (STAT3), the key mediator of the well-studied JAK-STAT pathway, which is essential for anti-obesity activity of leptin in the brain. After binding, STAT3 is phosphorylated by JAK2 and translocated to the nucleus, where it activates gene expression of targets such as POMC and suppressor of cytokine signaling 3 (SOCS3). SOCS3 binds to p-Tyr⁹⁸⁵ of LepRb and inhibits JAK2 activation and thereby mediates negative feedback inhibition of leptin signaling [53]. p-Tyr⁹⁸⁵ also functions as a binding site for the protein Tyr phosphatase 2 (SHP2); recruited SHP2 is subsequently phosphorylated by JAK2 and then recruits growth factor receptor-bound protein 2 (Grb2), an adaptor protein that mediates activation of extracellular signal-regulated

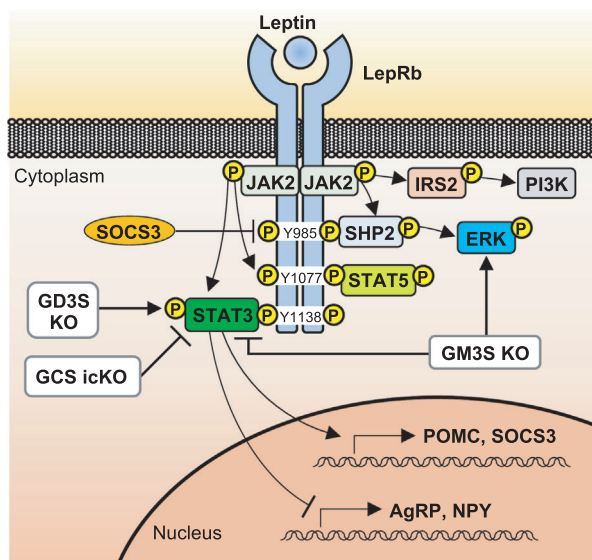


Fig. 4. Leptin receptor signaling pathways and altered signaling observed in ganglioside KO mice and cells. The increased levels of a-series gangliosides in the hypothalamus (i.e., GD3S KO) enhanced STAT3 phosphorylation, whereas lack of a-series gangliosides (i.e., GCS icKO and GM3S KO) reduced STAT3 phosphorylation, suggesting that a-series gangliosides positively regulate LepRb-STAT3 signaling. In contrast, the lack of a-series gangliosides or GM1b expressed in GM3S KO may enhance LepRb-ERK signaling.

kinase (ERK). Thus, SHP2 positively regulates leptin-mediated ERK activation, and the SHP2-ERK pathway plays an important role in leptin-dependent regulation of energy balance. Phosphorylation of LepRb Tyr¹⁰⁷⁷ similarly promotes activation of STAT5 through phosphorylation by JAK2. STAT5 is involved in central regulation of energy balance, but the LepRb-STAT5 pathway does not play an essential role in body weight regulation [54].

In vertebrates, gangliosides are expressed most abundantly in nerve tissues. Complex gangliosides GM1, GD1a, GD1b, and GT1b are the predominant species in mammalian brains [55]. Functional involvement of gangliosides in central regulation of energy homeostasis through LepRb signaling was first demonstrated using a mouse model with inducible KO of GlcCer synthase (GCS; *Ugcg*). GCS is essential for neuronal development; therefore, systemic KO mice were embryonic lethal, and the neuron-specific KO mice displayed severe developmental defects [56–58]. To circumvent these defects, R. Jennemann's group generated a tamoxifen-inducible neuron-specific GCS KO (GCS icKO) mouse model and used it to

investigate functional roles of neuronal GSLs in energy homeostasis [59]. icKO mice displayed progressive obesity, hypothermia, and reduced sympathetic activity. Their hypothalamic LepRb signaling was also reduced, as evidenced by neuronal activity (STAT3 phosphorylation and c-fos protein expression) following i.p. leptin administration. Interaction between LepRb and GM1/GD1a in mouse hypothalamic neuronal cell line N-41 was demonstrated by *in situ* proximity ligation assay and co-immunoprecipitation experiments. Treatment of N-41 cells with n-butyldeoxynojirimycin (NB-DNJ), a GCS-specific inhibitor that depletes GlcCer and its derived gangliosides, strongly reduced leptin-induced JAK phosphorylation. These findings indicate that a-series gangliosides positively regulate leptin metabolic activity by interacting with LepRb in hypothalamic neurons.

GD3 synthase (GD3S; *St8sia1*) KO mice, which lack b-series gangliosides (e.g., GD1b, GT1b), had serum leptin levels much lower than those of WT mice [60]. Leptin was accumulated in adipose tissues of KO mice, indicating deficient leptin secretion. Consistently, primary culture experiments with adipose-derived stromal vascular fractions (SVF) showed that secretion of leptin, but not of adiponectin (another important adipocyte-derived hormone), was notably lower in KO mice than in WT. Flow cytometric analyses revealed that SVF cells of WT expressed both a- and b-series gangliosides and that deficient leptin secretion in SVF cells of KO mice was restored by exogenous addition of b-series gangliosides (GD3, GD1b, GT1b) to culture medium. These findings, and results of experiments using ganglioside-depleted adipocytes and immunolocalization of leptin and caveolin-1, indicate that b-series gangliosides regulate leptin secretion from adipocytes in lipid rafts.

GD3S KO mice had greatly reduced serum leptin levels, but did not develop obesity; that is, their body weight was similar to that of WT. Hypothalamic leptin signaling was enhanced in the KO mice, as evidenced by STAT3 phosphorylation levels in ARC [61]. Overexpression of GD3S in N-41 cells, which enhanced expression of b-series gangliosides and suppressed that of a-series gangliosides, reduced leptin-induced STAT3 phosphorylation. Leptin-mediated interaction of LepRb with GM1 or GD1a was demonstrated by co-immunoprecipitation experiments. These findings indicate that increased levels of a-series gangliosides in the hypothalamus of KO mice enhanced central leptin signaling and that such enhancement compensated for deficient leptin secretion, resulting in seemingly normal energy expenditure.

Studies by our and R.L. Proia's groups demonstrated that GM3S KO mice with C57BL/6 background have seemingly normal obesity phenotype similar to WT, even with high-fat diet (HFD) feeding [5,62]. In contrast, obesity phenotype of KO mice with obese KK-Ay background was strikingly different from that of WT control [63]. WT KK-Ay mice were hyperphagic and developed severe, early-onset obesity, and diabetic pathology; in contrast, GM3S KO mice with KK-Ay background had significantly lower body weight and food intake and improved glucose and insulin tolerance. Hypothalamic sensitivity to leptin in WT KK-Ay, evaluated on the basis of c-fos immunoreactivity in the ARC following i.p. leptin administration, was greatly reduced by age 10 weeks because of development of 'leptin resistance', a state in which elevation or exogenous administration of leptin is not sufficient to reduce feeding or body weight [64]. In contrast, hypothalamic sensitivity to leptin in GM3S KO KK-Ay was maintained at age 10 weeks. GM3S KO in N-41 cells (which lack a-series gangliosides and instead express minor o-series ganglioside GM1b, whose synthesis does not require GM3S) resulted in suppression of leptin-induced STAT3 phosphorylation. In contrast, leptin-induced ERK phosphorylation was greatly enhanced in these cells. Leptin activates SHP2-ERK pathway and controls c-fos expression [65]; therefore, these findings suggest that LepRb-SHP2-ERK pathway is upregulated in GM3S KO and thereby maintains responsiveness to leptin in GM3S KO KK-Ay mice.

As summarized in Fig. 4, increased levels of a-series gangliosides in the hypothalamus (i.e., GD3S KO) enhanced STAT3 phosphorylation, whereas lack of a-series gangliosides (i.e., GCS icKO and GM3S KO) reduced STAT3 phosphorylation, suggesting that a-series gangliosides positively regulate LepRb-STAT3 signaling. In contrast, the lack of a-series gangliosides or GM1b expressed in GM3S KO may enhance LepRb-ERK signaling. In conclusion, GM3 and related gangliosides function in LepRb signaling, in a ganglioside species-specific manner, by modulating downstream signaling pathways essential for energy homeostasis. Molecular mechanisms underlying these effects remain to be elucidated, but likely involve direct interactions between LepRb and specific gangliosides. It is also possible that crosstalk occurs between LepRb and other receptors at the cell surface, whereby specific gangliosides affect hypothalamic neurons. Ongoing studies by our group and others will address these intriguing possibilities and clarify the mechanisms underlying ganglioside-dependent control of energy homeostasis.

Role of GM3 molecular species in TLR4 signaling

GM3 (Fig. 1A,B) is a predominant ganglioside in human sera, with concentration $10\text{--}15\text{ }\mu\text{g}\cdot\text{mL}^{-1}$ ($\sim 10\text{ }\mu\text{M}$) [12,66]. Fatty acids of serum GM3 are comprise long-chain fatty acid (LCFA), (16:0, 18:0, and 20:0); very-long-chain fatty acid (VLCFA), (22:0, 23:0, 24:0); unsaturated VLCFA, (22:1 and 24:1); and α -hydroxyl VLCFA (h24:0, h24:1) (Fig. 1B). Human sera contain similar levels of LCFA, VLCFA, and unsaturated VLCFA species and a smaller level of α -hydroxyl species. Altered expression patterns of various GM3 species have been observed in patients with metabolic disorders [4]; however, specific biological functions of these species are unclear.

We investigated effects of various GM3 species on innate immune responses of human peripheral blood CD14-positive cells (monocytes) [12]. GM3 species alone had no notable effects. VLCFA species (22:0, 24:0, h24:0) synergistically enhanced lipopolysaccharide (LPS)-mediated production of proinflammatory cytokines (IL-6, TNF- α , IL-12/23 p40), whereas LCFA species (16:0, 18:0) strongly inhibited this process. Unsaturated VLCFA (24:1) had no stimulatory effect, suggesting that desaturation is a protective modification against proinflammatory properties of VLCFA species. These enhancing and inhibitory effects were dose-dependent and were observed at physiological concentration ($<10\text{ }\mu\text{M}$).

Among various types of gangliosides, only VLCFA-GM3 species displayed dose-dependent synergistic activation; other complex gangliosides had inhibitory effects [12]. GM3 species displayed acyl-chain structure-dependent positive and negative regulation, but Cer, GlcCer, and LacCer had no such effects. Thus, innate immune responses are positively and negatively regulated by serum GM3 species in an acyl-chain-dependent manner (Fig. 5A).

Chronic inflammation is an important factor in pathogenesis of metabolic disorders [67,68]. Prolonged activation of innate immune responses by pattern recognition receptors such as Toll-like receptors (TLR) [69,70] leads to chronic inflammation. In metabolic disorders, TLR4 is activated by various ligands: (a) exogenous pathogen-associated molecular patterns (PAMPs), for example, elevated serum LPS levels [71], (b) endogenous damage-associated molecular patterns (DAMPs) released from activated macrophages and adipose tissues, for example, high-mobility group box-1 protein (HMGB1) [72,73], free fatty acids (FFAs) [74], and fetuin-A protein [39].

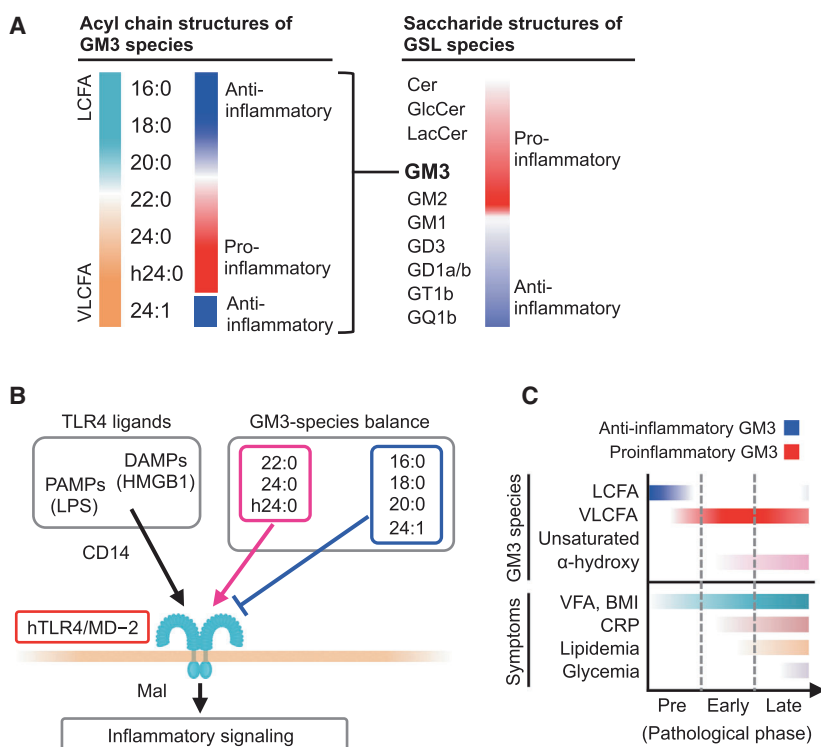


Fig. 5. Pathophysiological significance of GM3 molecular species. (A) Regulation of pro- and anti-inflammatory activity of GM3 species, precursor GSLs, and complex gangliosides, dependent on acyl-chain and saccharide-chain structure. (B) Regulation of hTLR4/MD-2 signaling by GM3 species balance between VLCFA species and LCFA/unsaturated VLCFA species. (C) Association between serum pro-/anti-inflammatory GM3 species and progression of metabolic disorders.

We investigated mechanisms underlying GM3-mediated innate immune responses were investigated by screening signaling pathways targeted by GM3 species. Monocytes were co-stimulated by exogenous PAMPs and endogenous DAMPs (including several TLR ligands) in combination with GM3 species. VLCFA species showed selective synergy with LPS, a TLR4 ligand, but not with other TLR ligands [12]. LCFA species strongly inhibited LPS-mediated cytokine production. Thus, TLR4-mediated cytokine production was selectively modulated by GM3 species. VLCFA species also strongly enhanced cytokine production mediated by HMGB1, an endogenous TLR4 ligand released from dead cells or visceral adipocytes in obese patients [72,73]. Interestingly, effects of GM3 22:0 and 24:0 were reversed by increased doses of GM3 16:0, 18:0, and 24:1. These findings indicate that GM3 species act as selective endogenous modulators of TLR4 signaling and that TLR4 activation is positively or negatively controlled by the balance of LCFA-, VLCFA-, and unsaturated VLCFA-GM3 species in serum (Fig. 5B).

We investigated pro-/anti-inflammatory roles of GM3 species in metabolic disorders by performing LC-MS/MS analysis of expression patterns of serum GM3 species in human sera [4,12]. Progressive increase in VLCFA-GM3 species and decrease in LCFA-GM3 species were correlated with increases of HOMA-IR

(homeostatic model assessment for insulin resistance) and serum C-reactive protein (CRP) and with severity of metabolic disorders. In patients with obesity (presymptomatic), hyperlipidemia, or hyperglycemia, LCFA species (16:0, 18:0, 20:0) were strongly reduced, whereas VLCFA species (22:0, 23:0, 24:0, h24:0) were elevated.

Early- and intermediate-phase increases of body mass index (BMI) and abdominal circumference were associated with strong reduction of LCFA species and increase of VLCFA species. Elevation of VLCFA-GM3 species is evidently characteristic of obesity and plays a pathogenic role in early stages of metabolic disorders. α -Hydroxy VLCFA-GM3 (h24:0) levels showed strong linear correlations with BMI and abdominal circumference and also with insulin resistance and chronic inflammation indicators such as ALT, HOMA-IR, and CRP. On the other hand, moderate reduction of VLCFA species and strong increase of unsaturated VLCFA species were observed in severe obesity and following onset of metabolic disorders (hyperlipidemia, hyperglycemia). Desaturation of VLCFA species evidently occurs following onset of metabolic disorders.

Our above findings, taken together, clearly indicate that pathogenesis of metabolic disorders via chronic inflammatory processes involves increases of VLCFA-GM3 species and decreases of LCFA-GM3 species

(Fig. 5C). In steady state, homeostasis is maintained by proper balance of GM3 species; in presymptomatic and early phases of metabolic disorders, VLCFA species increase and promote chronic inflammation and insulin resistance; in late phases, desaturation of VLCFA species occurs, but α -hydroxyl VLCFA species can still potentiate chronic inflammation.

In view of the notable increases of serum VLCFA-GM3 levels in metabolic disorders, we performed comparative studies using mouse models of obesity. *ob/ob* mice showed early onset of metabolic disorders and had an increased GM3 abundance in visceral adipose tissue [2,12]. We measured levels of various GM3 species by LC-MS/MS [12]. Epididymal adipose tissue of control C57/BL6 mice had 16:0, 18:0, 20:0, 22:0, 23:0, 24:0, and 24:1 as major GM3 species, and α -hydroxyl species as a minor component. *ob/ob* mice showed notably higher level of α -hydroxyl species: strong increase of VLCFA species (h22:0, h23:0, h24:0) and moderate increase of LCFA and unsaturated VLCFA species (h16:0, h18:0, h20:0, h24:1). Thus, increased VLCFA-GM3 level and α -hydroxylation occur in visceral adipose tissue in obesity and metabolic disorders. Feeding of HFD for 10 weeks resulted in obesity and increased GM3 levels [5,12]. LC-MS/MS analysis revealed greater increase of α -hydroxyl GM3 species in HFD-fed mice [12]. In comparison with *ob/ob* mice, predominant GM3 species in HFD-fed mice had shorter acyl chains (h18:0, h20:0, h22:0).

Crystal structure analysis of TLR4/MD-2 complex [75,76] indicated formation of two ligand-binding sites for LPS on the dimerization interface between two TLR4/MD-2 units. MD-2 forms hydrophobic pockets that bind to the acyl-chain moiety of LPS, while TLR4 leucine-rich repeats (LRR) form basic clusters that recognize the hydrophilic head group of LPS. We found that mutations of basic residues greatly reduced human TLR4 activation by VLCFA-GM3 [12]. MD-2-dependent recognition of GM3 acyl chain was evaluated by comparing inhibitory effects of GM3 16:0 on mTLR4/mMD-2, hTLR4/hMD-2, and mTLR4/hMD-2, a chimeric complex of mouse TLR4 and human MD-2. hTLR4/hMD-2 and chimeric mTLR4/hMD-2 activation was inhibited by 16:0 GM3 at physiological concentration, whereas mTLR4/mMD-2 activation was not. Thus, MD-2 is evidently involved in recognition of GM3 acyl-chain structure and provides a basis for molecular species selectivity [12].

To elucidate the mechanisms whereby GM3 species enhance or suppress TLR4 activation in an acyl-chain structure-dependent manner, we examined a ligand-macromolecular docking on hTLR4/hMD-2 complex. Binding modes of VLCFA-GM3 (24:0) and LCFA-GM3

(16:0) on the molecular surfaces around the hydrophobic pocket of hMD-2 and the basic residues of hTLR4 were determined. Docking models of hTLR4/hMD-2/GM3 (24:0 or 16:0) complex are shown in Fig. 6A,B. GM3 24:0 and 16:0 bound to hydrophobic pocket of hMD-2 via the fatty acid and sphingoid base (Fig 6C–E), similar to LPS and lipid IVa, respectively. The GM3 24:0 binding mode overlapped closely to that of Ra-LPS in the crystal structure of reference, and the GM3 24:0 saccharide chain was surrounded by basic residues of TLR4 (Fig. 6C). Basic residues of TLR4 (K341, K362, and R322) that interacted with LPS saccharide chain and showed conformational changes upon TLR4 activation [76,77] were closely associated with GM3 24:0 saccharide chain. In contrast, R264, a key residue in recognition of 4'-phosphate of LPS and triggering TLR4 activation [76], was far from GM3 24:0 saccharide chain. These findings indicate that VLCFA-GM3 is able to enhance TLR4 signaling without triggering activation.

The GM3 16:0 binding mode was compared to that of lipid IVa complexed with hMD-2 (Fig. 6E). Lipid IVa binding mode differed from that of LPS, showing reverse orientation of 4'-phosphate and acyl chains, which may inhibit hTLR4/hMD-2 dimer formation by presenting hydrophilic groups (phosphate, glucosamine) to lipophilic dimer interface [75,76] (Fig. 6C,E). Similarly, GM3 16:0 binding mode was opposite that of GM3 24:0, showing reverse orientation of saccharide chain and the acyl chain (Fig. 6D), thereby interfering with and suppressing TLR4 activation through presentation of saccharide chain to dimer interface (Fig. 6E). Lipid IVa and lipid A (LPS-core structure), in contrast, show the same binding orientations on mTLR4/mMD-2 [75]. These comparative analyses help clarify the mechanisms whereby various GM3 species enhance or reduce TLR4 activation in an acyl-chain structure-dependent manner [12].

Molecular mechanisms whereby GM3 species are secreted and targeted to TLR4/MD-2 complex remain to be elucidated. GM3 is presumably secreted into serum as part of a lipoprotein complex [4,66]. TLR4 is activated by LDL cholesterol [78], and Cer 24:0 is preferentially incorporated into LDL cholesterol [79]. We showed that serum VLCFA-GM3 level is correlated with non-HDL cholesterol, whereas serum LCFA-GM3 level is correlated with HDL cholesterol, indicating species-selective incorporation into lipoproteins [4,12]. Soluble-form CD14, a carrier protein for LPS, also enhances pro- and anti-inflammatory activity of GM3 species [12]. α -Hydroxylation of GM3 species, mediated by fatty acid-2 hydroxylase (FA2H), may promote secretion of GM3 species, since

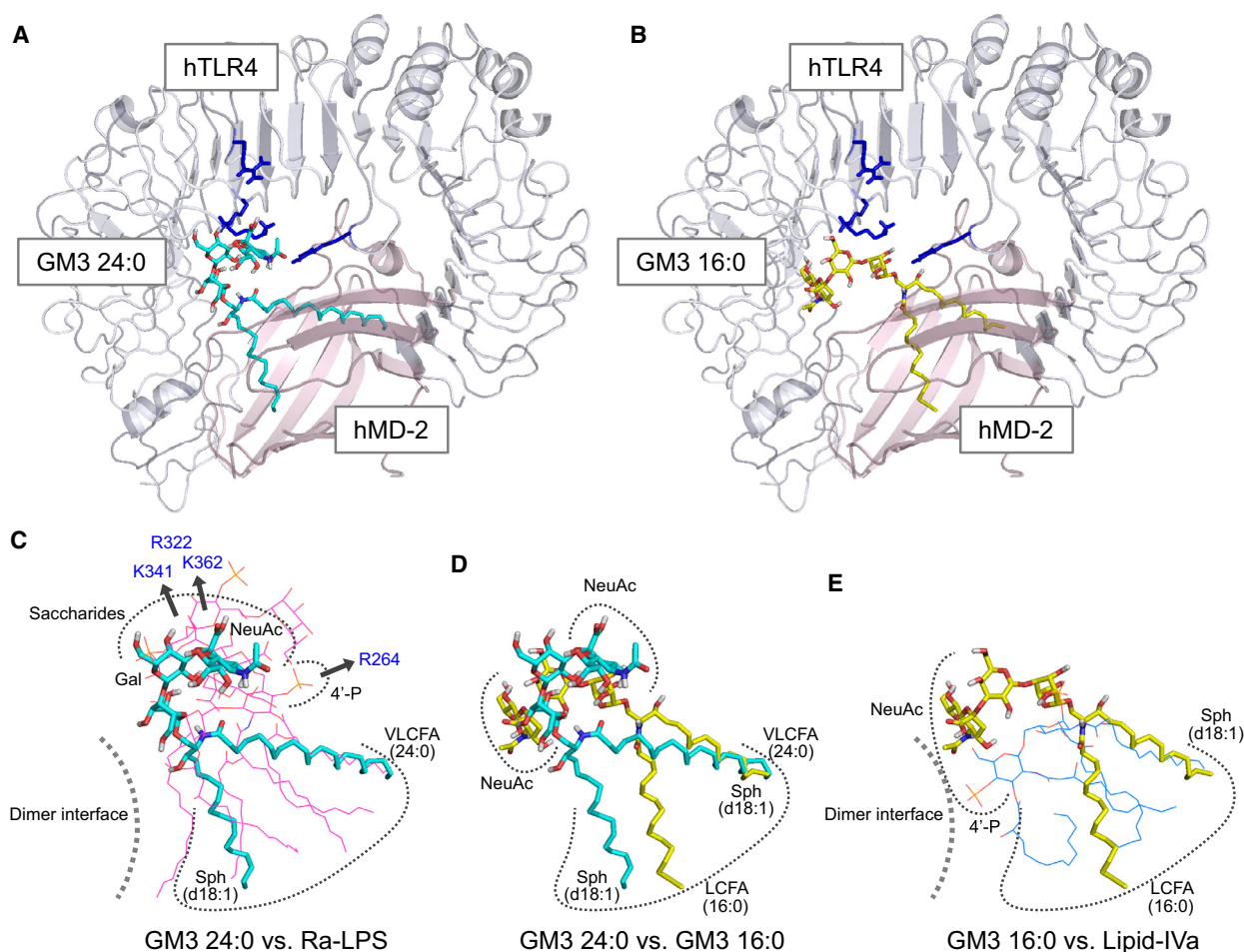


Fig. 6. Ligand macromolecular docking analysis reveals species-specific GM3 recognition by TLR4/MD-2. (A, B) Docking models of GM3 24:0 (A) and 16:0 (B) binding to human TLR4/MD-2 complex (3FXI). Blue color: basic residues of TLR4. (C–E) Superposition of GM3 24:0 (in docking model) vs. Ra-LPS (in 3FXI) (C), GM3 24:0 vs. GM3 16:0 (in docking model) (D), and GM3 16:0 vs. lipid IVa (in 2E59) (E). Basic residues and the dimer interface are indicated schematically.

α -hydroxylation reduces acyl-chain hydrophobicity and affects lipid diffusion [80].

Metabolic and biosynthetic pathways of the various GM3 species are comprised of complex mechanisms that depend on activities of several enzymes: ceramide synthases (CerSs), fatty acid elongases (Elovl), acyl-CoA desaturases, and ST3GAL5. Increased LCFA-Cer (16:0) and decreased VLCFA-Cer (22:0, 24:0) levels in obesity were correlated with progression of metabolic disorders [81,82]. Such alterations of Cer species are presumably due to imbalance of CerS2/6 expression and inhibition of β -oxidation. Imbalanced expression of Cer species in metabolic disorders results in reduced LCFA-GM3 and increased VLCFA-GM3 production. *Elovl6* KO inhibited progression of metabolic disorders by altering fatty acid composition [83]. Blocking of fatty acid elongation (16:0-to-18:0) in

these *Elovl6* KO mice resulted in increased 16:0 and decreased 18:0-to-24:0 fatty acid content. *Elovl6* deficiency may reduce expression levels of VLCFA-GM3 species and help maintain homeostatic balance between pro- and anti-inflammatory GM3 species. In resolution phase of innate immune responses, desaturases terminate inflammation by inducing fatty acid desaturation [84]. We found that desaturation of VLCFA-GM3 species occurs after onset and in severe metabolic disorders. Expression of both elongase and desaturase genes is regulated by SREBP-1, a key transcription factor in lipid signaling which is activated simultaneously with NF- κ B [83,84]. TNF- α and IL-1 β induce *St3gal5* expression and GM3 production in adipocytes [2,5], and production of α -hydroxy VLCFA-GM3 in obesity involves TLR4 signaling [12]. These findings, taken together, clearly indicate that fatty acid

structures and GM3 species expression levels are controlled by complex, precisely coordinated mechanisms.

Concluding remarks

GM3 is localized on plasma membrane as a component of membrane microdomains, which constitute signaling platforms for IR and play essential roles in regulation of signal transduction. GM3 species, varying widely in acyl-chain structure, are secreted abundantly into human serum and function as endogenous TLR4 modulators in an acyl-chain structure-dependent manner. TLR4 activation is selectively enhanced by VLCFA-GM3 species, but suppressed by LCFA and unsaturated VLCFA-GM3 species. Metabolic disorders are often characterized by increased VLCFA-GM3 and decreased LCFA-GM3 levels in serum, which contribute to disease progression via chronic inflammatory process. LC-MS/MS analysis of serum GM3 species will potentially facilitate evaluation of hidden risks of inflammatory diseases mediated by TLR4 signaling. The studies summarized here, by clarifying the pathophysiological roles of GM3 species, will lead to novel diagnostic and therapeutic approaches involving the development of anti-inflammatory drug.

Acknowledgements

The authors' studies described in this review were supported by a Grant-in-Aid for Scientific Research (B) from MEXT (to JI) (20H03452), the Takeda Foundation (JI), and the MEXT-Supported Program for the Strategic Research Foundation at Private Universities (S1201031). The authors are grateful to Dr S. Anderson for English editing of the manuscript.

Conflicts of interest

The authors declare no conflict of interest.

Author contributions

JI, KI, MN, and HK wrote the review. TN and KF contributed the significant parts of research involved in this review, LC-MS/MS analysis, and insightful structural/functional analysis of TLR4, respectively.

References

- Inokuchi J & Radin NS (1987) Preparation of the active isomer of 1-phenyl-2-decanoylamino-3-morpholino-1-propanol, inhibitor of murine glucocerebrosidase synthetase. *J Lipid Res* **28**, 565–571.
- Tagami S, Inokuchi JI, Kabayama K, Yoshimura H, Kitamura F, Uemura S, Ogawa C, Ishii A, Saito M, Ohtsuka Y *et al.* (2002) Ganglioside GM3 participates in the pathological conditions of insulin resistance. *J Biol Chem* **277**, 3085–3092.
- Sato T, Nihei Y, Nagafuku M, Tagami S, Chin R, Kawamura M, Miyazaki S, Suzuki M, Sugahara S, Takahashi Y *et al.* (2008) Circulating levels of ganglioside GM3 in metabolic syndrome: a pilot study. *Obes Res Clin Pract* **2**, 231–238.
- Veillon L, Go S, Matsuyama W, Suzuki A, Nagasaki M, Yatomi Y & Inokuchi J (2015) Identification of ganglioside GM3 molecular species in human serum associated with risk factors of metabolic syndrome. *PLoS One* **10**, e0129645.
- Nagafuku M, Sato T, Sato S, Shimizu K, Taira T & Inokuchi J (2015) Control of homeostatic and pathogenic balance in adipose tissue by ganglioside GM3. *Glycobiology* **25**, 303–318.
- Inokuchi J & Uemura S (2014) ST3 beta-galactoside alpha-2,3-sialyltransferase 5 (ST3GAL5). *Handbook of Glycosyltransferases and Related Genes* (Taniguchi N, Honke K, Fukuda M, Narimatsu H, Yamaguchi Y & Angata T, eds), Vol. 2, pp. 675–684, 2nd edn. Springer, Tokyo, Heidelberg, New York, Dordrecht, London.
- Inokuchi J (2010) Membrane microdomains and insulin resistance. *FEBS Lett* **584**, 1864–1871.
- Inokuchi J (2014) GM3 and diabetes. *Glycoconj J* **31**, 193–197.
- Inokuchi J (2011) Physiopathological function of hematoside (GM3 ganglioside). *Proc Jpn Acad Ser B Phys Biol Sci* **87**, 179–198.
- Kabayama K, Sato T, Saito K, Loberto N, Prinetti A, Sonnino S, Kinjo M, Igarashi Y & Inokuchi J (2007) Dissociation of the insulin receptor and caveolin-1 complex by ganglioside GM3 in the state of insulin resistance. *Proc Natl Acad Sci USA* **104**, 13678–13683.
- Kabayama K, Sato T, Kitamura F, Uemura S, Kang BW, Igarashi Y & Inokuchi J (2005) TNFalpha-induced insulin resistance in adipocytes as a membrane microdomain disorder: involvement of ganglioside GM3. *Glycobiology* **15**, 21–29.
- Kanoh H, Nitta T, Go S, Inamori KI, Veillon L, Nihei W, Fujii M, Kabayama K, Shimoyama A, Fukase K *et al.* (2020) Homeostatic and pathogenic roles of GM3 ganglioside molecular species in TLR4 signaling in obesity. *EMBO J* **39**, e101732.
- Chawla A, Nguyen KD & Goh YP (2011) Macrophage-mediated inflammation in metabolic disease. *Nat Rev Immunol* **11**, 738–749.
- Bays HE, Gonzalez-Campoy JM, Bray GA, Kitabchi AE, Bergman DA, Schorr AB, Rodbard HW & Henry RR (2008) Pathogenic potential of adipose tissue and metabolic consequences of adipocyte hypertrophy and

- increased visceral adiposity. *Expert Rev Cardiovasc Ther* **6**, 343–368.
- 15 de Ferranti S & Mozaffarian D (2008) The perfect storm: obesity, adipocyte dysfunction, and metabolic consequences. *Clin Chem* **54**, 945–955.
 - 16 Xu H, Barnes GT, Yang Q, Tan G, Yang D, Chou CJ, Sole J, Nichols A, Ross JS, Tartaglia LA *et al.* (2003) Chronic inflammation in fat plays a crucial role in the development of obesity-related insulin resistance. *J Clin Invest* **112**, 1821–1830.
 - 17 Matsuzawa Y (1997) Pathophysiology and molecular mechanisms of visceral fat syndrome: the Japanese experience. *Diabetes Metab Rev* **13**, 3–13.
 - 18 Saltiel AR (2012) Insulin resistance in the defense against obesity. *Cell Metab* **15**, 798–804.
 - 19 Samaan MC (2011) The macrophage at the intersection of immunity and metabolism in obesity. *Diabetol Metab Syndr* **3**, 29.
 - 20 Sorisky A, Molgat AS & Gagnon A (2013) Macrophage-induced adipose tissue dysfunction and the preadipocyte: should I stay (and differentiate) or should I go? *Adv Nutr* **4**, 67–75.
 - 21 Suganami T & Ogawa Y (2010) Adipose tissue macrophages: their role in adipose tissue remodeling. *J Leukoc Biol* **88**, 33–39.
 - 22 Shimizu K, Sakai M, Ando M, Chiji H, Kawada T, Mineo H & Taira T (2006) Newly developed primary culture of rat visceral adipocytes and their in vitro characteristics. *Cell Biol Int* **30**, 381–388.
 - 23 Sato T, Nagafuku M, Shimizu K, Taira T, Igarashi Y & Inokuchi J (2008) Physiological levels of insulin and IGF-I synergistically enhance the differentiation of mesenteric adipocytes. *Cell Biol Int* **32**, 1397–1404.
 - 24 Gadgil MD, Anderson CA, Kandula NR & Kanaya AM (2014) Dietary patterns in Asian Indians in the United States: an analysis of the metabolic syndrome and atherosclerosis in South Asians Living in America study. *J Acad Nutr Diet* **114**, 238–243.
 - 25 Istvan ES & Deisenhofer J (2001) Structural mechanism for statin inhibition of HMG-CoA reductase. *Science* **292**, 1160–1164.
 - 26 Stein EA (2002) An investigative look: selective cholesterol absorption inhibitors—embarking on a new standard of care. *Am J Manag Care* **8**, S36–S39, discussion S45–7.
 - 27 Betters JL & Yu L (2010) NPC1L1 and cholesterol transport. *FEBS Lett* **584**, 2740–2747.
 - 28 Altmann SW, Davis HR Jr, Zhu LJ, Yao X, Hoos LM, Tetzloff G, Iyer SP, Maguire M, Golovko A, Zeng M *et al.* (2004) Niemann-Pick C1 Like 1 protein is critical for intestinal cholesterol absorption. *Science* **303**, 1201–1204.
 - 29 Nakano T, Inoue I, Takenaka Y, Ono H, Katayama S, Awata T & Murakoshi T (2016) Ezetimibe promotes brush border membrane-to-lumen cholesterol efflux in the small intestine. *PLoS One* **11**, e0152207.
 - 30 Lin X, Racette SB, Ma L, Wallendorf M & Ostlund RE Jr (2017) Ezetimibe increases endogenous cholesterol excretion in humans. *Arterioscler Thromb Vasc Biol* **37**, 990–996.
 - 31 Jia L, Betters JL & Yu L (2011) Niemann-pick C1-like 1 (NPC1L1) protein in intestinal and hepatic cholesterol transport. *Annu Rev Physiol* **73**, 239–259.
 - 32 Wang J, Chu BB, Ge L, Li BL, Yan Y & Song BL (2009) Membrane topology of human NPC1L1, a key protein in enterohepatic cholesterol absorption. *J Lipid Res* **50**, 1653–1662.
 - 33 Brown MS, Radhakrishnan A & Goldstein JL (2018) Retrospective on cholesterol homeostasis: the central role of scap. *Annu Rev Biochem* **87**, 783–807.
 - 34 Davies JP, Levy B & Ioannou YA (2000) Evidence for a Niemann-pick C (NPC) gene family: identification and characterization of NPC1L1. *Genomics* **65**, 137–145.
 - 35 Zhang JH, Ge L, Qi W, Zhang L, Miao HH, Li BL, Yang M & Song BL (2011) The N-terminal domain of NPC1L1 protein binds cholesterol and plays essential roles in cholesterol uptake. *J Biol Chem* **286**, 25088–25097.
 - 36 Ge L, Qi W, Wang LJ, Miao HH, Qu YX, Li BL & Song BL (2011) Flotillins play an essential role in Niemann-Pick C1-like 1-mediated cholesterol uptake. *Proc Natl Acad Sci USA* **108**, 551–556.
 - 37 Simons K & Vaz WL (2004) Model systems, lipid rafts, and cell membranes. *Annu Rev Biophys Biomol Struct* **33**, 269–295.
 - 38 Wang J & Yu RK (2013) Interaction of ganglioside GD3 with an EGF receptor sustains the self-renewal ability of mouse neural stem cells in vitro. *Proc Natl Acad Sci USA* **110**, 19137–19142.
 - 39 Saslowsky DE, Cho JA, Chinnapen H, Massol RH, Chinnapen DJ-F, Wagner JS, De Luca HE, Kam W, Paw BH & Lencer WI (2010) Intoxication of zebrafish and mammalian cells by cholera toxin depends on the flotillin/reggie proteins but not Derlin-1 or -2. *J Clin Invest* **120**, 4399–4409.
 - 40 Nihei W, Nagafuku M, Hayamizu H, Odagiri Y, Tamura Y, Kikuchi Y, Veillon L, Kanoh H, Inamori KI, Arai K *et al.* (2018) NPC1L1-dependent intestinal cholesterol absorption requires ganglioside GM3 in membrane microdomains. *J Lipid Res* **59**, 2181–2187.
 - 41 Ohmi Y, Tajima O, Ohkawa Y, Yamauchi Y, Sugiura Y, Furukawa K & Furukawa K (2011) Gangliosides are essential in the protection of inflammation and neurodegeneration via maintenance of lipid rafts: elucidation by a series of ganglioside-deficient mutant mice. *J Neurochem* **116**, 926–935.
 - 42 Yoneshige A, Sasaki A, Miyazaki M, Kojima N, Suzuki A & Matsuda J (2010) Developmental changes in glycolipids and synchronized expression of nutrient transporters in the mouse small intestine. *J Nutr Biochem* **21**, 214–226.

- 43 Jennemann R, Kaden S, Sandhoff R, Nordstrom V, Wang S, Volz M, Robine S, Amen N, Rothermel U, Wiegandt H *et al.* (2012) Glycosphingolipids are essential for intestinal endocytic function. *J Biol Chem* **287**, 32598–32616.
- 44 Li PS, Fu ZY, Zhang YY, Zhang JH, Xu CQ, Ma YT, Li BL & Song BL (2014) The clathrin adaptor Numb regulates intestinal cholesterol absorption through dynamic interaction with NPC1L1. *Nat Med* **20**, 80–86.
- 45 Hegele RA, Guy J, Ban MR & Wang J (2005) NPC1L1 haplotype is associated with inter-individual variation in plasma low-density lipoprotein response to ezetimibe. *Lipids Health Dis* **4**, 16.
- 46 Weinglass AB, Kohler M, Schulte U, Liu J, Nketiah EO, Thomas A, Schmalhofer W, Williams B, Bildl W, McMasters DR *et al.* (2008) Extracellular loop C of NPC1L1 is important for binding to ezetimibe. *Proc Natl Acad Sci USA* **105**, 11140–11145.
- 47 Friedman JM & Halaas JL (1998) Leptin and the regulation of body weight in mammals. *Nature* **395**, 763–770.
- 48 Tartaglia LA, Dembski M, Weng X, Deng N, Culpepper J, Devos R, Richards GJ, Campfield LA, Clark FT, Deeds J *et al.* (1995) Identification and expression cloning of a leptin receptor, OB-R. *Cell* **83**, 1263–1271.
- 49 Bates SH, Stearns WH, Dundon TA, Schubert M, Tso AW, Wang Y, Banks AS, Lavery HJ, Haq AK, Maratos-Flier E *et al.* (2003) STAT3 signalling is required for leptin regulation of energy balance but not reproduction. *Nature* **421**, 856–859.
- 50 Yeo GS & Heisler LK (2012) Unraveling the brain regulation of appetite: lessons from genetics. *Nat Neurosci* **15**, 1343–1349.
- 51 Friedman J (2016) The long road to leptin. *J Clin Invest* **126**, 4727–4734.
- 52 Allison MB & Myers MG Jr (2014) 20 years of leptin: connecting leptin signaling to biological function. *J Endocrinol* **223**, T25–T35.
- 53 Bjorbak C, Lavery HJ, Bates SH, Olson RK, Davis SM, Flier JS & Myers MG Jr (2000) SOCS3 mediates feedback inhibition of the leptin receptor via Tyr985. *J Biol Chem* **275**, 40649–40657.
- 54 Singireddy AV, Inglis MA, Zuure WA, Kim JS & Anderson GM (2013) Neither signal transducer and activator of transcription 3 (STAT3) or STAT5 signaling pathways are required for leptin's effects on fertility in mice. *Endocrinology* **154**, 2434–2445.
- 55 Schnaar RL (2019) The biology of gangliosides. *Adv Carbohydr Chem Biochem* **76**, 113–148.
- 56 Yamashita T, Wada R, Sasaki T, Deng C, Bierfreund U, Sandhoff K & Proia RL (1999) A vital role for glycosphingolipid synthesis during development and differentiation. *Proc Natl Acad Sci USA* **96**, 9142–9147.
- 57 Yamashita T, Allende ML, Kalkofen DN, Werth N, Sandhoff K & Proia RL (2005) Conditional LoxP-flanked glucosylceramide synthase allele controlling glycosphingolipid synthesis. *Genesis* **43**, 175–180.
- 58 Jennemann R, Sandhoff R, Wang S, Kiss E, Gretz N, Zuliani C, Martin-Villalba A, Jager R, Schorle H, Kenzelmann M *et al.* (2005) Cell-specific deletion of glucosylceramide synthase in brain leads to severe neural defects after birth. *Proc Natl Acad Sci USA* **102**, 12459–12464.
- 59 Nordstrom V, Willershauser M, Herzer S, Rozman J, von Bohlen Und Halbach O, Meldner S, Rothermel U, Kaden S, Roth FC, Waldeck C *et al.* (2013) Neuronal expression of glucosylceramide synthase in central nervous system regulates body weight and energy homeostasis. *PLoS Biol* **11**, e1001506.
- 60 Ji S, Ohkawa Y, Tokizane K, Ohmi Y, Banno R, Furukawa K, Kiyama H & Furukawa K (2015) b-Series gangliosides crucially regulate leptin secretion in adipose tissues. *Biochem Biophys Res Commun* **459**, 189–195.
- 61 Ji S, Tokizane K, Ohkawa Y, Ohmi Y, Banno R, Okajima T, Kiyama H, Furukawa K & Furukawa K (2016) Increased a-series gangliosides positively regulate leptin/Ob receptor-mediated signals in hypothalamus of GD3 synthase-deficient mice. *Biochem Biophys Res Commun* **479**, 453–460.
- 62 Yamashita T, Hashiramoto A, Haluzik M, Mizukami H, Beck S, Norton A, Kono M, Tsuji S, Daniotti JL, Werth N *et al.* (2003) Enhanced insulin sensitivity in mice lacking ganglioside GM3. *Proc Natl Acad Sci USA* **100**, 3445–3449.
- 63 Inamori KI, Ito H, Tamura Y, Nitta T, Yang X, Nihei W, Shishido F, Imazu S, Tsukita S, Yamada T *et al.* (2018) Deficient ganglioside synthesis restores responsiveness to leptin and melanocortin signaling in obese KK^{ay} mice. *J Lipid Res* **59**, 1472–1481.
- 64 Cui H, Lopez M & Rahmouni K (2017) The cellular and molecular bases of leptin and ghrelin resistance in obesity. *Nat Rev Endocrinol* **13**, 338–351.
- 65 Banks AS, Davis SM, Bates SH & Myers MG Jr (2000) Activation of downstream signals by the long form of the leptin receptor. *J Biol Chem* **275**, 14563–14572.
- 66 Senn HJ, Orth M, Fitzke E, Wieland H & Gerok W (1989) Gangliosides in normal human serum. Concentration, pattern and transport by lipoproteins. *Eur J Biochem* **181**, 657–662.
- 67 Hotamisligil GS (2017) Inflammation, metaflammation and immunometabolic disorders. *Nature* **542**, 177–185.
- 68 Lumeng CN & Saltiel AR (2011) Inflammatory links between obesity and metabolic disease. *J Clin Invest* **121**, 2111–2117.
- 69 Moresco EM, LaVine D & Beutler B (2011) Toll-like receptors. *Curr Biol* **21**, R488–R493.

- 70 Kawai T & Akira S (2011) Toll-like receptors and their crosstalk with other innate receptors in infection and immunity. *Immunity* **34**, 637–650.
- 71 Cani PD, Amar J, Iglesias MA, Poggi M, Knauf C, Bastelica D, Neyrinck AM, Fava F, Tuohy KM, Chabo C *et al.* (2007) Metabolic endotoxemia initiates obesity and insulin resistance. *Diabetes* **56**, 1761–1772.
- 72 Guzman-Ruiz R, Ortega F, Rodriguez A, Vazquez-Martinez R, Diaz-Ruiz A, Garcia-Navarro S, Giral M, Garcia-Rios A, Cobo-Padilla D, Tinahones FJ *et al.* (2014) Alarmin high-mobility group B1 (HMGB1) is regulated in human adipocytes in insulin resistance and influences insulin secretion in beta-cells. *Int J Obes (Lond)* **38**, 1545–1554.
- 73 Harris HE, Andersson U & Pisetsky DS (2012) HMGB1: a multifunctional alarmin driving autoimmune and inflammatory disease. *Nat Rev Rheumatol* **8**, 195–202.
- 74 Shi H, Kokoeva MV, Inouye K, Tzameli I, Yin H & Flier JS (2006) TLR4 links innate immunity and fatty acid-induced insulin resistance. *J Clin Invest* **116**, 3015–3025.
- 75 Ohto U, Fukase K, Miyake K & Shimizu T (2012) Structural basis of species-specific endotoxin sensing by innate immune receptor TLR4/MD-2. *Proc Natl Acad Sci USA* **109**, 7421–7426.
- 76 Park BS, Song DH, Kim HM, Choi BS, Lee H & Lee JO (2009) The structural basis of lipopolysaccharide recognition by the TLR4-MD-2 complex. *Nature* **458**, 1191–1195.
- 77 Ohto U, Yamakawa N, Akashi-Takamura S, Miyake K & Shimizu T (2012) Structural analyses of human Toll-like receptor 4 polymorphisms D299G and T399I. *J Biol Chem* **287**, 40611–40617.
- 78 Stewart CR, Stuart LM, Wilkinson K, van Gils JM, Deng J, Halle A, Rayner KJ, Boyer L, Zhong R, Frazier WA *et al.* (2010) CD36 ligands promote sterile inflammation through assembly of a Toll-like receptor 4 and 6 heterodimer. *Nat Immunol* **11**, 155–161.
- 79 Boon J, Hoy AJ, Stark R, Brown RD, Meex RC, Henstridge DC, Schenk S, Meikle PJ, Horowitz JF, Kingwell BA *et al.* (2013) Ceramides contained in LDL are elevated in type 2 diabetes and promote inflammation and skeletal muscle insulin resistance. *Diabetes* **62**, 401–410.
- 80 Hama H (2010) Fatty acid 2-Hydroxylation in mammalian sphingolipid biology. *Biochim Biophys Acta* **1801**, 405–414.
- 81 Turpin SM, Nicholls HT, Willmes DM, Mourier A, Brodesser S, Wunderlich CM, Mauer J, Xu E, Hammerschmidt P, Bronneke HS *et al.* (2014) Obesity-induced CerS6-dependent C16:0 ceramide production promotes weight gain and glucose intolerance. *Cell Metab* **20**, 678–686.
- 82 Raichur S, Wang ST, Chan PW, Li Y, Ching J, Chaurasia B, Dogra S, Ohman MK, Takeda K, Sugii S *et al.* (2014) CerS2 haploinsufficiency inhibits beta-oxidation and confers susceptibility to diet-induced steatohepatitis and insulin resistance. *Cell Metab* **20**, 687–695.
- 83 Matsuzaka T, Shimano H, Yahagi N, Kato T, Atsumi A, Yamamoto T, Inoue N, Ishikawa M, Okada S, Ishigaki N *et al.* (2007) Crucial role of a long-chain fatty acid elongase, Elovl6, in obesity-induced insulin resistance. *Nat Med* **13**, 1193–1202.
- 84 Oishi Y, Spann NJ, Link VM, Muse ED, Strid T, Edillor C, Kolar MJ, Matsuzaka T, Hayakawa S, Tao J *et al.* (2017) SREBP1 contributes to resolution of pro-inflammatory TLR4 signaling by reprogramming fatty acid metabolism. *Cell Metab* **25**, 412–427.

<分子認識部門>

教授 細野雅祐

講師 菅原栄紀

講師 立田岳生

レクチンの抗腫瘍メカニズムの解明と糖脂質のかかわり 2021

1) シスプラチンの感受性に影響を及ぼす Gb3 の局在について

昨年度、Gb3 発現細胞として HeLa および Gb3 非発現細胞として A4GALT 欠損 HeLa (Δ Gb3-HeLa)を用いて、Gb3 の発現がシスプラチンの感受性に対して影響を与えるか否かについて検討し、 Δ Gb3-HeLa に対して HeLa の生存率が約 25% 低下することおよびこのメカニズムの一部に内因性アポトーシス制御分子の発現変化が関与していることを報告した。Gb3 は細胞内および細胞膜上に存在すると考えていることから、本年度はそのどちらに局在している Gb3 が抗がん剤の効果増強に寄与しているのかを検討した。まず始めに Δ Gb3-HeLa に PiggyBac Transposon Vector System を用いて A4GALT 遺伝子をゲノム上に組み込むことにより再度 Gb3 を発現させた Δ Gb3-HeLa/Gb3 を作製した。この細胞に発現している Gb3 は、HeLa と同様に細胞膜上および細胞内に局在することが示された (図 1)。これらの細胞を用いてシスプラチンの感受性を検討した結果、 Δ Gb3-HeLa のアポトーシス細胞の割合は HeLa より約 17% 低下した。一方、 Δ Gb3-HeLa/Gb3 では Δ Gb3-HeLa より約 20% 増加し、Gb3 を再発現させることによりシスプラチンに対する感受性が回復した。次に、細胞膜上に Gb3 を導入した Δ Gb3-HeLa+Gb3 を作製した。細胞膜上に導入された Gb3 は、導入直後と比較すると僅かな減少は認められるが 48 時間後まで維持されることが分かった (図 1)。この細胞を用いてシスプラチンに対する感受性を調べた結果、 Δ Gb3-HeLa および Δ Gb3-HeLa+Gb3 におけるアポトーシス細胞の割合に変化は見られなかった。これらの結果から、シスプラチンに対する感受性には、細胞膜上ではなく細胞内膜系に局在する Gb3 が関与している可能性が示唆された。今後は、オルガネラマーカースと抗 Gb3 抗体を用いた二重染色法による Gb3 の細胞内局在部位を検討すると共に Gb3 がシスプラチン感受性を増強する作用メカニズムを明らかにする。

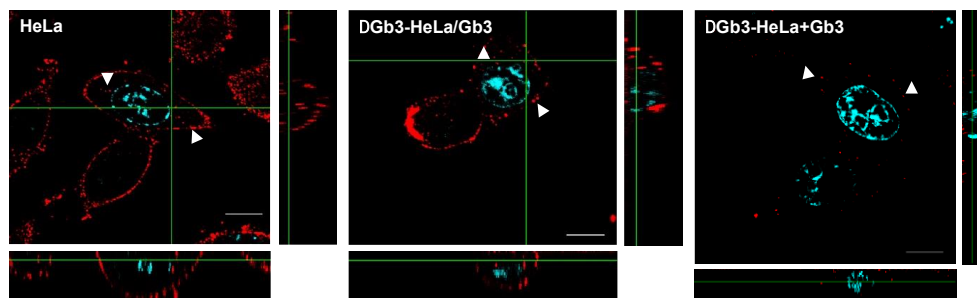


図 1. 共焦点顕微鏡による Gb3 発現部位の観察

2) Gb3 近傍に存在する分子の探索

細胞膜上に Gb3 を高発現していることが知られているバーキットリンパ腫細胞株 Raji において, SAL が Gb3 に結合することによりアポトーシス初期の状態を誘導するものの細胞死を誘導することなく, 細胞収縮および細胞増殖抑制を引き起こすことを報告している. これらの現象は, Gb3 の近傍に存在している分子あるいは SAL が Gb3 に結合した後に GEM にリクルートされる分子によって引き起こされるのではないかと考えている. Gb3 近傍の分子を探索する手法として本研究室では, これまでに抗 Gb3 マウスモノクローナル抗体および抗 Gb3 抗体に反応する Horseradish peroxidase (HRP) 標識マウス IgG 抗体を利用して Enzyme-mediated activation of radical sources (EMARS)法により検討を行ってきたが, 目的とするタンパク質の同定には至っていなかった. 本年度は, 研究対象である SAL を直接 HRP で標識した HRP-SAL を作製し, この HRP-SAL および EMARS 試薬として開発された FITC 標識 Aryl azide (Ar-Flu) を用いて EMARS 法を行った. さらにラフトに局在する分子を標的にする目的で EMARS 反応後に UltraRIPA lipid raft kit を利用してラフト画分の抽出を行い Gb3 近傍の分子の探索を試みた. HRP-SAL 処理および未処理の細胞から得られたラフト画分を SDS-PAGE で分離後, 抗 FITC 抗体を用いたウエスタンブロッティング法を行い比較したところ, 35 kDa 付近に認められるバンドは, HRP-SAL 処理した Raji のラフト画分でのみ検出された. さらにこの分子は, 抗 FITC 抗体を共有結合させた磁気ビーズを利用した免疫沈降により精製可能であった. 今後は, 得られた 35 kDa 付近のタンパク質を質量分析により同定し, SAL が Gb3 に結合することにより引き起こされる現象の詳細な分子機構を明らかにする.

3) ウシガエル (*Rana catesbeiana*) 卵から単離されたシアル酸結合性レクチン (sialic acids-binding lectin, cSBL) は, レクチンおよびリボヌクレアーゼ活性を併せ持つ多機能性タンパク質である. 正常細胞への毒性は低く, 多種類のがん細胞に対して高い抗腫瘍活性を発揮する. 本研究室では, cSBL の抗腫瘍効果のさらなる解明を目的に, cSBL 高感受性悪性中皮腫 H28 細胞を cSBL で持続処理することで cSBL 耐性細胞 (cSR) を樹立し, これを用いて cSBL を低濃度で長期間処理した際に発現が変化する遺伝子の特定を可能にした. 耐性度の高い cSR-A1 および B1 株をマイクロアレイ解析した結果, これまでに, cSR 細胞における発現変動のあった遺伝子 (differentially expressed genes :DEGs) を多数検出しており, cSR における多面的な遺伝子発現変化が明らかになっている. 今回 DEGs の詳細を解析したところ, ATP binding cassette (ABC) transporter である ABCC2 (MRP2) および ABCA1 の発現が低下していることが見出された (Table 1). ABCC2 はがん細胞に高発現し薬剤耐性に寄与することが知られている ABC transporter ファミリーの一種である.

Table 1. ABC transporter genes down-regulated in cSR cells compared with parent H28 cell line.

Probe ID ^a	Gene symbol	Description	Fold change ^b	Molecular functions ^c
A_23_P44569	<i>ABCC2</i>	ATP binding cassette subfamily C member 2	-17.3	ATPase-coupled transmembrane transporter activity organic anion transmembrane transporter activity
A_24_P235429	<i>ABCA1</i>	ATP binding cassette subfamily A member 1	-4.7	ATPase-coupled transmembrane transporter activity lipid transporter activity

^aData from Agilent Technologies, Inc.; ^bAverage expression ratio in cSR-A1 and -B1 cell lines were indicated as fold changes; ^cGO terms registered on each gene in molecular function field. Information was taken from the UniProt database (European Bioinformatics, UK, Swiss Institute of Bioinformatics, Switzerland, Protein Information Resource, USA) (<http://www.uniprot.org>) and the Entrez Gene database (National Center for Biotechnology Information, USA) (<http://www.ncbi.nlm.nih.gov/gene>).

そこで、*ABCC2* に着目しそのタンパク質レベルの発現を確認したところ、cSR-A1 および B1 細胞共に *ABCC2* の著しい発現の低下が観察され、タンパク質レベルでも *ABCC2* の発現が低下されることが確認された (Fig. 1). また、親株である H28 細胞において、cSBL 72 時間処理における *ABCC2* の発現変化を観察したところ、濃度依存的にその発現が低下する傾向が観察された (Fig. 2).

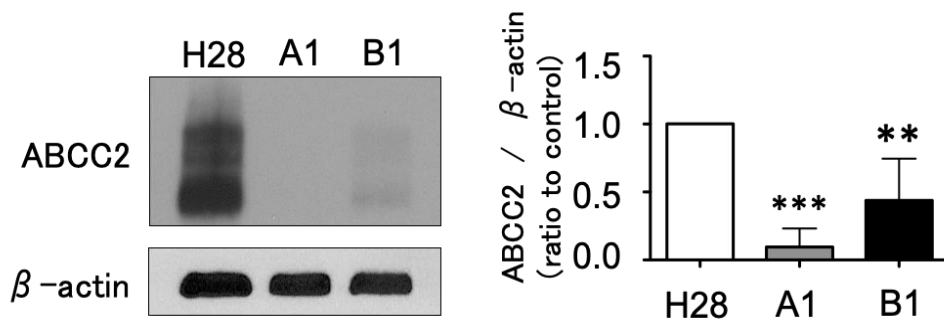


Fig. 1. *ABCC2* protein expression in H28 and cSR cells. The expression of *ABCC2* in each cell line was detected by western blotting. Densitometric quantification was performed using the results of three independent experiments (mean \pm SD). ** $P < 0.01$. *** $P < 0.001$. cSR: bullfrog sialic acid-binding lectin-resistant; SD: standard deviation.

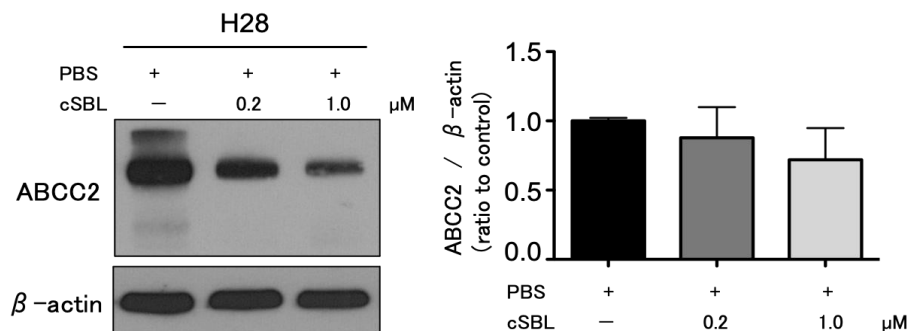


Fig. 2. ABCC2 protein expression in cSBL-treated H28 cells. The cells were treated with cSBL at 0.2 or 1.0 μ M for 72 hours. Then, the expression of ABCC2 was detected by western blotting. Densitometric quantification was performed using the results of three independent experiments (mean \pm SD). cSR: bullfrog sialic acid-binding lectin-resistant; SD: standard deviation

このことから cSBL は、持続的な長期間処理および 72 時間程度の短時間処理両方において ABCC2 の発現低下を誘導することが示唆された。ABCC2 はシスプラチンやドキソルビシンなど基質となる抗がん剤を細胞外に排出するポンプであり、その高発現はがん細胞の薬剤抵抗性へと寄与する。cSBL は ABCC2 の発現低下を介し、がん細胞における抗がん剤への感受性を増大させる可能性があり、cSBL をそれら抗がん剤と併用することが有用な治療戦略になる可能性がある。今回の発見が新しい抗がん治療戦略へつながることが期待される。

<発表論文>

1. Transcriptomic alterations in malignant pleural mesothelioma cells in response to long-term treatment with bullfrog sialic-acid binding lectin.
T. Tatsuta, A. Nakasato, S. Sugawara, M. Hosono, *Mol. Med. Rep.*, **23**, doi: 10.3892/mmr.2021.12106.
2. Discovery of antitumor effects of leczymses.
T. Tatsuta, M. Hosono, *Glycoconj. J.*, **39**, 157-165 (2021).

<学会発表>

- ・ナマズ卵レクチンはヒト子宮頸がん由来 HeLa におけるスニチニブの取り込みおよび排出に影響をおよぼす

菅原 栄紀, 高柳 円, 本田 捷太, 立田 岳生, 藤井 佑樹^a, 大関 泰裕^b,
伊藤 淳^c, 佐藤 信^c, 細野 雅祐

(長崎国際大学・薬学部^a, 横浜市大院・生命ナノ^b, 東北医薬大・医学部・泌尿器科学講座^c)

第 15 回東北糖鎖研究会, 岩手, 2021 年 10 月, 要旨集 p.8

- ・抗がん剤で誘導されるアポトーシスへの Gb3 の関与

八木橋 佳章, 菅原 栄紀, 菊地 聡大, 立田 岳生, 細野 雅祐
第 15 回東北糖鎖研究会, 岩手, 2021 年 10 月, 要旨集 p.18

- ・がん細胞に発現する Gb3 の抗がん剤感受性に与える影響について

八木橋 佳章, 菅原 栄紀, 菊地 聡大, 立田 岳生, 細野 雅祐

第 94 回日本生化学大会, 横浜, 2021 年 11 月, P-753

- ・ **確立された RNase 耐性がん細胞における AKR1B10 と ABCC2 の発現に対する cSBL の影響**

中里 ありす、立田 岳生、菅原 栄紀、細野 雅祐、第 94 回日本生化学大会、横浜、2021 年 11 月、演題番号 P-047

- ・ **膀胱がん細胞に対する cSBL の抗腫瘍効果について**

立田 岳生、中里 ありす、菅原 栄紀、伊藤 淳、佐藤 信、細野 雅祐、第 94 回日本生化学大会、横浜、2021 年 11 月、演題番号 P-505

- ・ **細胞内膜系 Gb3 はシスプラチンによるアポトーシスに関与する**

菅原 栄紀、八木橋 佳章、立田 岳生、細野 雅祐

第 44 回日本分子生物学会年会, 横浜, 2021 年 12 月, 2LBA-017

- ・ **悪性中皮腫細胞に発現する AKR1B10 および ABCC2 に対する cSBL の効果**

立田 岳生、中里 ありす、佐藤 彬翔、菅原 栄紀、細野 雅祐、日本薬学会第 142 年会、名古屋、2022 年 3 月、演題番号 26PO5-am1-04

- ・ **がん治療への応用を目指したウシガエル卵由来シアル酸結合性レクチン(cSBL) の基礎研究**

立田 岳生

第 43 回東北薬学セミナー, 仙台, 令和 3 年度日本薬学会東北支部奨励賞受賞講演, 2021 年 12 月

- ・ **悪性中皮腫細胞に発現する AKR1B10 および ABCC2 に対する cSBL の効果**

立田 岳生、中里 ありす、佐藤 彬翔、菅原 栄紀、細野 雅祐

日本薬学会第 142 年会, 名古屋, 2022 年 3 月, 演題番号 26PO5-am1-04



Discovery of antitumor effects of leczymses

Takeo Tatsuta¹ · Masahiro Hosono¹

Received: 29 September 2021 / Revised: 18 November 2021 / Accepted: 8 December 2021 / Published online: 23 January 2022
© The Author(s), under exclusive licence to Springer Science+Business Media, LLC, part of Springer Nature 2021

Abstract

Sialic-acid binding lectin from bullfrog (*Rana catesbeiana*) eggs, cSBL, is a cytotoxic ribonuclease (RNase) belonging to the RNase A superfamily. cSBL is cytotoxic to tumor cells, such as malignant pleural mesothelioma by inducing apoptotic cell death caused by the degradation of RNA in tumor cells. In addition, we have reported some data that cSBL could be involved in the endoplasmic reticulum stress pathway, and it was also assumed to cause apoptotic cell death. The most significant property of cSBL is its specificity toward malignant cells. Furthermore, since the antitumor activity of cSBL was confirmed by *in vivo* experiments using mouse xenograft models, it is expected to be a candidate for clinical chemotherapy. Here, we summarize the history of cSBL, alternatively called “leczyme,” with its present and future.

Keywords Lectin · Sialic acids · Ribonuclease · Antitumor activity · Apoptosis

Lectin meets ribonuclease

During the 1970s, Kawauchi *et al.* found some lectins from frog eggs belonging to the *genus Rana* with hemagglutinating activities [1, 2]. Among them, they succeeded in isolating a unique lectin that showed agglutinating activity for some murine ascites tumor cells, such as Ehrlich and AH109A, but not for human erythrocytes [3]. Since most of the investigators' interests concerning tumor cell agglutinin were limited to plant lectins at that time, animal lectins were rarely studied in membrane glycoconjugate research. The egg agglutinins were inhibited by ganglioside but not globoside, and sialidase-treated tumor cells lost their agglutinability. Therefore, these lectins were estimated to have affinities for sialo-glycoconjugates, including both glycolipids and glycoproteins, and reactivity specific for tumor cells [4]. Dr. Sen-itiroh Hakomori, who was our great mentor and the first director of the Cancer Research Institute of Tohoku College of Pharmaceutical Sciences (Fig. 1), was interested in these lectins, and consecutively supported us by providing ganglioside and globoside preparations from erythrocytes,

which were not commercially available during that period, along with a lot of variable advice. Although the primary structure of sialic-acid binding lectin from bullfrog (*Rana catesbeiana*) eggs (cSBL) was established using the peptide sequencing method by Titani *et al.*, we could not find any similarity in the early protein database [5]. Three years later, the sequence of the homolog, *Rana japonica* egg lectin (jSBL) was elucidated and the similarities between frog sialic acid-binding lectins (SBLs) and ribonuclease (RNase) A were found to be around 30% [6], and SBLs showed pyrimidine-specific RNase activity [7]. An RNase purified from *R. catesbeiana* oocytes collected in Taiwan by Liao *et al.*, and named RC-RNase, was found to be identical to cSBL [8]. Subsequently, SBLs met RNase for the first time. In this way, Nitta *et al.* proposed the name catalytic lectin (Leczyme) as a multifunctional molecule with lectin and enzymatic activity [9].

Leczymses show antitumor effect

The antitumor effects of leczymses, including cSBL and jSBL, on cultured cell lines were first reported by Nitta *et al.* in 1994 [10]. They showed that both leczymses significantly inhibited mouse leukemia P388 and L1210 cell proliferation *in vitro*. Furthermore, *in vivo* experiments were carried out and the survival time of mice inoculated with cSBL-treated Sarcoma 180 cells was prolonged, and the

This article belongs to the Topical Collection: Tribute to Professor Sen-itiroh Hakomori

✉ Masahiro Hosono
mhosono@tohoku-mpu.ac.jp

¹ Division of Cell Recognition, Institute of Molecular Biomembrane and Glycobiology, Tohoku Medical and Pharmaceutical University, 4-4-1 Komatsushima, Aoba-ku, Sendai 981-8558, Japan

Fig. 1 The nomenclature plate on the former building of Cancer research institute of Tohoku pharmaceutical university (left). Snapshots of Prof. Sen-itiroh Hakomori (center) and Dr. Hiroaki Kawauchi (right) in their youth, in 1965



administered of an injection of cSBL increased the survival rates of Sarcoma 180- or Mep II ascites-bearing mice; for 10 days of continuous cSBL injection, Sarcoma 180- or Mep II-bearing mice receiving an injection of 0.5 mg/kg of cSBL had 67% and 50% survival, respectively, after 45 days. As significant side effects were not observed after a 50 mg/kg injection of cSBL, 1/3 of the lethal dose for normal mice, the maximum concentration used in this experiment (2 mg/kg) was estimated to be a safe dose *in vivo*. Nitta *et al.* consecutively reported another study concerning the establishment of cSBL-resistant P388 cells (RC-150) and their behavior on cSBL treatment [11]. cSBL bound to and agglutinated both P388 and RC-150 cells; however, the internalization of cSBL was observed only in parent P388 cells, but not in resistant RC-150 cells, indicating that the uptake of cSBL is essential for antitumor activity. At this point, cSBL has been reported to bind to a wide variety of cancer cells, although it shows little response to normal erythrocytes, leukocytes, and fibroblasts [12]. Combined with these results, it has attracted attention as a new anticancer substance with few side effects.

Leczyme as antitumor ribonucleases

Since 1990, as antitumor RNases have been successively reported based on the new trend of the research, the antitumor activity of cSBL has been studied, focusing on its properties not only as a lectin but also as an RNase, and it is now known that cSBL indeed exerts RNase activity accompanying with cytotoxicity in cancer cells (Fig. 2). To date, many types of antitumor RNases have been identified. They are derived from a variety of species, including plants, bacteria, fungi, and animals. RNase MC2 from *Momordica charantia* [13, 14], TBN1 from *Lycopersicon esculentum* [15], barnase from *Bacillus amyloliquefaciens* [16], binase from *Bacillus intermedius* [17, 18], α -sarcin from *Aspergillus giganteus* [19], and mushroom RNases [20, 21] are typical antitumor RNases [22]; however, the most extensively investigated is vertebrate pancreatic-type RNases (RNase A superfamily), such as BS-RNase from *Bos taurus* [23, 24], and Onconase from *Rana pipiens* [25, 26]. Bovine

pancreatic RNase A (EC 3.1.27.5) [27], the best-known member of this family, was the first RNase reported to have antitumor activity *in vitro* and *in vivo* [28–33]. However, as extremely high amounts of RNase A were required to show a positive effect, RNases could not maintain their position as candidates for new antitumor agents. The reasons for this are described below.

Tumoricidal mechanisms of RNases

Although their mechanism of action is still not fully understood, there is a commonly accepted consensus regarding their mechanisms [34, 35]. The proposed mechanisms of RNase-induced cytotoxicity are summarized as follows. (i) Binding to the cell surface: Antitumor RNases interact with specific or nonspecific targets on the cell surface. Some membrane proteins, glycosaminoglycans, or lipids could be the target [36–38]. (ii) Internalization into cells: RNases are internalized by endocytosis. The endocytic mechanism is still poorly understood. Even though there are controversial reports on whether the route is mediated by clathrin / AP-2-mediated [39] or clathrin- and caveolae-independent pathways [40], depending on the difference in cells, it has been suggested that RNases go through diverse routes to cross the membrane of different cell lines [41]. RNases can translocate through distinct organelles, such as endosomes, lysosomes, ER, and the trans-Golgi network, and reach the cytosol [42]. Some RNases engineered to have a nuclear localization sequence can be transported into the nucleus [43]. (iii) Evasion of the cytosolic RNase inhibitor protein (RI): RNases can be captured by RI and lose their enzymatic activity. Thus, the antitumor RNases need to be insensitive to the RI or evade the RI (saturating the RI with RNase or capturing by other molecules that impair the interaction with RI) [34]. (iv) Degradation of cellular RNA: RNases hydrolyze RNA in the cytosol or the nucleus. Differences in the efficiency of these four steps can affect cell susceptibility [44]. The ribotoxic effect of RNase can transduce apoptotic signals [45] and sometimes autophagy [46]. Some studies have reported other details about the mechanisms by which antitumor RNases induce cell death, such as the involvement

of miRNA [47, 48], and pleiotropic effects on transcription changes [49–51]. Signal transduction induced by RNA damage caused by antitumor RNases still needs to be elucidated. cSBL is a vertebrate pancreatic-type RNase with an antitumor activity that induces apoptosis in cancer cells through the above-mentioned steps. Some experiences of the antitumor effect of cSBL obtained so far will be described in the following sections.

Binding of cSBL on cancer cell surface

As described above, cSBL was found to be an agglutinin in tumor cells [3]. Nitta *et al.* reported that it agglutinates various types of tumor cells but not normal cells,

and this agglutination was inhibited by glycoconjugates containing sialic acids. Furthermore, they investigated cSBL binding on several cancer and normal cells and found that cSBL binds to a majority of cancer cells, while normal cells exhibit low reactivity [12, 52]. The binding of cSBL to the cell surface was inhibited by the coexistence of sialoglycoproteins and sialidase-treated cells, evading the cytotoxicity of cSBL [10]. By adding benzyl- α -N-acetylgalactosamine to the culture medium, the cells became resistant to cSBL. Thus, the involvement of O-linked glycoconjugates containing sialic acids has been suggested as the target of cSBL on cancer cell membranes [53]. However, the details of the carbohydrate-binding properties of cSBL remain unclear.

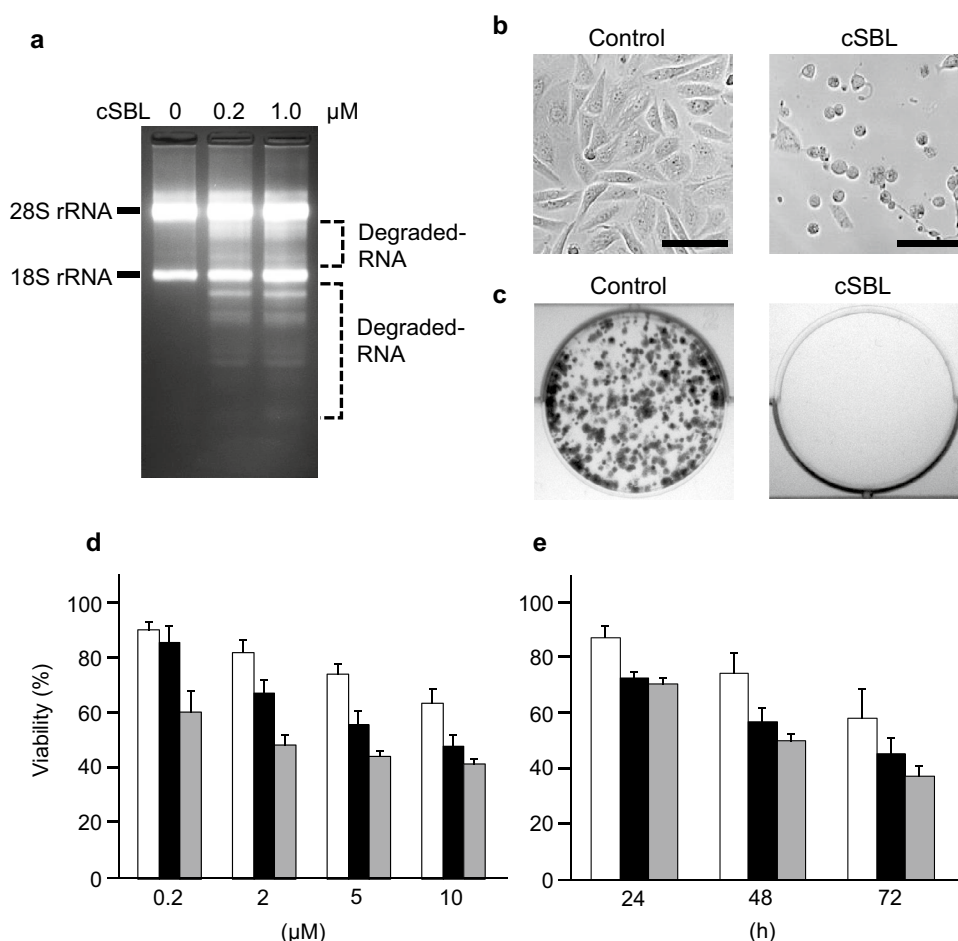


Fig. 2 Cytotoxic effect of cSBL on mesothelioma cell lines. **(a)** Cellular RNA-degrading effect of sialic-acid binding lectin from *Rana catesbeiana* eggs (cSBL) in malignant mesothelioma H28 cells. The cells were treated with cSBL at indicated concentration for 24 h and total RNA was extracted using a Direct-zol RNA mini prep kit (Zymo ResearchCo., CA). Then, electrophoresis was performed on 1.5% agarose gel. **(b)** Morphological change of cSBL-treated H28 cells. The cells were treated with or without cSBL (5 μ M) for 72 h. Cell morphology was observed using light microscope. Magnification; 10 \times (scale: 100 μ m) **(c)** Effect of cSBL on H28 cell proliferation.

After cSBL (5 μ M) treatment for 24 h, H28 cells (1×10^3 /well) were plated in 6-well dishes. After 12 days, cells were fixed and stained with 0.1% crystal violet. **(d)** Viability of cSBL-treated mesothelioma cell lines. Three mesothelioma cell lines, MESO-1 (white), MESO-4 (black) and H28 (gray) were treated with cSBL at various concentration for 48 h. The viability was determined by WST-1 assay. The ratio of viability against control cells was calculated. Data are expressed as mean \pm S.D. from three independent experiments in triplicate. **(e)** Cells were treated with cSBL (5 μ M) for indicated time. The viability was determined by the same method as described above

Internalization of cSBL to cancer cells

RNA cleavage in cSBL-treated Jurkat cells was observed after 3 h; thus, it was apparent that cSBL exerts RNase activity in the cells [54]. To evaluate the effects of cSBL on breast cancer, Kariya *et al.* confirmed the localization of cSBL in MDA-MB-231 cells by a immunofluorescence analysis [55]. cSBL was observed in the perinuclear region after 6 h of treatment. Moreover, the cSBL mutant lacking RNase activity by replacing His103 (essential site for its RNase activity) with Ala (H103A) was also transported to the perinuclear region in the same cells, indicating that cSBL internalizes into cancer cells regardless of its RNase activity, and the perinuclear area could be somehow the cSBL acting site.

RI refractoriness of cSBL

The RI, an acidic protein with a molecular weight of ca. 50 kDa, which is present in almost all mammalian cells, has a leucine-rich repeat structure and forms a characteristic horseshoe shape throughout the molecule [56–58]. The RI non-covalently binds to RNase A at a ratio of 1: 1, and the dissociation constant is of the order of fM, indicating its strong affinity [59, 60]. Therefore, the presence of this inhibitor is an obstacle for intracellular RNases to exert their RNA-degrading activity and cytotoxicity. However, like other frog RNases, cSBL does not interact with the mammalian RI, and the RNase and tumor cell agglutination activities of cSBL are not affected by this inhibitor [61]. This RI-insensitive feature of cSBL is one of the major differences from other mammalian RNases and provides a great advantage for its antitumor activity.

cSBL-induced degradation of cellular RNA

cSBL has conserved catalytic amino acid residues at the same position as other RNase A superfamily members. It also has eight cysteine residues that can form four disulfide bonds. cSBL is essentially a pyrimidine-base-specific RNase [7]. While bovine (RNase A), turtle, and chicken RNases are essentially cytosine base-preferential [62, 63], cSBL appears to be a uracil-preferential RNase because the hydrolysis rate of the dinucleotide phosphate UpX consistently exceeds that of CpX (X = A, G, U, and C) [61]. This property is similar to that of ONC and iguana RNase [64]. As mentioned above, once cSBL internalizes into cancer cells, it exerts its RNase activity and degrades cellular RNA followed by the execution of apoptosis, as discussed in the next section.

cSBL-induced apoptosis

The first report concerning cSBL-induced apoptosis was presented by Nitta *et al.* in collaboration with Dr. Hakomori at the 1999 International Meeting on Ribonucleases. cSBL induced apoptotic morphological changes, such as nuclear condensation and the disappearance of microvilli in mouse leukemia P388 cells. Subsequently, they revealed that the activation of caspase-8 and -3, enhancement of annexin V binding, induction of DNA fragmentation, and expression of Fas antigen and tumor necrosis factor (TNF) receptor occurred in cSBL-treated p388 cells [65]. In 2001, Hu *et al.* reported that cSBL causes caspase-7 activation in human breast cancer MCF-7 cells that lack caspase-3 expression, and that apoptosis is prevented by the overexpression of Bcl-X_L in the cells [66]. Therefore, even though observations in the early study on cSBL-induced cell death showed that protein synthesis was reduced in cSBL-treated cells [10], it was suggested that cSBL elicits an inducing signal of apoptosis.

After 2013, our group clarified the details of cSBL-induced apoptosis in collaboration with Dr. Hakomori's group [54, 67, 68]. We used human leukemia Jurkat cells and observed typical apoptosis-like changes, such as nuclear fragmentation/condensation, the translocation of phosphatidylserine to the outer layer of the cell membrane, the activation of the caspase family, and the fragmentation of DNA in cSBL-treated cells. DNA fragmentation was completely suppressed by the total caspase inhibitor z-VAD-fmk, revealing that cSBL induces apoptosis in a caspase-dependent manner. We performed experiments using 5,5',6,6'-tetrachloro-1,1', 3,3'-tetraethylbenzimidazolylcarbocyanine iodide (JC-1), which is a mitochondrial membrane depolarization-detecting reagent. The decrease in mitochondrial membrane potential was almost completely suppressed by z-VAD-fmk pretreatment in TNF-related apoptosis-inducing ligand (TRAIL) -treated cells, which induced apoptosis via the extrinsic pathway. In contrast, the decrease in mitochondrial membrane potential in cSBL-treated cells was not affected by z-VAD-fmk; that is, cSBL caused strong mitochondrial damage upstream of caspase activation, indicating that cSBL induced apoptosis via the intrinsic pathway [54]. Furthermore, a signal transduction analysis revealed that the endoplasmic reticulum stress pathway may also be involved in cSBL-induced apoptosis. In cSBL-treated Jurkat cells, the markers of endoplasmic reticulum stress, such as an increased expression of calnexin and immunoglobulin heavy chain binding protein/glucose-regulated protein 78 and the activation of caspase-4 was observed. In addition, pretreatment with the caspase-4 specific inhibitor z-LEVD-fmk attenuated cSBL-induced DNA fragmentation. A comparative study using thapsigargin, an inducer of endoplasmic reticulum stress apoptosis revealed that the mitochondrial

pathway contributes significantly to cSBL-induced apoptosis [68]. RNase activity has been shown to be required for cSBL to degrade RNA and cause cell death in cancer cells; however, it remains unclear how cSBL-induced RNA degradation leads to apoptosis. In our study conducted on human leukemia, malignant mesothelioma, and breast cancer cell lines, JNK and p38 mitogen-activated protein kinases (MAPK) were strongly activated by cSBL treatment, suggesting that these activations may be involved in cSBL-induced

apoptosis. Since treatment with p38 inhibitor and knockdown of p38 attenuated cSBL-induced cell death [55], we speculate that RNA degradation by cSBL activates these stress kinases, which leads to apoptosis. On the contrary, inhibition of caspases [54] and p38 MAPK [55] did not completely recover cSBL-induced cell death, although there were statistically significant differences between pretreatment with inhibitors and the control. cSBL might be involved in a p38- and caspase-independent cell death-inducing pathway, or when

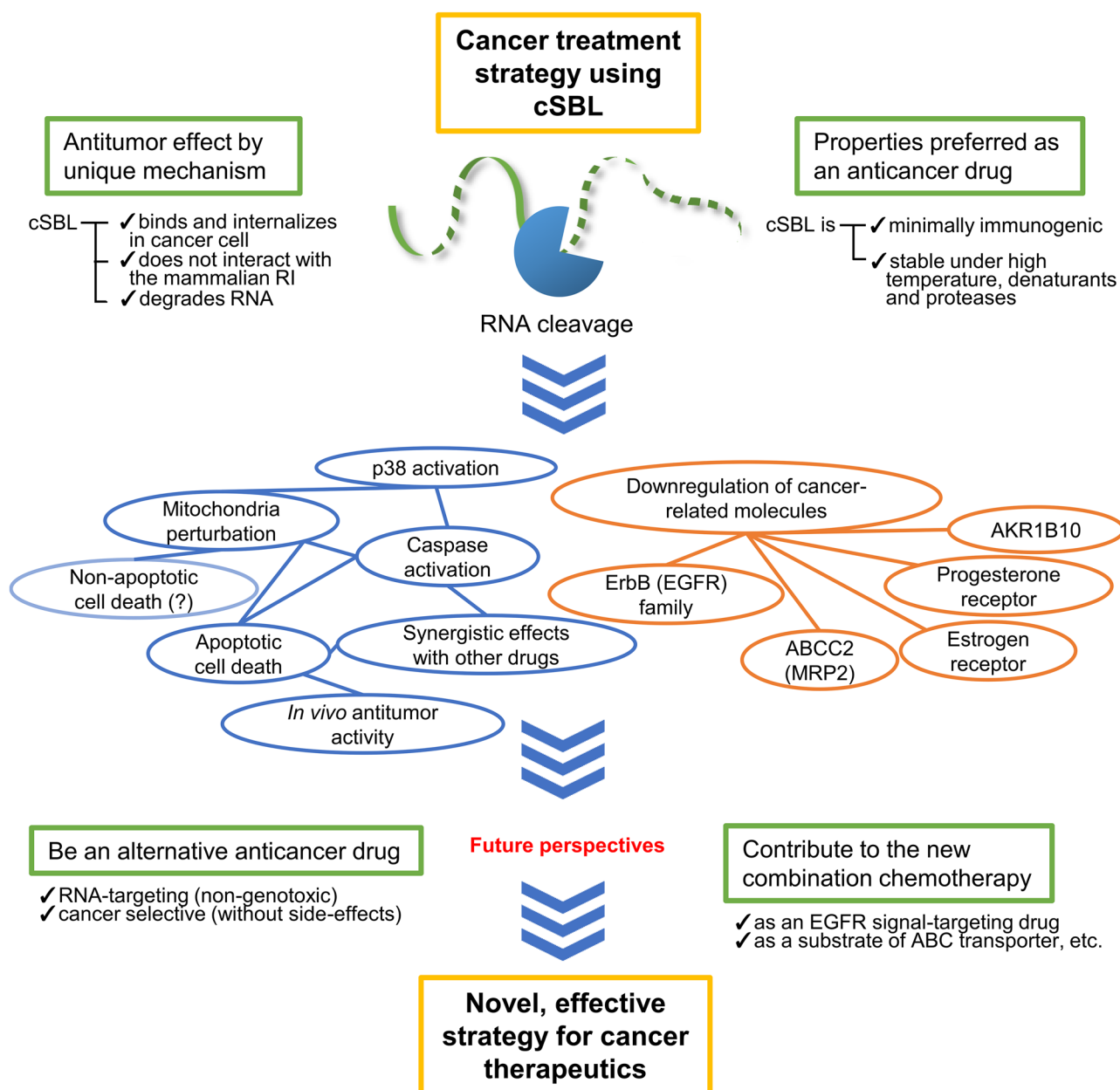


Fig. 3 Scheme of cancer treatment strategy using cSBL. The antitumor mechanism and the preferable properties of cSBL as a chemotherapeutics are summarized. Some events caused by cSBL in cancer cells were mapped and the related events are connected by lines.

cSBL may be an alternative anticancer agent. New combinations with other drugs are expected leading to new and more efficient cancer treatment strategies

the action of stress kinases and caspases is suppressed, the dramatic effect of RNA breakdown may lead to cell death via a different pathway.

Other features of cSBL-induced antitumor effect

The antitumor effects of cSBL have been verified in many cell lines [69–73], and various studies have reported its high selectivity for cancer cells. Although most of these reports show that cSBL induces apoptosis, a study conducted by Ying *et al.* reported that cSBL can trigger not only apoptosis but also autophagocytosis in MCF-7 cells [74]. It has been reported that cSBL has a highly synergistic cytotoxic effect with other reagents. Combined with the TRAIL, which has been shown to have cytotoxic effects on malignant mesothelioma cell lines, or pemetrexed, a key drug for the treatment of malignant mesothelioma, effectively decreases the viability of mesothelioma cells [67, 71]. Furthermore, the combination with interferon gamma (IFN- γ) induced synergistic cytotoxicity in some hepatoma cells with different differentiation stages. It should be noted that the effects of cSBL or cSBL/IFN- γ on different hepatoma cells were correlated with the differentiation extent but not the proliferation rate of the cells [75]. Antitumor effects have been reported not only in ascites cancer-bearing mice [10] but also in human glioma and malignant mesothelioma xenograft mouse models [70, 72]. In every *in vivo* examination, cSBL exerted significant antitumor effects without undesired adverse effects. Although few studies have compared cSBL with other RNases, Tang *et al.* reported that cSBL has a higher cancer specificity than ONC because it is toxic to normal human HS-68 foreskin fibroblasts; however, cSBL is not toxic as per their study [76]. Attenuation of apoptosis-inducing effects by cSBL is observed during the differentiation of cancer cells by retinoic acids or dimethyl sulfoxide in human leukemia HL60 cells, the overexpression of Bcl-2 in human breast cancer MCF-7 cells, the reduced expression of Hsp70 by treatment with quercetin, and the disruption of cell membrane cholesterol by methyl β -D-cyclodextrin in mouse leukemia P388 cells [77–80]. On the contrary, cSBL internalization into the cells is enhanced by Japanese encephalitis virus (JEV) infection of the baby hamster kidney BHK-21 cells, which causes enhanced apoptosis in JEV-infected BHK-21 cells, indicating that cSBL also possesses antiviral activity [81]. Our recent studies revealed that cSBL induces apoptosis by decreasing estrogen receptor, progesterone receptor, and ErbB family proteins in several breast cancer cell lines [73]; long-term treatment with cSBL causes pleiotropic changes, including a decreased expression of aldo-keto reductase 1B10 and adenosine triphosphate-binding cassette transporter C2 in malignant mesothelioma

H28 cells [82]. The information described above is expected to lead to useful applications, such as the effective combination of cSBL with other drugs. Furthermore, cSBL has several potential advantages as a cytotoxic RNase. Members of the pancreatic RNase superfamily, including cSBL, are expected to be minimally immunogenic because of their compact structure and homology with human pancreatic RNase [83]. In addition, they exhibit high thermal stability and strong resistance to protein denaturants and proteases [84, 85]. Taken together, cSBL is expected to be an anticancer drug in a new field because it shows unique and cancer-selective antitumor effects by a unique mechanism targeting RNA. The potential role of cSBL in anticancer therapy were summarized in Fig. 3.

In conclusion, an understanding of the total ability of cSBL or leczyne is still underway. However, RNA-targeted chemotherapeutic strategies are attractive for the development of non-toxic anticancer agents. Cancer cell selectivity of cSBL, in particular, could make it a potential candidate for future cancer medicine.

Acknowledgements It is well known that Dr. Sen-itiroh Hakomori was the pioneer in the research fields of membrane glycolipids and cancer cell biology and also the front runner of biomembrane researchers worldwide. We have been able to get this far on our improved leczyne research because of Dr. Hakomori's help. It is our duty to develop our project toward translational research on clinical cancer chemotherapy, showing our appreciation for him.

Funding This study was supported by a Grant-in-Aid for Scientific Research(C) [grant no. 21K07198 (to Takeo Tatsuta)].

Compliance with ethical standards

Ethical approval This article does not contain any unpublished studies with human or animals performed by any of the authors.

Conflicts of interest The authors have no conflicts of interest to declare that are relevant to the content of this article.

References

1. Kawauchi, H., Sakakibara, F., Watanabe, K.: Agglutinins of frog eggs: A new class of proteins causing preferential agglutination of tumor cells. *Experientia* **31**, 364–365 (1975). <https://doi.org/10.1007/BF01922588>
2. Sakakibara, F., Takayanagi, G., Kawauchi, H., Watanabe, K., Hakomori, S.: An anti-A-like lectin of *Rana catesbeiana* eggs showing unusual reactivity. *Biochim. Biophys. Acta* **444**, 386–395 (1976). [https://doi.org/10.1016/0304-4165\(76\)90382-2](https://doi.org/10.1016/0304-4165(76)90382-2)
3. Sakakibara, F., Takayanagi, G., Ise, H., Kawauchi, H.: Isolation of two agglutinins with different biological properties from the eggs of *Rana catesbeiana*. *Yakugaku Zasshi* **97**, 855–862 (1977). https://doi.org/10.1248/yakushi1947.97.8_855
4. Sakakibara, F., Kawauchi, H., Takayanagi, G., Ise, H.: Egg lectin of *Rana japonica* and its receptor glycoprotein of Ehrlich tumor cells. *Cancer Res.* **39**, 1347–1352 (1979)

5. Titani, K., Takio, K., Kuwada, M., Nitta, K., Sakakibara, F., Kawauchi, H., Takayanagi, G., Hakomori, S.I.: Amino acid sequence of sialic acid binding lectin from frog (*Rana catesbeiana*) eggs. *Biochemistry* **26**, 2189–2194 (1987). <https://doi.org/10.1021/bi00382a018>
6. Kamiya, Y., Oyama, F., Oyama, R., Sakakibara, F., Nitta, K., Kawauchi, H., Takayanagi, Y., Titani, K.: Amino acid sequence of a lectin from Japanese frog (*Rana japonica*) eggs. *J. Biochem.* **108**, 139–143 (1990). <https://doi.org/10.1093/oxfordjournals.jbchem.a123153>
7. Okabe, Y., Katayama, N., Iwama, M., Watanabe, H., Ohgi, K., Irie, M., Nitta, K., Kawauchi, H., Takayanagi, Y., Oyama, F.: Comparative base specificity, stability, and lectin activity of two lectins from eggs of *Rana catesbeiana* and *R. japonica* and liver ribonuclease from *R. catesbeiana*. *J. Biochem.* **109**, 786–790 (1991). <https://doi.org/10.1093/oxfordjournals.jbchem.a123457>
8. Liao, Y.D.: A pyrimidine-guanine sequence-specific ribonuclease from *Rana catesbeiana* (bullfrog) oocytes. *Nucleic Acids Res.* **20**, 1371–1377 (1992). <https://doi.org/10.1093/nar/20.6.1371>
9. Nitta, K., Ozaki, K., Tsukamoto, Y., Hosono, M., Ogawakono, Y., Kawauchi, H., Takayanagi, Y., Tsuiki, S., Hakomori, S.: Catalytic lectin (leczyme) from bullfrog (*Rana catesbeiana*) eggs. *Int. J. Oncol.* **9**, 19–23 (1996). <https://doi.org/10.3892/ijo.9.1.19>
10. Nitta, K., Ozaki, K., Ishikawa, M., Furusawa, S., Hosono, M., Kawauchi, H., Sasaki, K., Takayanagi, Y., Tsuiki, S., Hakomori, S.: Inhibition of cell proliferation by *Rana catesbeiana* and *Rana japonica* lectins belonging to the ribonuclease superfamily. *Cancer Res.* **54**, 920–927 (1994)
11. Nitta, K., Ozaki, K., Tsukamoto, Y., Furusawa, S., Ohkubo, Y., Takimoto, H., Murata, R., Hosono, M., Hikichi, N., Sasaki, K.: Characterization of a *Rana catesbeiana* lectin-resistant mutant of leukemia P388 Cells. *Cancer Res.* **54**, 928–934 (1994)
12. Nitta, K., Takayanagi, G., Kawauchi, H., Hakomori, S.: Isolation and characterization of *Rana catesbeiana* lectin and demonstration of the lectin-binding glycoprotein of rodent and human tumor cell membranes. *Cancer Res.* **47**, 4877–4883 (1987)
13. Fang, E.F., Zhang, C.Z.Y., Zhang, L., Fong, W.P., Ng, T.B.: *In vitro* and *in vivo* anticarcinogenic effects of RNase MC2, a ribonuclease isolated from dietary bitter melon, toward human liver cancer cells. *Int. J. Biochem. Cell Biol.* **44**, 1351–1360 (2012). <https://doi.org/10.1016/j.biocel.2012.04.013>
14. Fang, E.F., Zhang, C.Z.Y., Fong, W.P., Ng, T.B.: RNase MC2: A new *Momordica charantia* ribonuclease that induces apoptosis in breast cancer cells associated with activation of MAPKs and induction of caspase pathways. *Apoptosis* **17**, 377–387 (2012). <https://doi.org/10.1007/s10495-011-0684-z>
15. Matousek, J., Podzimek, T., Pouckova, P., Stehlik, J., Skvor, J., Lipovova, P., Matousek, J.: Antitumor activity of apoptotic nuclease TBN1 from *L. esculentum*. *Neoplasia* **57**, 339–348 (2010). https://doi.org/10.4149/neo_2010_04_339
16. Prior, T.I., Kunwar, S., Pastan, I.: Studies on the activity of barnase toxins *in vitro* and *in vivo*. *Bioconjug. Chem.* **7**, 23–29 (1996). <https://doi.org/10.1021/bc9500655>
17. Ilinskaya, O., Decker, K., Koschinski, A., Dreyer, F., Repp, H.: *Bacillus intermedius* ribonuclease as inhibitor of cell proliferation and membrane current. *Toxicology* **156**, 101–107 (2001). [https://doi.org/10.1016/S0300-483X\(00\)00335-8](https://doi.org/10.1016/S0300-483X(00)00335-8)
18. Cabrera-Fuentes, H.A., Aslam, M., Saffarzadeh, M., Kolpakov, A., Zelenikhin, P., Preissner, K.T., Ilinskaya, O.N.: Internalization of *Bacillus intermedius* ribonuclease (BINASE) induces human alveolar adenocarcinoma cell death. *Toxicol.* **69**, 219–226 (2013). <https://doi.org/10.1016/j.toxicol.2013.03.015>
19. Olmo, N., Turnay, J., González de Buitrago, G., López de Silanes, I., Gavilanes, J.G., Lizarbe, M.A.: Cytotoxic mechanism of the ribotoxin α -sarcin: Induction of cell death via apoptosis. *Eur. J. Biochem.* **268**, 2113–2123 (2001). <https://doi.org/10.1046/j.1432-1327.2001.02086.x>
20. Ng, T.B.: Peptides and proteins from fungi. *Peptides* **25**, 1055–1073 (2004). <https://doi.org/10.1016/j.peptides.2004.03.013>
21. Wong, J.H., Ng, T.B., Cheung, R.C.F., Ye, X.J., Wang, H.X., Lam, S.K., Lin, P., Chan, Y.S., Fang, E.F., Ngai, P.H.K., Xia, L.X., Ye, X.Y., Jiang, Y., Liu, F.: Proteins with antifungal properties and other medicinal applications from plants and mushrooms. *Appl. Microbiol. Biotechnol.* **87**, 1221–1235 (2010). <https://doi.org/10.1007/s00253-010-2690-4>
22. Hameş, E.E., Demir, T.: Microbial ribonucleases (RNaseS): Production and application potential. *World J. Microbiol. Biotechnol.* **31**, 1853–1862 (2015). <https://doi.org/10.1007/s11274-015-1945-8>
23. Kotchetkov, R., Cinatl, J., Krivtchik, A.A., Vogel, J.U., Matousek, J., Pouckova, P., Kornhuber, B., Schwabe, D., Cinatl, J.J.: Selective activity of BS-RNase against anaplastic thyroid cancer. *Anticancer Res.* **21**, 1035–1042 (2001)
24. Fiorini, C., Gotte, G., Donnarumma, F., Picone, D., Donadelli, M.: Bovine seminal ribonuclease triggers Beclin1-mediated autophagic cell death in pancreatic cancer cells. *Biochim. Biophys. Acta* **1843**, 976–984 (2014). <https://doi.org/10.1016/j.bbamer.2014.01.025>
25. Saxena, S.K., Shogen, K., Ardel, W.: ONCONASE® and its therapeutic potential. *Lab. Med.* **34**, 380–387 (2003). <https://doi.org/10.1309/3td26gxn65gce1bg>
26. Shlyakhovenko, V.O.: Ribonucleases. Possible New Approach. *Cancer Ther.* **2016**, 2–8 (2016)
27. Raines, R.T.: Ribonuclease A. *Chem. Rev.* **98**, 1045–1066 (1998). <https://doi.org/10.1021/cr960427h>
28. Ledoux, L.: Action of ribonuclease on neoplastic growth. II. Action on Landschütz ascites cells *in vitro*. *Biochim. Biophys. Acta* **20**, 369–377 (1956). [https://doi.org/10.1016/0006-3002\(56\)90298-0](https://doi.org/10.1016/0006-3002(56)90298-0)
29. Ledoux, L., Brachet, J.: Remarks on preparations of ribonuclease from different manufacturing sources. *Biochim. Biophys. Acta* **16**, 290 (1955). [https://doi.org/10.1016/0006-3002\(55\)90219-5](https://doi.org/10.1016/0006-3002(55)90219-5)
30. Section, C.: Action of ribonuclease on two solid tumours *in vivo* **1955**, 36–37 (1955)
31. Ledoux, L.: Action of ribonuclease on certain ascites tumours. *Nature* **175**, 258–259 (1955). <https://doi.org/10.1038/175258b0>
32. Ledoux, L., Revell, S.H.: Action of ribonuclease on neoplastic growth. I. Chemical aspects of normal tumour growth: The Landschütz ascites tumour. *Biochim. Biophys. Acta* **18**, 416–426 (1955). [https://doi.org/10.1016/0006-3002\(55\)90106-2](https://doi.org/10.1016/0006-3002(55)90106-2)
33. Ledoux, L., Baltus, E.: The effects of ribonuclease on cells of Ehrlich carcinoma. *Experientia* **10**, 500–501 (1954). <https://doi.org/10.1007/BF02166182>
34. Ribó, M., Benito, A., Vilanova, M.: Antitumor ribonucleases. In: *Nucleic Acids and Molecular Biology*, pp. 55–88. Springer-Verlag, Berlin Heidelberg, (2011)
35. Kanwar, S.S., Kumar, R.: Ribonuclease as anticancer therapeutics. *Enz. Eng.* **06**, 6–13 (2017). <https://doi.org/10.4172/2329-6674.1000162>
36. Torrent, M., Nogués, M.V., Boix, E.: Eosinophil cationic protein (ECP) can bind heparin and other glycosaminoglycans through its RNase active site. *J. Mol. Recognit.* **24**, 90–100 (2011). <https://doi.org/10.1002/jmr.1027>
37. Chao, T.Y., Lavis, L.D., Raines, R.T.: Cellular uptake of ribonuclease A relies on anionic glycans. *Biochemistry* **49**, 10666–10673 (2010). <https://doi.org/10.1021/bi1013485>
38. Eller, C.H., Chao, T.Y., Singarapu, K.K., Ouerfelli, O., Yang, G., Markley, J.L., Danishefsky, S.J., Raines, R.T.: Human cancer antigen Globo H is a cell-surface ligand for human ribonuclease 1. *ACS*

- Cent. Sci. **1**, 181–190 (2015). <https://doi.org/10.1021/acscentsci.5b00164>
39. Rodríguez, M., Torrent, G., Bosch, M., Rayne, F., Dubremetz, J.F., Ribó, M., Benito, A., Vilanova, M., Beaumelle, B.: Intracellular pathway of Onconase that enables its delivery to the cytosol. *J. Cell Sci.* **120**, 1405–1411 (2007). <https://doi.org/10.1242/jcs.03427>
 40. Haigis, M.C., Raines, R.T.: Secretory ribonucleases are internalized by a dynamin-independent endocytic pathway. *J. Cell Sci.* **116**, 313–324 (2003). <https://doi.org/10.1242/jcs.00214>
 41. Gotte, G., Menegazzi, M.: Biological activities of secretory RNaseS: Focus on their oligomerization to design antitumor drugs. *Front. Immunol.* **10**, 2626 (2019). <https://doi.org/10.3389/fimmu.2019.02626>
 42. Benito, A., Vilanova, M., Ribó, M.: Intracellular routing of cytotoxic pancreatic-type ribonucleases. *Curr. Pharm. Biotechnol.* **9**, 169–179 (2008). <https://doi.org/10.2174/138920108784567281>
 43. Bosch, M., Benito, A., Ribo, M., Puig, T., Beaumelle, B., Vilanova, M., Abdelmelek, H., Ribo, M., Puig, T., Beaumelle, B., Vilanova, M., Ribó, M., Puig, T., Beaumelle, B., Vilanova, M.: A nuclear localization sequence endows human pancreatic ribonuclease with cytotoxic activity. *Biochemistry* **43**, 2167–2177 (2004). <https://doi.org/10.1021/bi035729+>
 44. Haigis, M.C., Kurten, E.L., Raines, R.T.: Ribonuclease inhibitor as an intracellular sentry. *Nucleic Acids Res.* **31**, 1024–1032 (2003). <https://doi.org/10.1093/nar/gkg163>
 45. Iordanov, M.S., Wong, J., Newton, D.L., Rybak, S.M., Bright, R.K., Flavell, R.A., Davis, R.J., Magun, B.E.: Differential requirement for the stress-activated protein kinase/c-Jun NH2-terminal kinase in RNA damage-induced apoptosis in primary and in immortalized fibroblasts. *Mol. Cell Biol. Res. Commun.* **4**, 122–128 (2000). <https://doi.org/10.1006/mcbr.2000.0266>
 46. Fiorini, C., Cordani, M., Gotte, G., Picone, D., Donadelli, M.: Onconase induces autophagy sensitizing pancreatic cancer cells to gemcitabine and activates Akt/mTOR pathway in a ROS-dependent manner. *Biochim. Biophys. Acta* **1853**, 549–560 (2015). <https://doi.org/10.1016/j.bbamcr.2014.12.016>
 47. Qiao, M., Zu, L.D., He, X.H., Shen, R.L., Wang, Q.C., Liu, M.F.: Onconase downregulates microRNA expression through targeting microRNA precursors. *Cell Res.* **22**, 1199–1202 (2012). <https://doi.org/10.1038/cr.2012.67>
 48. Zhao, H., Ardelt, B., Ardelt, W., Shogen, K., Darzynkiewicz, Z.: The cytotoxic ribonuclease Onconase targets RNA interference (siRNA). *Cell Cycle* **7**, 3258–3261 (2008). <https://doi.org/10.4161/cc.7.20.6855>
 49. Altomare, D.A., Rybak, S.M., Pei, J., Maizel, J.V., Cheung, M., Testa, J.R., Shogen, K.: Onconase responsive genes in human mesothelioma cells: Implications for an RNA damaging therapeutic agent. *BMC Cancer* **10**, 34 (2010). <https://doi.org/10.1186/1471-2407-10-34>
 50. Vert, A., Castro, J., Ribó, M., Benito, A., Vilanova, M.: Activating transcription factor 3 is crucial for antitumor activity and to strengthen the antiviral properties of Onconase. *Oncotarget* **8**, 11692–11707 (2017). <https://doi.org/10.18632/oncotarget.14302>
 51. Vert, A., Castro, J., Ribó, M., Benito, A., Vilanova, M.: A nuclear-directed human pancreatic ribonuclease (PE5) targets the metabolic phenotype of cancer cells. *Oncotarget* **7**, 18309–18324 (2016). <https://doi.org/10.18632/oncotarget.7579>
 52. Tatsuta, T., Sugawara, S., Takahashi, K., Ogawa, Y., Hosono, M., Nitta, K.: Leczyme: A new candidate drug for cancer therapy. *BioMed Res. Int.* **2014**, 421415 (2014). <https://doi.org/10.1155/2014/421415>
 53. Irie, M., Nitta, K., Nonaka, T.: Biochemistry of frog ribonucleases. *Cell. Mol. Life Sci.* **54**, 775–784 (1998). <https://doi.org/10.1007/s000180050206>
 54. Tatsuta, T., Hosono, M., Sugawara, S., Kariya, Y., Ogawa, Y., Hakomori, S., Nitta, K.: Sialic acid-binding lectin (leczyme) induces caspase-dependent apoptosis-mediated mitochondrial perturbation in Jurkat cells. *Int. J. Oncol.* **43**, 1402–1412 (2013). <https://doi.org/10.3892/ijo.2013.2092>
 55. Kariya, Y., Tatsuta, T., Sugawara, S., Kariya, Y., Nitta, K., Hosono, M.: RNase activity of sialic acid-binding lectin from bullfrog eggs drives antitumor effect via the activation of p38 MAPK to caspase-3/7 signaling pathway in human breast cancer cells. *Int. J. Oncol.* **49**, 1334–1342 (2016). <https://doi.org/10.3892/ijo.2016.3656>
 56. Kobe, B., Deisenhofer, J.: Crystal structure of porcine ribonuclease inhibitor, a protein with leucine-rich repeats. *Nature* **366**, 751–756 (1993). <https://doi.org/10.1038/366751a0>
 57. Dickson, K.A., Haigis, M.C., Raines, R.T.: Ribonuclease inhibitor: Structure and function. *Prog. Nucleic Acid Res. Mol. Biol.* **80**, 349–374 (2005). [https://doi.org/10.1016/S0079-6603\(05\)80009-1](https://doi.org/10.1016/S0079-6603(05)80009-1)
 58. Lee, F.S., Vallee, B.L.: Structure and action of mammalian ribonuclease (angiogenin) inhibitor. *Prog. Nucleic Acid Res. Mol. Biol.* **44**, 1–30 (1993). [https://doi.org/10.1016/s0079-6603\(08\)60215-9](https://doi.org/10.1016/s0079-6603(08)60215-9)
 59. Lee, F.S., Shapiro, R., Vallee, B.L.: Tight-binding inhibition of angiogenin and ribonuclease A by placental ribonuclease inhibitor. *Biochemistry* **28**, 225–230 (1989). <https://doi.org/10.1021/bi00427a031>
 60. Vicentini, A.M., Kieffer, B., Matthies, R., Meyhack, B., Hemmings, B.A., Stone, S.R., Hofsteenge, J.: Protein chemical and kinetic characterization of recombinant porcine ribonuclease inhibitor expressed in *Saccharomyces cerevisiae*. *Biochemistry* **29**, 8827–8834 (1990). <https://doi.org/10.1021/bi00489a046>
 61. Nitta, K., Oyama, F., Oyama, R., Sekiguchi, K., Kawauchi, H., Takayanagi, Y., Hakomori, S., Titani, K.: Ribonuclease activity of sialic acid-binding lectin from *Rana catesbeiana* eggs. *Glycobiology* **3**, 37–45 (1993). <https://doi.org/10.1093/glycob/3.1.37>
 62. Hayano, K., Iwama, M., Sakamoto, H., Watanabe, H., Sanda, A., Ohgi, K., Irie, M.: Characterization of poly C preferential ribonuclease from chicken liver. *J. Biochem.* **114**, 156–162 (1993). <https://doi.org/10.1093/oxfordjournals.jbchem.a124132>
 63. Katoh, H., Yoshinaga, M., Yanagita, T., Ohgi, K., Irie, M., Beintema, J.J., Meinsma, D.: Kinetic studies on turtle pancreatic ribonuclease: A comparative study of the base specificities of the B2 and P0 sites of bovine pancreatic ribonuclease A and turtle pancreatic ribonuclease. *Biochim. Biophys. Acta* **873**, 367–371 (1986). [https://doi.org/10.1016/0167-4838\(86\)90085-3](https://doi.org/10.1016/0167-4838(86)90085-3)
 64. Zhao, W., Beintema, J.J., Hofsteenge, J.: The amino acid sequence of iguana (*Iguana iguana*) pancreatic ribonuclease. *Eur. J. Biochem.* **219**, 641–646 (1994). <https://doi.org/10.1111/j.1432-1033.1994.tb19979.x>
 65. Nitta, K.: Leczyme. *Methods Enzymol.* **341**, 368–374 (2001)
 66. Hu, C.C.A., Tang, C.H.A., Wang, J.J.: Caspase activation in response to cytotoxic *Rana catesbeiana* ribonuclease in MCF-7 cells. *FEBS Lett.* **503**, 65–68 (2001). [https://doi.org/10.1016/S0014-5793\(01\)02691-6](https://doi.org/10.1016/S0014-5793(01)02691-6)
 67. Tatsuta, T., Hosono, M., Takahashi, K., Omoto, T., Kariya, Y., Sugawara, S., Hakomori, S., Nitta, K.: Sialic acid-binding lectin (leczyme) induces apoptosis to malignant mesothelioma and exerts synergistic antitumor effects with TRAIL. *Int. J. Oncol.* **44**, 377–384 (2014). <https://doi.org/10.3892/ijo.2013.2192>
 68. Tatsuta, T., Hosono, M., Miura, Y., Sugawara, S., Kariya, Y., Hakomori, S., Nitta, K.: Involvement of ER stress in apoptosis induced by sialic acid-binding lectin (leczyme) from bullfrog eggs. *Int. J. Oncol.* **43**, 1799–1808 (2013). <https://doi.org/10.3892/ijo.2013.2128>
 69. Tatsuta, T., Sugawara, S., Takahashi, K., Ogawa, Y., Hosono, M., Nitta, K.: Cancer-selective induction of apoptosis by leczyme.

- Front. Oncol **4**, 1–6 (2014). <https://doi.org/10.3389/fonc.2014.00139>
70. Chen, J.N., Yiang, G.T., Lin, Y.F., Chou, P.L., Wu, T.K., Chang, W.J., Chen, C., Yu, Y.L.: Rana catesbeiana ribonuclease induces cell apoptosis via the caspase-9/–3 signaling pathway in human glioblastoma DBTRG, GBM8901 and GBM8401 cell lines. *Oncol. Lett.* **9**, 2471–2476 (2015). <https://doi.org/10.3892/ol.2015.3117>
 71. Satoh, T., Tatsuta, T., Sugawara, S., Hara, A., Hosono, M.: Synergistic anti-tumor effect of bullfrog sialic acid-binding lectin and pemetrexed in malignant mesothelioma. *Oncotarget* **8**, 42466–42477 (2017). <https://doi.org/10.18632/oncotarget.17198>
 72. Tatsuta, T., Satoh, T., Sugawara, S., Hara, A., Hosono, M., Im, C., Kawano, T., Tatsuta, T., Koide, Y., Yamamoto, D., Ozeki, Y., Nitta, K., Hosono, M., Kieber-Emmons, T., Monzavi-Karbassi, B., Hutchins, L.F., Pennisi, A., Makhoul, I.: Sialic acid-binding lectin from bullfrog eggs inhibits human malignant mesothelioma cell growth *in vitro* and *in vivo*. *PLoS ONE* **13**, 1–15 (2018). <https://doi.org/10.1371/journal.pone.0190653>
 73. Tatsuta, T., Sato, S., Sato, T., Sugawara, S., Suzuki, T., Hara, A., Hosono, M.: Sialic acid-binding lectin from bullfrog eggs exhibits an anti-tumor effect against breast cancer cells including triple-negative phenotype cells. *Molecules* **23**, 2714 (2018). <https://doi.org/10.3390/molecules23102714>
 74. Yiang, G.T., Yu, Y.L., Chou, P.L., Tsai, H.F., Chen, L.A., Chen, Y.H., Su, K.J., Wang, J.J., Bau, D.T., Wei, C.W.: The cytotoxic protein can induce autophagocytosis in addition to apoptosis in MCF-7 human breast cancer cells. *In Vivo* **26**, 403–409 (2012)
 75. Hu, C.C.A., Lee, Y.H., Tang, C.H.A., Cheng, J.T., Wang, J.J.: Synergistic cytotoxicity of Rana catesbeiana ribonuclease and IFN- γ , on hepatoma cells. *Biochem. Biophys. Res. Commun.* **280**, 1229–1236 (2001). <https://doi.org/10.1006/bbrc.2001.4272>
 76. Tang, C.H.A., Hu, C.C.A., Wei, C.W., Wang, J.J.: Synergism of Rana catesbeiana ribonuclease and IFN- γ triggers distinct death machineries in different human cancer cells. *FEBS Lett.* **579**, 265–270 (2005). <https://doi.org/10.1016/j.febslet.2004.11.086>
 77. Wei, C.W., Hu, C.C.A., Tang, C.H.A., Lee, M.C., Wang, J.J.: Induction of differentiation rescues HL-60 cells from Rana catesbeiana ribonuclease-induced cell death. *FEBS Lett.* **531**, 421–426 (2002). [https://doi.org/10.1016/S0014-5793\(02\)03577-9](https://doi.org/10.1016/S0014-5793(02)03577-9)
 78. Tseng, H.H., Yu, Y.L., Chen, Y.L.S., Chen, J.H., Chou, C.L., Kuo, T.Y., Wang, J.J., Lee, M.C., Huang, T.H., Chen, M.H.C., Yiang, G.T.: RC-RNase-induced cell death in estrogen receptor positive breast tumors through down-regulation of Bcl-2 and estrogen receptor. *Oncol. Rep.* **25**, 849–853 (2011). <https://doi.org/10.3892/or.2010.1114>
 79. Tatsuta, T., Hosono, M., Ogawa, Y., Inage, K., Sugawara, S., Nitta, K.: Downregulation of Hsp70 inhibits apoptosis induced by sialic acid-binding lectin (Ieczyme). *Oncol. Rep.* **31**, 13–18 (2014). <https://doi.org/10.3892/or.2013.2814>
 80. Ogawa, Y., Sugawara, S., Tatsuta, T., Hosono, M., Nitta, K., Fujii, Y., Kobayashi, H., Fujimura, T., Taka, H., Koide, Y., Hasan, I., Matsumoto, R., Yasumitsu, H., Kanaly, R.A., Kawsar, S.M.A., Ozeki, Y.: Sialyl-glycoconjugates in cholesterol-rich microdomains of P388 cells are the triggers for apoptosis induced by Rana catesbeiana oocyte ribonuclease. *Glycoconj. J.* **31**, 171–184 (2014). <https://doi.org/10.1007/s10719-013-9513-7>
 81. Lee, Y.H., Wei, C.W., Wang, J.J., Chiou, C.T.: Rana catesbeiana ribonuclease inhibits Japanese encephalitis virus (JEV) replication and enhances apoptosis of JEV-infected BHK-21 cells. *Antiviral Res.* **89**, 193–198 (2011). <https://doi.org/10.1016/j.antiviral.2011.01.002>
 82. Tatsuta, T., Nakasato, A., Sugawara, S., Hosono, M.: Transcriptional alterations in malignant pleural mesothelioma cells in response to long-term treatment with bullfrog sialic acid-binding lectin. *Mol. Med Rep.* **23** (2021). <https://doi.org/10.3892/mmr.2021.12106>
 83. Costanzi, J., Sidransky, D., Navon, A., Goldsweig, H.: Ribonucleases as a novel pro-apoptotic anticancer strategy: Review of the preclinical and clinical data for ranpirnase. *Cancer Invest.* **23**, 643–650 (2005). <https://doi.org/10.1080/07357900500283143>
 84. Notomista, E., Catanzano, F., Graziano, G., Dal Piaz, F.D., Barone, G., D'Alessio, G., Di Donato, A.: Onconase: An unusually stable protein. *Biochemistry* **39**, 8711–8718 (2000). <https://doi.org/10.1021/bi000415x>
 85. Rosenberg, H.F., Zhang, J., Di Liao, Y.D., Dyer, K.D.: Rapid diversification of RNase A superfamily ribonucleases from the bullfrog. *Rana catesbeiana*. *J. Mol. Evol.* **53**, 31–38 (2001). <https://doi.org/10.1007/s002390010188>

Publisher's Note Springer Nature remains neutral with regard to jurisdictional claims in published maps and institutional affiliations.

Transcriptomic alterations in malignant pleural mesothelioma cells in response to long-term treatment with bullfrog sialic acid-binding lectin

TAKEO TATSUTA, ARISU NAKASATO, SHIGEKI SUGAWARA and MASAHIRO HOSONO

Division of Cell Recognition, Institute of Molecular Biomembrane and Glycobiology,
Tohoku Medical and Pharmaceutical University, Sendai, Miyagi 981-8558, Japan

Received February 3, 2021; Accepted March 29, 2021

DOI: 10.3892/mmr.2021.12106

Abstract. Malignant pleural mesothelioma (MPM) is a universally lethal type of cancer that is increasing in incidence worldwide; therefore, the development of new drugs for MPM is an urgent task. Bullfrog sialic acid-binding lectin (cSBL) is a multifunctional protein that has carbohydrate-binding and ribonuclease activities. cSBL exerts marked antitumor activity against numerous types of cancer cells, with low toxicity to normal cells. Although *in vitro* and *in vivo* studies revealed that cSBL was effective against MPM, the mechanism by which cSBL exerts antitumor effects is not fully understood. To further understand the mechanism of action of cSBL, the present study aimed to identify the key molecules whose expression was affected by cSBL. The present study established cSBL-resistant MPM cells. Microarray analyses revealed that there were significant pleiotropic changes in the expression profiles of several genes, including multiple genes involved in metabolic pathways in cSBL-resistant cells. Furthermore, the expression of some members of the aldo-keto

reductase family was revealed to be markedly downregulated in these cells. Among these, it was particularly interesting that cSBL action reduced the level of AKR1B10, which has been reported as a biomarker candidate for MPM prognosis. These findings revealed novel aspects of the effect of cSBL, which may contribute to the development of new therapeutic strategies for MPM.

Introduction

Malignant pleural mesothelioma (MPM) is an aggressive cancer of the mesothelial cells lining the pleural surface of the chest wall and lung (1). The main cause of carcinogenesis of this disease is thought to be exposure to an environmental carcinogen, asbestos (2); furthermore, the involvement of SV40 and exposure to radiation have been suggested as cofactors (3,4). The MPM patient prognosis is very poor and available therapies have still a limited impact on MPM progression (5). Until recently, antifolate and platinum combination chemotherapy was the only established treatment (6,7). These days, the development of immune-checkpoint inhibitors has contributed to the improvement of MPM treatment. The data from the phase III trial (NCT02899299) designed to evaluate nivolumab plus ipilimumab compared with conventional chemotherapy (pemetrexed and cisplatin or carboplatin) showed a statistically significant overall survival (OS) benefit in patients with previously untreated, unresectable MPM, and, only recently, the FDA has finally approved nivolumab plus ipilimumab for previously untreated unresectable MPM (8). Although the nivolumab and ipilimumab combination has extended the OS (a median OS of 18.1 months compared to 14.1 months for platinum-based standard of chemotherapy) (8), the prognosis is still poor, and research such as identification of new biomarkers in invasive mesothelioma (9), and search for new drugs for MPM (10) have been actively conducted for further improvement of MPM care. In particular, the development of drugs through different mechanisms of action will continue to be required in the future.

A major focus in cancer research is the development of new therapeutic agents that induce cell death in malignant neoplasms but do not increase inflammation or have significant side effects in normal tissue. Cytotoxic ribonucleases

Correspondence to: Dr Masahiro Hosono, Division of Cell Recognition, Institute of Molecular Biomembrane and Glycobiology, Tohoku Medical and Pharmaceutical University, 4-4-1 Komatsushima, Aobaku, Sendai, Miyagi 981-8558, Japan
E-mail: mhosono@tohoku-mpu.ac.jp

Abbreviations: RNase, ribonuclease; ONC, onconase; cSBL, bullfrog sialic acid-binding lectin; DEG, differentially expressed gene; ATF3, activating transcription factor 3; cSR, cSBL-resistant; DOX, doxorubicin; AKR, aldo-keto reductase; KEGG, Kyoto Encyclopedia of Genes and Genomes; RT-qPCR, reverse transcription quantitative polymerase chain reaction; PPI, protein-protein interaction; SLC47A2, solute carrier family 47 member 2; CBR, carbonyl reductase; GAPDH, glyceraldehyde-3-phosphate dehydrogenase; RR, resistance rate; RIN[®], RNA integrity number equivalent; GO, Gene Ontology

Key words: antitumor drug, sialic acid-binding lectin, cytotoxic ribonucleases, microarray profiling, metabolism of cancer cells, aldo-keto reductase

(RNases) are a new field of anticancer drug candidates that target RNA and several cytotoxic RNases have been reported to have antitumor effects (11,12). The vertebrate-secreted RNase superfamily, also called the RNase A superfamily, includes several cytotoxic RNases, such as onconase (ONC) from *Rana pipiens* (13) and a variant of human pancreatic ribonuclease carrying a nuclear localization signal (PE5) (14). Unlike clinically used chemotherapeutic drugs that target DNA synthesis and transcription, cytotoxic RNases are believed to be non-mutagenic because they target RNA functions, such as RNA translation or gene regulation (15).

Sialic acid-binding lectin from *Rana catesbeiana* (cSBL), also known as RC-RNase, is a multifunctional protein that binds carbohydrates and has a ribonuclease activity (16–18). It was originally identified as a lectin that recognizes sialic acid-containing complexes (17), and protein sequence analysis revealed that it belonged to the vertebrate-secreted RNase superfamily (19). It has previously been identified that cSBL has remarkable antitumor activity against many types of cancer cells and low toxicity in normal cells (20–25). This effect was observed in not only *in vitro* experiments but also *in vivo* studies (18,20,26). Our own recent studies revealed that cSBL induced apoptosis in cancer cells via the intrinsic pathway (27,28), and that the RNase activity of cSBL was essential for its antitumor effect (29). The effectiveness of cSBL has also been studied for in MPM. We reported that although cSBL had very low cytotoxicity in the normal pleural mesothelial cell line Met5A, it efficiently reduced the viability of MPM cells including H28, Meso-1, Meso-4, H2452 and MSTO cells (30,31). We found that pemetrexed + cSBL exhibited a strong synergistic effect that was even superior to the standard regimen of pemetrexed + cisplatin (31). Furthermore, *in vivo* study revealed that cSBL showed a significant tumor growth inhibitory effect in multiple MPM xenograft models without any adverse effects, even under conditions where previously established pemetrexed administration had little or no effect (26). However, the antitumor mechanism of cSBL is still unclear, especially when the response of cancer cells to cSBL application is concerned.

Despite the potential of RNases in cancer treatment, few studies have identified genes whose expression was altered by cytotoxic RNases. This may be because the RNA extracted from cytotoxic RNase-treated cells is likely to be degraded by the RNA-catabolizing action of the RNase. Therefore, it is technically difficult to assess differentially expressed genes (DEGs) in cytotoxic RNase-treated cells. In recent years, some remarkable research breakthroughs have been made in studies using microarray analysis. Previous studies using microarray technology have been able to determine that ONC caused upregulation of activating transcription factor 3 (ATF3), which was important for its antitumor effect of ONC (32,33), and that PE5 caused pleiotropic effects, including gene expression changes mainly related to metabolism (34). These studies pioneered the study of gene expression after treatment with cytotoxic RNases. However, these findings were reported only in conditions in which there was little RNA degradation, that is, there was very little antitumor effect. Moreover, no gene expression studies have involved cSBL.

To further understand the antitumor effects of cSBL, we treated cSBL-sensitive MPM cells with cSBL to establish

cSBL-resistant (cSR) cells. Then, microarray analysis was performed to identify significantly altered genes in the cSBL-sensitive and cSR cell lines.

Materials and methods

Reagents. cSBL was isolated from acetone-dried powder of unfertilized bullfrog body-cavity eggs using sequential chromatography with Sephadex G75, DEAE-cellulose, hydroxyapatite, and SP-Sepharose (Cytiva), as previously described (17). For the preparation of ONC, ONC cDNA was cloned into the pET-11d plasmid (Merck KGaA) in conjunction with the *pelB* sequence. BL21 (DE3) pLysS cells (Promega) were transformed with the plasmid, and its expression was induced by adding isopropyl β -D-1-thiogalactopyranoside (0.2 mM) at 34°C for 72 h. ONC recombinant protein was purified from the culture liquid by sequential chromatography with Sephadex G75, DEAE-cellulose, hydroxyapatite, and SP-Sepharose. Doxorubicin (DOX) was purchased from Sigma-Aldrich. The anti-caspase-3 antibody (cat. no. #9662), peroxidase-conjugated anti-mouse IgG and anti-rabbit IgG antibodies (cat. no. #7074 and #7076, respectively) were purchased from Cell Signaling Technology. The anti-aldo-keto reductase (AKR) 1B10 antibody (cat. no. ab96417) was purchased from Abcam (Cambridge, UK). The anti- β -actin antibody (clone AC-74, cat. no. A2228) was purchased from Sigma-Aldrich.

Establishment of cSBL-resistant cell lines. H28 cells were purchased from the American Type Culture Collection. For the establishment of cSR cell lines, cells were cultured with complete medium containing stepwise increasing concentrations of cSBL. The starting concentration was 0.01 μ M in which H28 cells could manage to survive, and the final concentration was set as 0.5 μ M, which is 50 times higher than the initial concentration. The cells were passaged approximately 50 times to reach the final concentration. These resistant cells were proven to be stably resistant even after at least 10 passages in drug-free complete medium. After that, cells were cloned using limiting dilution. We confirmed five resistant clones, which were designated cSR-A1, -A2, -B1, -B2 and -C1. To ensure that these clones were permanent and stable, they were cultured for five passages in the presence of 0.5 μ M cSBL. For the analyses described here, cultures of less than 20 passages after the cloning were used. All cell lines were cultured in RPMI 1640 medium (Nissui) supplemented with 10% fetal bovine serum, penicillin-G (100 U/ml), and streptomycin (100 g/ml) (Thermo Fisher Scientific, Inc.). Cells were maintained in a 5% CO₂ incubator at 37°C under humidified conditions. Cell morphology was observed using an IX71 microscope (Olympus).

Colony formation assay. Cells were seeded in 6-well plates (Corning, cat. no. 353046, 1x10³ cells per well). After 24 h, cells were treated with medium alone or with cSBL (1, 5, 10, 25, or 50 nM) for 12 days. Then, cells were fixed with para-formaldehyde for 15 min and stained with crystal violet for 10 min. Colonies were photographed by Gel Doc XR system (Bio-Rad Laboratories, Inc.) and counted using Quantity One software (Bio-Rad Laboratories, Inc.). Each experiment was performed in triplicate.

WST-8 assay. The WST-8 assay was performed to determine the cell viability. Cells (5×10^4 cells/ml) cultured in 96-well plates (Corning, cat. no. 353072, 100 μ l/well) were treated with cSBL, ONC, or DOX at the indicated concentrations for 72 h. Then, the cells were incubated with Cell Count Reagent SF (Nacalai Tesque Inc.) for 1–4 h. The absorbance of the resulting product at 450 nm was measured, and the background absorbance at 650 nm was subtracted. Experiments were conducted in triplicate.

Western blotting. Cells (5×10^4 cells/ml) were cultured in 6-well plates (Corning, cat. no. 353046, 4 ml/well) and treated with cSBL or control. Whole cell lysates were prepared using extraction buffer [150 mM NaCl, 10 mM Tris-HCl (pH 7.4), 5 mM EDTA, 1% Nonidet P-40, 0.1% sodium deoxycholate, and 0.1% sodium dodecyl sulfate] supplemented with complete™ Mini EDTA-free protease inhibitor cocktail tablets (one tablet/10 ml; Roche Applied Science). Soluble proteins were collected, and the protein concentration was measured using a BCA protein assay kit (Thermo Fisher Scientific, Inc., cat. no. 23227) according to the manufacturer's instructions. Proteins were separated using 10 or 14% SDS-PAGE and transferred onto Immobilon-P transfer membranes (Thermo Fisher Scientific, Inc.). The membranes were sequentially incubated with primary and secondary antibodies diluted in Can Get Signal solution (Toyobo Co., Ltd.). Protein bands were detected using ECL Prime Western Blotting Detection Reagent (Cytiva). The relative density of the protein bands was measured using ImageJ 1.51s software (National Institutes of Health). Experiments were repeated in triplicates.

Total RNA isolation. Total RNA was isolated from cells using TRI Reagent (Molecular Research Center) and purified using the SV Total RNA Isolation System (Promega) according to the manufacturer's instructions. RNA samples were quantified using an ND-1000 spectrophotometer (NanoDrop Technologies), and the quality was confirmed using a 2200 TapeStation (Agilent Technologies). The RNA integrity number equivalent (RIN[®]), which was an index of RNA degradation, was calculated from the 28S and 18S ribosomal RNA band peak values and other band peak values in the electrophoretic image. For the subsequent cDNA labeling, the Agilent Low-Input QuickAmp Labeling kit (Agilent Technologies, cat. no. 5190-2305) was used.

Gene expression microarrays. cDNA was amplified, labeled, and hybridized to a 60K Agilent 60-mer oligomicroarray according to the manufacturer's instructions. All hybridized microarray slides were scanned using an Agilent scanner. Relative hybridization intensities and background hybridization values were calculated using Agilent Feature Extraction Software (9.5.1.1).

Data analysis and filter criteria. Raw signal intensities and flags for each probe were calculated from hybridization intensities (gProcessedSignal) and spot information (gIsSaturated, etc.), according to the procedures recommended by Agilent. [Flag criteria on GeneSpring Software was as follows: Absent (A): 'Feature is not positive and significant' and 'Feature is not above background,' Marginal (M):

'Feature is not Uniform,' 'Feature is Saturated,' and 'Feature is a population outlier,' and Present (P): others.]. The raw signal intensities of two samples were log₂-transformed and normalized by quantile algorithm with the Bioconductor preprocessCore library package (35,36). We selected probes that called the P flag in at least two samples. To identify up- and downregulated genes, we calculated Z-scores (37) and ratios (non-log scaled fold-change) from the normalized signal intensities of each probe to compare control and experimental samples. Then, we established the following criteria for differentially regulated genes: Upregulated genes: Z-score ≥ 2.0 and ratio ≥ 1.5 -fold and downregulated genes: Z-score ≤ -2.0 and ratio ≤ 0.66 . Data have been deposited in NCBI's Gene Expression Omnibus repository (38) (<http://www.ncbi.nih.gov/geo>) under the accession number: GSE 162286.

Functional annotation of DEGs in cSR cell lines. DEGs in cSR cells were characterized functionally using a hypergeometric test to find overrepresented gene ontology terms in the three main broad ontologies (biological process, molecular function, and cellular component) (39,40). DEGs were also mapped to the Kyoto Encyclopedia of Genes and Genomes (KEGG) (41), which assigns proteins to pathways, to find overrepresented pathways. The analyses were done using the Database for Annotation, Visualization, and Integrated Discovery online tool (42).

Network analysis. GeneMANIA (43), an online database that identifies other proteins associated with a set of input genes, was used to generate protein-protein interaction (PPI) network images. The associations between co-expression, colocalization, predicted related genes, shared protein domains, genetic interactions, and physical interactions were determined using GeneMANIA.

Reverse transcription quantitative polymerase chain reaction (RT-qPCR). mRNA expression of the top five downregulated genes (*THY1*, *AKR1B15*, *AKR1B10*, *SLC47A2*, and *CBR1*) were examined using RT-qPCR. Cells (2×10^5) were cultured for 48 h, and total RNA was extracted using an AllPrep RNA/Protein kit (Qiagen, cat. no. 80404). cDNA was synthesized from total RNA (1 μ g) using a SuperScript VILO cDNA Synthesis Kit (Invitrogen, cat. no. 11754050). RT-qPCR was performed using a LightCycler 480 system with the LightCycler 480 Probes Master Kit (Roche Diagnostics, cat. no. 04707494001). PCR primers using a TaqMan/probe library assay were designed by the Universal Probe Library Assay Design Center (<https://www.roche-applied-science.com/sis/rtqcr/upl/center.jsp>). The expression levels of these genes were standardized relative to the mRNA expression level of *GAPDH* (as a housekeeping gene) based on their average cycle threshold values.

Statistical analysis. The results from three or more independent experiments were expressed as the mean \pm standard deviation. Statistical analyses were conducted using GraphPad Prism 5.0 (GraphPad Software, Inc.), and comparisons were made using one-way analysis of variance followed by Bonferroni's post hoc test. $P < 0.05$ was considered statistically significant.

Results

Establishment of cSR cells. cSR cells were established by adding different cSBL concentrations at the low range to the culture medium. Five clones were obtained by limiting-dilution cloning. The sensitivity of the clones to cSBL was assessed using colony formation assay. As shown in Fig. 1A (upper panel), no colonies were found in parental H28 cells treated with cSBL at concentrations of 25 nM or higher. In contrast, all five clones showed resistance to cSBL. We calculated IC₅₀ values from dose-response curves (Fig. 1B). The resistant rate (RR) represented the ratio of the IC₅₀ value in cSR cells to the IC₅₀ value in H28 cells (Fig. 1A, lower panel). cSR-A1 and cSR-B1 had the highest RRs (15.3 and 14.5, respectively); therefore, these two clones were utilized in subsequent experiments.

Analysis of cSR cell lines characteristics. The growth curves of H28, cSR-A1, and cSR-B1 cells were examined (Fig. 2A). There was no significant difference in the growth rates among these three cell lines. However, cSR cells tended to show shrunken morphology in low-density culture conditions, even though no difference was observed in high-density culture conditions (Fig. 2B). The cSBL resistance was then evaluated. After treating cells with cSBL, ONC, or DOX for 72 h, the cell viability was measured using the WST-8 assay, dose-response curves were prepared, and the IC₅₀ values and RRs were calculated (Fig. 2C). The RRs of cSR cells to cSBL in the WST-8 assay were 4.4 (A1) and 4.6 (B1), which were lower than those obtained in the colony formation assay. Further, the RRs to ONC and DOX were lower than to cSBL; the RRs to ONC for cSR-A1 and cSR-B1 were 1.6 and 2.0, respectively, and the corresponding RRs to DOX were 0.7 and 1.0, respectively. Similar to what we observed for cSBL, cSR cells tended to show some resistance to RNA-targeted ONC. However, for DOX, a DNA-damaging anticancer drug, the RRs of cSR cells did not exceed 1, i.e., the effect of DOX was not different between parent H28 and cSR cells. Since it has been shown that the antitumor effect of cSBL was due to the induction of apoptosis, we examined whether the cSR cells had reduced apoptosis after cSBL treatment. Cells were treated with cSBL (1 or 5 μM) for 72 h, and protein was extracted to examine the levels of cleaved caspase-3 (Fig. 2D). There was less cleaved caspase-3 in cSBL-treated cSR-B1 cells than in H28 cells, but the difference was not significant. Taken together, our results indicate that cSR cells become resistant to cSBL after long-term treatment with low concentrations, but they have relatively weak resistance to short-term treatment with high concentrations. In addition, there was no significant difference between H28 and cSR cells in terms of proliferation, morphology, or apoptosis after treatment with high cSBL concentrations.

Altered gene expression in cSR cell lines. Total RNA was extracted from H28, cSR-A1, and cSR-B1 cells and RNA quality was evaluated. All samples had RIN^e values of 10.0 (Fig. S1), indicating that RNA could be extracted in a condition when it was hardly degraded. Therefore, these samples were used for microarray analyses. A comparison of the expression profiles in the cSR-A1, cSR-B1, and parental H28 cell lines revealed that 1254 genes (623 upregulated and 631 downregulated) were dysregulated in cSR-A1 cells and

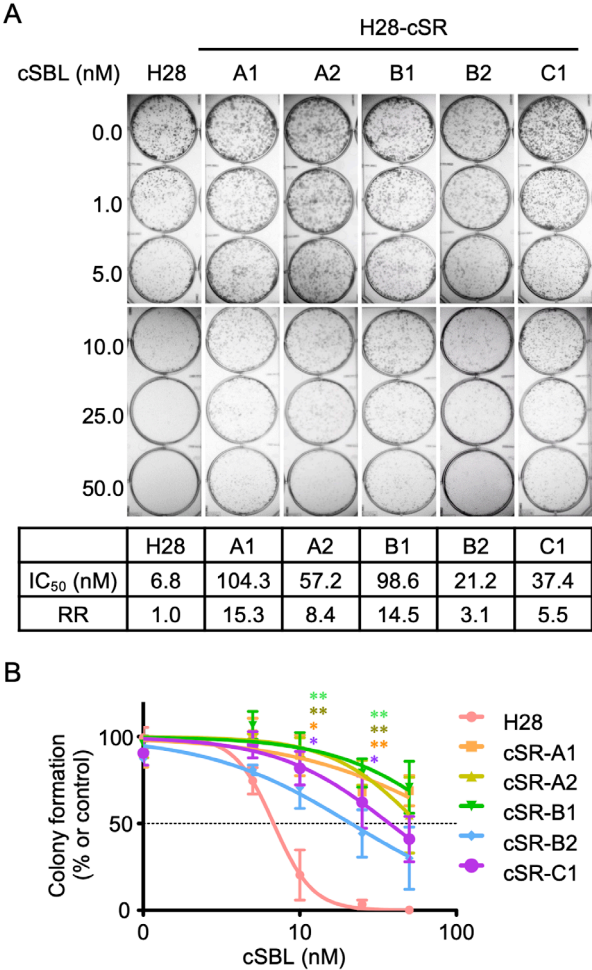


Figure 1. Effect of cSBL on colony formation in H28 and cSR cells. (A) Colony formation assays are performed in the absence or presence of cSBL (1 to 50 nM). Representative images from three independent experiments are shown. IC₅₀ values and RRs of each cell line are indicated below the images. (B) Colony numbers in (A) are counted and dose-response curves are depicted. Each data point represents the mean ± SD of three independent experiment. The statistical significance of the colony formation of the cells compared to the control H28 cells were shown. *P<0.05, **P<0.01 vs. H28. cSBL, bullfrog sialic acid-binding lectin; cSR, cSBL-resistant; RR, resistance rate; SD, standard deviation.

1,225 genes (608 upregulated and 617 downregulated) were dysregulated in cSR-B1 cells compared to H28 cells. Among them, 927 genes (440 upregulated and 487 downregulated) were common DEGs out of 37,756 known coding transcripts on the microarray (2.46%). The fold change ranged from 1.5- to 934.8-fold for upregulated genes and 1.5- to 755.7-fold for downregulated genes. The top 20 up- and downregulated genes in cSR cell lines are listed in Table SI.

GO enrichment analysis. To further understand the functional relevance of DEGs in cSR cell lines, we performed gene ontology analysis. The 927 DEGs were used to extract the associated ontologies based on three broad ontology categories: ‘biological process,’ ‘molecular function,’ and ‘cellular component.’ In all cases, a P-value ≤0.05 was considered statistically significant. The 20 most enriched GO terms for the DEGs are listed in Table SII. There were 123 significantly enriched GO terms in the biological process category.

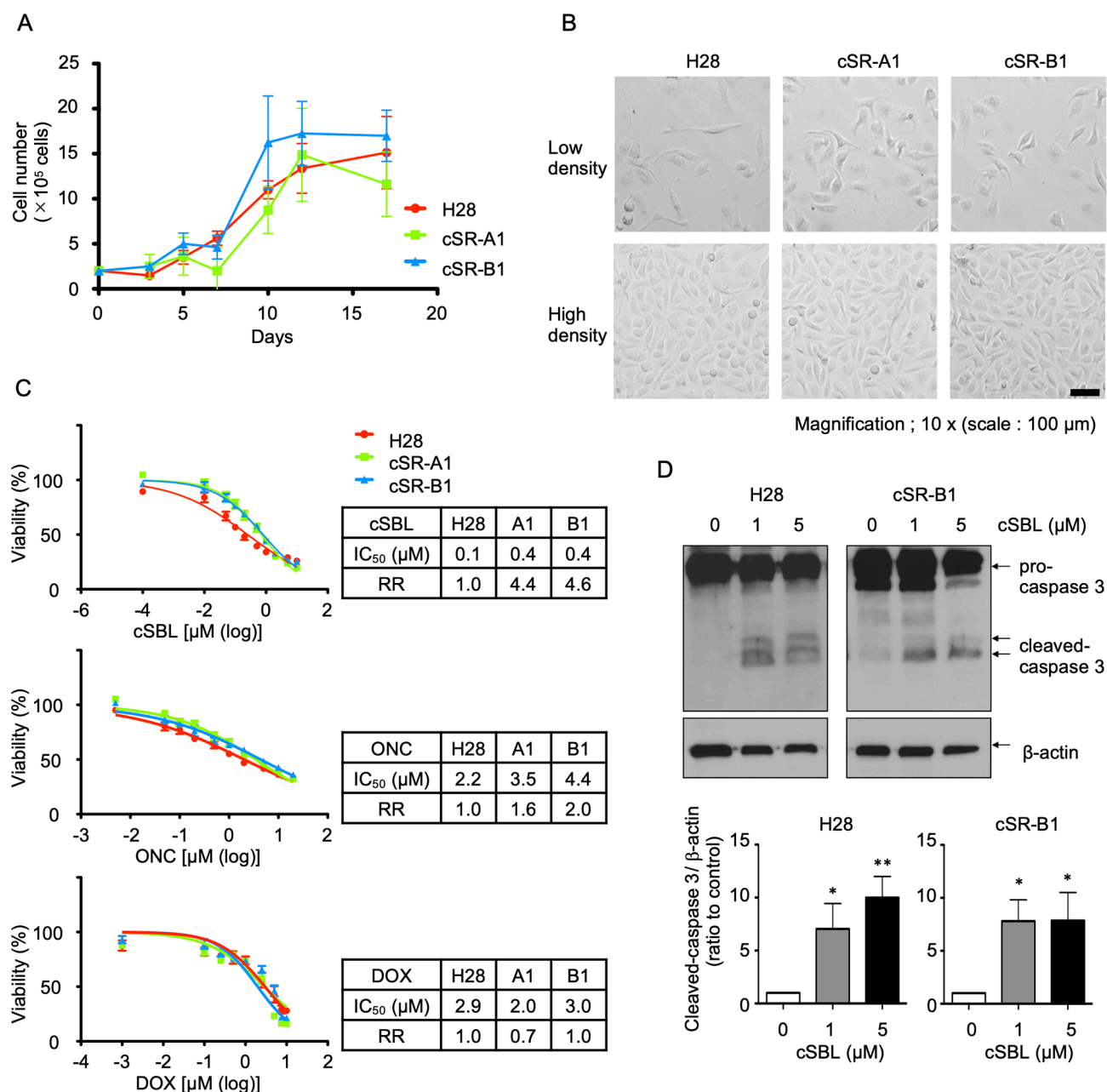


Figure 2. Analysis of cSR cell line characteristics. (A) Growth of H28 and cSR cells. Cells are seeded at 2×10^5 cells/well and counted at the timepoints (3 to 17 days) as indicated. Each data point represents the mean \pm SD of three independent experiment. (B) Morphology of H28 and cSR cells. Cells are seeded at 1×10^5 cells/well. After 24 h (low density) or 72 h (high density), cell morphology is observed. Scale bar, 100 μ m. (C) Effect of cSBL, ONC, and DOX on H28 and cSR cells. Viability of cells treated with the drugs are measured by the WST-8 assay. IC₅₀ values and RRs are calculated from the depicted dose-response curves. Each data point represents the mean \pm SD of three independent experiment performed in triplicates. (D) Apoptosis induction in H28 and cSR-B1 cells treated with cSBL. Cells are treated with cSBL (1 or 5 μ M), and the expression of cleaved caspase-3 is detected using western blotting. Densitometric quantification is performed using the results of three independent experiments (mean \pm SD). The statistical significance of the bands compared to the non-treated control were shown. * $P < 0.05$, ** $P < 0.01$ vs. 0 μ M cSBL. cSR, cSBL-resistant; cSBL, bullfrog sialic acid-binding lectin; ONC, onconase; DOX, doxorubicin; RR, resistance rate; SD, standard deviation.

The most significant term was oxidation-reduction process (GO:0055114). Interestingly, the GO terms included not only terms related to cancer characteristics, such as cell proliferation (GO:0008284, GO:0008285), adhesion (GO:0007155, GO:0007162), migration (GO:0016477), and apoptosis (GO:0006915), but also several metabolic processes related to lipids (GO:0006869), cellular protein (GO:0044267), and drugs (GO:00171449). In the molecular function category, 36 functions were enriched, and the most significantly enriched

term was integrin binding (6.87E-07). There were several other binding functions, including growth factors [IGF (GO:0005520), FGF (GO:0017134), TGF (GO:0050431), and EGF (GO:0005154)] and other cell membrane molecules such as receptors (GO:0005102), heparin (GO:0005102), and syndecan (GO:0045545). Thirty-two components were enriched in the cellular component category. The top four GO terms in cellular component included 'extracellular' [extracellular space (GO:0005615), extracellular exosome

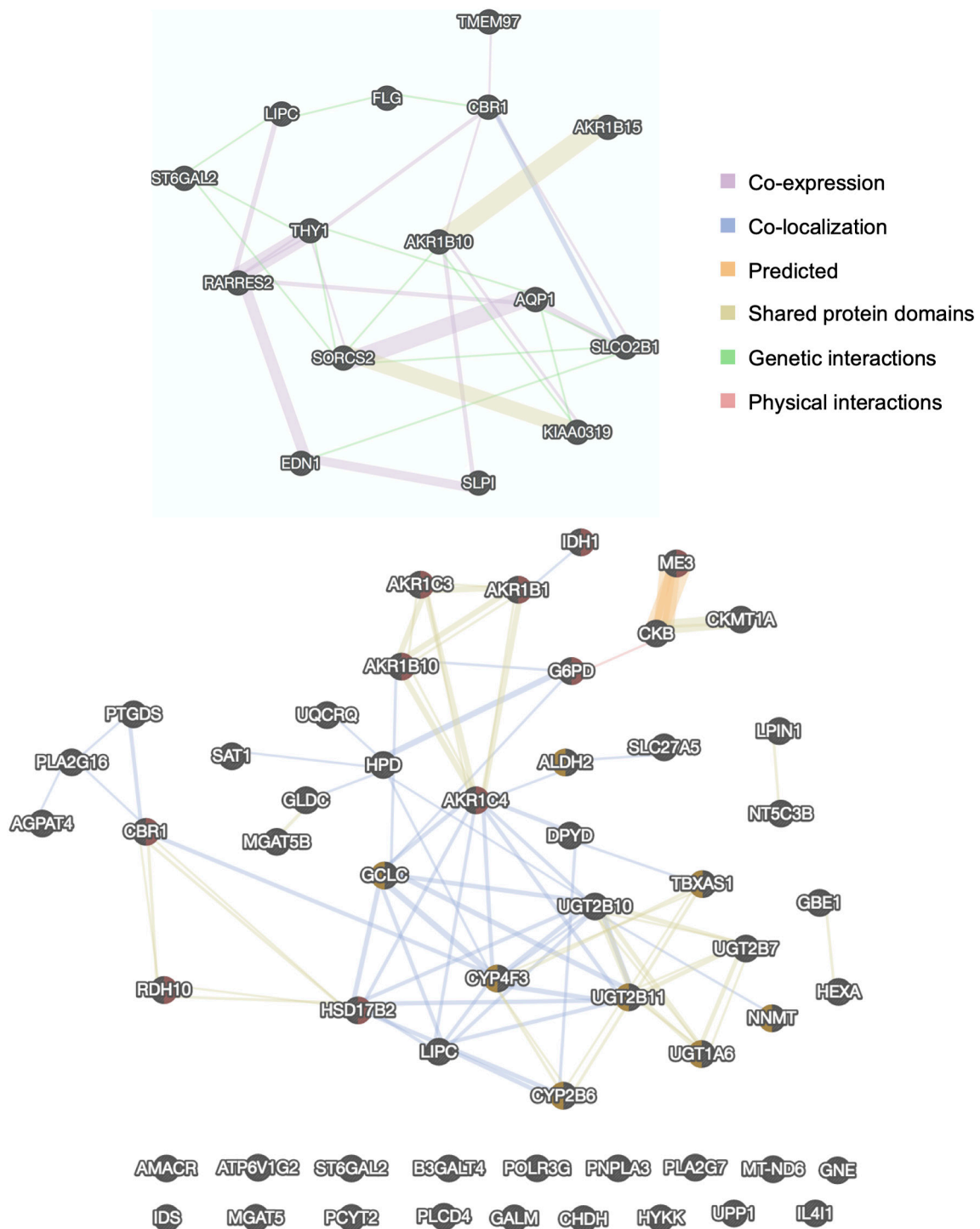


Figure 3. The protein-protein interaction networks of the top 10 up- and downregulated DEGs (upper panel) and the 57 genes involved in metabolic pathways (lower panel). Different colors represent diverse bioinformatics methods. DEGs, differentially expressed genes.

(GO:0070062), extracellular matrix (GO:0031012), and extracellular region (GO:0005576)]. They were followed by terms related to the cell membrane, such as cell surface (GO:0009986), basement membrane (GO:0005604), and plasma membrane (GO:0005886). Altogether, it appears that there are many differences between parental H28 cells and cSR cells in cellular functions, especially in association with cancer characteristics and metabolic processes. Extracellular- and cell membrane-associated GO terms were highly enriched in the DEGs of cSR cell lines.

Pathway analysis. To analyze the signaling pathways affected by DEGs in cSR cell lines, we analyzed DEGs using the KEGG database. Table SIII shows the 18 significantly affected pathways in cSR cell lines. Among the significantly enriched pathways (determined by a hypergeometric test where $P < 0.05$), ‘metabolism of xenobiotics by cytochrome P450’ was the most significant. Additionally, there were several pathways involved in various metabolic processes. Fifty-seven genes were involved in metabolic pathways, all related to lipid and carbohydrate metabolism. These results

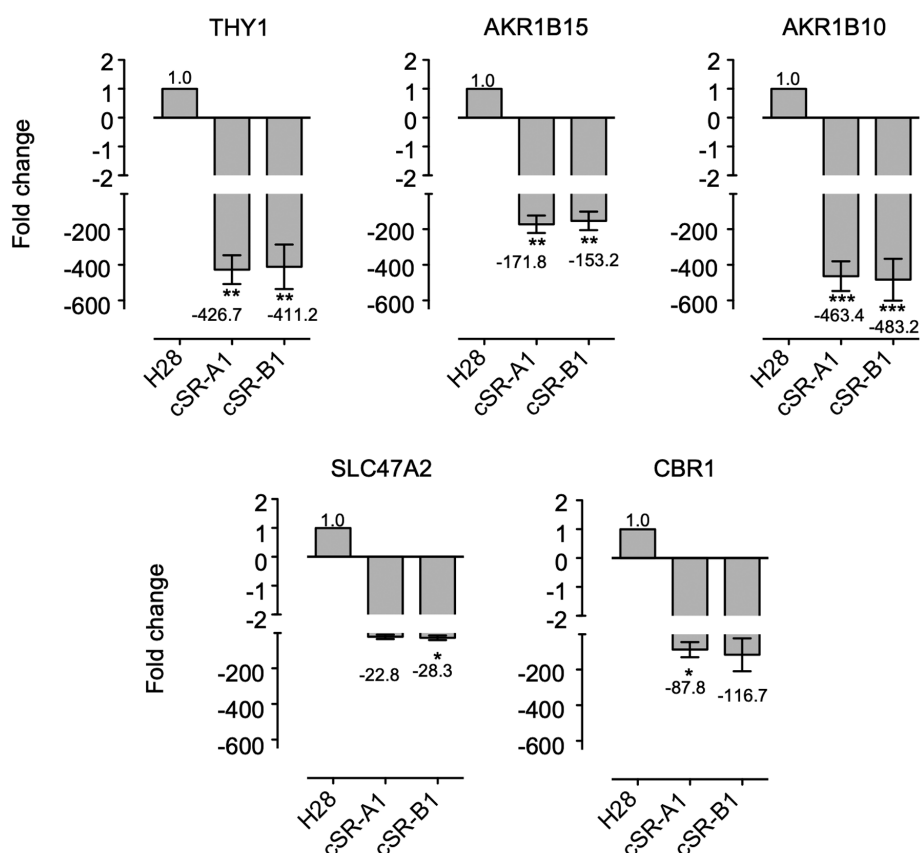


Figure 4. Expression of *THY1*, *AKR1B15*, *AKR1B10*, *SLC47A2*, and *CBR1* mRNA in H28 and cSR cells. Quantitative RT-PCR is performed using specific primers and *GAPDH* (control gene). The expression levels of genes are normalized to the level of *GAPDH*, and the level of the corresponding gene in H28 cells (control cell line) is set at 1. Data are presented as mean \pm SD of three independent experiment performed in triplicates, and the mean values are indicated on the X axis titles. * $P < 0.05$, ** $P < 0.01$, *** $P < 0.001$ vs. H28. cSR, bullfrog sialic acid-binding lectin-resistant; RT-PCR, reverse transcription polymerase chain reaction; SD, standard deviation; *THY1*, Thy-1 Cell Surface Antigen (CD90); *AKR*, aldo-keto reductase; *SLC47A2*, solute carrier family 47 member 2; *CBR1*, carbonyl reductase; *GAPDH*, glyceraldehyde-3-phosphate dehydrogenase.

prompted our interest in further analysis of the interactions among these DEGs.

PPI network analysis. The networks of proteins encoded by the top 10 up- and downregulated DEGs and the 57 genes in the KEGG metabolic pathways were identified using the GeneMANIA PPI network (Fig. 3). The color of the line represents the type of interaction, and the size of the node indicates the degree of interaction in the PPI, where larger nodes have more interactions. These data demonstrated there were some protein families whose expression was affected in cSR cells, such as AKR or UDP-glucuronosyltransferase. However, there were no significant hub proteins in either PPI network, suggesting that long-term exposure of cSBL affected gene expression in a pleiotropic fashion.

RT-qPCR analysis. As indicated above, we found that the expressions of some AKR family members were affected in cSR cells (Fig. 3). Two of these genes, *AKR1B15* and *AKR1B10*, were among the top three most downregulated genes in cSR cells (Table SI). Therefore, we were interested in the AKR family, which has been reported to be associated with cancer, and conducted subsequent studies focusing on highly downregulated genes in cSR cells. In order to confirm the reproducibility of the microarray, we compared gene

expression patterns between parental and cSR cells using RT-qPCR. As shown in Fig. 4, *THY1*, *AKR1B15*, *AKR1B10*, *SLC47A2*, and *CBR1* all had reduced expression in cSR-A1 and cSR-B1 cells. These genes had 22.8- to 483.2-fold decreased expression, and this downregulation was similar in both cSR-A1 and cSR-B1 cells. Although these fold changes were different from those observed in the microarray analysis, they were in the same direction. Therefore, RT-qPCR confirmed that the microarray experiments were valid and showed that the changes were highly significant.

Confirmation of *AKR1B10* downregulation using western blot. Next, we further examined protein expression of the AKR family members that were downregulated in cSR cells. We found that the expression of six AKR family genes were decreased from 9.1- to 562.0-fold in the microarray analysis (Table I). We focused on *AKR1B10*, which has been reported to be associated with cancer (44) and whose antibody was commercially available. The expression of *AKR1B10* at the protein level was confirmed using western blotting. A significant decrease in *AKR1B10* expression was observed in cSR-A1 and cSR-B1 cells compared to H28 cells (Fig. 5). Therefore, the decreased expression of *AKR1B10* as detected by the microarray analysis was also observed at the protein level.

Table I. Gene expression changes of AKR family in cSR cells.

Gene symbol	Fold change ^a
<i>AKR1B15</i>	-562.0
<i>AKR1B10</i>	-548.5
<i>AKR1C1</i>	-54.0
<i>AKR1C4</i>	-24.7
<i>AKR1B1</i>	-11.4
<i>AKR1C3</i>	-9.1

^aFold change in microarray analysis.

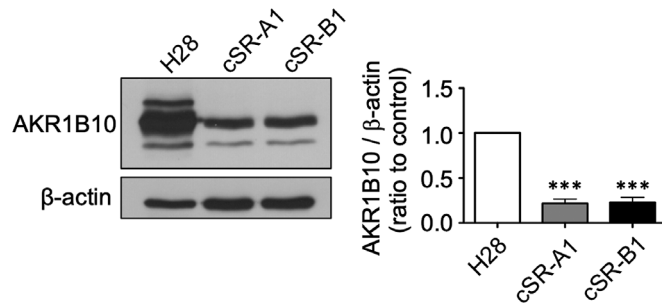


Figure 5. AKR1B10 protein expression in H28 and cSR cells. The expression of AKR1B10 in each cell line is detected using western blotting. Densitometric quantification is performed using the results of three independent experiments (mean \pm SD). *** $P < 0.001$ vs. H28. cSR, bullfrog sialic acid-binding lectin-resistant; SD, standard deviation.

Further investigation of DEGs other than the AKR family in cSR cells. Finally, we further investigated genes that showed expression fluctuations based on the results of microarray analysis. We found that the expression of some members of ATP-binding cassette (ABC) transporter superfamily was decreased in cSR cells (Table SIV). The expression of *ABCC2* was -17.3 times lower and *ABCA1* was -4.7 times lower in cSR cells.

Discussion

In this study, we produced cSR cells by treating sensitive H28 cells with low doses of cSBL over a long period. We also succeeded in identifying genes whose expression was altered in cSR cells (Table SI). The GO analysis and pathway analysis indicated that these genes were related to cell proliferation and cell membrane, as well as sugar and lipid metabolism (Tables SII and SIII). We also found that AKR1B10 was significantly reduced in cSR cells at the protein level (Fig. 5). These findings indicate that long-term treatment of cancer cells with cSBL alters many metabolic genes and reduces the expression of AKR family genes, revealing a new aspect of the antitumor effect of cSBL.

Analysis of cSR cell lines characteristics revealed that although cSR cells tended to exhibit shrunken morphology in low-density culture conditions, we could not detect significant differences in morphology in high-density culture conditions, proliferation or apoptosis after treatment with high cSBL concentrations (Fig. 2). The reason for the morphological change

observed in low-density culture conditions is unclear, but we speculate that this change may have been caused by changes in expression of genes related to the morphology, adhesion or migration. Indeed, GO enrichment analysis showed there were some enriched GO terms such as cell surface and plasma membrane in cellular component category or integrin binding in molecular function category. The RRs to cSR were high (15.3 and 14.5 for cSR-A1 and -B1, respectively) in the colony assay but low (4.4 and 4.6 for cSR-A1 and -B1, respectively) in the WST-8 assay (Figs. 1 and 2). By the nature of the experiment, the colony assay observed colony forming ability for a relatively long time (12 days) in the presence of low concentrations of cSBL (1-50 nM) and the WST-8 assay monitored survival changes in the presence of high concentrations of cSBL (0.01-10 μ M) for a short period of time (72 h). This indicates that cSR cells are resistant to long-term treatment with low concentrations of cSBL, but under short-term treatment conditions with relatively high concentrations, the apoptosis-inducing effect of cSBL is also observed in cSR cells. In other words, it is suggested that even in cSR cells that have acquired resistance by some mechanism in this long-term treatment, intracellular RNA is cleaved and apoptosis is induced by cSBL treatment exceeding a certain concentration. The dramatic mechanism of action that involves RNA cleavage may interfere with the ability of cancer cells to develop high resistance to cSBL.

Experiments that require RNA extracted from cytotoxic RNase-treated cells, such as RNA expression analysis, are difficult to perform. Such experiments often have low accuracy because the extracted RNA is presumably not intact in the cells that are treated with cytotoxic doses of RNase, and the RNase may degrade RNA even during the cell lysing step. However, several recent reports identified DEGs in cytotoxic RNase-treated cells using microarray technology. These experiments were carried out in very strict conditions, such as including only RNA with acceptable concentrations and $A_{260/280}$ ratios or high RIN values, as it was done in this experiment (32-34). Some of the identified genes whose expression was affected by cSBL treatment were also identified in a microarray examining cells treated with PE5. Since we used resistant cells, the identified DEGs may include genes involved in the resistance to cSBL. However, the decrease in the AKR family detected here was also observed in the short-term treatment of PE5; PE5 is known to reduce the expression of *AKR1A1*, a member of the AKR family (34). Therefore, the downregulation of AKR family members might be a universal response of cancer cells to cytotoxic RNase or involved in the antitumor effects of cytotoxic RNases. The microarray analyses revealed that there were significant pleiotropic changes including those in the expression of multiple genes involved in metabolic pathways in cSBL-resistant cells (Table SIII). Some of these metabolic pathway related genes are listed among the top 20 list of genes up- or down-regulated in cSR cells (Table SI). Among the up-regulated genes, the increase in expression of *LIPC* which catalyzes the hydrolysis of triglycerides and phospholipids (45), was the highest (934.8 fold higher in cSR cells, Table SI). *ST6GAL2*, which showed the third largest change (126.7 fold higher in cSR cells, Table SI), is an enzyme that transfers sialic acid from the donor of substrate CMP-sialic acid to galactose containing acceptor substrates (46). It is interesting to note that the expression

level of this enzyme was elevated, because the presence of sialic acids at the cell surface is thought to be important for the effect of cSBL (20). In this study, because we found that the expressions of some AKR family members were affected in cSR cells, further investigations were focused mainly on strongly downregulated genes in cSR cells.

The AKR superfamily is a family of enzymes that reversibly reduce carbonyl groups (47). These proteins catalyze a variety of metabolic oxidation-reduction reactions, including reduction of glucose, glucocorticoids, small carbonyl metabolites, glutathione conjugates, and phospholipid aldehydes (48). More than 150 proteins belonging to this superfamily are classified into 15 families (AKR1 to AKR15) based on the similarity of amino acid sequences. Each family is further subdivided into subfamilies, which have 60% or higher similarity at the amino acid level (47). The largest family, AKR1, is subdivided into six subfamilies (AKR1A, AKR1B, AKR1C, AKR1D, AKR1E, and AKR1G). In humans, there are 14 AKR superfamily proteins, nine of which belong to the AKR1 family (49). Our microarray analysis revealed that multiple AKR genes were downregulated in cSR cells. In addition, when we focused on AKR1B10, which is involved in resistance to anticancer drugs and has attracted attention as a new target in cancer therapy (49), we found that its expression was significantly reduced at the protein level in cSR cells. AKR1B10 has been reported to be overexpressed in lung cancer (50), liver cancer (51,52), breast cancer (50), pancreatic cancer (53), and oral squamous cell carcinoma (54). One of the roles of AKR1B10 in cancer cells is to suppress the production of retinoic acid, a cell differentiation-promoting factor. Retinoic acid is produced from retinol via retinal and binds to the nuclear receptors, retinoic acid receptor and retinoid X receptor, to promote cell differentiation (55). AKR1B10 is thought to promote cancer cell proliferation and survival by reducing retinal to retinol, thereby decreasing intracellular retinoic acid production (56,57). In addition, AKR1B10 promotes cancer cell survival by reducing cytotoxic aldehydes produced by lipid peroxidation, such as 4-hydroxynonenal (58,59), and is involved in resistance to anticancer drugs such as cisplatin, mitomycin C, anthracyclines (doxorubicin and idarubicin), and docetaxel (60-62). Therefore, AKR1B10 has potential not only as a cancer biomarker but also as a novel therapeutic target for cancer treatment and may promote chemosensitization. Although reports on AKR1B10 in MPM are very limited, AKR1B10 may also be associated with malignancy in MPM, as in the other cancer cases indicated above. A study aimed to search for novel biomarkers in malignant mesothelioma performed by Mundt *et al* (63), identified that AKR1B10 was one of the prognostic mesothelioma biomarker candidates. Patients with high AKR1B10 levels had a mean survival time that was 5.5 months shorter than that in patients with low AKR1B10 expression levels (5.5 vs. 11.0 months, respectively; N=14 for high and 13 for low expression level). Usami *et al* (64) established two morphologically distinct MPM cell lines, Y-MESO-8A (epithelial-like) and Y-MESO-8D (spindle-like) from the same patient. Microarray analysis to determine differences in gene expression in these cells showed that the expression of *AKR1B10* and *AKR1C3* in Y-MESO-8D were 17.8 and 6.35 times higher, respectively, than that of Y-MESO-8A (64). Another report showed that

under serum starvation conditions, AKT was phosphorylated in Y-MESO-8D but not in Y-MESO-8A (65). However, there are no reports related to the function of AKR1B10 in those cells. Detailed investigations focusing on the function of AKR1B10 in MPM are needed. It is interesting to note that decreased AKR1B10 expression was observed at the protein level in cells established by long-term exposure to cSBL. It is possible that cSBL could be used to promote chemosensitivity to anticancer drugs. Indeed, Toyooka and Hayakawa's group has succeeded in developing a novel AKR1B10 inhibitor that suppressed cisplatin resistance in non-small cell lung cancer cells. It also blocked the proliferative and metastatic potential in these cells (66). Now we are working on the comprehensive investigation of the effect of cSBL on AKR family including impact of several anticancer drugs in cSR cells.

In addition to *AKR1B10*, the expression levels of *AKR1B1*, *AKR1C1*, *AKR1C3* and *AKR1C4* were reduced in cSR, and it has also been reported that they were involved in resistance to cisplatin, daunorubicin or DOX (52,67,68). Furthermore, we found that the expression of some members of the ATP-binding cassette (ABC) transporter superfamily, which contributed to chemotherapeutic resistance, was reduced in cSR cells (Table SIV). In humans, there are 49 known ABC genes classified into seven different families (A-G) depending on their amino acid sequence (68). They serve a variety of functions other than drug resistance and can be expressed as channels, receptors and transporters (69). The members involved in drug efflux from human cells do not belong to one particular family (69). Among the ABC transporters found to be reduced in cSR cells, ABCC2 has been reported to contribute to resistance against methotrexate, doxorubicin, cisplatin (68), and ABCA1 is responsible for transporting cholesterol and phospholipids (70), but has also been reported to contribute to resistance to Nitidine, a cytotoxic benzophenanthridine alkaloid (71). Shukla *et al* reported that several ABC transporter genes were endogenously overexpressed in three MPM cell lines as compared to untransformed LP9/TERT1 mesothelial cells (ABCB1 in MO, ABCC3 in ME-26, and ABCA2, ABCC5 and ABCA7 in HMESO cells) (9). Hudson *et al* (72) compared expression of genes involved in the response to chemotherapy between II-45 rat MPM cells and normal 4/4 RM.4 mesothelial cells, and between established chemo-resistant cell lines and parental II-45 cells, respectively. They found that ABCB1 and ABCG2 were endogenously overexpressed in II-45 MPM cells compared to 4/4 RM.4 normal cells; furthermore, levels of ABCB1 in cisplatin resistant II-45 cells, and ABCC2 in pemetrexed or combination (cisplatin plus pemetrexed) resistant II-45 cells were significantly increased compared to parental II-45 cells. Those reports indicate that although the molecular species which are involved in the chemoresistance differ depending on the cell type, ABC transporter superfamily members are associated with inherent and acquired drug resistance in MPM. Furthermore, ABCB5 is now considered as one of a therapeutic target in MPM, because ABCB5 is upregulated in MPM-initiating cells generated from primary MPM samples (73). Our previous studies have shown that cSBL had a stronger apoptosis-inducing effect on multidrug resistant K562 leukemia cells that overexpressed ABCB1 than on their parent K562 cells (27). Since we found that the expression of *ABCC2* was reduced in cSR, it was suggested that cSBL was effective

against MPM regardless of intrinsic drug resistance and may be able to reduce MPM resistance to chemotherapeutic agents that are substrates for ABCC2. Indeed, although the difference was not statistically significant in our experimental conditions, cSR-A1 tended to be more sensitive to DOX (Fig. 2).

In conclusion, we found that long-term treatment with cSBL affected malignant mesothelioma cells by dysregulating multiple genes. The detected DEGs may include genes other than those directly affected by the cSBL application. Currently, examinations of the direct effect of cSBL treatment and combination research with other drugs are being conducted. Because cSBL significantly reduced the expression of AKR family members, especially AKR1B10, it may offer new possibilities for cancer therapy. We believe that investigation of other genes whose expression was changed in cSR cells will further elucidate the antitumor effect of cSBL. Furthermore, by enhancing the effect of cSBL itself and searching for effective concomitant drugs using information obtained in this study, our results can be expected to lead to the establishment of novel, more effective cancer treatments.

Acknowledgements

Not applicable.

Funding

This research was funded by a Grant-in-Aid for Young Scientists (B) (grant no. 17K15029) to Takeo Tatsuta.

Availability of data and materials

The datasets used and/or analyzed in the current study are available from the corresponding author on reasonable request.

Authors' contributions

TT and MH conceived and designed the study. TT, AN and SS acquired and analyzed the data. TT and MH confirmed the authenticity of all the raw data. TT prepared the draft of the manuscript, including the figures. All authors read and approved the final manuscript.

Ethics approval and consent to participate

Not applicable.

Patient consent for publication

Not applicable.

Competing interests

The authors declare that they have no competing interests.

References

1. Cakiroglu E and Senturk S: Genomics and functional genomics of malignant pleural mesothelioma. *Int J Mol Sci* 21: 6342, 2020.
2. Cugell DW and Kamp DW: Asbestos and the pleura: A review. *Chest* 125: 1103-1117, 2004.
3. Thanh TD, Van Tho N, Lam NS, Dung NH, Tabata C and Nakano Y: Simian virus 40 may be associated with developing malignant pleural mesothelioma. *Oncol Lett* 11: 2051-2056, 2016.
4. Farioli A, Ottone M, Morganti AG, Compagnone G, Romani F, Cammelli S, Mattioli S and Violante FS: Radiation-induced mesothelioma among long-term solid cancer survivors: A longitudinal analysis of SEER database. *Cancer Med* 5: 950-959, 2016.
5. Yap TA, Aerts JG, Popat S and Fennell DA: Novel insights into mesothelioma biology and implications for therapy. *Nat Rev Cancer* 17: 475-488, 2017.
6. Van Meerbeeck JP, Gaafar R, Manegold C, Van Klaveren RJ, Van Marck EA, Vincent M, Legrand C, Bottomley A, Debruyne C, Giaccone G, *et al*: Randomized phase III study of cisplatin with or without raltitrexed in patients with malignant pleural mesothelioma: An intergroup study of the European organisation for research and treatment of cancer lung cancer group and the National Cancer Institute. *J Clin Oncol* 23: 6881-6889, 2005.
7. Vogelzang NJ, Rusthoven JJ, Symanowski J, Denham C, Kaukel E, Ruffie P, Gatzemeier U, Boyer M, Emri S, Manegold C, *et al*: Phase III study of pemetrexed in combination with cisplatin versus cisplatin alone in patients with malignant pleural mesothelioma. *J Clin Oncol* 21: 2636-2644, 2003.
8. Wright K: FDA approves nivolumab plus ipilimumab for the treatment of advanced HCC. *Oncology (Willist Park)* 34: 693606, 2020.
9. Shukla A, Hillegass JM, MacPherson MB, Beuschel SL, Vacek PM, Pass HI, Carbone M, Testa JR and Mossman BT: Blocking of ERK1 and ERK2 sensitizes human mesothelioma cells to doxorubicin. *Mol Cancer* 9: 314, 2010.
10. Pouliquen DL, Nawrocki-Raby B, Nader J, Blandin S, Robard M, Birembaut P and Grégoire M: Evaluation of intracavitary administration of curcumin for the treatment of sarcomatoid mesothelioma. *Oncotarget* 8: 57552-57573, 2017.
11. Makarov AA and Ilinskaya ON: Cytotoxic ribonucleases: Molecular weapons and their targets. *FEBS Lett* 540: 15-20, 2003.
12. Fang EF and Ng TB: Ribonucleases of different origins with a wide spectrum of medicinal applications. *Biochim Biophys Acta* 1815: 65-74, 2011.
13. Wus Y, Mikulski SM, Ardeli W, Rybakt SM and Youlet RJ: A cytotoxic ribonuclease. *J Biol Chem* 268: 10686-10693, 1993.
14. Bosch M, Benito A, Ribó M, Puig T, Beaumelle B and Vilanova M: A nuclear localization sequence endows human pancreatic ribonuclease with cytotoxic activity. *Biochemistry* 43: 2167-2177, 2004.
15. Balandin TG, Edelweiss E, Andronova NV, Treshalina EM, Sapozhnikov AM and Deyev SM: Antitumor activity and toxicity of anti-HER2 immunoRNase scFv 4D5-dibarnase in mice bearing human breast cancer xenografts. *Invest New Drugs* 29: 22-32, 2011.
16. Nitta K, Ozaki K, Tsukamoto Y, Hosono M, Ogawakono Y, Kawauchi H, Takayanagi Y, Tsuiki S and Hakomori S: Catalytic lectin (leczyme) from bullfrog (*Rana catesbeiana*) eggs: Mechanism of tumoricidal activity. *Int J Oncol* 9: 19-23, 1996.
17. Nitta K, Takayanagi G, Kawauchi H and Hakomori S: Isolation and characterization of *Rana catesbeiana* lectin and demonstration of the lectin-binding glycoprotein of rodent and human tumor cell membranes. *Cancer Res* 47: 4877-83, 1987.
18. Nitta K, Ozaki K, Tsukamoto Y, Furusawa S, Ohkubo Y, Takimoto H, Murata R, Hosono M, Hikichi N, Sasaki K, *et al*: Characterization of a *Rana catesbeiana* lectin-resistant mutant of leukemia P388 cells. *Cancer Res* 54: 928-934, 1994.
19. Titani K, Takio K, Kuwada M, Nitta K, Sakakibara F, Kawauchi H, Takayanagi G and Hakomori S: Amino acid sequence of sialic acid binding lectin from frog (*Rana catesbeiana*) eggs. *Biochemistry* 26: 2189-2194, 1987.
20. Nitta K, Ozaki K, Ishikawa M, Furusawa S, Hosono M, Kawauchi H, Sasaki K, Takayanagi Y, Tsuiki S and Hakomori S: Inhibition of cell proliferation by *Rana catesbeiana* and *Rana japonica* lectins belonging to the ribonuclease superfamily. *Cancer Res* 54: 920-927, 1994.
21. Tatsuta T, Sugawara S, Takahashi K, Ogawa Y, Hosono M and Nitta K: Cancer-selective induction of apoptosis by leczyme. *Front Oncol* 4: 139, 2014.
22. Tatsuta T, Hosono M, Ogawa Y, Inage K, Sugawara S and Nitta K: Downregulation of Hsp70 inhibits apoptosis induced by sialic acid-binding lectin (leczyme). *Oncol Rep* 31: 13-18, 2014.

23. Tatsuta T, Sugawara S, Takahashi K, Ogawa Y, Hosono M and Nitta K: Leczyme: A new candidate drug for cancer therapy. *Biomed Res Int* 2014; 421415, 2014.
24. Chen JN, Yang GT, Lin YF, Chou PL, Wu TK, Chang WJ, Chen C and Yu YL: *Rana catesbeiana* ribonuclease induces cell apoptosis via the caspase-9/-3 signaling pathway in human glioblastoma DBTRG, GBM8901 and GBM8401 cell lines. *Oncol Lett* 9: 2471-2476, 2015.
25. Tatsuta T, Sato S, Sato T, Sugawara S, Suzuki T, Hara A and Hosono M: Sialic acid-binding lectin from bullfrog eggs exhibits an anti-tumor effect against breast cancer cells including triple-negative phenotype cells. *Molecules* 23: 2714, 2018.
26. Tatsuta T, Satoh T, Sugawara S, Hara A and Hosono M: Sialic acid-binding lectin from bullfrog eggs inhibits human malignant mesothelioma cell growth in vitro and in vivo. *PLoS One* 13: e0190653, 2018.
27. Tatsuta T, Hosono M, Sugawara S, Kariya Y, Ogawa Y, Hakomori S and Nitta K: Sialic acid-binding lectin (leczyme) induces caspase-dependent apoptosis-mediated mitochondrial perturbation in Jurkat cells. *Int J Oncol* 43: 1402-1412, 2013.
28. Tatsuta T, Hosono M, Miura Y, Sugawara S, Kariya Y, Hakomori S and Nitta K: Involvement of ER stress in apoptosis induced by sialic acid-binding lectin (leczyme) from bullfrog eggs. *Int J Oncol* 43: 1799-1808, 2013.
29. Kariya Y, Tatsuta T, Sugawara S, Kariya Y, Nitta K and Hosono M: RNase activity of sialic acid-binding lectin from bullfrog eggs drives antitumor effect via the activation of p38 MAPK to caspase-3/7 signaling pathway in human breast cancer cells. *Int J Oncol* 49: 1334-1342, 2016.
30. Tatsuta T, Hosono M, Takahashi K, Omoto T, Kariya Y, Sugawara S, Hakomori S and Nitta K: Sialic acid-binding lectin (leczyme) induces apoptosis to malignant mesothelioma and exerts synergistic antitumor effects with TRAIL. *Int J Oncol* 44: 377-384, 2014.
31. Satoh T, Tatsuta T, Sugawara S, Hara A and Hosono M: Synergistic anti-tumor effect of bullfrog sialic acid-binding lectin and pemetrexed in malignant mesothelioma. *Oncotarget* 8: 42466-42477, 2017.
32. Altomare DA, Rybak SM, Pei J, Maizel JV, Cheung M, Testa JR and Shogen K: Onconase responsive genes in human mesothelioma cells: Implications for an RNA damaging therapeutic agent. *BMC Cancer* 10: 34, 2010.
33. Vert A, Castro J, Ribó M, Benito A and Vilanova M: Activating transcription factor 3 is crucial for antitumor activity and to strengthen the antiviral properties of Onconase. *Oncotarget* 8: 11692-11707, 2017.
34. Vert A, Castro J, Ribó M, Benito A and Vilanova M: A nuclear-directed human pancreatic ribonuclease (PE5) targets the metabolic phenotype of cancer cells. *Oncotarget* 7: 18309-18324, 2016.
35. Bolstad BM, Irizarry RA, Astrand M and Speed TP: A comparison of normalization methods for high density oligonucleotide array data based on variance and bias. *Bioinformatics* 19: 185-193, 2003.
36. Gentleman R, Carey V, Bates D, Bolstad B, Dettling M, Dudoit S, Ellis B, Gautier L, Ge Y, Gentry J, *et al*: Bioconductor: Open software development for computational biology and bioinformatics. *Genome Biol* 5: R80, 2004.
37. Dudoit S, Gentleman RC and Quackenbush J: Open source software for the analysis of microarray data. *Biotechniques* 34: 496-501, 2003.
38. Edgar R, Domrachev M and Lash AE: Gene Expression Omnibus: NCBI gene expression and hybridization array data repository. *Nucleic Acids Res* 30: 207-210, 2002.
39. Ashburner M, Ball CA, Blake JA, Botstein D, Butler H, Cherry JM, Davis AP, Dolinski K, Dwight SS, Eppig JT, *et al*: Gene ontology: Tool for the unification of biology. *The Gene Ontology Consortium. Nat Genet* 25: 25-29, 2000.
40. The Gene Ontology Consortium: The Gene Ontology Resource: 20 years and still GOing strong. *Nucleic Acids Res* 47: D330-D338, 2019.
41. Kanehisa M: KEGG: Kyoto encyclopedia of genes and genomes. *Nucleic Acids Res* 28: 27-30, 2000.
42. Dennis G Jr, Sherman BT, Hosack DA, Yang J, Gao W, Lane HC and Lempicki RA: DAVID: Database for annotation, visualization, and integrated discovery. *Genome Biol* 4: R60, 2003.
43. Warde-Farley D, Donaldson SL, Comes O, Zuberi K, Badrawi R, Chao P, Franz M, Grouios C, Kazi F, Lopes CT, *et al*: The GeneMANIA prediction server: Biological network integration for gene prioritization and predicting gene function. *Nucleic Acids Res* 38 (Web Server issue): W214-W220, 2010.
44. Balendiran GK, Martin HJ, El-Hawari Y and Maser E: Cancer biomarker AKR1B10 and carbonyl metabolism. *Chem Biol Interact* 178: 134-137, 2009.
45. Thuren T: Hepatic lipase and HDL metabolism. *Curr Opin Lipidol* 11: 277-283, 2000.
46. Takashima S, Tsuji S and Tsujimoto M: Characterization of the second type of human beta-galactoside alpha 2,6-sialyltransferase (ST6Gal II), which sialylates Galβ1,4GlcNAc structures on oligosaccharides preferentially: Genomic analysis of human sialyltransferase genes. *J Biol Chem* 277: 45719-45728, 2002.
47. Jez JM, Flynn TG and Penning TM: A nomenclature system for the aldo-keto reductase superfamily. *Adv Exp Med Biol* 414: 579-589, 1997.
48. Barski OA, Tipparaju SM and Bhatnagar A: The aldo-keto reductase superfamily and its role in drug metabolism and detoxification. *Drug Metab Rev* 40: 553-624, 2008.
49. Mindnich RD and Penning TM: Aldo-keto reductase (AKR) superfamily: Genomics and annotation. *Hum Genomics* 3: 362-370, 2009.
50. Fukumoto SI, Yamauchi N, Moriguchi H, Hippo Y, Watanabe A, Shibahara J, Taniguchi H, Ishikawa S, Ito H, Yamamoto S, *et al*: Overexpression of the aldo-keto reductase family protein AKR1B10 is highly correlated with smokers' non-small cell lung carcinomas. *Clin Cancer Res* 11: 1776-1785, 2005.
51. Cao D, Fan ST and Chung SSM: Identification and characterization of a novel human aldose reductase-like gene. *J Biol Chem* 273: 11429-11435, 1998.
52. Distefano JK and Davis B: Diagnostic and prognostic potential of akr1b10 in human hepatocellular carcinoma. *Cancers (Basel)* 11: 486, 2019.
53. Chung YT, Matkowskyj KA, Li H, Bai H, Zhang W, Tsao MS, Liao J and Yang GY: Overexpression and oncogenic function of aldo-keto reductase family 1B10 (AKR1B10) in pancreatic carcinoma. *Mod Pathol* 25: 758-766, 2012.
54. Fang CY, Lin YH and Chen CL: Overexpression of AKR1B10 predicts tumor recurrence and short survival in oral squamous cell carcinoma patients. *J Oral Pathol Med* 48: 712-719, 2019.
55. Huang P, Chandra V and Rastinejad F: Retinoic acid actions through mammalian nuclear receptors. *Chem Rev* 114: 233-254, 2014.
56. Huang L, He R, Luo W, Zhu YS, Li J, Tan T, Zhang X, Hu Z and Luo D: Aldo-Keto reductase family 1 member B10 inhibitors: Potential drugs for cancer treatment. *Recent Pat Anticancer Drug Discov* 11: 184-196, 2016.
57. Ruiz FX, Porté S, Parés X and Farrés J: Biological role of aldo-keto reductases in retinoic acid biosynthesis and signaling. *Front Pharmacol* 3: 58, 2012.
58. Wang C, Yan R, Luo D, Watabe K, Liao DF and Cao D: Aldo-keto reductase family 1 member B10 promotes cell survival by regulating lipid synthesis and eliminating carbonyls. *J Biol Chem* 284: 26742-26748, 2009.
59. Shen Y, Zhong L, Johnson S and Cao D: Human aldo-keto reductases 1B1 and 1B10: A comparative study on their enzyme activity toward electrophilic carbonyl compounds. *Chem Biol Interact* 191: 192-198, 2011.
60. Matsunaga T, Suzuki A, Kezuka C, Okumura N, Iguchi K, Inoue I, Soda M, Endo S, El-Kabbani O, Hara A and Ikari A: Aldo-keto reductase 1B10 promotes development of cisplatin resistance in gastrointestinal cancer cells through down-regulating peroxisome proliferator-activated receptor-γ-dependent mechanism. *Chem Biol Interact* 256: 142-153, 2016.
61. Matsunaga T, Yamane Y, Iida K, Endo S, Banno Y, El-Kabbani O and Hara A: Involvement of the aldo-keto reductase, AKR1B10, in mitomycin-c resistance through reactive oxygen species-dependent mechanisms. *Anticancer Drugs* 22: 402-408, 2011.
62. Zhong L, Shen H, Huang C, Jing H and Cao D: AKR1B10 induces cell resistance to daunorubicin and idarubicin by reducing C13 ketonic group. *Toxicol Appl Pharmacol* 255: 40-47, 2011.
63. Mundt F, Johansson HJ, Forshed J, Arslan S, Metintas M, Dobra K, Lehtiö J and Hjerpe A: Proteome screening of pleural effusions identifies galectin 1 as a diagnostic biomarker and highlights several prognostic biomarkers for malignant mesothelioma. *Mol Cell Proteomics* 13: 701-715, 2014.
64. Usami N, Fukui T, Kondo M, Taniguchi T, Yokoyama T, Mori S, Yokoi K, Horio Y, Shimokata K, Sekido Y and Hida T: Establishment and characterization of four malignant pleural mesothelioma cell lines from Japanese patients. *Cancer Sci* 97: 387-394, 2006.

65. Suzuki Y, Murakami H, Kawaguchi K, Taniguchi T, Fujii M, Shinjo K, Kondo Y, Osada H, Shimokata K, Horio Y, *et al*: Activation of the PI3K-AKT pathway in human malignant mesothelioma cells. *Mol Med Rep* 2: 181-188, 2009.
66. Endo S, Xia S, Suyama M, Morikawa Y, Oguri H, Hu D, Ao Y, Takahara S, Horino Y, Hayakawa Y, *et al*: Synthesis of potent and selective inhibitors of Aldo-Keto reductase 1B10 and their efficacy against proliferation, metastasis, and cisplatin resistance of lung cancer cells. *J Med Chem* 60: 8441-8455, 2017.
67. Pleblich M, Soldan M, Hungerer C, Koch L and Maser E: Increased resistance of tumor cells to daunorubicin after transfection of cDNAs coding for anthracycline inactivating enzymes. *Cancer Lett* 255: 49-56, 2007.
68. Shiiba M, Yamagami H, Yamamoto A, Minakawa Y, Okamoto A, Kasamatsu A, Sakamoto Y, Uzawa K, Takiguchi Y and Tanzawa H: Mefenamic acid enhances anticancer drug sensitivity via inhibition of aldo-keto reductase 1C enzyme activity. *Oncol Rep* 37: 2025-2032, 2017.
69. Vasiliou V, Vasiliou K and Nebert DW: Human ATP-binding cassette (ABC) transporter family. *Hum Genomics* 3: 281-290, 2009.
70. Pasello M, Giudice AM and Scotlandi K: The ABC subfamily A transporters: Multifaceted players with incipient potentialities in cancer. *Semin Cancer Biol* 60: 57-71, 2020.
71. Iwasaki H, Okabe T, Takara K, Yoshida Y, Hanashiro K and Oku H: Down-regulation of lipids transporter ABCA1 increases the cytotoxicity of nitidine. *Cancer Chemother Pharmacol* 66: 953-959, 2010.
72. Hudson AL, Weir C, Moon E, Harvie R, Klebe S, Clarke SJ, Pavlakis N and Howell VM: Establishing a panel of chemo-resistant mesothelioma models for investigating chemo-resistance and identifying new treatments for mesothelioma. *Sci Rep* 4: 6152, 2014.
73. Milosevic V, Kopecka J, Salaroglio IC, Libener R, Napoli F, Izzo S, Orecchia S, Ananthanarayanan P, Bironzo P, Grosso F, *et al*: Wnt/IL-1 β /IL-8 autocrine circuitries control chemoresistance in mesothelioma initiating cells by inducing ABCB5. *Int J Cancer* 146: 192-207, 2020.



This work is licensed under a Creative Commons Attribution-NonCommercial-NoDerivatives 4.0 International (CC BY-NC-ND 4.0) License.

<細胞制御学>

教授 顧 建国

准教授 福田 友彦

准教授 伊左治 知弥

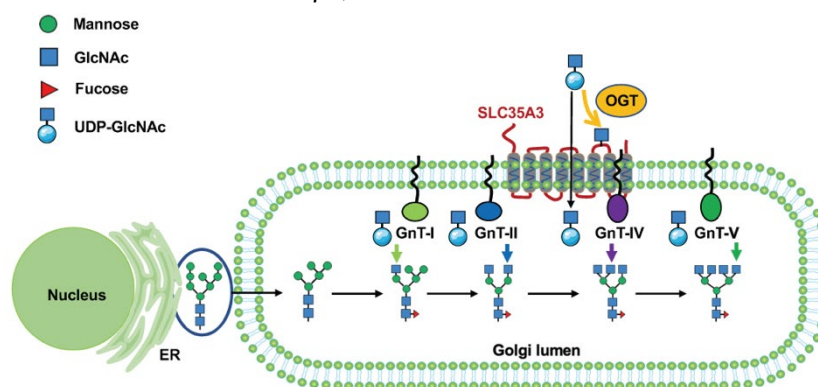
助教 黒田 喜幸

糖鎖間の相互作用と糖鎖生合成の制御機構の解析

糖鎖修飾は、タンパク質の翻訳後修飾の中で最も多く、哺乳動物細胞において普遍かつ重要なプロセスである。糖鎖の変化は癌や糖尿病を含む多くの疾患の特徴でもある。しかし、糖鎖の生合成に関わる分子機序は必ずしも明らかになっていない。私達は、N型糖鎖と O-GlcNAc 修飾の生合成において共通の糖鎖のドナー基質である UDP-GlcNAc に注目し、これら 2 種類の糖鎖修飾の関係を明らかにした。O-GlcNAc 修飾は O-GlcNAc 転移酵素(OGT)によって Ser/Thr 残基に単一の GlcNAc 残基が UDP-GlcNAc から転移することで生合成される可逆的な修飾である。一方、N 型糖鎖は小胞体にてマンノースがトリミングされた後、ゴルジ装置において種々の糖転移酵素によって生合成される複雑な修飾である。私達は、OGT のノックダウン細胞 (OGT-KD) を用いて解析した。O-GlcNAc 修飾の減少は、GlcNAc 分岐型糖鎖を増加させると考えられた。しかし、予想に反して、レクチンブロット、HPLC および質量分析により、分岐型の N-型糖鎖の生成は野生型細胞と比較して OGT-KD で有意に減少していることがわかった。GlcNAc 分岐型の減少がどのような糖鎖構造で生じているのか検討したところ、興味深いことに、この低下したのは GlcNAc 転移酵素 IV (GnT-IV) によって触媒される β 1,4-GlcNAc 分岐型であった。OGT-KD と GnT-IV に触媒される構造特異性の関係を明らかにするため、哺乳動物細胞の主要な UDP-GlcNAc 輸送体である SLC35A3 に焦点を当てて検討した。驚いたことに、SLC35A3 を欠損させた細胞(SLC35A3-KO)では、OGT-KD と同様に β 1,4-GlcNAc 分岐型の N 型糖鎖の生成が有意的に減少し

た。さらに、共免疫沈降実験により、

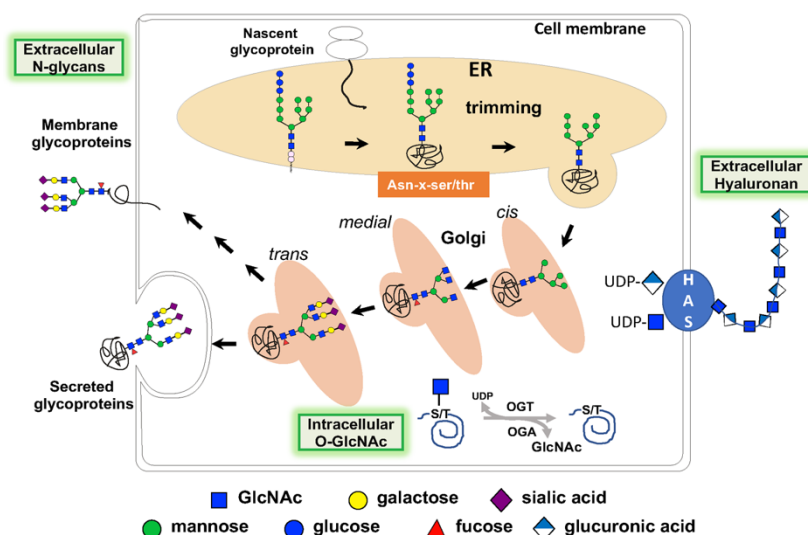
SLC35A3 は GnT-IV と相互作用するが、 β 1,6-GlcNAc 分岐型を触媒する GnT-V とは相互作用しないこ



とが示された。また、ウェスタンブロットおよび化学酵素標識により、OGT が SLC35A3 を修飾し、その修飾が SLC35A3 の安定性向上に大きく寄与することが確認された。さらに、OGT-KD 細胞で観察された現象と同様に、SLC35A3-KO は細胞の伸展を促進し、細胞の遊走と細胞増殖を抑制する。以上の結果は、上図に示したように O-GlcNAc 化を介した OGT-SLC35A3-GnT-IV の相互作用により N-型糖鎖の生合成と機能が特異的に制御されることを示している。本研究は、O-GlcNAc と N 型糖鎖間の cross-talk を初めて明らかにした研究である。現在、シアル酸とフコースの輸送体である SLC35A1 と SLC35C1 に焦点を当て、輸送体の機能と糖鎖修飾との関連にも着目して検討を行っている。

一方、癌化に伴い糖鎖の発現が変化することはよく知られている。例えば、癌細胞における O-GlcNAc や N 型糖鎖の分岐の増加のみならず、ヒアルロン酸の増加も知られている。下図に示すようにこの 3 種類の糖鎖は、UDP-GlcNAc を共通のドナー基質として、OGT、

ヒアルロン酸合成酵素 (HAS) および GlcNAc 転移酵素 (GnT) によってそれぞれ生合成されている。上述のように共通の基質を利用しているため糖鎖の相互関係が示唆されるが、これらの相互作用はよくわからな



い。そこで、私達はこれら 3 つの糖鎖の生合成に相互関係が存在すると作業仮説をたて、検証した。膵癌細胞株である PANC-1 の OGT-遺伝子抑制 (KD) 細胞と HAS2 遺伝子欠損 (KO) 細胞株を樹立し、O-GlcNAc 修飾とヒアルロン酸の生合成を阻害した際、他の糖鎖修飾がどうなるかを検討した。その結果、O-GlcNAc の合成を低下させた OGT-KD 細胞では全体および細胞表面の N 型糖鎖の分岐が著しく減少していたことをレクチンブロットと FACS で明らかにした。さらに、ヒアルロン酸結合タンパクを用いてヒアルロン酸の合成量を検討したところ、有意に増加していた。

一方、ヒアルロン酸の合成を抑制した HAS2KO 細胞において O-GlcNAc 修飾は減少していたが、分岐型 N 型糖鎖の発現に顕著な変化は確認されなかった。これらの結果

から、3つの糖鎖生合成の相互関係はより複雑であることが示唆される。

現在は HPLC を用いた細胞内 UDP-GlcNAc 濃度の変化の解析を行っている。さらに複合型及び混成型 N 型糖鎖の合成の鍵となる反応を触媒する酵素を欠損させた GnT-I KO 細胞の樹立を行い、分岐型糖鎖の生合成が阻害された際のヒアルロン酸と O-GlcNAc 修飾の変化の検討を行うことで3種類の糖鎖生合成の相互関係を明らかにしようとしている。

<論文発表>

1. Regulation of hyaluronan production by $\beta 2$ adrenergic receptor signaling. Kuroda, Y. and Higashi, H. *Biochem. Biophys. Res. Commun.* 575, 50-55, 2021
2. $\alpha 1,6$ -Fucosyltransferase contributes to cell migration and proliferation as well as to cancer stemness features in pancreatic carcinoma. Liang C., Fukuda, T., Isaji, T., Duan, C., Song, W., Wang, Y. and Gu, J. *Biochim Biophys Acta Gen Subj.*, 1865, 3239-3252, 2021
3. Loss of core fucosylation suppressed the humoral immune response in Salmonella typhimurium infected mice. Zahid, D., Zhang, N., Fang, H., Gu, J., Li, M. and Li, W. *J. Microbiol. Immunol. Infect.* 54, 606-615, 2021
4. N-linked Glycans in the Epithelial-Mesenchymal Transition: Implications for Cancer Metastasis. Gu, J. *Comprehensive Glycoscience* 2nd edition, Elsevier, 440-443, 2021
5. O-GlcNAcylation Regulates $\beta 1,4$ -GlcNAc-branched N-glycan Biosynthesis Via the OGT/SLC35A3/GnT-IV Axis. Song, W., Isaji, T., Nakano, M., Liang C., Fukuda, T. and Gu, J. *FASEB J.*, 36: e22149. doi: 10.1096/fj.202101520R. 2022

<学会発表>

糖鎖によるインテグリンとその下流分子の機能制御と特異性

顧建国, 第1回オルガネラゾーン 研究会, Web 開催, 2021 年 6 月

膵がん細胞のがん幹細胞性の獲得と細胞移動・増殖における FUT8 の役割

梁 彩霞, 福田 友彦, 伊左治 知弥, 黒田 喜幸, 顧 建国

第15回東北糖鎖研究会, Web 開催, 2021 年 9 月, P. 10

O-GlcNAcylation Regulates β 1,4-GlcNAc-branched N-glycan Biosynthesis Via the OGT/SLC35A3/GnT-IV Axis

宋 万里, 伊左治 知弥, 中の 三弥子, 福田 友彦, 黒田 喜幸, 顧 建国
第 15 回東北糖鎖研究会, Web 開催, 2021 年 9 月, P. 26

ゴルジ体における N-型糖鎖の多様性の制御とその意義

伊左治 知弥

第 19 回生物化学若手研究者セミナー, Web 開催, 2021 年 10 月

Focal adhesion kinase (FAK)の O-GlcNAc 修飾による細胞接着斑の形成と細胞機能の制御

伊左治 知弥, 大山 嘉順, 孫 玉涵, 福田 友彦, 黒田 喜幸, 顧 建国
第 40 回日本糖質学会年会, 鹿児島, 2021 年 10 月, 3A-11

O-GlcNAcylation regulates β 1,4-GlcNAc-branched N-glycan biosynthesis via the OGT/SLC35A3/GnT-IV Axis

宋 万里, 伊左治 知弥, 中の 三弥子, 福田 友彦, 黒田 喜幸, 顧 建国
第 40 回日本糖質学会年会, 鹿児島, 2021 年 10 月, P-046

Focal adhesion kinase の O-GlcNAc 修飾による細胞機能の制御

伊左治 知弥, 大山 嘉順, 孫 玉涵, 福田 友彦, 黒田 喜幸, 顧 建国
第 94 回日本生化学会, Web 開催, 2021 年 11 月, 1T13m-08 (P-020)

O-GlcNAcylation regulates β 1,4-GlcNAc-branched N-glycan biosynthesis via the OGT/SLC35A3/GnT-IV Axis

宋 万里, 伊左治 知弥, 中の 三弥子, 福田 友彦, 黒田 喜幸, 顧 建国
第 94 回日本生化学会, Web 開催, 2021 年 11 月, 1T13m-08 (P-020)

Regulatory function of glycosylation in cancer and its application

顧 建国

中国科学院西北高原生物研究所学術セミナー, 特別講演, 西寧市 (Web 開催) 2021 年 12 月

N-型糖鎖による膜受容体の機能制御とその特異性

顧建国、第2回オルガネラゾーン 研究会, 東京, 2022 年 3 月

RESEARCH ARTICLE

O-GlcNAcylation regulates β 1,4-GlcNAc-branched N-glycan biosynthesis via the OGT/SLC35A3/GnT-IV axis

Wanli Song¹ | Tomoya Isaji¹ | Miyako Nakano² | Caixia Liang¹ |
 Tomohiko Fukuda¹ | Jianguo Gu¹

¹Division of Regulatory Glycobiology, Institute of Molecular Biomembrane and Glycobiology, Tohoku Medical and Pharmaceutical University, Sendai, Japan

²Graduate School of Integrated Sciences for Life, Hiroshima University, Higashi-hiroshima, Japan

Correspondence

Jianguo Gu, Division of Regulatory Glycobiology, Institute of Molecular Biomembrane and Glycobiology, Tohoku Medical and Pharmaceutical University, 4-4-1 Komatsushima, Aoba-ku, Sendai, Miyagi 981-8558, Japan.
 Email: jgu@tohoku-mpu.ac.jp

Funding information

Japan Society for the Promotion of Science, Grant/Award Number: 19H03184 and 19K07049; Ministry of Education, Culture, Sports, Science, and Technology of Japan, Grant/Award Number: 20H04909

Abstract

N-Linked glycosylation and O-linked N-acetylglucosamine (O-GlcNAc) are important protein post-translational modifications that are orchestrated by a diverse set of gene products. Thus far, the relationship between these two types of glycosylation has remained elusive, and it is unclear whether one influences the other via UDP-GlcNAc, which is a common donor substrate. Theoretically, a decrease in O-GlcNAcylation may increase the products of GlcNAc-branched N-glycans. In this study, via examination by lectin blotting, HPLC, and mass spectrometry analysis, however, we found that the amounts of GlcNAc-branched tri-antennary N-glycans catalyzed by N-acetylglucosaminyltransferase IV (GnT-IV) and tetra-antennary N-glycans were significantly decreased in O-GlcNAc transferase knockdown cells (OGT-KD) compared with those in wild type cells. We examined this specific alteration by focusing on SLC35A3, which is the main UDP-GlcNAc transporter in mammals that is believed to modulate GnT-IV activation. It is interesting that a deficiency of SLC35A3 specifically leads to a decrease in the amounts of GlcNAc-branched tri- and tetra-antennary N-glycans. Furthermore, co-immunoprecipitation experiments have shown that SLC35A3 interacts with GnT-IV, but not with N-acetylglucosaminyltransferase V. Western blot and chemoenzymatic labeling assay have confirmed that OGT modifies SLC35A3 and that O-GlcNAcylation contributes to its stability. Furthermore, we found that SLC35A3-KO enhances cell spreading and suppresses both cell migration and cell proliferation, which is similar to the phenomena observed in the OGT-KD cells. Taken together, these data are the first to demonstrate that O-GlcNAcylation specifically governs the biosynthesis of tri- and tetra-antennary N-glycans via the OGT-SLC35A3-GnT-IV axis.

Abbreviations: 2-AB, 2-aminobenzamide; CRISPR/Cas-9, clustered regularly interspaced short palindromic repeats/caspase-9; DMEM, Dulbecco's modified Eagle's medium; DOX, doxycycline; FBS, fetal bovine serum; GAPDH, glyceraldehyde-3-phosphate dehydrogenase; GnGnbi-PA, pyridylamine-labeled GlcNAc-terminated bi-antennary glycan; GnT-IV, N-acetylglucosaminyltransferase IV; GnT-V, N-acetylglucosaminyltransferase V; GU, glucose units; HBP, hexosamine biosynthetic pathway; KD, knockdown; KO, knockout; PBS, phosphate-buffered saline; shRNA, short hairpin RNA; UDP-GlcNAc, diphosphate β -D-N-acetylglucosamine; VSV, vesicular stomatitis virus glycoprotein; WT, wild type.

This is an open access article under the terms of the Creative Commons Attribution-NonCommercial-NoDerivs License, which permits use and distribution in any medium, provided the original work is properly cited, the use is non-commercial and no modifications or adaptations are made.

© 2022 The Authors. *The FASEB Journal* published by Wiley Periodicals LLC on behalf of Federation of American Societies for Experimental Biology.

KEYWORDS

cell adhesion, GlcNAc branching, *N*-glycan biosynthesis, *O*-GlcNAcylation, SLC35A3

1 | INTRODUCTION

Among multiple post-translational modifications (PTMs), protein glycosylation is a common and important process in cells,^{1–3} and altered glycosylation is a hallmark of many diseases including cancers⁴ and diabetes.⁵ *N*-Glycans are extremely complex and conserved PTMs are found in the secretory pathways of proteins. Thousands of proteins are known to be *N*-glycosylated, which plays a considerable role in processes such as cell-cell and cell-extracellular matrix recognition, the selective localization of proteins, and immune responses.^{2,6,7} Biosynthesis of *N*-glycans in the endoplasmic reticulum (ER) and the Golgi apparatus involves complex machinery and several steps that include enzymatic reactions and transportation. *N*-Glycosylation is often associated with other PTMs such as phosphorylation⁷ and ubiquitination.^{8,9} For example, an increase in *N*-acetylglucosaminyltransferase III (GnT-III) produced by E-cadherin lead to a reduced level of phosphorylation in β -catenin through EGF receptor or Src signaling and contribute to the suppression of cancer metastasis.^{10,11} One of the unique features of *N*-glycans is the GlcNAc-branched complex structure, that is, sequentially synthesized first by *N*-acetylglucosaminyltransferase I (GnT-I) and GnT-II, and then by GnT-III, GnT-IV, or GnT-V to produce functionally diverse *N*-glycosylated proteins. Furthermore, GlcNAc-branched structures are reported to be involved in the pathogenesis of type 2 diabetes,^{5,12,13} and in the growth, invasion, and metastasis of cancers.^{14,15} The loss of GnT-IV provokes endocytosis, which decreases the cell surface residency of Glut2 and contributes to type 2 diabetes.¹² Higher levels of GnT-IV expression have been observed in choriocarcinoma,¹⁶ hepatocarcinoma,¹⁷ and pancreatic cancer,¹⁸ which suggests that production by GnT-IV promotes invasion and metastasis. Another important factor that cannot be ignored in *N*-glycan biosynthesis is UDP-GlcNAc, a donor substrate that is produced by the hexosamine biosynthetic pathway (HBP) as an essential substrate in protein *N*-glycosylation pathways. UDP-GlcNAc is considered to be a nutritional sensor and an important regulator of cell signaling that concerns cell function.^{19,20}

Unlike the complex *N*-glycans that decorate proteins, *O*-GlcNAcylation is a simple protein PTM, where a single moiety of GlcNAc acts on the serine or threonine residue of target proteins without further elongation or modification into more complex structures.^{21–23} *O*-GlcNAcylation is a widespread and dynamic modification that is controlled by only a single pair of enzymes: *O*-GlcNAc transferase

(OGT) and *O*-GlcNAcase (OGA). UDP-GlcNAc as a single substrate is used by OGT for *O*-GlcNAcylation. Previous studies have shown that *O*-GlcNAcylation induces a conformational change that initiates protein folding,²⁴ competes with phosphorylation in the same, or proximal, serine or threonine residual,^{25,26} disrupts protein-protein interactions,^{27,28} serves as a protein recruiting signal,²⁹ and regulates protein stability.^{30,31} Furthermore, *O*-GlcNAcylation plays a fundamental role in chronic diseases such as diabetes, Alzheimer's disease, cardiovascular disease, and cancers.^{25,32–34} Numerous cancer cells show higher levels of *O*-GlcNAcylation, which makes these cancers more aggressive, and noteworthy examples include prostate cancer,³⁵ leukemia,³⁶ breast cancer,³⁷ hepatocellular carcinoma,³⁸ and pancreatic cancer.³⁹ The suppression of OGT expression in breast or colon cancer cells decreases cell migration and invasion.^{40,41}

An increase in the UDP-GlcNAc pool via HBP flux in hyperglycemic cells upregulates *O*-GlcNAcylation⁴² and increases the production of GlcNAc-branched *N*-glycans in mammary carcinoma cells.⁴³ Conversely, the loss of OGT in *Caenorhabditis elegans* caused a more than twofold increase in total UDP-GlcNAc compared with that found in wild type.⁴⁴ Although amounts of UDP-GlcNAc affect *N*-glycosylation as well as *O*-GlcNAcylation, it is unclear whether there is an interplay between *O*-GlcNAcylation and *N*-glycosylation. It would be reasonable to speculate that suppression of *O*-GlcNAcylation should increase amounts of UDP-GlcNAc for *N*-glycosylation pathways, which would increase the production of GlcNAc-branched *N*-glycans. In the present study, however, we found that OGT knockdown did decrease—rather than increase—the production of β 1,4-GlcNAc-branched tri-*N*-glycans catalyzed by GnT-IV. The main molecular mechanism could be explained by the fact that *O*-GlcNAcylation regulates the stability of SLC35A3, a main UDP-GlcNAc transporter, which specifically interacts with GnT-IV. These findings are the first to describe how *O*-GlcNAcylation specifically governs the biosynthesis of tri-antennary *N*-glycans.

2 | MATERIALS AND METHODS

2.1 | Antibodies and reagents

The experiments were performed using the following antibodies: biotinylated *Datura stramonium* agglutinin (DSA; B-1185), Concanavalin A (ConA; B-1005), and

Sambucus nigra agglutinin (SNA; B-1305) ABC kit was acquired from Vector Laboratories; mAb against O-GlcNAc (CTD110.6, 9875S) and a peroxidase-conjugated secondary antibody against rabbit (7074S) were from Cell Signaling Technology. Peroxidase-conjugated secondary antibodies against mouse (AP124P) were from Millipore; mAb against α -tubulin (T6199), an antibody against FLAG (F1804), and anti-FLAG conjugated to agarose (Sigma, A2220), VSV (V5507) and anti-VSV-Glycoprotein-Agarose antibody (A1970) were from Sigma, doxycycline hyclate (D9891) was acquired from Sigma-Aldrich, and cycloheximide (CHX, #037-20991) was purchased from Wako (Tokyo, Japan).

2.2 | Cell lines and cell culture

The HeLa and 293T cells were acquired from the RIKEN Bioresource Research Center (Japan). All cells were cultured in DMEM containing 10% fetal bovine serum (FBS, Gibco) under the standard protocol at 37°C and 5% CO₂.

2.3 | Expression plasmids and transfection

We used the Gateway™ cloning system from Invitrogen for all overexpression experiments. The Gateway™ entry vectors were constructed as follows. The cDNA sequences for SLC35A3 were cloned from HeLa cells then inserted into pENTR/D-TOPO vectors with 2 × VSV or 3 × FLAG at the N terminus using the in-fusion method (Takara Bio Inc.). The cDNA sequences of GnT-IVa and GnT-IVb were cloned from HeLa cells and GnT-V was amplified from GnT-V pENTR/D-TOPO vectors in our lab⁴⁵ and inserted into pENTR/D-TOPO vectors with 3 × FLAG at the C terminus using the in-fusion method. The resultant cDNAs in entry vectors were confirmed by DNA sequencing. Using LR clonase (Invitrogen), the subcloned cDNAs in entry vectors were transferred into pcDNA3.1-RfA for transient expression. Plasmid diagrams for different tagged proteins were shown in Figure S3. Transfection was performed using PEI MAX (molecular mass, 40 kDa; Polysciences Inc.) following the dictates of the United States patent application (number US20110020927A1) with minor modifications. Briefly, before transfection, 3–5 × 10⁶ cells were seeded on either 10- or 6-cm dishes and were then incubated for 24 h. Expression vectors with PEI MAX (1 mg/ml in 0.2 M hydrochloric acid) were pre-incubated for 20 min at a 1:3 ratio in 1 ml of a solution that contained 20 mM CH₃COONa buffer and 150 mM NaCl at pH 4.0. After incubation for 6 h, the conditioned medium was replaced with a normal culture medium for further incubation for 48 h.

2.4 | Lectin blot, immunoprecipitation, and western blot

The labeled cells were washed with cold PBS and then lysed in the cell lysate buffer (20 mM Tris-HCl, pH 7.4, 150 mM NaCl, 1% Triton X-100) with protease and phosphatase inhibitors (Nacalai Tesque, Kyoto, Japan) for 30 min. Protein concentrations were determined using a BCA protein assay kit (Pierce). An equal amount of protein from each sample was loaded to either 7.5% or 15% SDS-PAGE (sodium dodecyl sulfate-polyacrylamide gel electrophoresis) and transferred to PVDF membranes (Millipore Sigma). The samples were then incubated either with the indicated primary and secondary antibodies or with biotinylated lectins as indicated. Immunoreactive bands were detected using either an immobilon Western Chemiluminescent HRP Substrate (Millipore) or a Vectastain ABC kit (Vector Laboratories) according to the manufacturer's instructions. For immunoprecipitation, cell lysates (500–1000 µg) were immunoprecipitated with anti-VSV-Glycoprotein-Agarose (5 µl) or anti-FLAG conjugated agarose (10 µl) at 4°C for 2 h with rotation, and then the immunoprecipitates were washed twice with lysis buffer and subjected either to 7.5% or 15% SDS-PAGE, then transferred to PVDF membranes. The membranes were incubated with primary and secondary antibodies as indicated.

2.5 | PCR for mRNA expression analysis

Total RNA was extracted from the cells using TRIzol Reagent (Invitrogen) according to the manufacturer's instructions. Total RNA (1 µg) was reverse-transcribed using a PrimeScript RT reagent kit (Takara Bio Inc.). The gene expression levels were detected via RT-PCR, and GAPDH was performed as a control. The PCR primer sequences are listed in Table S1. PCR amplification was electrophoresed on 1.5% agarose gel in TAE buffer containing 40 mM Tris-acetate and 1 mM EDTA at pH 8.0. Finally, the DNA ladder was visualized with ethidium bromide staining under UV light. The relative expression levels were obtained by quantifying the intensities of the bands from three independent experiments and then normalized to GAPDH, and the value of WT cells at 4 h was set as 1.

2.6 | Preparation of N-glycans labeled with 2-aminobenzamide (2-AB)

N-Glycan analysis was performed with minor modification, as reported previously.⁴⁶ The cells (4–6 × 10⁷) were homogenized in 1.5 ml of PBS containing a protease

inhibitor mixture (Nacalai Tesque, Kyoto, Japan) using a Potter-Elvehjem homogenizer. The homogenized cell lysates were centrifuged at 1000× g for 10 min at 4°C, and the supernatants were further centrifuged at 100 000× g for 30 min at 4°C. Then precipitates were lysed in 100 µl lysis buffer (20 mM Tris-HCl, pH 7.4, 150 mM NaCl, 50 mM EPPS, 1% Triton X-100) containing protease and phosphatase inhibitors. Protein concentrations were determined using a BCA protein assay kit (Pierce). The same amounts of proteins from each sample (1 mg) were incubated with *N*-Glycosidase F (Takara Bio Inc.) at 37°C for 72 h according to the manufacturer's instructions and then precipitated with cold ethanol at −20°C overnight. After centrifugation at 25 000× g for 20 min, the supernatants containing *N*-glycans were dried via a rotary vacuum evaporator. Those released *N*-glycans were added to Supelclean ENVI-Carb SPE tubes (3.0 ml, 0.25 g; Sigma-Aldrich) and eluted with a mixed solution [50-mM ammonium acetate buffer (pH 7.0)/acetonitrile (40/60)].⁴⁷ After drying, *N*-glycans were incubated with 30 µl of 1 M 2-AB and 0.24 M 2-picoline borane in 10% acetic acid in methanol and purified with HyperSep™ Diol Cartridges (1 ml, 50 mg; Thermo Fisher Scientific).

2.7 | Analysis of *N*-glycans by normal and reversed-phase HPLC

To avoid the complexity of the *N*-glycans produced by sialylation and galactosylation, these *N*-glycans were labeled with 2-AB, treated with α2-3, -6, -8, and -9 neuraminidase A (NEB #P0722, cloned from *Arthrobacter ureafaciens*) and β1-4 galactosidase (NEB #P0745S, cloned from *Streptococcus pneumoniae*), and then analyzed on a normal-phase HPLC system (JASCO) using an amide-80 HILIC column (250 × 4.6 mm; Tosoh). Elution was performed at a flow rate of 0.8 ml/min at 45°C using 0.05% TFA in acetonitrile as solvent A and 0.05% TFA in MilliQ water as solvent B. The column was pre-equilibrated with 30% solvent B, and after injection of a sample for 8 min, the 2-AB-labeled *N*-glycans were separated using a linear gradient of 30%–60% solvent B for 120 min. The 2-AB-labeled *N*-glycans were detected using a fluorescence detector (JASCO) at excitation and emission wavelengths of 330 and 420 nm, respectively. Fractions corresponding to fluorescence peaks were collected and then subjected either to a reversed-phase HPLC or to MS for further analysis. A glucose oligomer ladder (GU) labeled with 2-AB (Agilent) was used as a standard to separate the peaks in the same column under the same conditions, and the GU values are shown at the top of the figure.

ODS-80TM columns (150 × 4.6 mm and 250 × 4.6 mm; Tosoh) were used for reversed-phase HPLC, and elution

was performed at a flow rate of 1.0 ml/min at 55°C using 20-mM ammonium acetate buffer (pH 4.0) as solvent A and the same buffer containing 1% 1-butanol as solvent B. The column was pre-equilibrated with 4% of solvent B, and after injection of a sample for 10 min, the 2-AB-labeled *N*-glycans were separated employing a linear gradient of 4%–100% of solvent B for 60 min. Fractions corresponding to fluorescence peaks were collected and then subjected either to a normal-phase HPLC or to MS for further analysis. The elution patterns of two-dimensional 2-pyridylaminated *N*-glycans on normal and reversed-phase HPLC are very useful for identifying specific *N*-glycan structures.^{48,49} For example, when using normal-phase HPLC, the elution time of β1,4-GlcNAc-branched (tri-antennary) *N*-glycans approximates that of β1,6-GlcNAc-branched (tri'-antennary) *N*-glycans, while those elution times are quite different in reversed-phase HPLC. The elution time for bi-antennary GlcNAc *N*-glycans was between the times for tri'-antennary and tri-antennary GlcNAc *N*-glycans, as shown in Figure S2B.

2.8 | Analysis of *N*-glycan structures by mass spectrometry (MS)

When the 2-AB-labeled *N*-glycans separated using LC (ODS or Amide column)-FD (fluorescence detection) were dried, each dried residue was dissolved using 20 µl of a solution of 0.05% trifluoroacetic acid/50% acetonitrile, and a portion of the solution was used for MS and MS/MS analysis as follows. The 2-AB-labeled *N*-glycans were introduced into an ESI source using an Accela HPLC system (Thermo Fisher Scientific) with an injection volume of 5 µl of a flow solvent solution of 0.05% trifluoroacetic acid/50% acetonitrile with a flow rate of 200 µl/min without column separation. The *N*-glycan structures were analyzed via LTQ Orbitrap XL (hybrid linear ion trap-orbitrap mass spectrometer; Thermo Fisher Scientific). In the MS setting, the voltage of the capillary source was set at 5.0 kV, and the temperature of the transfer capillary was maintained at 330°C. The capillary and tube lens voltages were set at 35 and 130 V, respectively. MS data were obtained in a positive ion mode over a mass that ranged from *m/z* 350 to *m/z* 2500, as measured using orbitrap (resolution, 60 000; mass accuracy, 5 ppm). MS/MS data were obtained via an ion trap (data-dependent top 3, CID). Xcalibur software ver. 2.2. (Thermo Fisher Scientific) was used to analyze the MS and MS/MS data. Monoisotopic masses were assigned with possible monosaccharide compositions using a GlycoMod software tool (the mass tolerance for precursor ions is ±0.005 Da, <https://web.expasy.org/glycomod/>), and the proposed glycan structures were

further verified via annotation using a fragmentation mass-matching approach based on the MS/MS data, although MS/MS data were not sufficiently obtained due to an insufficient quantity. These glycomic raw data and the identification results for glycan-structure analysis by MS were shown in Tables S2 and S3.

2.9 | Chemoenzymatic labeling assay

The chemoenzymatic labeling and biotinylation of proteins in cell lysates were carried out using the Click-iT O-GlcNAc enzymatic labeling system (Invitrogen). Briefly, the whole cell lysate of 293T cells transfected with an expression plasmid for VSV-SLC35A3 was immunoprecipitated and then labeled with labeling enzymes GalT and UDP-GalNAz according to the Click-iT O-GlcNAc enzymatic labeling system protocol (Invitrogen). Labeled proteins were conjugated with an alkyne-biotin compound, once again following the Click-iT protein analysis detection kit protocol (Invitrogen). Control experiments were performed in the absence of GalT and UDP-GalNAz. Biotinylated and control samples were then subjected to 15% SDS-PAGE and transferred to a PVDF membrane for further detection using an ABC kit (Vector Laboratories).

2.10 | Assay for protein stability

Analysis of SLC35A3 stability was carried out using a cycloheximide chase assay, as reported previously.⁵⁰ The inducible OGT-KD-293T cells were transfected with VSV-SLC35A3 for 48 h with or without DOX, and then these cells were cultured with cycloheximide (CHX, #037-20991; Wako, Tokyo, Japan) at a final concentration of 50 µg/ml and harvested at indicated times. The band densities of VSV-SLC35A3 and α -tubulin on western blots were scanned. Normalization was performed by dividing the VSV signal by the α -tubulin signal at each time point to determine the percentage of the initial SLC35A3 level (0 h of CHX treatment with the density at 0 h set as 1).

2.11 | Establishment of SLC35A3-KO HeLa cells

Lenti-CRISPR v2 was a gift from Feng Zhang (Addgene plasmid #52961).⁵¹ The target site on human SLC35A3 Exon 5 (5'-TCAGCTGGTTCTCAATTTGT-3'), which was chosen from the human GeCKOv2 CRISPR knock-out pooled library,⁵² was cloned into the lentiviral expression vector, and the resultant vectors containing

SLC35A3-specific gRNA were confirmed by DNA sequencing. To prepare the viruses, PEI MAX was used to transfect the resultant vector into 293T cells with packaging plasmids. HeLa cells were then infected by the obtained viruses and selected for stable integration with 2 µg/ml puromycin for 72 h. Stable independent clones were isolated using a limiting dilution. The SLC35A5-KO was confirmed by genomic sequences. Genomic DNAs were isolated from several clones of the KO cells, and amplified by PCR using forward primer (5'-AAAGCTCTCCTTTGCACTCC-3') and reverse primer (5'-GACAAGAGCATTGCCAGATATT-3').

2.12 | Enzymatic assays for GnT-IVb and GnT-V

To confirm whether the C-terminally tagged GnT-IVb and GnT-V were still active, enzymatic activities were performed as described previously,⁵³ with minor modification. In brief, 50 µg of enzyme sauces extract from 293T cells transfected with or without (con) expression vector of GnT-IVb or GnT-V, were incubated at 37°C for indicated times with different buffers as described⁵³ containing 20-µM pyridylamine-labeled GlcNAc-terminated biantennary glycan (GnGnbi-PA) and 20 mM UDP-GlcNAc in the total volume of 10 µl. 30 µl of 10 mM EDTA (pH 7.0) or MilliQ water was added after the incubation, and the enzyme reactions were stopped by boiling for 2 min. Then the reaction mixtures were centrifuged at 20 000× g for 15 min at 4°C. We injected 20 µl of the resulting supernatant into an HPLC system equipped with an ODS-80TM column (250 × 4.6 mm; Tosoh) to separate the products and substrates. The products of GnT-IVb were isocratically eluted at a flow rate of 1.2 ml/min at 50°C using 50-mM ammonium acetate buffer (pH 4.0) containing 0.12% 1-butanol. The products of GnT-V were isocratically eluted at a flow rate of 1 ml/min at 55°C using a 20-mM ammonium acetate buffer (pH 4.0) containing 0.1% 1-butanol. Fluorescence was monitored using excitation and emission wavelengths of 320 and 400 nm.

2.13 | Wound-healing assay

A wound was scratched into a confluent cell layer on 6-cm dishes using a 200-µl pipette tip, and after 24 h incubation, the floating cells were gently removed. The cells were further cultured in the medium supplemented with 5% FBS for 24 h. The wound gaps were photographed under a phase-contrast microscope (Olympus, Tokyo, Japan) at 0 and 24 h. The migration distance was evaluated, and then the cell migration rate was quantified relative to the WT (100%).

2.14 | Cell proliferation

Cells were cultured at a rate of 2000 cells per 100 μ l of culture medium per well of 96-well plates and stopped at different times by adding 10 μ l of 5 mg/ml 3-[4,5-dimethylthiazol-2-yl]-2,5-diphenyltetrazolium bromide (MTT; Dojindo, Kumamoto, Japan) with further incubation for 4 h at 37°C. After the removal of the medium, 100 μ l of DMSO (Millipore Sigma) was added to dissolve the resultant formazan crystals within the cells. The optical absorbance was assessed at 490 nm using a microplate reader (SpectraMax® iD5; Molecular Devices). Cell proliferation rates were determined by relative increases (folds) compared with corresponding cells at the replating time (0 h).

2.15 | Statistical analysis

Each experiment included at least three independent procedures. GraphPad Prism® 5.0 software (GraphPad Software, Inc., La Jolla, CA) was used for statistical analysis, and $p < .05$ was considered statistically significant (* $p < .05$; ** $p < .01$; *** $p < .001$; n.s, no significance by two-tail unpaired t -test or the analysis of variance (ANOVA) tests).

3 | RESULTS

3.1 | Changes in the expression levels of GlcNAc-branched *N*-glycans in OGT-KD Cells

First, we used the OGT knockdown (OGT-KD) HeLa cells to investigate *N*-glycan expression via lectin blot. These cells were previously established by the DOX-dependent inducible shRNA KD system in our lab.⁵⁴ O-GlcNAcylation is highly dynamic and often occurs transiently in response to diverse environmental and physiological cues. Hence, lectin blots were performed at several different time points after cell replating. As shown in Figure 1A, the O-GlcNAcylation levels in the wild-type cells (WT) gradually increased at the indicated times, although these levels were persistently suppressed in the OGT-KD cells in the presence of DOX. We believed that a decrease in OGT would increase the production of GlcNAc-branched *N*-glycans in OGT-KD cells. Surprisingly, lectin blot analysis using DSA, which preferentially recognizes β 1,4-linked GlcNAc glycans, showed that the reactive abilities with DSA were decreased in the OGT-KD cells compared with that in WT (Figure 1B). The underlying molecular mechanism for

the increase in O-GlcNAc and DSA staining 48–72 h after replating in the WT cells requires further study. On the other hand, the reactive abilities with ConA lectin (Figure 1C) and SNA lectin (Figure 1D) did not seem to cause significant changes between OGT-KD and WT cells. These results prompted us to investigate whether OGT-KD alters the expression levels of the glycotransferase genes that are involved in the biosynthetic pathways of GlcNAc-branched *N*-glycans. Results obtained from a semi-quantitative RT-PCR using the primers listed in Table S1 showed no significant differences between the WT and OGT-KD cells after each cell replating at indicated times (Figure S1).

3.2 | OGT-KD specifically decreased β 1, NAc-branched tri- and tetra-antennary *N*-glycans

To further identify and characterize the GlcNAc-branched *N*-glycan structures, *N*-glycans were released by the treatment with PNGase F and labeled with 2-aminobenzamide (2-AB), and further treated with sialidase and galactosidase, as described in the section for “Experimental procedures.” The *N*-glycans then were analyzed via normal-phase HPLC, and each peak was subjected to mass spectrometry (MS) analysis. The *N*-glycan structures in each peak were verified, as shown in Figure S2A, and glycan assignments, precursor m/z , and charges observed were shown in Table S2.

To distinguish the products of GlcNAc-branched *N*-glycans catalyzed by GnT-IV or by GnT-V, each corresponding peak separated in normal-phase HPLC was further subjected to reversed-phase HPLC, and peaks 3, 4, and 5 were further confirmed by MS (Table S3). Attempts to verify the proposed glycan structures after reversed-phase HPLC were pursued via annotation using a fragmentation mass-matching approach based on the MS/MS data. Although, the tri-antennary glycans were of low abundance precluding acquiring MS/MS spectra of sufficient quality, the elution patterns of two-dimensional 2-pyridylaminated *N*-glycans on normal and reversed-phase HPLC,^{48,49} verified that peaks 4, 5, and 6 contained tri-, tri⁻, and tetra-antennary *N*-glycans, respectively, as shown in Figure S2B. To directly compare these complex types of *N*-glycans, samples were purified by reversed-phase HPLC to remove the high-mannose types and the remaining types of *N*-glycans were then analyzed via normal-phase HPLC. As shown in Figure 2A, the amounts of β 1,4-GlcNAc-branched (tri-antennary) and tetra-antennary *N*-glycans were lower in OGT-KD cells than in the WT cells. The ratios of tri-antennary or tetra-antennary *N*-glycans versus the sum of the four species

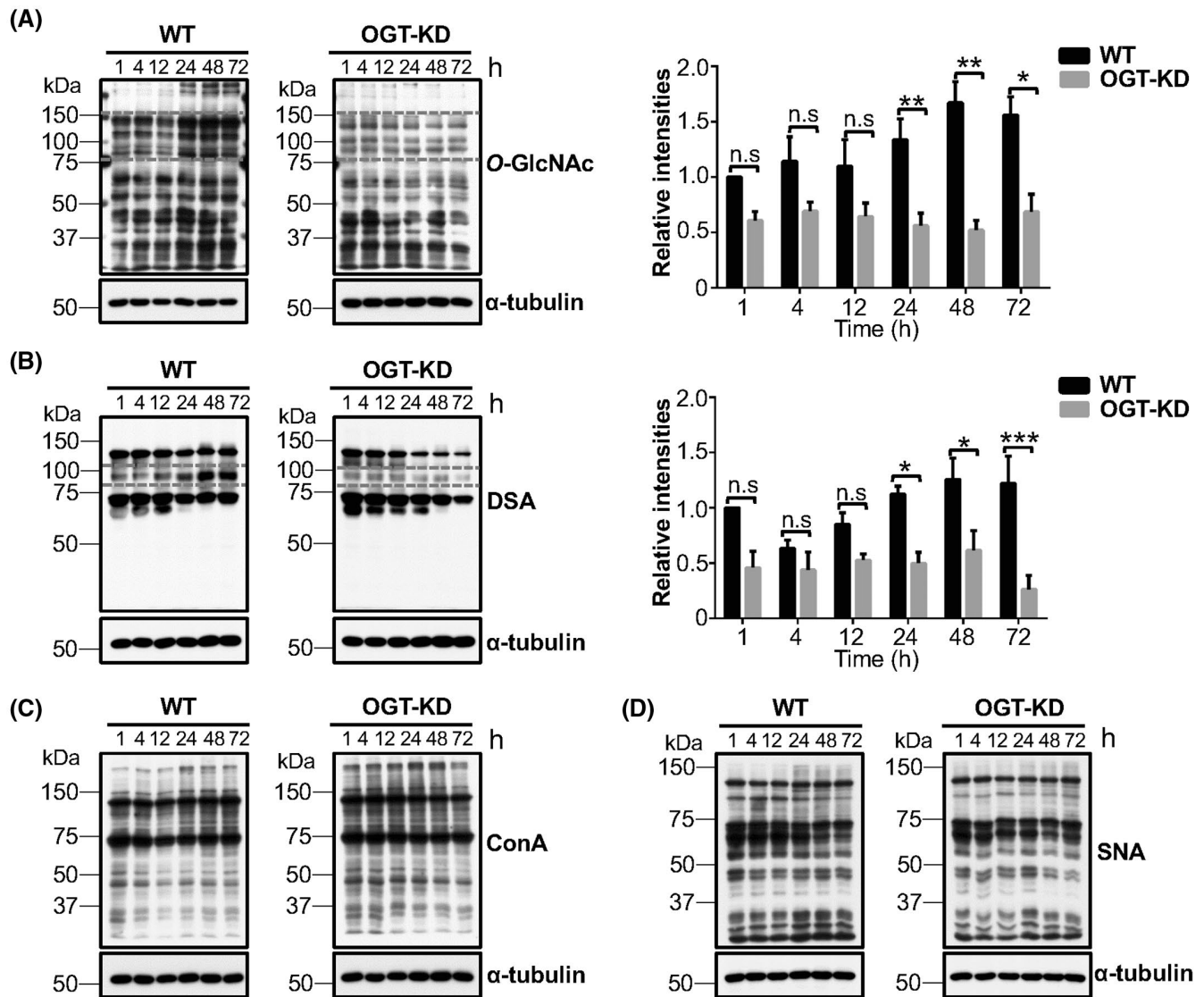


FIGURE 1 Comparison of glycan changes after cell replating at different times between WT and OGT-KD cells. HeLa cells pretreated with (OGT-KD) or without (WT) DOX at 0.1 $\mu\text{g}/\text{ml}$ for 24 h, were seeded on culture dishes and then harvested at different times as indicated. The same amounts of cell lysates were subjected to 7.5% SDS-PAGE gel and stained either with the indicated antibody or with lectins. (A) A representative western blot analyzed by the anti-O-GlcNAc antibody. The relative intensities were obtained by quantifying the intensities of the bands that fell between 75–150 kDa from 3 independent experiments and then normalized to α -tubulin. And the value of WT cells at 1 h was set as 1. Values represent the mean \pm SE. * $p < .05$; ** $p < .01$; *** $p < .001$; n.s, no significance by two-way analysis of variance (ANOVA). (B) Lectin blotting with DSA lectin, which preferentially recognizes β 1-4 GlcNAc-branched glycans. The relative intensities were obtained by quantifying the intensities of the bands that fell between 75–100 kDa from three independent experiments and then normalized to α -tubulin. And the value of WT cells at 1 h was set as 1. Lectin blot analysis with ConA (C) and SNA (D), which preferentially recognizes high mannose types of glycans and α 2,6 sialylated *N*-glycans, respectively

areas for *N*-glycans (bi-, tri-, tri', and tetra-antennary) consistently showed a significant reduction in OGT-KD cells compared with that in the WT cells (Figure 2B). By contrast, the ratios of bi-antennary and β 1,6-GlcNAc-branched (tri'-antennary) *N*-glycans in OGT-KD cells showed a slight increase compared with that in WT cells. The data suggest that O-GlcNAcylation specifically regulates the biosynthesis of tri-antennary *N*-glycans catalyzed by GnT-IV.

3.3 | SLC35A3, a UDP-GlcNAc transporter, was modified by O-GlcNAc

To explore the underlying molecular mechanisms responsible for the effect of O-GlcNAcylation on the expression of tri- and tetra-antennary *N*-glycans, we focused on the UDP-GlcNAc transporter. Previous studies had revealed that deficient UDP-GlcNAc transporter activity caused a decrease in the production of GlcNAc-branched

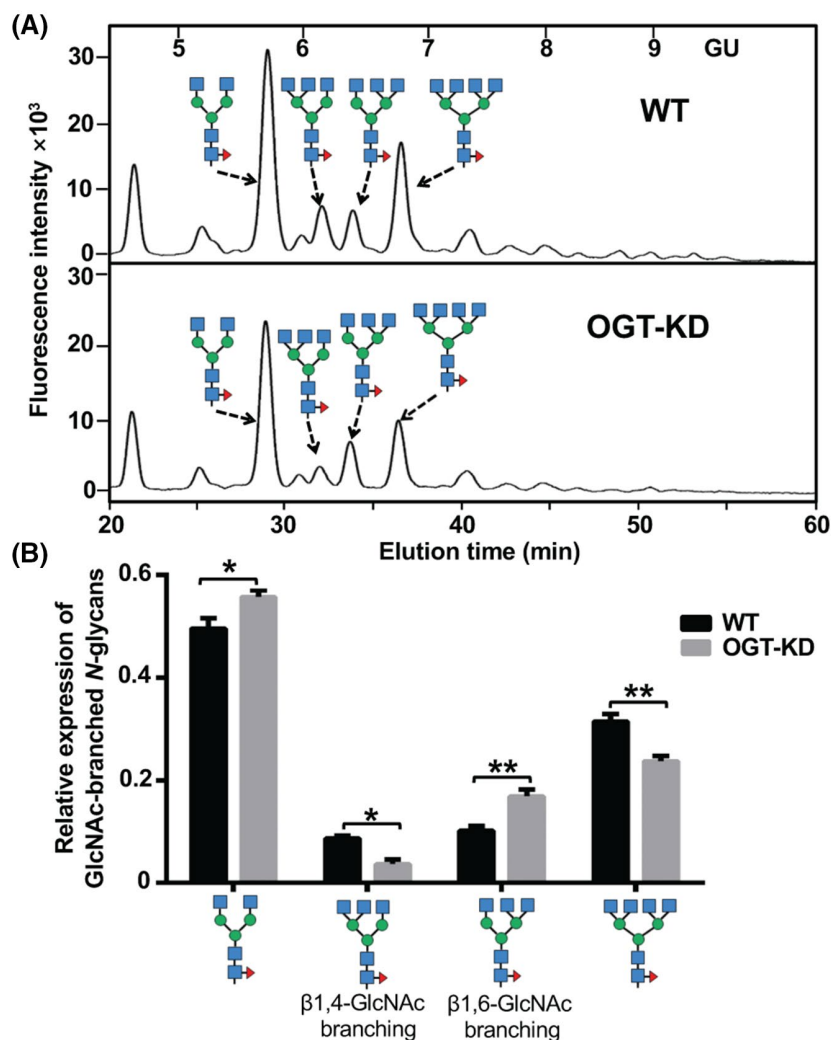


FIGURE 2 Analysis of GlcNAc-branched *N*-glycans isolated from WT and OGT-KD cells. The *N*-glycans labeled with 2-AB were prepared as described in the “Experimental procedures” section. To avoid complexity from sialylation and galactosylation, these *N*-glycans were treated with neuraminidase A and β 1-4 galactosidase and were further purified by reversed-phase HPLC to remove the high mannose types of *N*-glycans. (A) A representative elution pattern for the complex types of major *N*-glycans on a normal-phase HPLC in WT and OGT-KD cells. Based on analysis using mass spectrometry combined with the two-dimensional elution patterns of *N*-glycans on normal and reversed-phase HPLC as described in the “Experimental procedures” section, the major peaks could be assigned as putative *N*-glycan structures. (B) Relative expression of GlcNAc-branched *N*-glycans. The ratio represents each peak area against the sum of the 4 peaks areas (bi-, tri-, tri-, and tetra-antennary *N*-glycans), which was set as 1. The data were obtained from three independent experiments. Values represent the mean \pm SE. * $p < .05$; ** $p < .01$ by two-way analysis of variance (ANOVA)

N-glycans.⁵⁵ In addition, SLC35A3 has been considered one of the main UDP-GlcNAc transporters that play important roles in the biosynthesis of complex *N*-glycans.^{56–58}

Based on the results of those studies, we speculated that the UDP-GlcNAc transporter might be modified by OGT, thereby affecting the biosynthesis of branched *N*-glycans. To test this hypothesis, we constructed an expression vector containing human SLC35A3 tagged with VSV (vesicular stomatitis virus glycoprotein) or FLAG (Figure S3) and overexpressed them in the HeLa, 293T, or DOX-induced OGT-KD 293T cells.⁵⁴ As expected, western

blot analysis showed that SLC35A3 containing either a VSV tag (Figure 3A) or a FLAG tag (Figure S4) containing neither serine nor threonine residue, was detected by the anti-*O*-GlcNAc antibody. *O*-GlcNAcylation levels for SLC35A3 were significantly decreased in OGT-KD cells, compared with those in WT cells (Figure 3A). To further confirm the existence of *O*-GlcNAcylation in SLC35A3, we conducted a chemoenzymatic-labeling assay using an azido-GalNAc sugar, as described in the “Experimental procedures” section, and SLC35A3 was clearly labeled. These data proved that SLC35A3 is an *O*-GlcNAcylated protein (Figure 3B).

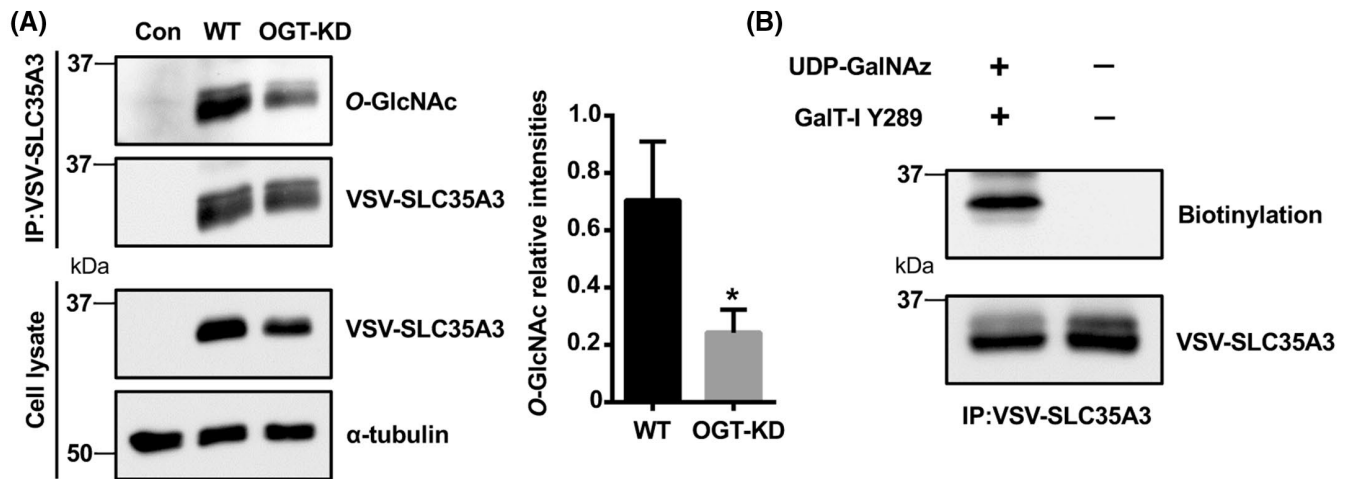


FIGURE 3 Determination of *O*-GlcNAcylation on SLC35A3. (A) 293T cells transfected without (Con) or with VSV-SLC35A3, were incubated without (WT) or with DOX (OGT-KD). The cell lysates and immunoprecipitates (IP) with anti-VSV antibodies were subjected to 15% SDS-PAGE gel and western blotting either with anti-*O*-GlcNAc or the indicated antibodies, respectively. The experiments were independently repeated at least three times. The relative intensity refers to *O*-GlcNAcylated SLC35A3 against total SLC35A3. Values represent the mean \pm SE. * $p < .05$ (two-tail unpaired *t*-test). (B) Confirmation of *O*-GlcNAcylation on SLC35A3. Cell lysates of 293T cells transfected with SLC35A3 were immunoprecipitated (IP) with anti-VSV antibodies, followed by click chemistry labeling of *O*-GlcNAc residues with (+) or without (–) GalT and UDP-GalNAz, and were detected using an ABC kit as described in the “Experimental procedures” section. The experiments were independently repeated at least three times

3.4 | Suppression of *O*-GlcNAcylation in SLC35A3 reduced its stability

Moreover, we found that the *O*-GlcNAcylation of SLC35A3 contributed to its stability. When cells were treated with cycloheximide, a protein synthesis inhibitor, the decay of SLC35A3 in the OGT-KD cells was significantly faster than that in WT cells (Figure 4), which suggests that *O*-GlcNAcylation regulates the synthesis of branched *N*-glycans most likely via the modulation of SLC35A3 stability.

3.5 | Decrease in the expression levels of tri- and tetra-antennary *N*-glycans in SLC35A3 knockout (SLC35A3-KO) cells

To confirm whether regulation of SLC35A3 is a key factor for the decreased expression of tri- and tetra-antennary *N*-glycans in the OGT-KD cells as described above, we established SLC35A3-KO HeLa cells, which were confirmed by DNA sequencing (Figure S5). A representative elution pattern for the four species of *N*-glycans (bi-, tri-, tri', and tetra-antennary) on a normal-phase HPLC appears in Figure 5A. Interestingly, the relative expression levels of tri- and tetra-antennary *N*-glycans, but not the tri'-antennary *N*-glycans, were significantly decreased in the SLC35A3-KO cells compared with those in WT cells (Figure 5B), which is similar to that in OGT-KD cells. By contrast, the ratios of bi-antennary *N*-glycans in

SLC35A3-KO cells showed an increase compared with that in the WT cells. These data further suggest that *O*-GlcNAcylation affects the synthesis of tri- and tetra-antennary *N*-glycans via SLC35A3.

3.6 | SLC35A3 is specifically associated with GnT-IV

To further understand why SLC35A3-KO resulted in a specific decrease in tri-antennary *N*-glycans, but not in tri'-antennary *N*-glycans, we speculated that there could be an interaction between SLC35A3 and GnT-IV. For this purpose, 293T were transiently transfected with plasmids enabling the expressions of SLC35A3 tagged with VSV and GnT-IVa, GnT-IVb, or GnT-V tagged with FLAG. Intriguingly, the immunoprecipitates with anti-VSV antibody contained FLAG-GnT-IVb (Figure 6A) or FLAG-GnT-IVa (Figure S6A), but not FLAG-GnT-V. The interaction between GnT-IVb and SLC35A3 was also confirmed in HeLa cells (Figure S6B). Since GnT-IVa expression is known to be tissue-specific, whereas GnT-IVb is more ubiquitously expressed,^{59,60} so we selected GnT-IVb for further study. The C-terminally tagged GnT-IVb and GnT-V displayed the expected enzymatic activities using pyridylamine-labeled GlcNAc-terminated bi-antennary glycan (GnGnbi-PA) as a substrate (Figure S7). Furthermore, we found that OGT-KD decreased the complex formation between SLC35A3 and GnT-IVb (Figure 6B). Thus, we concluded that OGT regulates

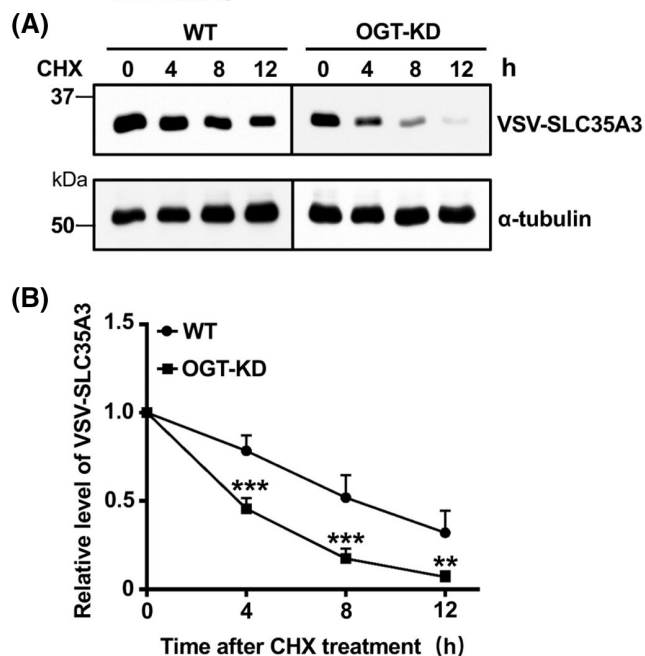


FIGURE 4 Effect of O-GlcNAcylation on SLC35A3 stability. (A) 293T cells were transfected with SLC35A3 and were treated without (WT) or with DOX (OGT-KD). After transfection for 48 h, these cells were treated with cycloheximide (CHX), a protein synthesis inhibitor, for indicated times. Total cell lysates were used for western blotting with an anti-VSV antibody. α -tubulin was used as load control. (B) Quantitative analysis of the turn-over for SLC35A3. The percentage of SLC35A3 at each indicated time point was normalized by comparing the density with that at time 0, and the density at 0 h was set as 1. The data were obtained from three independent experiments. Values represent the mean \pm SE. ** $p < .01$; *** $p < .001$ by two-way analysis of variance (ANOVA)

SLC35A3 stability and SLC35A3-GnT-IVb complex formation, which plays a crucial role in the biosynthesis of tri-antennary N-glycans.

3.7 | OGT-KD and SLC35A3-KO alter cell morphology and inhibit cell migration and proliferation

To gain insight into the roles of OGT in SLC35A3-mediated functions, we further compared the cellular biologic functions between OGT-KD and SLC35A3-KO cells. Our previous study demonstrated that OGT-KD led to an increase in cell spreading and an alteration in the cell shape from elongated spindle shapes to a more rounded morphology.⁵⁴ A similar phenomenon was also observed in the SLC35A3-KO cells (Figure 7A). We further used a wound-healing assay to compare the cell migration and found that the wound closure capabilities of both OGT-KD and SLC35A3-KO cells were significantly suppressed, compared with those in the WT cells

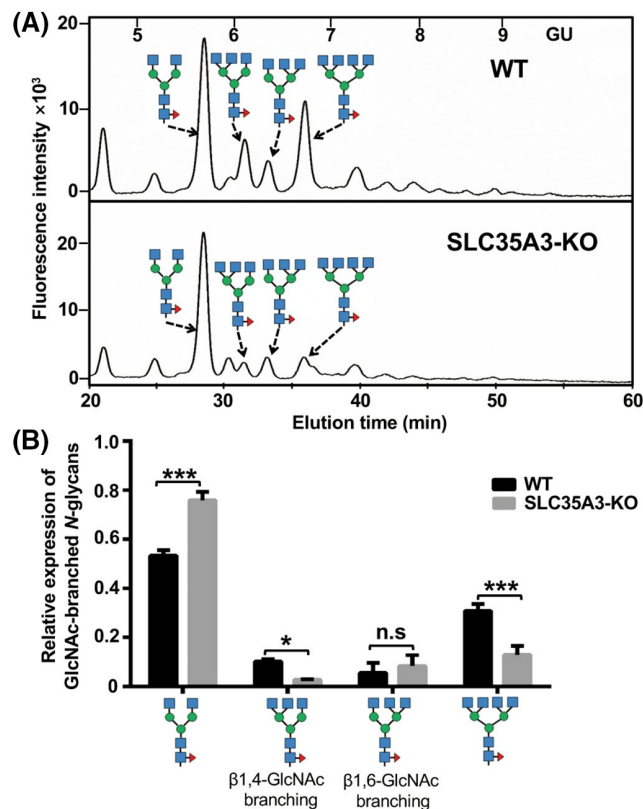


FIGURE 5 Analysis of GlcNAc-branched N-glycans isolated from WT and SLC35A3-KO cells. The methods for the analysis of GlcNAc-branched N-glycans are described in Figure 2. (A) A representative elution pattern for the complex types of major N-glycans on a normal-phase HPLC in WT and SLC35A3-KO cells. (B) Relative expression of GlcNAc-branched N-glycans. Values represent the mean \pm SE. * $p < .05$; *** $p < .001$; n.s., no significance by two-way analysis of variance (ANOVA)

(Figure 7B). Moreover, cell proliferation was also significantly decreased in both OGT-KD and SLC35A3-KO cells compared with that in the WT cells (Figure 7C). Taken together, these data functionally support the existence of a novel regulatory mechanism of O-GlcNAcylation that impacts the biosynthesis of tri-antennary N-glycans via the OGT-SLC35A3-GnT-IV axis.

4 | DISCUSSION

In the present study, we clearly showed that O-GlcNAcylation interacts with N-glycosylation. OGT-KD specifically decreased the biosynthesis of β 1,4-GlcNAc-branched tri- and tetra-antennary N-glycans via SLC35A3, a UDP-GlcNAc transporter, and served as a central hub that specifically interacted with GnT-IV. The suppression of O-GlcNAcylation on SLC35A3 affects its stability and the specific complex formation with GnT-IV, which specifically decreases the biosynthesis

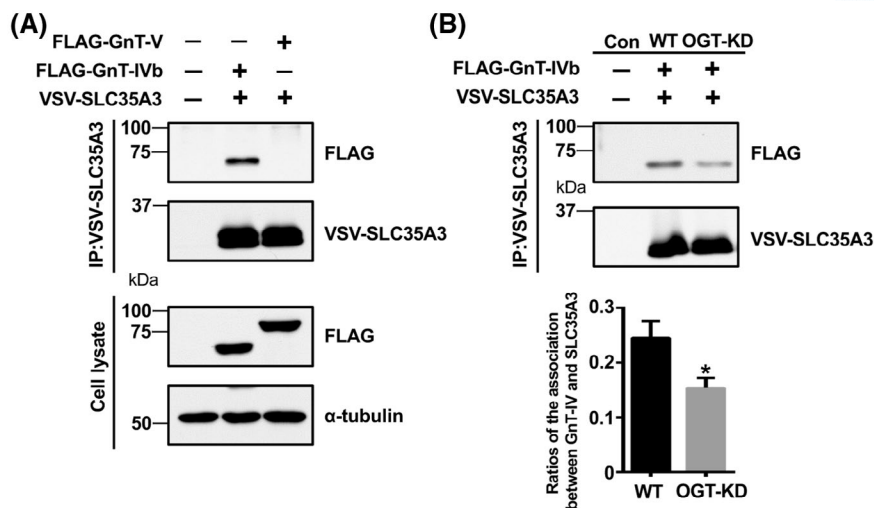


FIGURE 6 Complex formation between SLC35A3 and GnT-IV. (A) 293T cells co-transfected without (–) or with (+) expression vectors containing SLC35A3 and either GnT-IVb or GnT-V, were immunoprecipitated (IP) by the indicated antibodies. The cell lysates and immunoprecipitates were subjected to 7.5% SDS-PAGE gel and blotted with the indicated antibodies, respectively. (B) Effects of OGT-KD on the interaction between SLC35A3 and GnT-IVb. Cell lysates obtained from the WT and OGT-KD 293T cells that were transfected without (Con) or with expression plasmids of SLC35A3 and GnT-IVb were immunoprecipitated (IP) with an anti-FLAG antibody. The immunoprecipitates were blotted with the indicated antibodies. Ratios of SLC35A3 in those immunoprecipitates were quantitatively calculated from three independent experiments. Values represent the mean \pm SE. * $p < .05$ (two-tail unpaired t -test)

of β 1,4-GlcNAc-branched N -glycans (Figure 8). The identification and specific functional analysis of O -GlcNAcylated sites on SLC35A3 require further study. The specificity for the biosynthesis of these N -glycans in OGT-KD cells could also be confirmed using SLC35A3-KO. Furthermore, the effect of SLC35A3-KO on cell adhesion, migration, and proliferation was similar to that observed in the OGT-KD cells. Collectively, these results clearly show a novel crosstalk pathway between O -GlcNAcylation and N -glycosylation via the axis of OGT/SLC35A3/GnT-IV, which may help us to further understand the functions of O -GlcNAcylation and the regulation of N -glycan biosynthesis.

Generally, different PTMs often coordinate with each other, and O -GlcNAcylation is no exception. Given the importance of O -GlcNAcylation in multiple fundamental cellular processes, it is reasonable to assume that O -GlcNAcylation is involved in the pathological conditions of many diseases such as diabetes, neurological disorders, cardiovascular disease, and tumor progression.^{25,32,33} UDP-GlcNAc is an essential common donor substrate for O -GlcNAcylation as well as GlcNAc-branched N -glycosylation. Complex types of N -glycans cannot be fully synthesized without an efficient delivery of UDP-GlcNAc from the cytosol to the Golgi lumen. For example, SLC35A3-KD resulted in a decrease in the amount of UDP-GlcNAc in the Golgi lumen, which reduced the production of tri- and tetra-antennary N -glycans.⁵⁵ The loss of OGT in *C. elegans* caused a more than two-fold increase in total UDP-GlcNAc.⁴⁴ Thus, O -GlcNAcylation

may reciprocally interact with N -glycosylation through a shared pool of UDP-GlcNAc. We assumed that the production of GlcNAc-branched N -glycans would increase in OGT-KD HeLa cells. However, the results in the present study clearly contradicted our speculation.

Why OGT-KD specifically decreased the tri- and tetra-antennary N -glycans is intriguing. Dorota Maszczak-Seneczko et al. previously showed that the silencing of SLC35A3 reduces the GlcNAc-branched N -glycans, and then speculated that SLC35A3 might supply UDP-GlcNAc as a substrate mainly for GnT-IV and GnT-V.⁵⁵ Their assumptions provided a hint that SLC35A3 could be modified by OGT at the cytoplasmic domains since SLC35A3 is a type III multi-transmembrane protein. As expected, OGT did modify SLC35A3 with O -GlcNAc. The O -GlcNAcylation contributed to its stability at the protein level (Figure 4). Furthermore, SLC35A3-KO specifically decreased the production of tri- and tetra-antennary N -glycans, which was partially supported by the results of the previous study of SLC35A3-KD CHO and HeLa cells.⁵⁵ Although we observed those changes in GlcNAc-branched N -glycans in the current study, we cannot exclude changes in other types of glycans. Moreover, we believe that O -GlcNAcylation may also modify other transporters besides SLC35A3, which would result in changes in other types of N -glycans or other glycosylation pathways rather than exclusively the N -glycosylation pathway.

However, our observation could not be simply explained by a decrease in UDP-GlcNAc concentrations in the Golgi lumen for GnT-IV and GnT-V in either

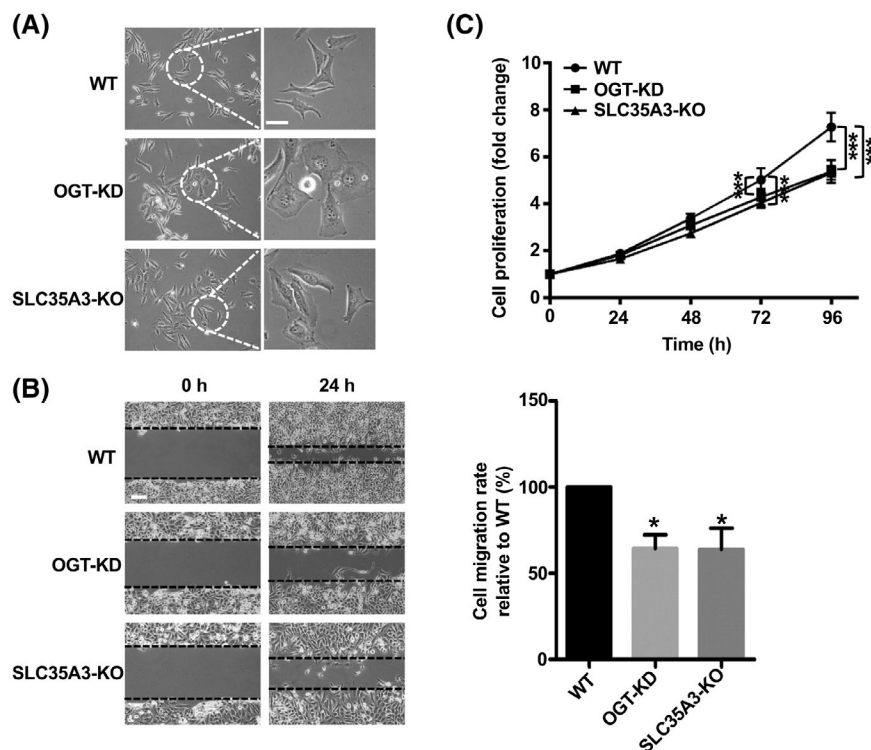


FIGURE 7 Comparison of effects of either OGT-KD or SLC35A3-KO on cell morphologies, cell migration, and proliferation. (A) HeLa cells treated with (OGT-KD) or without (WT) DOX, or SLC35A3-KO HeLa cells were pre-incubated for 24 h and then replated on culture dishes. After incubation for 48 h, cells were photographed under a phase-contrast microscope. An enlarged view is shown in the right panel. Scale bars, 15 μ m. (B) Cells as indicated were grown to more than 90% confluence, and the monolayers were incised with a pipette in each well. Photographs were taken by phase-contrast microscopy at 0 and 24 h. The migration distance was evaluated and then the cell migration rate was quantified (right panel). The migration rate for the WT cells was set as 100%. Experiments were independently repeated three times. Values represent the mean \pm SE. * p < .05 by one-way analysis of variance (ANOVA). Scale bars, 50 μ m. (C) The WT, OGT-KD, and SLC35A3-KO cells were supplied with DMEM containing 5% FBS seeded on 96-well dishes. The value after incubation for 6 h was set as 0 points (0 h), cells were further incubated, and cell numbers were measured at the indicated times (24, 48, 72, or 96 h) using MTT assay. The relative rate of cell proliferation was shown as increased folds at indicated times compared with that at 0 h, which was set as 1. Experiments were independently repeated three times. Values represent the mean \pm SE. *** p < .001 by two-way analysis of variance (ANOVA)

SLC35A3-KO or OGT-KD cells because GnT-IV has lower K_m values than those of GnT-V with UDP-GlcNAc as a donor substrate.⁶¹ Thus, a decrease in UDP-GlcNAc should have a greater impact on the production of GnT-V compared with that of GnT-IV. Apparently, this was not the case for the present study, as described above. Interestingly, the co-immunoprecipitation analysis revealed that SLC35A3 specifically interacts with GnT-IV rather than with GnT-V, which strongly suggests the specificity of SLC35A3 for tri-antennary *N*-glycan biosynthesis and further supports our observations. The FRET approach in A375 and 293 cells, however, showed that SLC35A3 and GnT-V seemed to be close in the Golgi membrane, although the association could not be detected by co-immunoprecipitation.^{55,62} Whether the difference is due to cell lines, association strength between molecules, or other mechanisms involved will require further study. In addition, we also noticed that the increase in *O*-GlcNAc and DSA staining 48–72 h after replating, but the mRNA

levels of those transferases involved in the biosynthetic pathways of GlcNAc-branched *N*-glycans showed no significant differences at indicated times in the WT cells. We speculated that diverse environmental cues such as cell adhesion and the cell cycle during the timepoints may influence the glycosylation and secretory pathways of glycoproteins and their expression levels. The underlying molecular mechanism will require further study.

This study also showed that SLC35A3 may not be one of the main UDP-GlcNAc transporters for *N*-glycosylation since the biosynthesis of bi-antennary *N*-glycans was not significantly blocked in the SLC35A3-KO cells. The recent study by Bozena Szulc et al. also came to a similar conclusion, they also speculated that SLC35A3 is not the main supplier of UDP-GlcNAc for *N*-glycosylation and speculated there is a more efficient multi-protein complex that functions as a single transporter of UDP-GlcNAc for *N*-glycosylation.⁶³ In addition, SLC35A3 has been reported to either directly or indirectly interact with SLC35A2,⁵⁸

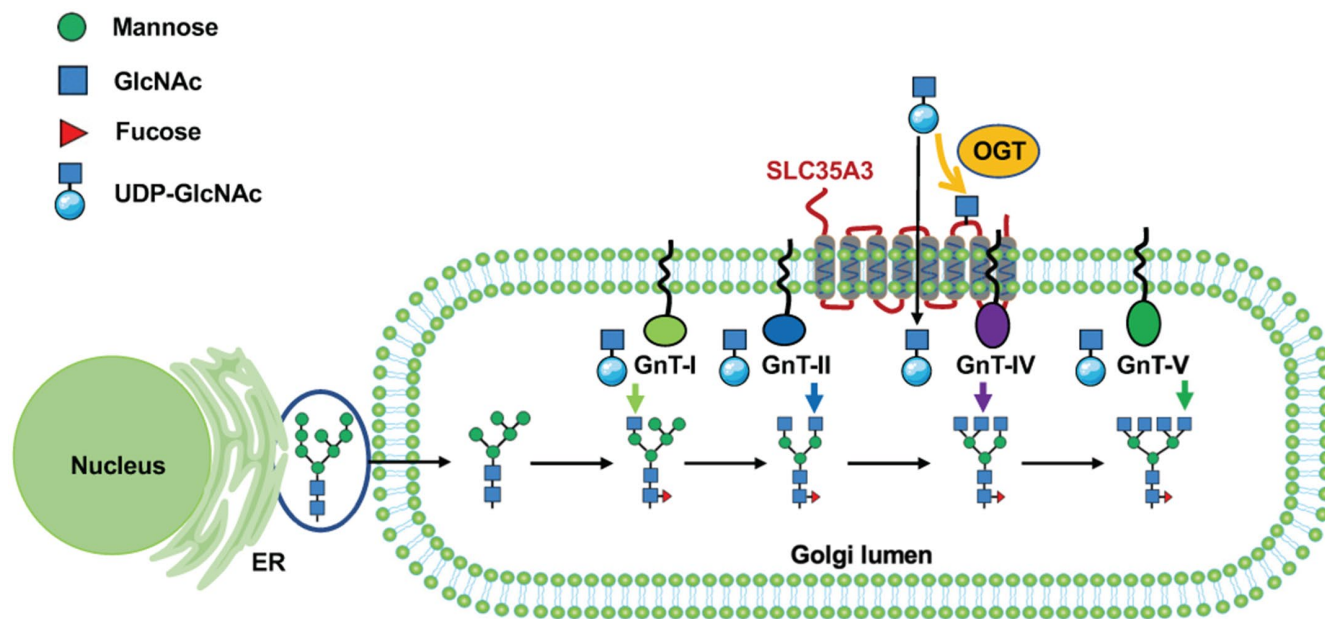


FIGURE 8 Schematic diagram of the proposed molecular mechanism for regulation of the biosynthesis of β 1,4-GlcNAc-branched *N*-glycans by *O*-GlcNAcylation. Biosynthesis of *N*-glycans in the endoplasmic reticulum (ER) and the Golgi apparatus involves complex machinery that incorporates both enzymatic reactions and transportation. Once a glycoprotein with the high mannose type of *N*-glycan is transported from the ER to the Golgi lumen, it is sequentially modified first by GnT-I and GnT-II, and then by GnT-III, GnT-IV, or GnT-V to produce a diverse GlcNAc-branched functional glycoprotein. In the present study, we found that OGT could modify SLC35A3, a UDP-GlcNAc transporter. Suppression of *O*-GlcNAcylation on SLC35A3 affects its stability and the specific complex formation with GnT-IV, which specifically decreases the biosynthesis of β 1,4-GlcNAc-branched *N*-glycans. These data are the first to demonstrate a novel crosstalk pathway between *O*-GlcNAcylation and *N*-glycosylation via the axis of OGT-SLC35A3-GnT-IV

SLC35A4,⁶⁴ GnT-IV,⁶² and GnT-V,^{55,62,64} and the interactions among glycosyltransferases and nucleotide sugar transporters to form multi-enzyme/multi-transporter complexes in the Golgi membranes may facilitate the efficient synthesis of complex *N*-glycans.⁶⁴ It is also possible, however, that some Golgi-resident nucleotide sugar transporters may specifically serve corresponding glycosyltransferases. For example, SLC35A2 interacts with B4GalT1, which is widely expressed in all tissues and is considered quite important in the galactosylation of *N*-glycans. Also, a deficiency in either SLC35A2 or B4GalT1 results in a significant lack of galactose moieties on *N*-glycans.^{65–67}

Emerging data have clearly shown that *O*-GlcNAcylation plays critical role in the progress of human diseases, particularly diseases such as cancers, diabetes, and Alzheimer's disease.^{25,32–34} The regulation of *O*-GlcNAcylation may be directly involved in diabetes. OGT and *O*-GlcNAc-modified protein levels are increased in the pancreatic islets, as well as in the tissues of the sciatic nerve, kidney, and liver in diabetic rats.⁶⁸ Curiously, a decrease in *O*-GlcNAcylation caused by the overexpression of OGA in the pancreatic β cells of transgenic mice led to a decrease in insulin secretion.⁶⁹ On contrary, it is well known that a loss of GnT-IV inhibits GlcNAc-branching formation on Glut-2, which decreases Glut-2 stability on the cell surface and promotes its endocytosis, which

decreases insulin secretion and results in the pathogenesis of type 2 diabetes in mice.¹² Based on these observations together with the results of this study, it would be very interesting to investigate the relationship between *O*-GlcNAcylation and Glut-2 expression on the cell surface.

Cell migration is a central process in the development and maintenance of multicellular organisms.⁷⁰ In the previous study, we found that the suppression of *O*-GlcNAcylation inhibited integrin-mediated cell migration due to an aberrant increase in cell-ECM adhesion via an enhancement of focal-adhesion plaque formation.⁵⁴ The present study also revealed another potential mechanism whereby *O*-GlcNAcylation could regulate the modification of GlcNAc-branched *N*-glycans on membrane proteins such as integrins to govern cell migration. Therefore, it will be very important for glycobiology to examine the effects of both *O*-GlcNAcylation and *N*-glycosylation rather than focusing on one or the other.

ACKNOWLEDGMENTS

This work was supported in part by a Grant-in-Aid for Scientific Research (19H03184 to J.G. and 19K07049 to T.I.) from the Japan Society for the Promotion of Science; and by a Grant-in-Aid for Scientific Research on Innovative Areas (20H04909 to J.G.) from the Ministry

of Education, Culture, Sports, Science, and Technology of Japan.

DISCLOSURES

The authors declare no conflicts of interest and no competing financial interests.

AUTHOR CONTRIBUTIONS

Wanli Song, Tomoya Isaji and Jianguo Gu designed the research; Wanli Song performed all experiments. Wanli Song, Tomoya Isaji, and Caixia Liang performed the PCR analysis. Miyako Nakano performed the mass spectrometry analysis. Wanli Song, Tomoya Isaji, Caixia Liang, and Tomohiko Fukuda assisted with the experiments. Tomoya Isaji, Tomohiko Fukuda, and Jianguo Gu analyzed and interpreted the data. Wanli Song and Jianguo Gu wrote and revised the manuscript. All authors approved the final version of the manuscript.

REFERENCES

- Gabius HJ. The sugar code: why glycans are so important. *Biosystems*. 2018;164:102-111.
- Reily C, Stewart TJ, Renfrow MB, Novak J. Glycosylation in health and disease. *Nat Rev Nephrol*. 2019;15:346-366.
- Ohtsubo K, Marth JD. Glycosylation in cellular mechanisms of health and disease. *Cell*. 2006;126:855-867.
- Varki A, Kannagi R, Toole B, Stanley P. Glycosylation changes in cancer. In: Varki A, Cummings RD, Esko JD, Stanley P, Hart GW, Aebi M, Darvill AG, Kinoshita T, Packer NH, Prestegard JH, Schnaar RL, Seeberger PH, eds. *Essentials of Glycobiology*. Cold Spring Harbor Laboratory Press; 2015:597-609.
- Rudman N, Gornik O, Lauc G. Altered N-glycosylation profiles as potential biomarkers and drug targets in diabetes. *FEBS Lett*. 2019;593:1598-1615.
- Sun S, Hu Y, Ao M, et al. N-GlycositeAtlas: a database resource for mass spectrometry-based human N-linked glycoprotein and glycosylation site mapping. *Clin Proteomics*. 2019;16:35.
- Zhao YY, Takahashi M, Gu JG, et al. Functional roles of N-glycans in cell signaling and cell adhesion in cancer. *Cancer Sci*. 2008;99:1304-1310.
- Yoshida Y, Tanaka K. Cytosolic N-glycans: triggers for ubiquitination directing proteasomal and autophagic degradation. *BioEssays*. 2018;40:1700215.
- Yoshida Y, Mizushima T, Tanaka K. Sugar-recognizing ubiquitin ligases: action mechanisms and physiology. *Front Physiol*. 2019;10:104.
- Yoshimura M, Ihara Y, Matsuzawa Y, Taniguchi N. Aberrant glycosylation of E-cadherin enhances cell-cell binding to suppress metastasis. *J Biol Chem*. 1996;271:13811-13815.
- Kitada T, Miyoshi E, Noda K, et al. The addition of bisecting N-acetylglucosamine residues to E-cadherin down-regulates the tyrosine phosphorylation of beta-catenin. *J Biol Chem*. 2001;276:475-480.
- Ohtsubo K, Takamatsu S, Minowa MT, Yoshida A, Takeuchi M, Marth JD. Dietary and genetic control of glucose transporter 2 glycosylation promotes insulin secretion in suppressing diabetes. *Cell*. 2005;123:1307-1321.
- Ohtsubo K, Chen MZ, Olefsky JM, Marth JD. Pathway to diabetes through attenuation of pancreatic beta cell glycosylation and glucose transport. *Nat Med*. 2011;17:1067-1075.
- Schachter H. Biosynthetic controls that determine the branching and microheterogeneity of protein-bound oligosaccharides. *Biochem Cell Biol*. 1986;64:163-181.
- Kizuka Y, Taniguchi N. Enzymes for N-glycan branching and their genetic and nongenetic regulation in cancer. *Biomolecules*. 2016;6:25.
- Niimi K, Yamamoto E, Fujiwara S, et al. High expression of N-acetylglucosaminyltransferase IVa promotes invasion of choriocarcinoma. *Br J Cancer*. 2012;107:1969-1977.
- Fan J, Wang S, Yu S, He J, Zheng W, Zhang J. N-acetylglucosaminyltransferase IVa regulates metastatic potential of mouse hepatocarcinoma cells through glycosylation of CD147. *Glycoconj J*. 2012;29:323-334.
- Ide Y, Miyoshi E, Nakagawa T, et al. Aberrant expression of N-acetylglucosaminyltransferase-IVa and IVb (GnT-IVa and b) in pancreatic cancer. *Biochem Biophys Res Commun*. 2006;341:478-482.
- Wellen KE, Thompson CB. Cellular metabolic stress: considering how cells respond to nutrient excess. *Mol Cell*. 2010;40:323-332.
- Biwi J, Biot C, Guerardel Y, Vercoutter-Edouart A-S, Lefebvre T. The many ways by which O-GlcNAcylation may orchestrate the diversity of complex glycosylations. *Molecules*. 2018;23:2858.
- Hart GW, Housley MP, Slawson C. Cycling of O-linked beta-N-acetylglucosamine on nucleocytoplasmic proteins. *Nature*. 2007;446:1017-1022.
- Bond MR, Hanover JA. A little sugar goes a long way: the cell biology of O-GlcNAc. *J Cell Biol*. 2015;208:869-880.
- Hart GW. Dynamic O-linked glycosylation of nuclear and cytoskeletal proteins. *Annu Rev Biochem*. 1997;66:315-335.
- Simanek EE, Huang D-H, Pasternack L, et al. Glycosylation of threonine of the repeating unit of RNA polymerase II with β -linked N-acetylglucosamine leads to a turnlike structure. *J Am Chem Soc*. 1998;120:11567-11575.
- Hart GW, Slawson C, Ramirez-Correa G, Lagerlof O. Cross talk between O-GlcNAcylation and phosphorylation: roles in signaling, transcription, and chronic disease. *Annu Rev Biochem*. 2011;80:825-858.
- Liu C, Shi Y, Li J, et al. O-GlcNAcylation of myosin phosphatase targeting subunit 1 (MYPT1) dictates timely disjunction of centrosomes. *J Biol Chem*. 2020;295:7341-7349.
- Yang X, Su K, Roos MD, Chang Q, Paterson AJ, Kudlow JE. O-linkage of N-acetylglucosamine to Sp1 activation domain inhibits its transcriptional capability. *Proc Natl Acad Sci USA*. 2001;98:6611-6616.
- Yang X, Qian K. Protein O-GlcNAcylation: emerging mechanisms and functions. *Nat Rev Mol Cell Biol*. 2017;18:452-465.
- Gewinner C, Hart G, Zachara N, Cole R, Beisenherz-Huss C, Groner B. The coactivator of transcription CREB-binding protein interacts preferentially with the glycosylated form of Stat5. *J Biol Chem*. 2004;279:3563-3572.
- Chu CS, Lo PW, Yeh YH, et al. O-GlcNAcylation regulates EZH2 protein stability and function. *Proc Natl Acad Sci USA*. 2014;111:1355-1360.
- Yang WH, Kim JE, Nam HW, et al. Modification of p53 with O-linked N-acetylglucosamine regulates p53 activity and stability. *Nat Cell Biol*. 2006;8:1074-1083.

32. Copeland RJ, Han G, Hart GW. O-GlcNAcomics—Revealing roles of O-GlcNAcylation in disease mechanisms and development of potential diagnostics. *Proteomics Clin Appl*. 2013;7:597-606.
33. Kamigaito T, Okaneya T, Kawakubo M, Shimojo H, Nishizawa O, Nakayama J. Overexpression of O-GlcNAc by prostate cancer cells is significantly associated with poor prognosis of patients. *Prostate Cancer Prostatic Dis*. 2014;17:18-22.
34. Zhao L, Shah JA, Cai Y, Jin J. 'O-GlcNAc Code' mediated biological functions of downstream proteins. *Molecules*. 2018;23:1967.
35. Gu Y, Gao J, Han C, et al. O-GlcNAcylation is increased in prostate cancer tissues and enhances malignancy of prostate cancer cells. *Mol Med Rep*. 2014;10:897-904.
36. Shi Y, Tomic J, Wen F, et al. Aberrant O-GlcNAcylation characterizes chronic lymphocytic leukemia. *Leukemia*. 2010;24:1588-1598.
37. Ferrer CM, Lynch TP, Sodi VL, et al. O-GlcNAcylation regulates cancer metabolism and survival stress signaling via regulation of the HIF-1 pathway. *Mol Cell*. 2014;54:820-831.
38. Zhu Q, Zhou L, Yang Z, et al. O-GlcNAcylation plays a role in tumor recurrence of hepatocellular carcinoma following liver transplantation. *Med Oncol*. 2012;29:985-993.
39. Ma Z, Vocadlo DJ, Vosseller K. Hyper-O-GlcNAcylation is anti-apoptotic and maintains constitutive NF- κ B activity in pancreatic cancer cells. *J Biol Chem*. 2013;288:15121-15130.
40. Xu D, Wang W, Bian T, Yang W, Shao M, Yang H. Increased expression of O-GlcNAc transferase (OGT) is a biomarker for poor prognosis and allows tumorigenesis and invasion in colon cancer. *Int J Clin Exp Pathol*. 2019;12:1305-1314.
41. Gu Y, Mi W, Ge Y, et al. GlcNAcylation plays an essential role in breast cancer metastasis. *Cancer Res*. 2010;70:6344-6351.
42. Peterson SB, Hart GW. New insights: a role for O-GlcNAcylation in diabetic complications. *Crit Rev Biochem Mol Biol*. 2016;51:150-161.
43. Lau KS, Partridge EA, Grigorian A, et al. Complex N-glycan number and degree of branching cooperate to regulate cell proliferation and differentiation. *Cell*. 2007;129:123-134.
44. Ghosh SK, Bond MR, Love DC, Ashwell GG, Krause MW, Hanover JA. Disruption of O-GlcNAc cycling in *C. elegans* perturbs nucleotide sugar pools and complex glycans. *Front Endocrinol*. 2014;5:197.
45. Sato Y, Isaji T, Tajiri M, et al. An N-glycosylation site on the beta-propeller domain of the integrin α 5 subunit plays key roles in both its function and site-specific modification by beta1,4-N-acetylglucosaminyltransferase III. *J Biol Chem*. 2009;284:11873-11881.
46. Isaji T, Im S, Gu W, et al. An oncogenic protein Golgi phosphoprotein 3 up-regulates cell migration via sialylation. *J Biol Chem*. 2014;289:20694-20705.
47. Tanabe K, Ikenaka K. In-column removal of hydrazine and N-acetylation of oligosaccharides released by hydrazinolysis. *Anal Biochem*. 2006;348:324-326.
48. Tomiya N, Awaya J, Kuroki M, Endo S, Arata Y, Takahashi N. Analyses of N-linked oligosaccharides using a two-dimensional mapping technique. *Anal Biochem*. 1988;171:73-90.
49. Tomiya N, Lee YC, Yoshida T, et al. Calculated two-dimensional sugar map of pyridylaminated oligosaccharides: elucidation of the jack bean alpha-mannosidase digestion pathway of Man9GlcNAc2. *Anal Biochem*. 1991;193:90-100.
50. Kao S-H, Wang W-L, Chen C-Y, et al. Analysis of protein stability by the cycloheximide chase assay. *Bio Protoc*. 2015;5:e1374.
51. Sanjana NE, Shalem O, Zhang F. Improved vectors and genome-wide libraries for CRISPR screening. *Nat Methods*. 2014;11:783-784.
52. Shalem O, Sanjana NE, Hartenian E, et al. Genome-scale CRISPR-Cas9 knockout screening in human cells. *Science*. 2014;343:84-87.
53. Takamatsu S, Korekane H, Ohtsubo K, et al. N-acetylglucosaminyltransferase (GnT) assays using fluorescent oligosaccharide acceptor substrates: GnT-III, IV, V, and IX (GnT-Vb). In: Brockhausen I, ed. *Glycosyltransferases: Methods and Protocols*. Humana Press; 2013:283-298.
54. Xu Z, Isaji T, Fukuda T, Wang Y, Gu J. O-GlcNAcylation regulates integrin-mediated cell adhesion and migration via formation of focal adhesion complexes. *J Biol Chem*. 2019;294:3117-3124.
55. Maszczak-Seneczko D, Sosicka P, Olczak T, Jakimowicz P, Majkowski M, Olczak M. UDP-N-acetylglucosamine transporter (SLC35A3) regulates biosynthesis of highly branched N-glycans and keratan sulfate. *J Biol Chem*. 2013;288:21850-21860.
56. Edvardson S, Ashikov A, Jallas C, et al. Mutations in SLC35A3 cause autism spectrum disorder, epilepsy and arthrogryposis. *J Med Genet*. 2013;50:733-739.
57. Toscanini MA, Favaro MB, Gonzalez Flecha FL, Ebert B, Rautengarten C, Bredeston LM. Conserved Glu-47 and Lys-50 residues are critical for UDP-N-acetylglucosamine/UMP antiport activity of the mouse Golgi-associated transporter Slc35a3. *J Biol Chem*. 2019;294:10042-10054.
58. Maszczak-Seneczko D, Sosicka P, Majkowski M, Olczak T, Olczak M. UDP-N-acetylglucosamine transporter and UDP-galactose transporter form heterologous complexes in the Golgi membrane. *FEBS Lett*. 2012;586:4082-4087.
59. Oguri S, Yoshida A, Minowa MT, Takeuchi M. Kinetic properties and substrate specificities of two recombinant human N-acetylglucosaminyltransferase-IV isozymes. *Glycoconj J*. 2006;23:473-480.
60. Takamatsu S, Antonopoulos A, Ohtsubo K, et al. Physiological and glycomic characterization of N-acetylglucosaminyltransferase-IVa and -IVb double deficient mice. *Glycobiology*. 2010;20:485-497.
61. Lau KS, Dennis JW. N-Glycans in cancer progression. *Glycobiology*. 2008;18:750-760.
62. Maszczak-Seneczko D, Sosicka P, Kaczmarek B, et al. UDP-galactose (SLC35A2) and UDP-N-acetylglucosamine (SLC35A3) Transporters Form Glycosylation-related Complexes with Mannoside Acetylglucosaminyltransferases (Mgats). *J Biol Chem*. 2015;290:15475-15486.
63. Szulc B, Sosicka P, Maszczak-Seneczko D, et al. Biosynthesis of GlcNAc-rich N- and O-glycans in the Golgi apparatus does not require the nucleotide sugar transporter SLC35A3. *J Biol Chem*. 2020;295:16445-16463.
64. Khoder-Agha F, Sosicka P, Escrivá Conde M, et al. N-acetylglucosaminyltransferases and nucleotide sugar transporters form multi-enzyme-multi-transporter assemblies in Golgi membranes in vivo. *Cell Mol Life Sci*. 2019;76:1821-1832.
65. Wiertelak W, Sosicka P, Olczak M, Maszczak-Seneczko D. Analysis of homologous and heterologous interactions between UDP-galactose transporter and beta-1,4-galactosyltransferase 1 using NanoBiT. *Anal Biochem*. 2020;593:113599.

66. Guo S, Sato T, Shirane K, Furukawa K. Galactosylation of N-linked oligosaccharides by human beta-1,4-galactosyltransferases I, II, III, IV, V, and VI expressed in Sf-9 cells. *Glycobiology*. 2001;11:813-820.
67. Guillard M, Morava E, de Ruijter J, et al. B4GALT1-congenital disorders of glycosylation presents as a non-neurologic glycosylation disorder with hepatointestinal involvement. *J Pediatr*. 2011;159:1041-1043.e2.
68. Akimoto Y, Hart GW, Wells L, et al. Elevation of the post-translational modification of proteins by O-linked N-acetylglucosamine leads to deterioration of the glucose-stimulated insulin secretion in the pancreas of diabetic Goto-Kakizaki rats. *Glycobiology*. 2007;17:127-140.
69. Soesanto Y, Luo B, Parker G, Jones D, Cooksey RC, McClain DA. Pleiotropic and age-dependent effects of decreased protein modification by O-linked N-acetylglucosamine on pancreatic β -cell function and vascularization. *J Biol Chem*. 2011;286:26118-26126.
70. Franz CM, Jones GE, Ridley AJ. Cell migration in development and disease. *Dev Cell*. 2002;2:153-158.

SUPPORTING INFORMATION

Additional supporting information may be found in the online version of the article at the publisher's website.

How to cite this article: Song W, Isaji T, Nakano M, Liang C, Fukuda T, Gu J. O-GlcNAcylation regulates β 1,4-GlcNAc-branched N-glycan biosynthesis via the OGT/SLC35A3/GnT-IV axis. *FASEB J*. 2022;36:e22149. doi:[10.1096/fj.202101520R](https://doi.org/10.1096/fj.202101520R)

5.25 N-Linked Glycans in the Epithelial-Mesenchymal Transition: Implications for Cancer Metastasis

Jianguo Gu, Division of Regulatory Glycobiology, Institute of Molecular Biomembrane and Glycobiology, Tohoku Medical and Pharmaceutical University, Sendai, Japan

© 2021 Elsevier B.V. All rights reserved.

Glossary

EMT (epithelial-mesenchymal transition) EMT is a biologic process that allows polarized epithelial cells, which normally interact with basement membrane, to undergo multiple biochemical changes that enable them to acquire a mesenchymal cell phenotype, which includes enhanced migratory capacity, invasiveness, and greatly increased production of extracellular matrix as well as EMT biomarkers such as fibronectin, N-cadherin and vimentin.

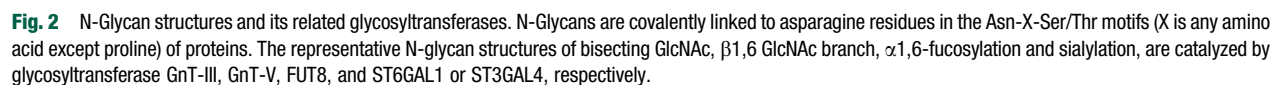
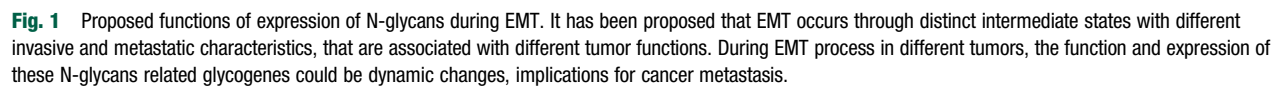
MET (mesenchymal-epithelial transition) MET is a reversible biological process of EMT, which is also shown to occur in normal development and cancer metastasis.

Epithelial-mesenchymal transition (EMT) is a biological process that allows polarized epithelial cells to undergo multiple biochemical changes that enable them to acquire a mesenchymal phenotype, and migrate to secondary sites.¹ EMT is characterized by a loss of cell-cell adhesion and acquisition of cell motility, and has been featured by a decreased expression of cell-cell adhesion molecules and epithelial markers such as E-cadherin, and an increased expression of intermediate filament proteins and mesenchymal cell markers including N-cadherin and integrins (Fig. 1). Therefore, at a cell adhesion view, EMT could be easily believed as a decreased cell-cell adhesion and an increased integrin-mediated cell-ECM (extracellular matrix) adhesion. EMT has evolved as a critical developmental program, is essential for gastrulation, somitogenesis and neural crest delamination during embryonic development. However, this process is also recapitulated under pathological conditions, prominently in invasion and cancer metastasis, and also associated with tumor stemness and resistance to therapy in cancer.² To understand the molecular mechanisms involved in EMT is critical for developing effective treatments for tumor growth and cancer metastasis.

E-cadherin is the core transmembrane protein of the adherens junction and is required for binding and localization of a number of important cytoplasmic proteins, termed catenins, that connect the cadherin complex to the actin cytoskeleton and several signaling pathways.³ The catenin family comprises α -catenin, β -catenin and γ -catenin (plakoglobin). The regulation of cadherin-mediated adhesion and associated adherence junctions is thought to underlie the dynamics of inter-cellular adhesive interactions, which are regulated during tissue development and homeostasis, as well as during tumor cell progression. In epithelial derived tumors, loss of cell-cell adhesion is correlated with down-regulation of E-cadherin as well as increased proliferation and tumor invasiveness. Therefore, most studies have focused on the identification and characterization of transcriptional repressors of E-cadherin expression in epithelial tumor cells. The most prominent factors identified in these studies included the related factors, Slug, Snail, SIP1 and Twist, which are best known for their roles in early embryogenesis and tumor progression⁴ (Fig. 1).

On the other hand, E-cadherin can be post-translationally modified by phosphorylation, O-linked and N-linked glycosylation. Casein kinase II, a serine-threonine kinase, phosphorylates the cytosolic tail of E-cadherin and enhances binding to α -catenin.⁵ Cytoplasmic O-GlcNAcylation of the E-cadherin cytosolic tail has been shown to occur in response to endoplasmic reticulum stress and inactivate E-cadherin-mediated intercellular adhesion by preventing its transport to the cell membrane.⁶ N-Glycosylation of E-cadherin has a great impact on its mediate cell adhesion. Enhanced expression of the first enzyme of N-glycosylation, DPAGT1, is activated by the Wnt/ β -catenin pathway which results in strong N-glycosylation of E-cadherin and reduction of cell-cell adhesion in adherens junctions.⁷ In normal epithelial cells, E-cadherin has been shown to harbor mainly bisecting N-glycans due to the activity of N-acetylglucosaminyltransferase III (GnT-III) enzyme (Fig. 2). In carcinoma cells, GnT-III is frequently downregulated by promoter methylation, and its counterpart N-acetylglucosaminyltransferase V (GnT-V) is up-regulated leading to the formation of tri- and tetra-antennary complex N-glycans on cadherins and other proteins. This results in E-cadherin internalization to the cytoplasm and disruption of cell-cell contacts, which compromises the associated signaling pathways, resulting in EMT, invasion and metastasis.⁸ E-cadherin-mediated cell adhesion can be regulated by GnT-III. Overexpression of GnT-III increased the retention of E-cadherin at the cell border, which might result in an enhancement of E-cadherin-mediated homotypic adhesion.^{9,10} In contrast, inhibition of GnT-V expression in fibrosarcoma cells resulted in decreased levels of β 1,6 GlcNAc branched N-glycans on N-cadherin, an antagonist of E-cadherin in EMT, increased cell-cell contacts, and decreased migration and invasion.¹¹ Thus, expression of E-cadherin is regulated, not only by transcriptional factors, but also by post-transcriptional modifications such as N-glycosylation (Fig. 1).

During the TGF- β -induced EMT, the expression of GnT-III was significantly suppressed, while GnT-V was promoted.^{12,13} GnT-III is usually believed as an important glycosyltransferase in N-glycan biosynthetic pathways, since GnT-V cannot use the bisected oligosaccharide as a substrate.¹⁴ Introduction of a bisecting GlcNAc blocks further branching and elongation of N-glycans catalyzed by GnT-V. Conversely, overexpression of GnT-III suppressed the TGF- β -induced EMT, and inhibited the metastasis of multiple types of carcinomas. Inhibition of GnT-V expression prevented liver fibrosis and suppressed TGF- β 1-induced EMT in hepatocytes by



Increasing evidence demonstrates that sialylation plays fundamental roles in normal biological processes, such as cell proliferation, cell differentiation, apoptosis and cell signaling.^{22,23} The role of sialylation in TGF- β -induced EMT had also been investigated using the EMT and MET (mesenchymal-epithelial transition, the converse process of EMT) models. The β -galactoside α 2,6 sialyltransferase 1 (ST6GAL1), an enzyme that primarily creates terminal α 2,6 sialic acid linkages on N-glycans (Fig. 2), is specifically upregulated during TGF- β induced EMT. Knockdown of ST6GAL1 clearly inhibited EMT with the concomitant increase in E-cadherin. Interestingly, overexpression of ST6GAL1, but not β -galactoside α 2,3 sialyltransferase 4 (ST3GAL4) promoted EMT, indicating the specific role of ST6GAL1 during the EMT process.²⁴ It had been demonstrated that the effects of GnT-III on cell migration are dependent on the cell sialylation pattern on integrins.²⁵ GnT-III plays an anti-migratory role under an α 2,6 hyposialylated context. The overexpression of GnT-III dramatically suppresses α 2,3 sialylation, while increases α 2,6 sialylation on integrins. High expression of α 2,6 sialylation could antagonize the inhibitory effects of GnT-III and endow the cells with high

migratory ability. So, it is reasonable to consider that the decrease in α 2,3 sialylation is, at least partially, due to the reduced branches of N-glycans. Also, the down-regulated α 2,3 sialylation after GnT-III overexpression could be also attributed to the branch specificities of sialyltransferases. In fact, previous reports showed that a low degree of branching favors α 2,6 sialylation, but not favor α 2,3 sialylation.^{26–28}

Since α 2,3- and α 2,6-sialyltransferases may compete with common substrates to a certain extent, and this competition is manifested in specific glycoproteins such as β 1 integrin. Very recently, interestingly, among the three α 2,3-sialyltransferases (ST3GAL3, ST3GAL4, and ST3GAL6) involved in the synthesis of N-glycans, ST3GAL4 deficiency (KO) alone reciprocally increased the levels of α 2,6-sialylation, while the overexpression of ST3GAL4 conversely decreased the α 2,6-sialylation levels of β 1 integrin.²⁹ The ST3GAL3 KO and ST3GAL6 KO cells expressed more E-cadherin on the cell surface, compared to the ST3GAL4 KO cells. Therefore, when evaluating the effect of α 2,3-sialylation, the influences of α 2,6-sialylation could not be neglected, since the α 2,6-sialylation of β 1 plays important roles in cell adhesion and EMT as described above. Although the detailed molecular mechanism for the roles of different sialylation remain unclear, one could be explained that the α 2,6-sialylation but not α 2,3-sialylation of N-glycan is able to inhibit its binding to galectin-3.³⁰ Tumor cells exhibit significant changes in cell surface glycosylation.³¹ Certain glycan structures are closely associated with cell invasion and cell survival, which provide important sources of markers for tumor progression. It has been reported that the ST6GAL1 is highly expressed in induced pluripotent stem (iPS) cells and cancer stem cells (CSCs).³² Taking together, EMT program may relate with CSCs, or cells with stem cell-like properties, systematic analysis of functions of N-glycans, especially roles of N-glycosylation in glycoproteins expressed on the cell surface will provide insight into EMT as well as the development of promising therapeutic methods for cancers.

Recently, EMT has recently been proposed that, rather than being a binary process, it occurs through distinct intermediate states with different invasive, metastatic and differentiation characteristics, that are associated with different tumor functions³³ (Fig. 1). The diversity and heterogeneity of N-glycans in different kinds of tumors or/and different states even in the same tumor cells, may have important implications for our understanding of tumor heterogeneity, growth, invasion, metastasis and resistance to therapy.

References

- Thiery, J. P.; Sleeman, J. P. Complex Networks Orchestrate Epithelial-Mesenchymal Transitions. *Nat. Rev. Mol. Cell Biol.* **2006**, *7* (2), 131–142. [16493418](#).
- Hugo, H.; Ackland, M. L.; Blick, T.; Lawrence, M. G.; Clements, J. A.; Williams, E. D.; et al. Epithelial–Mesenchymal and Mesenchymal–Epithelial Transitions in Carcinoma Progression. *J. Cell. Physiol.* **2007**, *213* (2), 374–383. [17680632](#).
- Takeichi, M. Cadherins: A Molecular Family Important in Selective Cell-Cell Adhesion. *Annu. Rev. Biochem.* **1990**, *59*, 237–252. [2197976](#).
- Vernon, A. E.; LaBonne, C. Tumor Metastasis: A New Twist on Epithelial-Mesenchymal Transitions. *Curr. Biol.* **2004**, *14* (17), R719–R721. [15341765](#).
- Lickert, H.; Bauer, A.; Kemler, R.; Stappert, J. Casein Kinase II Phosphorylation of E-Cadherin Increases E-Cadherin/Beta-Catenin Interaction and Strengthens Cell-Cell Adhesion. *J. Biol. Chem.* **2000**, *275* (7), 5090–5095. [10671552](#).
- Zhu, W.; Leber, B.; Andrews, D. W. Cytoplasmic O-Glycosylation Prevents Cell Surface Transport of E-Cadherin During Apoptosis. *EMBO J.* **2001**, *20* (21), 5999–6007. [11689440](#).
- Sengupta, P. K.; Bouchie, M. P.; Nita-Lazar, M.; Yang, H. Y.; Kukuruzinska, M. A. Coordinate Regulation of N-Glycosylation Gene DPAGT1, Canonical Wnt Signaling and E-Cadherin Adhesion. *J. Cell Sci.* **2013**, *126* (Pt 2), 484–496. [23178939](#). [3613180](#).
- Pinho, S. S.; Figueiredo, J.; Cabral, J.; Carvalho, S.; Dourado, J.; Magalhaes, A.; et al. E-Cadherin and Adherens Junctions Stability in Gastric Carcinoma: Functional Implications of Glycosyltransferases Involving N-Glycan Branching Biosynthesis, N-Acetylglucosaminyltransferases III and V. *Biochim. Biophys. Acta* **2013**, *1830* (3), 2690–2700. [23671930](#).
- Yoshimura, M.; Nishikawa, A.; Ihara, Y.; Taniguchi, S.; Taniguchi, N. Suppression of Lung Metastasis of B16 Mouse Melanoma by N-Acetylglucosaminyltransferase III Gene Transfection. *Proc. Natl. Acad. Sci. U. S. A.* **1995**, *92* (19), 8754–8758. [7568011](#).
- Yoshimura, M.; Ihara, Y.; Matsuzawa, Y.; Taniguchi, N. Aberrant Glycosylation of E-Cadherin Enhances Cell-Cell Binding to Suppress Metastasis. *J. Biol. Chem.* **1996**, *271* (23), 13811–13815. [8662832](#).
- Guo, H. B.; Johnson, H.; Randolph, M.; Pierce, M. Regulation of Homotypic Cell-Cell Adhesion by Branched N-Glycosylation of N-Cadherin Extracellular EC2 and EC3 Domains. *J. Biol. Chem.* **2009**, *284* (50), 34986–34997. [19846557](#). [2787361](#).
- Xu, Q.; Isaji, T.; Lu, Y.; Gu, W.; Kondo, M.; Fukuda, T.; et al. Roles of N-Acetylglucosaminyltransferase III in Epithelial-to-Mesenchymal Transition Induced by Transforming Growth Factor Beta1 (TGF-Beta1) in Epithelial Cell Lines. *J. Biol. Chem.* **2012**, *287* (20), 16563–16574. [22451656](#). [3351319](#).
- Xu, Q.; Akama, R.; Isaji, T.; Lu, Y.; Hashimoto, H.; Kariya, Y.; et al. Wnt/Beta-Catenin Signaling Down-Regulates N-Acetylglucosaminyltransferase III Expression: The Implications of Two Mutually Exclusive Pathways for Regulation. *J. Biol. Chem.* **2011**, *286* (6), 4310–4318. [21115490](#). [3039325](#).
- Gu, J.; Taniguchi, N. Regulation of Integrin Functions by N-Glycans. *Glycoconj. J.* **2004**, *21* (1–2), 9–15. [15467392](#).
- Liu, J.; Zhang, Z.; Tu, X.; Liu, J.; Zhang, H.; Zhang, J.; et al. Knockdown of N-Acetylglucosaminyl Transferase V Ameliorates Hepatotoxin-Induced Liver Fibrosis in Mice. *Toxicol. Sci.* **2013**, *135* (1), 144–155. [23798564](#).
- Terao, M.; Ishikawa, A.; Nakahara, S.; Kimura, A.; Kato, A.; Moriawaki, K.; et al. Enhanced Epithelial-Mesenchymal Transition-Like Phenotype in N-Acetylglucosaminyltransferase V Transgenic Mouse Skin Promotes Wound Healing. *J. Biol. Chem.* **2011**, *286* (32), 28303–28311. [21697088](#). [3151074](#).
- Chen, C. Y.; Jan, Y. H.; Juan, Y. H.; Yang, C. J.; Huang, M. S.; Yu, C. J.; et al. Fucosyltransferase 8 as a Functional Regulator of Non-small Cell Lung Cancer. *Proc. Natl. Acad. Sci. U. S. A.* **2013**, *110* (2), 630–635. [23267084](#). [3545778](#).
- Yang, X.; Liu, S.; Yan, Q. Role of Fucosyltransferase IV in Epithelial-Mesenchymal Transition in Breast Cancer Cells. *Cell Death Dis.* **2013**, *4*, e735. [23887626](#). [3730415](#).
- Guo, J.; Li, X.; Tan, Z.; Lu, W.; Yang, G.; Guan, F. Alteration of N-Glycans and Expression of Their Related Glycogenes in the Epithelial-Mesenchymal Transition of HCV29 Bladder Epithelial Cells. *Molecules* **2014**, *19* (12), 20073–20090. [25470275](#). [6271757](#).
- Anugraham, M.; Jacob, F.; Nixdorf, S.; Everest-Dass, A. V.; Heinzlmann-Schwarz, V.; Packer, N. H. Specific Glycosylation of Membrane Proteins in Epithelial Ovarian Cancer Cell Lines: Glycan Structures Reflect Gene Expression and DNA Methylation Status. *Mol. Cell. Proteomics* **2014**, *13* (9), 2213–2232. [24855066](#). [4159645](#).
- Sethi, M. K.; Thaysen-Andersen, M.; Smith, J. T.; Baker, M. S.; Packer, N. H.; Hancock, W. S.; et al. Comparative N-Glycan Profiling of Colorectal Cancer Cell Lines Reveals Unique Bisecting GlcNAc and Alpha-2,3-Linked Sialic Acid Determinants Are Associated With Membrane Proteins of the More Metastatic/Aggressive Cell Lines. *J. Proteome Res.* **2014**, *13* (1), 277–288. [24295106](#).
- Schultz, M. J.; Swindall, A. F.; Bellis, S. L. Regulation of the Metastatic Cell Phenotype by Sialylated Glycans. *Cancer Metastasis Rev.* **2012**, *31* (3–4), 501–518. [22699311](#). [4079276](#).
- Bull, C.; Stoel, M. A.; den Brok, M. H.; Adema, G. J. Sialic Acids Sweeten a Tumor's Life. *Cancer Res.* **2014**, *74* (12), 3199–3204. [24830719](#).

24. Lu, J.; Isaji, T.; Im, S.; Fukuda, T.; Hashii, N.; Takakura, D.; et al. Beta-Galactoside Alpha2,6-Sialyltransferase 1 Promotes Transforming Growth Factor-Beta-Mediated Epithelial-Mesenchymal Transition. *J. Biol. Chem.* **2014**, *289* (50), 34627–34641. [25344606](#). 4263869.
25. Lu, J.; Isaji, T.; Im, S.; Fukuda, T.; Kameyama, A.; Gu, J. Expression of N-Acetylglucosaminyltransferase III Suppresses alpha2,3-Sialylation, and Its Distinctive Functions in Cell Migration Are Attributed to alpha2,6-Sialylation Levels. *J. Biol. Chem.* **2016**, *291* (11), 5708–5720. [26801611](#). 4786709.
26. Joziassse, D. H.; Bergh, M. L.; ter Hart, H. G.; Koppen, P. L.; Hooghwinkel, G. J.; Van den Eijnden, D. H. Purification and Enzymatic Characterization of CMP-Sialic Acid: Beta-Galactosyl1—3-N-Acetylglactosaminide Alpha 2—3-Sialyltransferase From Human Placenta. *J. Biol. Chem.* **1985**, *260* (8), 4941–4951. [3988739](#).
27. Joziassse, D. H.; Schiphorst, W. E.; Van den Eijnden, D. H.; Van Kuik, J. A.; Van Halbeek, H.; Vliegthart, J. F. Branch Specificity of Bovine Colostrum CMP-Sialic Acid: Gal Beta 1—4GlcNAc-R Alpha 2—6-Sialyltransferase. Sialylation of bi-, tri-, and Tetraantennary Oligosaccharides and Glycopeptides of the N-Acetylglactosamine Type. *J. Biol. Chem.* **1987**, *262* (5), 2025–2033. [3546284](#).
28. Guo, H. B.; Nairn, A.; Harris, K.; Randolph, M.; Alvarez-Manilla, G.; Moremen, K.; et al. Loss of Expression of N-Acetylglucosaminyltransferase Va Results in Altered Gene Expression of Glycosyltransferases and Galectins. *FEBS Lett.* **2008**, *582* (4), 527–535. [18230362](#). 3971636.
29. Qi, F.; Isaji, T.; Duan, C.; Yang, J.; Wang, Y.; Fukuda, T.; et al. ST3GAL3, ST3GAL4, and ST3GAL6 Differ in Their Regulation of Biological Functions Via the Specificities for the Alpha2,3-Sialylation of Target Proteins. *FASEB Journal* **2020**, *34* (1), 881–897. [31914669](#).
30. Lu, J.; Gu, J. Significance of Beta-Galactoside Alpha2,6 Sialyltransferase 1 in Cancers. *Molecules* **2015**, *20* (5), 7509–7527. [25919275](#).
31. Pinho, S. S.; Reis, C. A. Glycosylation in Cancer: Mechanisms and Clinical Implications. *Nat. Rev. Cancer* **2015**, *15* (9), 540–555. [26289314](#).
32. Swindall, A. F.; Londono-Joshi, A. I.; Schultz, M. J.; Fineberg, N.; Buchsbaum, D. J.; Bellis, S. L. ST6Gal-I Protein Expression is Upregulated in Human Epithelial Tumors and Correlates With Stem Cell Markers in Normal Tissues and Colon Cancer Cell Lines. *Cancer Res.* **2013**, *73* (7), 2368–2378. [23358684](#). 4038408.
33. Pastushenko, I.; Brisebarre, A.; Sifrim, A.; Fioramonti, M.; Revenco, T.; Boumahdi, S.; et al. Identification of the Tumour Transition States Occurring During EMT. *Nature* **2018**, *556* (7702), 463–468. [29670281](#).

＜糖鎖構造生物学部門＞

教授 山口 芳樹

講師 真鍋 法義

助手 大野 詩歩

糖鎖構造解析のための技術基盤の構築

生体分子としての糖鎖の機能を明らかにするためには、糖鎖の立体構造の特徴を理解し、レクチンや抗体など糖鎖結合分子による認識の構造基盤を解明することが重要であるとの立場で研究を進めている。本年度は昨年度に引き続き、糖鎖構造解析（実験および計算）の技術基盤の構築、および糖鎖に関連するタンパク質の大量発現システムの構築を目指した。

I. 糖鎖の動的構造解析

リビトール ($C_5H_{12}O_5$) は非環状の糖アルコールであり、分子中央に対称面をもつメソ化合物である(図 1)。生体内の構成成分としてはグラム陽性菌の細胞壁中に見られるタイコ酸の構成成分として報告されており、哺乳動物ではジストログリカン上の *O*-マンノース糖鎖中にも見出されている。リビトールリン酸トランスフェラーゼの遺伝的欠乏は筋ジストロフィーを引き起こすことから、骨格筋の機能においてリビトールは重要な役割を示すことが分かる。ラミニンは、リビトールを含有している

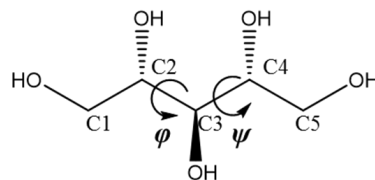


図 1. リビトールの化学構造と二面角の定義

O-マンノース糖鎖と相互作用することが知られており、リビトールはその非環状構造からラミニンと *O*-マンノース糖鎖を架橋する際のヒンジとして機能している可能性がある。したがって、リビトールの構造とコンホメーションダイナミクスを明らかにすることは、*O*-マンノース糖鎖の機能解明に貢献することができる。しかし、環状糖と比較して、非環状糖アルコールの構造特性とコンホメーションダイナミクスに関する知見は限られている。我々は NMR と計算化学的手法により、リビトールの安定構造および動的構造の解析を行った(1)。

結晶中でのリビトールのコンホメーションを解析するため、データベース (PDB および Cambridge Crystallographic Data Centre) からリビトール主鎖二面角を調べたところ、リビトール主鎖二面角は 180° , 60° , -60° を中心に分布していた。しかし二面角 φ と ψ は独立しておらず、相手の二面角の値を避けるような相反性が存在した。また、固

体および溶液中のリビトールの構造に関する情報を得るため、固体および溶液 ^{13}C -NMR を測定し、両 NMR スペクトルを比較したところ、リビトールの固体 ^{13}C -NMR において、C1 および C5 に由来するシグナルは異なる化学シフトを与えた。一方、溶液 ^{13}C -NMR を測定したところ、C1 と C5、C2 と C4 は同じ化学シフトで観測された。よって、リビトールは非対称なコンホメーションを安定構造とし得るが、溶液中では各コンホメーション間をすばやく遷移していることが示唆された。さらに、溶液 NMR において溶液中でのリビトールのコンホメーションの割合を評価するため、スピン結合定数 (3J) を求めカープラス型の式から二面角の情報を得ることを試みた。しかし、リビトールの ^1H -NMR スペクトルにおいてカップリングに高次の項が観察されたため、270 MHz、400 MHz、600 MHz の各共鳴周波数において ^1H -NMR スペクトルを測定し、NMR スペクトルの反復シミュレーションを行うことで 3J 値を求めた。その結果、リビトール主鎖二面角 φ および ψ の占有数の合計の比は、 $180^\circ : 60^\circ : -60^\circ = 55 : 7 : 38$ と見積もられた。この比から水溶液中においても φ と ψ は相反性を持つことが示唆された。さらにリビトールは分子中央に対称面をもつため、二面角 φ と ψ を区別して議論するために分子動力学計算を行い、コンホメーションの時間変化を観察した。その結果、データベース解析の結果で見られたように、 φ と ψ の一方が 180° 付近の場合、もう一方は $\pm 60^\circ$ 付近を占有する折れ曲がり構造であることが示唆された。同様にリビトールの 2 位と 4 位の水酸基が水素に置換されている 1,3,5-ペンタノールの分子動力学計算を行ったところ、リビトールよりも柔軟性が高く、直線構造を優先的に占有する傾向がみられた。これは、2 位と 4 位の水酸基がなくなることで直線構造を占有するようになったことを示していた。

以上から、リビトールは水溶液中で二面角 φ と ψ が相反性を持つ複数の非対称なコンホメーションの安定配座間を遷移していることが明らかになった(1)。さらにリビトールは、環状糖よりも柔軟な二面角を有するが、ある程度決まった二面角(180° , 60° , -60°)をとり、2 位と 4 位の水酸基間の反発により、非対称の折れ曲がり構造を安定構造とする傾向がみられた。以上の知見は、リビトールの動的構造と、*O*-マンノース糖鎖の機能解明のための基礎となる。

II. 糖タンパク質の構造機能関連の解析と応用

免疫グロブリン G (IgG) の Fc 領域と Fc γ 受容体および補体成分との相互作用は、Fc 領域に結合している糖鎖に依存している。溶液 NMR 法により Fc 領域に結合している糖鎖に着目して構造解析を行った。その結果、糖鎖のガラクトース残基の欠損が、Fc 領域の構造的なゆらぎを引き起こすことが示された(2)。

免疫グロブリン A (IgA) および免疫グロブリン M (IgM) は、通常、J 鎖の寄与に

より 2 量体または 5 量体になり，高分子 Ig 受容体 (pIgR) の分泌成分 (SC) に結合して粘膜表面に輸送される．IgA と IgM は，様々な免疫反応，特に粘膜免疫において極めて重要な役割を担っている．J 鎖と SC を含む IgA と IgM の立体構造やこれらの分子のジスルフィド結合や N 型糖鎖修飾について概説した(3)．

抗体薬物複合体 (ADC) は，細胞障害性薬剤をモノクローナル抗体に結合させたバイオ医薬品の一種であり，標的薬物送達を可能にする．近年，部位特異的結合により，薬物と抗体の比率を制御した ADC 製剤が様々な糖鎖工学的手法により開発されており，ADC 製剤の治療域，有効性，製造バッチ間の一貫性が向上している．抗体-薬物複合化のための様々な糖鎖工学的アプローチを要約し，次世代の ADC 開発における利点についてまとめた(4)．

III. レクチン受容体の構造と機能に関する研究

糖鎖は一般に分岐構造を有しており，そこから生み出される多様性は細胞接着や細胞内シグナリングなど，様々な生理機能を調節していることが明らかとなりつつある．最近になり，レクチンや糖転移酵素が糖鎖の分岐構造を特異的に認識する現象が見出されており，これまでのレクチンの認識の概念では単純に証明できないような新しい知見が数多く報告されている．この糖鎖を特徴づける分岐構造に着目し，核磁気共鳴 (NMR) 法や X 線結晶構造解析法などの手法により，糖鎖の各分岐それぞれに個性がもたらされる構造的な要因や，分岐型糖鎖に作用するレクチン・糖転移酵素の特異な性質の一端を明らかにした(5)．

$\beta(1,3)$ -グルカンは，真菌や植物の細胞壁の構成成分である．病原体の β グルカンは，宿主の防御システムにおいて非自己成分として認識されている．長鎖の β グルカンは三重らせん構造を形成することができ，その三次構造は β グルカン結合タンパク質との相互作用に深く影響すると考えられている． β グルカンの 3 次元的な構造特性と β グルカン結合タンパク質との相互作用の様式について総説としてまとめた(6)．また，レクチン受容体の立体構造情報の蓄積により，微生物糖鎖の認識様式はいくつかのグループに分類されることがわかってきた．代表的な哺乳類レクチン受容体による病原体の認識機構について，知見をまとめた(7)．

SHA は，ヒト B 型赤血球を凝集させる L-ラムノースおよび D-ガラクトース結合型レクチン受容体である．ゲノム解析とタンパク質生化学的解析を用いて，SHA を分泌する *Streptomyces* 株を同定し，これらの推定タンパク質の発現と結合活性を検討した(8)．

IV. その他

本年度も内外の共同研究を進め、主に生体分子の構造・モデル解析を行うことによって成果発表に貢献した。脳内に蓄積する蛋白質線維を感度よく検出することは、神経変性疾患の発症を早期に捉えることにつながるため、様々な PET プローブが世界中で開発されている。しかしながら、前頭側頭葉変性症 (FTLD) のタウ封入体の高感度検出は困難であった。PM-PBB3 というイメージングプローブが開発され、様々なタウ沈着物を検出することに成功した(9)。

自然発症の頭蓋内圧亢進症 (SIH) は、脳脊髄液 (CSF) の漏出によって引き起こされる。SIH の診断に 2 つのアイソフォームを持つトランスフェリンが有用なバイオマーカーとして利用できることを示した(10)。また、アルツハイマー病患者において、トランスフェリン上の糖鎖が高くマンノシル化していることを示した(11)。これは、アルツハイマー病の新しいバイオマーカーになり得る。

腸管運動異常はいくつかのミトコンドリア脳筋症の特徴であり、TYMP や POLG などの遺伝子の変異が、これらの希少疾患に関連していることが判明している。新たにリガーゼ III (LIG3) 遺伝子に腸管運動障害、脳症、神経筋異常を特徴とするミトコンドリア脳筋症を引き起こす変異を同定した(12)。

<発表論文>

1. Ohno, S., Manabe, N., Yamaguchi, T., Uzawa, J., and Yamaguchi, Y. (2021) Ribitol in solution is an equilibrium of asymmetric conformations. *Molecules* **26**, 5471
2. Yanaka, S., Yamaguchi, Y., Takizawa, T., Miyanoiri, Y., Yogo, R., Shimada, I., and Kato, K. (2021) NMR assignments of the *N*-glycans of the Fc fragment of mouse immunoglobulin G2b glycoprotein. *Biomol NMR Assign* **15**, 187-192
3. Pan, S., Manabe, N., and Yamaguchi, Y. (2021) 3D structures of IgA, IgM, and components. *Int J Mol Sci* **22**, 12776
4. Manabe, S., and Yamaguchi, Y. (2021) Antibody glycoengineering and homogeneous antibody-drug conjugate preparation. *Chem Rec* **21**, 3005-3014
5. 山口芳樹. (2021) 分岐型糖鎖の高次構造と相互作用原理の解明. *BIO Clinica* **36**, 79-84
6. Manabe, N., and Yamaguchi, Y. (2021) 3D structural insights into β -glucans and their binding proteins. *Int J Mol Sci* **22**, 1578
7. Manabe, N., and Yamaguchi, Y. (2021) 3D structural view of pathogen recognition by mammalian lectin receptors. *Front Mol Biosci* **8**, 670780

8. Fujita-Yamaguchi, Y., Muramatsu, H., Tapia, A., Bagramyan, K., Desai, M., Takehana, Y., Igarashi, M., Yamaguchi, Y., and Kalkum, M. (2021) Proteolytic processing, maturation, and unique synteny of the *Streptomyces* hemagglutinin SHA. *Microbiol Spectr* **9**, e0076621
9. Tagai, K., Ono, M., Kubota, M., Kitamura, S., Takahata, K., Seki, C., Takado, Y., Shinotoh, H., Sano, Y., Yamamoto, Y., Matsuoka, K., Takuwa, H., Shimojo, M., Takahashi, M., Kawamura, K., Kikuchi, T., Okada, M., Akiyama, H., Suzuki, H., Onaya, M., Takeda, T., Arai, K., Arai, N., Araki, N., Saito, Y., Trojanowski, J. Q., Lee, V. M. Y., Mishra, S. K., Yamaguchi, Y., Kimura, Y., Ichise, M., Tomita, Y., Zhang, M. R., Suhara, T., Shigeta, M., Sahara, N., Higuchi, M., and Shimada, H. (2021) High-contrast *in vivo* imaging of tau pathologies in Alzheimer's and non-Alzheimer's disease tauopathies. *Neuron* **109**, 42-58 e48
10. Iijima, J., Hoshi, K., Ito, H., Kanno, M., Murakami, Y., Takahashi, K., Matsumoto, K., Yamaguchi, Y., Nakajima, M., Miyajima, M., Arai, H., Kanai, M., Kitazume, S., Honda, T., and Hashimoto, Y. (2021) Total transferrin in cerebrospinal fluid is a novel biomarker for spontaneous intracranial hypotension. *Fukushima J Med Sci* **67**, 64-70
11. Hoshi, K., Ito, H., Abe, E., Fuwa, T. J., Kanno, M., Murakami, Y., Abe, M., Murakami, T., Yoshihara, A., Ugawa, Y., Saito, T., Saido, T. C., Matsumoto, K., Yamaguchi, Y., Furukawa, K., Arai, H., Kanai, M., Miyajima, M., Arai, H., Ogawa, N., Akatsu, H., Hashizume, Y., Tateno, H., Honda, T., and Hashimoto, Y. (2021) Transferrin biosynthesized in the brain is a novel biomarker for Alzheimer's disease. *Metabolites* **11**, 616
12. Bonora, E., Chakrabarty, S., Kellaris, G., Tsutsumi, M., Bianco, F., Bergamini, C., Ullah, F., Isidori, F., Liparulo, I., Diquigiovanni, C., Masin, L., Rizzardi, N., Cratere, M. G., Boschetti, E., Papa, V., Maresca, A., Cenacchi, G., Casadio, R., Martelli, P., Matera, I., Ceccherini, I., Fato, R., Raiola, G., Arrigo, S., Signa, S., Sementa, A. R., Severino, M., Striano, P., Fiorillo, C., Goto, T., Uchino, S., Oyazato, Y., Nakamura, H., Mishra, S. K., Yeh, Y. S., Kato, T., Nozu, K., Tanboon, J., Morioka, I., Nishino, I., Toda, T., Goto, Y. I., Ohtake, A., Kosaki, K., Yamaguchi, Y., Nonaka, I., Iijima, K., Mimaki, M., Kurahashi, H., Raams, A., MacInnes, A., Alders, M., Engelen, M., Linthorst, G., de Koning, T., den Dunnen, W., Dijkstra, G., van Spaendonck, K., van Gent, D. C., Aronica, E. M., Picco, P., Carelli, V., Seri, M., Katsanis, N., Duijkers, F. A. M., Taniguchi-Ikeda, M., and De Giorgio, R. (2021) Biallelic variants in *LIG3* cause a novel mitochondrial neurogastrointestinal encephalomyopathy. *Brain* **144**, 1451-1466

<学会発表>

- ・液体クロマトグラフィー/イオンモビリティ質量分析法を利用した 57 種類の *N*-結合型糖鎖の保持時間・衝突断面積・*m/z* のデータセット

真鍋法義, 大野詩歩, 川瀬泰司^a, 廣瀬賢治^a, 山口芳樹

(日本ウォーターズ^a)

第 33 回バイオメディカル分析科学シンポジウム (BMAS2021), 京都, 2021 年 9 月, 演題番号 P23

- ・MUC1 糖ペプチドと抗 MUC1 抗体 MY.1E12 の NMR 相互作用解析とドッキングシミュレーション

國府 涼香, 倉谷 太豪, 高橋 優花, 大野 詩歩, 真鍋 法義, 清水 弘樹^a,

千葉 靖典^a, 伝田 香里^b, 築地 信^c, 入村 達郎^b, 山口 芳樹

(産総研細胞分子工学^a, 順天堂大院医^b, 星薬科大薬^c)

第 15 回東北糖鎖研究会, 岩手, 2021 年 9 月, 演題番号 O-5

- ・非環状糖鎖成分リビトールリン酸の構造解析

大野 詩歩, 真鍋 法義, 田村 純一^a, 山口 芳樹

(鳥取大農^a)

第 15 回東北糖鎖研究会, 岩手, 2021 年 9 月, 演題番号 P-7

- ・Structural role of *N*-glycosylation on human IgA and J chain

Pan Shunli, Noriyoshi Manabe, Yoshiki Yamaguchi

第 15 回東北糖鎖研究会, 岩手, 2021 年 9 月, 演題番号 P-8

- ・新規ミスセンス変異を認めた本邦初の B4GALNT1 関連神経変性症の 1 例

中村 勝哉^{a,b}, 土田 奈緒美^c, 井ノ口 仁一, 小島 朋美^a, 池田 淳司^b, 小平 農^b, 稲森 啓一郎, 永福 正和, 新田 昂大, 真鍋 法義, 大野 詩歩, 山口 芳樹, 下畑 享良^d, 松本 直通^e, 古庄 知己^{a,e,f}, 関島 良樹^b

(信州大学医学部附属病院 遺伝子医療研究センター^a, 信州大学医学部 脳神経内科 リウマチ・膠原病内科^b, 横浜市立大学大学院医学研究科 遺伝学^c, 岐阜大学大学院医学系研究科 脳神経内科学分野^d, 信州大学医学部 遺伝医学教室^e, 信州大学医学部 クリニカル・シーケンス学講座^f)

日本人類遺伝学会第 66 回大会第 28 回日本遺伝子診療学会大会合同開催

横浜, 2021 年 10 月, 演題番号 P15-16

- ・タンデムリビトールリン酸含有 *O*-マンノシルグリカンの系統的合成とその糖鎖

田村 純一^a, 田村 敬裕^a, 真鍋 法義, 大野 詩歩, 山口 芳樹, 萬谷 博^b, 遠藤 玉夫^b

(鳥取大院連大農^a, 都健康長寿研^b)

第 40 回日本糖質学会年会, 鹿児島, 2021 年 10 月, 演題番号 1B-01(A)

• **NMR 法による GlcA/Xyl リピートとラミニンの相互作用様式の解析**

真鍋 法義, 大野 詩歩, 田村 敬裕^a, 田村 純一^a, 萬谷 博^b, 遠藤 玉夫^b, 山口 芳樹

(鳥取大院連大農^a, 都健康長寿研^b)

第 40 回日本糖質学会年会, 鹿児島, 2021 年 10 月, 演題番号 1C-03(B)

• **抗 iPS 細胞抗体 R-17F と lacto-*N*-fucopentaose I の相互作用解析**

大野 詩歩, 齋藤 祐希, 真鍋 法義, 湯浅 徳行^a, 松崎 祐二^a, 築地 信^b, 川寄 敏祐^c, 山口 芳樹

(東京化成工業^a, 星薬大薬^b, 立命館大^c)

第 40 回日本糖質学会年会, 鹿児島, 2021 年 10 月, 演題番号 P-127

• **全ヒト糖鎖関連遺伝子 Variant の網羅的抽出と解析**

西原 祥子^a, 木下 聖子^a, 梅谷 内晶^a, 細田 正恵^a, 伊藤 和義^a, 山口 芳樹, 真鍋 法義, 大野 詩歩, 稲森 啓一郎, 井ノ口 仁一, 灘中 里美^b, 北川 裕之^b, 城田 松之^c, 木下 賢吾^c

(創価大糖鎖生命システム融合研究所^a, 神戸薬科大^b, 東北大東北メディカル・メガバンク機構^c)

第 40 回日本糖質学会年会, 鹿児島, 2021 年 10 月, 演題番号 3C-02(A)

• **3D structural view of β -glucan and its receptors**

Yoshiki Yamaguchi and Noriyoshi Manabe

第 65 回日本医真菌学会総会・学術総会/真菌症フォーラム 2021, Tokyo, Japan, Oct. 2021, 16:10-17:50

• **水溶性・不溶性 β -glucan と Dectin-1 受容体との相互作用解析**

真鍋 法義

第 5 回東北医真菌研究会, 仙台, 2021 年 12 月

• **Structural role of *N*-glycosylation on human IgA and J-chain**

Shunli Pan, Noriyoshi Manabe, Yoshiki Yamaguchi

日本薬学会第 142 年会, オンライン開催, 2022 年 3 月, 演題番号 26P06-am1-10S

• **MUC1 糖ペプチドと抗 MUC1 抗体 MY.1E12 の相互作用解析**

國府 涼香, 倉谷 太豪, 高橋 優花, 大野 詩歩, 真鍋 法義, 清水 弘樹^a, 千葉 靖典^a, 伝田 香里^b, 築地 信^c, 入村 達郎^b, 山口 芳樹

(産総研細胞分子工学^a, 順天堂大院医^b, 星薬科大薬^c)

日本薬学会第 142 年会, オンライン開催, 2022 年 3 月, 演題番号 26P01-am1-46S

• **Lacto-*N*-fucopentaose I の立体構造および抗 iPS 細胞抗体 R-17F との相互作用の解析**

大野 詩歩, 大内 陽翔, 齋藤 祐希, 真鍋 法義, 湯浅 徳行^a, 松崎 祐二^a, 築地 信^b, 川崎 敏祐^c, 山口 芳樹

(東京化成工業^a, 星薬科大薬^b, 立命館大^c)

日本薬学会第 142 年会, オンライン開催, 2022 年 3 月, 演題番号 26L-pm09

• **NMR 法による α Xyl- β GlcA の繰り返し構造とラミニンの相互作用解析**

真鍋 法義, 大野 詩歩, 伊藤 良汰, 田村 敬裕^a, 田村 純一^a, 萬谷 博^b, 遠藤 玉夫^b, 山口 芳樹

(鳥取大院連大農^a, 都健康長寿研^b)

日本薬学会第 142 年会, オンライン開催, 2022 年 3 月, 演題番号 27C-pm05

• **Dectin-1 と不溶性 β -グルカン・*Euglena gracilis* EOD-1 由来 paramylon との相互作用解析**

千葉 花子, 真鍋 法義, 内藤 淳子^a, 西田 典永^a, 高橋 円^a, 大野 尚仁^b, 山口 芳樹

(神鋼環境ソリューション^a, 東京薬大薬^b)

日本薬学会第 142 年会, オンライン開催, 2022 年 3 月, 演題番号 28N-pm11S



Review

3D Structures of IgA, IgM, and Components

Shunli Pan, Noriyoshi Manabe  and Yoshiki Yamaguchi * 

Division of Structural Glycobiology, Institute of Molecular Biomembrane and Glycobiology, Tohoku Medical and Pharmaceutical University, 4-4-1 Komatsushima, Aoba-ku, Sendai 981-8558, Miyagi, Japan; 22052501@is.tohoku-mpu.ac.jp (S.P.); manabe@tohoku-mpu.ac.jp (N.M.)

* Correspondence: yyoshiki@tohoku-mpu.ac.jp; Tel.: +81-22-727-0208

Abstract: Immunoglobulin G (IgG) is currently the most studied immunoglobulin class and is frequently used in antibody therapeutics in which its beneficial effector functions are exploited. IgG is composed of two heavy chains and two light chains, forming the basic antibody monomeric unit. In contrast, immunoglobulin A (IgA) and immunoglobulin M (IgM) are usually assembled into dimers or pentamers with the contribution of joining (J)-chains, which bind to the secretory component (SC) of the polymeric Ig receptor (pIgR) and are transported to the mucosal surface. IgA and IgM play a pivotal role in various immune responses, especially in mucosal immunity. Due to their structural complexity, 3D structural study of these molecules at atomic scale has been slow. With the emergence of cryo-EM and X-ray crystallographic techniques and the growing interest in the structure–function relationships of IgA and IgM, atomic-scale structural information on IgA-Fc and IgM-Fc has been accumulating. Here, we examine the 3D structures of IgA and IgM, including the J-chain and SC. Disulfide bridging and N-glycosylation on these molecules are also summarized. With the increasing information of structure–function relationships, IgA- and IgM-based monoclonal antibodies will be an effective option in the therapeutic field.



Citation: Pan, S.; Manabe, N.; Yamaguchi, Y. 3D Structures of IgA, IgM, and Components. *Int. J. Mol. Sci.* **2021**, *22*, 12776. <https://doi.org/10.3390/ijms222312776>

Academic Editor: Manlio Ferrarini

Received: 6 November 2021

Accepted: 23 November 2021

Published: 26 November 2021

Publisher's Note: MDPI stays neutral with regard to jurisdictional claims in published maps and institutional affiliations.



Copyright: © 2021 by the authors. Licensee MDPI, Basel, Switzerland. This article is an open access article distributed under the terms and conditions of the Creative Commons Attribution (CC BY) license (<https://creativecommons.org/licenses/by/4.0/>).

Keywords: IgA; IgM; J-chain; secretory component; glycosylation; molecular assembly; disulfide bridge; 3D structure

1. Introduction

Immunoglobulins (Igs) are categorized into several classes (IgM, IgD, IgA, IgG, and IgE), and all play an invaluable role in the immune response to pathogens. Natural IgG is a monomer composed of two heavy chains and two light chains. This simple structure allows relatively easy expression and purification. IgG is the most studied immunoglobulin class and is frequently used in antibody therapeutics. In contrast, IgA was initially considered to be a non-inflammatory antibody for the maintenance of mucosal homeostasis [1]. It has since been found that the different assembly forms of IgA and IgM and their interaction with different receptors allow them to actively or passively inhibit or initiate inflammatory responses, thus forming the basis of mucosal immunity [2–4]. Unlike IgG, IgA and IgM are assembled into dimers or pentamers in the presence of J-chains. Moreover, they are transported to the mucosal surfaces by a secretory component (SC) as the first-line defense against infections [5]. Due to this structural complexity and inherent flexibility, 3D structural study at atomic scale has only recently commenced. Until now, structure–function relationships could only be discussed in crude terms based on low-resolution images and homology models. Without detailed knowledge of the 3D atomic structure and species differences, the development of this class of antibody therapeutics has been impeded. This situation is improving rapidly, and now atomic-scale structural information on IgA and IgM molecules is available due to the use of cryogenic electron microscopy (cryo-EM) and X-ray crystallographic techniques, which reveal the mode of molecular assembly. Electron densities originating from attached N-linked glycans have

been partially solved, and these should help gain a greater understanding of the role of *N*-glycan modifications in the functions of IgM and IgA.

2. Structure of IgA

IgA plays an important role in mucosal immunity and is the most abundant immunoglobulin, with even more being produced than the sum of the other immunoglobulins [6]. Unlike other human immunoglobulins, IgA exists either as a monomer or as soluble polymers. Only polymeric IgA can bind to polymeric immunoglobulin receptors (pIgR) for transcytosis, with the presence of J-chain being required for binding [7–9]. In common with other immunoglobulins, the IgA monomer consists of two identical heavy chains and two identical light chains forming a Y-shape structure (Figure 1). Each chain extends a variable region from its N-terminal, followed by a constant region. The heavy chains of IgA are composed of four domains (V_H , $C_{\alpha 1}$, $C_{\alpha 2}$, and $C_{\alpha 3}$), while the light chains are divided into two domains (V_L and C_L) [10]. The hinge region of IgA lies between the $C_{\alpha 1}$ and $C_{\alpha 2}$ structural domains of each heavy chain. The hinge affords the flexibility to the whole IgA molecule. This is critical for its activity, and it is this region that differs most between the two subclasses IgA1 and IgA2 (being particularly extensive in human IgA1 but absent in human IgA2). Unlike IgG, there is an 18-residue tailpiece extension at the C-terminus of the IgA and IgM heavy chains, which is essential for immunoglobulin assembly [11]. Fab is composed of V_H , $C_{\alpha 1}$, V_L , and C_L domains and engaged in antigen binding. Fc comprises two $C_{\alpha 2}$ and two $C_{\alpha 3}$ domains, responsible for triggering effector functions through interaction with complements or Fc_{α} receptors [3]. Fc is stabilized by several intra-molecular disulfide bonds, Cys266–Cys323 ($C_{\alpha 2}$), Cys369–Cys432 ($C_{\alpha 3}$), and every Cys242 forms an inter-chain disulfide bond with the Cys299 of another chain (Figure 1). The major differences between IgA1 and IgA2 are the hinge region (an octapeptide sequence Pro-Ser-Thr-Pro-Pro-Thr-Pro-Ser is repeated in IgA1) and the number and location of *O*- and *N*-glycans [7,12,13]. The Cys133 of IgA1 $C_{\alpha 1}$ forms a disulfide bond with the light chain, which is absent in IgA2 [14]. There are three IgA2 allotypic variants: m1, m2, and mn. These allotypes differ in disulfide bridging between a heavy chain and light chain so that Cys220 forms a covalent linkage when followed by Arg221 (IgA2 m2 and IgA2 mn) but not by Pro221 (IgA2 m1). In IgA2 m1, the replacement of Arg221 with Pro221 introduces a kink in the peptide backbone, which precludes the formation of heavy chain-light chain disulfide bridges but instead induces the formation of light chain-light chain disulfide bonds [13–16]. In contrast to the previous speculation that IgA2 mn could form heavy chain-light chain disulfide bonds in the absence of Cys220, mutation of Cys241 or Cys242 interferes with such disulfide bond formation [17]. Serum IgA molecules are mostly monomeric, while secretory IgA molecules are found as dimers and, to a lesser extent, as trimers and tetramers. In the dimer, two IgA molecules are linked together by another polypeptide designated as J-chain. Dimeric IgA is bound by the pIgR on the basolateral surface of epithelial cells, followed by the secretory component (SC) of the receptor covalently binding to dIgA to form secretory IgA (sIgA) [18,19].

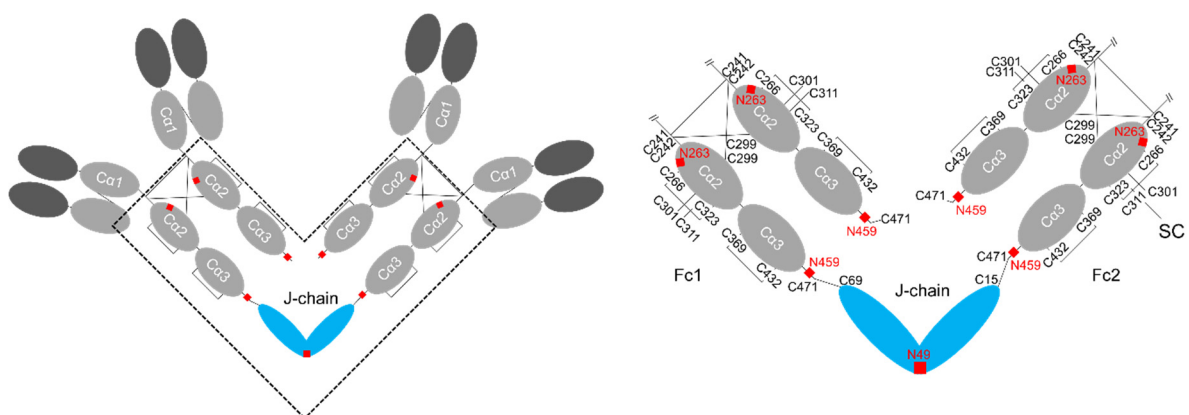


Figure 1. Schematic drawings of human IgA. Disulfide bonding and *N*-glycosylation sites are indicated.

Crystallization is often difficult due to the inherent flexibility of intact IgA monomers. Earlier electron microscopy (EM) studies showed that sIgA has a double-Y-like shape [20]. With the significant advances in cryo-EM in recent years, three-dimensional structures of sIgA-Fc dimers have been determined [21]. The two Fc α are arranged in a boomerang-like shape with four tailpiece β -strands bundled together to mediate the interactions between the two Fc α molecules (Figure 2) [21,22]. The dIgA is further stabilized through disulfide bridges between the Fc tail (Cys471) and the J-chain (Cys15 or Cys69), in which two parallel β -strands of Fc1 and Fc2 extend to the bottom and top sheets of the twisted J-chain β -sandwich. In the sIgA structure, interactions between SC domains and dIgA (disulfide bonding between Cys468 of SC and Cys311 in the C α 2 domain) stabilize a bent and tilted relationship (an angle of 110° caudally) between two IgA monomers. Two or three additional Fcs are added to the plane of the original dimer to form a higher-order multimer [21–25].

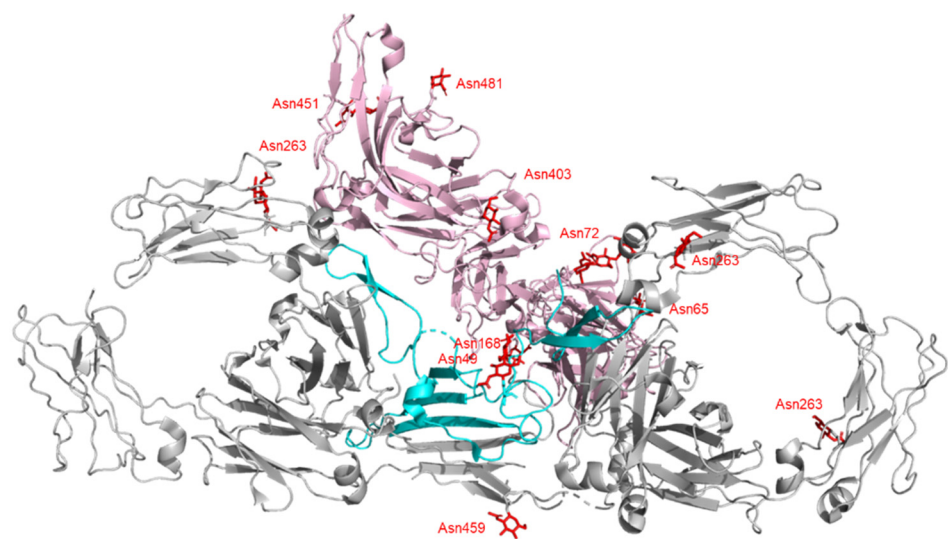


Figure 2. 3D structure of human IgA-Fc dimer (gray) in complex with J-chain (sky blue) and SC (pink) determined by cryo-EM analysis (PDB ID: 6UE7). Glycan residues are shown in red with stick representation.

Amino acid sequences of IgA show significant species differences in mammals and birds; however, *N*-linked glycosylation sites of the tailpiece are well conserved [26]. Both isotypes of IgA have two conserved *N*-linked glycosylation sites, Asn263 in C α 2 and Asn459 in the tail piece. Asn263 has mostly biantennary complex-type glycan with α 2-6-linked sialic acids, while Asn459 is dominated by triantennary glycan with α 2-6 and α 2-3-linked sialic acids [27,28]. *N*-linked glycans at Asn263 in C α 2 are located on the outer surface of Fc to avoid potential instability caused by considerable surface exposure of the unpaired C α 2 structural domain [23,29]. Recent studies suggest that *N*-glycan attached on Asn263 does not impact IgA binding to Fc α R1 [30], consistent with earlier reports [31,32]. Asn459 in the IgA2 tail piece has complex- and high mannose-type glycans but is not fully glycosylated [33]. The glycan controls the formation of IgA polymers, and sialic acid residues found in the complex *N*-linked glycan mediate antiviral activity [30,33]. The sialic acid residues directly interact with certain viruses, seemingly acting as bait to neutralize them [30]. Human IgA2 has additional *N*-glycosylation sites (Asn166 in the C α 1 and Asn337 in the C α 2), and IgA2m(2) has an additional *N*-linked glycan at Asn211 in the C α 1 domain. These additional sites attach more neutralizing glycans, which creates a greater proinflammatory response of neutrophils and macrophages [31,34–36]. However, details of the mechanism are not known.

3. Structure of IgM

Immunoglobulin M (IgM) is another abundant antibody subclass active in human mucosal immunity, providing the first line of defense against pathogens [18,37]. The predominant form of mouse and human IgM antibodies is pentameric, but there are also small amounts of hexamers and monomers [38]. The multiple antigen-binding sites give IgM a higher apparent affinity for antigen. Each IgM monomer is composed of two heavy chains with five domains (V_H , $C_{\mu 1}$, $C_{\mu 2}$, $C_{\mu 3}$, and $C_{\mu 4}$) and two light chains with two domains (V_L , C_L). The heavy chains are covalently linked with an inter-chain disulfide bond Cys337–Cys337, and each light chain is bonded to Cys136 in the heavy chain (Figure 3). Every Fc is stabilized with two intra-molecular disulfide bonds: Cys367–Cys426 ($C_{\mu 3}$) and Cys474–Cys536 ($C_{\mu 4}$). According to the sequence alignment, $C_{\mu 1}$, $C_{\mu 3}$, and $C_{\mu 4}$ of IgM are equivalent to the $C_{\gamma 1}$, $C_{\gamma 2}$, and $C_{\gamma 3}$ of IgG. $C_{\mu 2}$ of IgM is an additional constant domain that corresponds to the hinge region of IgG, providing the flexibility necessary for binding to antigens on cell surfaces. Cys414 of the $C_{\mu 3}$ domain is essential for IgM polymerization and can form an inter-monomeric disulfide bond with the Cys414 of an adjacent monomer. Like IgA, there is a tailpiece with a short 18 amino acid peptide sequence at the C-terminus of the heavy chain. The Cys575–Cys575 disulfide bond in the tailpieces is critical for IgM polymerization. Five IgM monomers are linked by disulfide bonds to each other and to the J-chain to form a pentamer, while the J-chain is absent in the IgM hexamer [38–43].

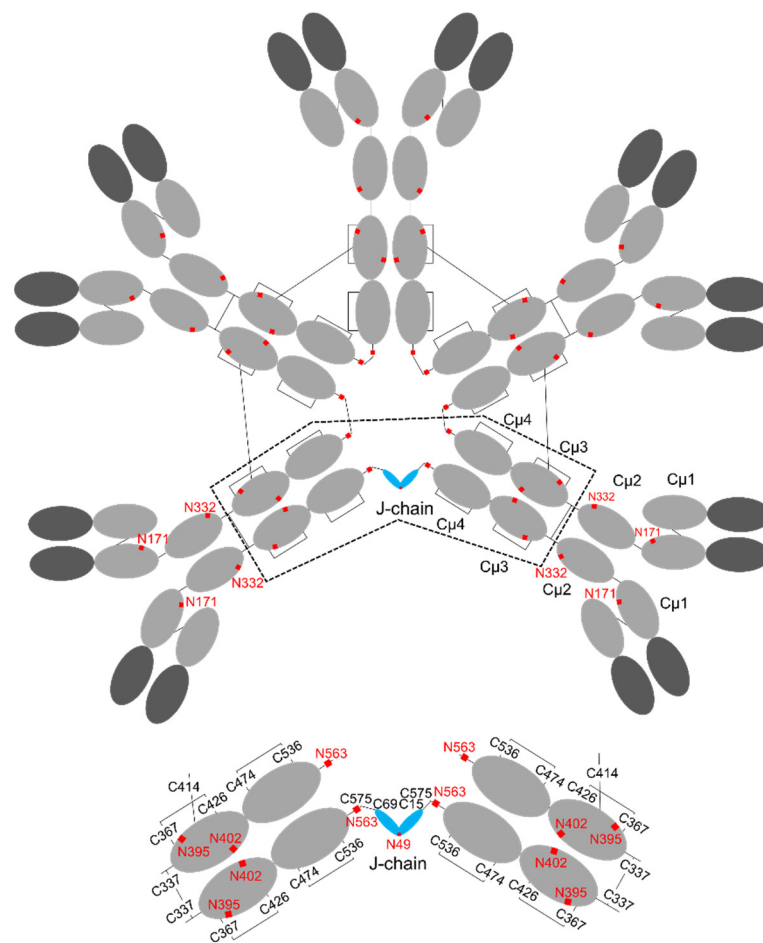


Figure 3. Schematic drawings of human IgM pentamer. Disulfide bonding and N-glycosylation sites are indicated.

The molecular size of a fully assembled IgM complex is nearly a million Daltons; hence, determination of its detailed structure is challenging. Earlier studies suggested

that the pentamer in the presence of the J-chain has a star-like appearance with five-fold symmetry [44,45]. However, a recent cryo-EM study proves that five Fc_{μ} units are arranged in almost perfect hexagonal symmetry with a 61° gap occupied by the J-chain, and a triangular SC perpendicularly docked to the Fc_{μ} -J near-planar structure to form secretory IgM (sIgM) [46] (Figure 4). $C_{\mu}3$ - $C_{\mu}4$ and the tailpiece play important roles in the formation of IgM pentamers. Two neighboring $C_{\mu}3$ -Cys414 form interchain disulfide bonds, and two neighboring IgM- $C_{\mu}4$ domains interact with each other by their FG loops (a loop between F and G strands). Ten tailpieces are arranged into two five-stranded parallel β -sheets. The two β -sheets stack together in an antiparallel fashion, which is critical for IgM pentamer stability. Cys575 residues of two adjacent Fc_{μ} form a disulfide bond and Cys575 on the side of the hexagonal gap is linked to the J-chain, which is essential for IgM oligomerization [44,46,47].

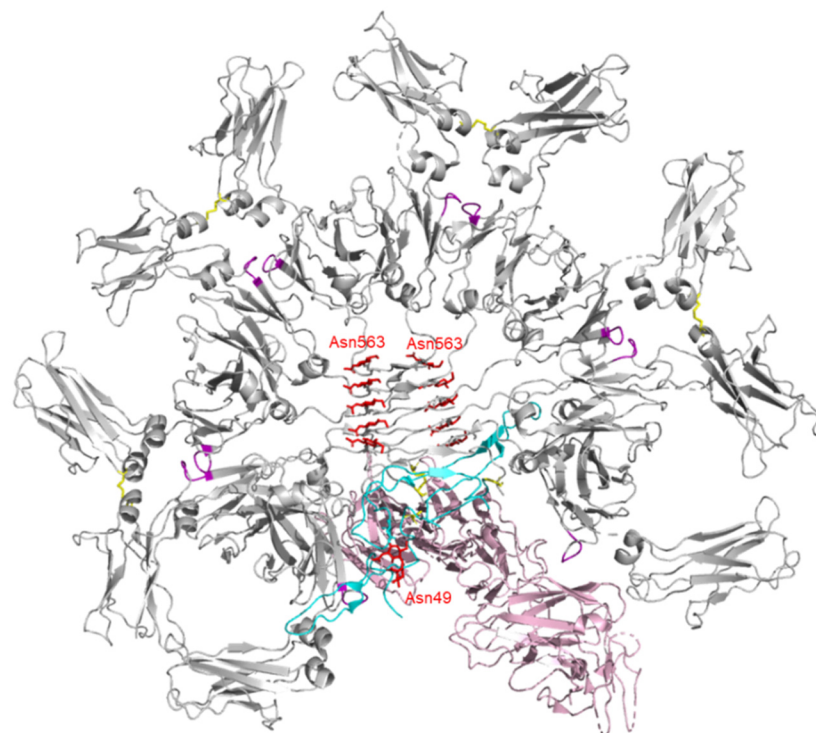


Figure 4. 3D structure of human IgM-Fc pentamer (gray) in complex with J-chain (sky blue) and SC (pink) determined by cryo-EM analysis (PDB ID: 6KXS). Cys414 disulfide bonds and FG loops in Fc are highlighted in yellow and magenta, respectively. Glycan residues are shown in red with stick representation.

There are five conserved *N*-glycosylation sites: Asn171 ($C_{\mu}1$), Asn332 ($C_{\mu}2$), Asn395 ($C_{\mu}3$), Asn402 ($C_{\mu}3$), and Asn563 (tailpiece): Asn171, Asn332, and Asn395 are exposed to solvent with complex-type glycans (differences in glycan branching and sialylation) attached. These glycans are vulnerable to enzymatic processing and involved in the binding of IgM to T-cell surface receptors (asialo IgM remains bound, while sialylated IgM is internalized) [48]. The glycosylation of Asn402 (as with Asn297 of IgG) is crucial for complement activation with high mannose-type glycans. Asn563 of the tailpiece, located in the center of the IgM polymer, possesses high-mannose-type glycans which facilitate assembly of the IgM monomer and are necessary to prevent IgM aggregation [49,50].

4. Structure of J-chain

The J-chain was identified in 1971 in fractions from sIgA and sIgM, but not in those from IgG, IgE, and IgD [51]. It is highly conserved among different species, and there is no other homologous protein [52]. Human J-chain is a 15-kDa acidic polypeptide composed

of 137 amino acids, including six Cys residues involved in intramolecular disulfide bridges (Cys12–Cys100, Cys71–Cys91, and Cys108–Cys133) and two in intermolecular (Cys15 and Cys69) disulfides to the Fc of IgM and IgA (Figure 5) [53]. Although various predictions of the structure of the J-chain have been made based on the pattern of disulfide bonds, its structure has not been resolved until recently. Now, with the structures of sIgA and sIgM determined, the three-dimensional structure of the J-chain is resolved in their polymers. As predicted, the J-chain consists almost entirely of β -sheets and loops in the IgA dimer and the IgM pentamer [21,46,53]. In the IgA dimer, the central region of the J-chain contains four β -strands (β 1– β 4) and three hairpins (Figure 5). β 1– β 3 strands are assembled into a β -sheet together with two tailpiece strands of Fc $_{\alpha}$ 2. Strand β 4 is packed onto the tailpieces of Fc $_{\alpha}$ 1 to form another β -sheet. These two β -sheets fold into a single β -sandwich-like domain through strong hydrophobic interactions. β -hairpins 1 and 2 interact with the top surface of Fc2, while the bottom surface of Fc1 interacts with β -hairpin 3. β -hairpin 1, β 3– β 4 loop, β -hairpin 2, and C-terminal β -hairpin 3 form four lassos to further interact with the Fc $_{\alpha}$. Cys69 and Cys15 of the J-chain form disulfide bonds with the penultimate cysteine residues Cys471 of Fc $_{\alpha}$ 1 and Fc $_{\alpha}$ 2, which are the foundation for the locking of two IgA monomers to the J-chain [21,22,25]. As in the IgA dimer, the J-chain forms a radially centered β sandwich-like structure with the tailpieces of five Fcs in the IgM pentamer. The β 3 and β 4 strands are packed on the tailpieces of Fc5 and Fc1 through a disulfide bond Cys15 (J-chain)–Cys575 (Fc1), while the β 2– β 3 loop interacts with the base of Fc5 through a disulfide bond C69 (J-chain)–Cys575 (Fc5). The hairpin of the C-terminal wing forms extensive hydrophobic interactions with Fc1 and also interplays with pIgR/SC, allowing the IgM to attach to the receptor [46]. The biggest difference between the J-chains of the sIgA and sIgM structures is that β -hairpin 2 in the IgA dimer is not observed in IgM [54]. The structure of the J-chain without IgA/IgM has not been reported yet. There is a conserved *N*-glycosylation site at Asn49 of the human J-chain. The attached oligosaccharides are represented in three forms, each differing in the amount of sialic acid, 30% contain two sialic acid residues, 55% contain a sialic acid residue on the α 1,3-linked mannose branch, and 15% have no sialic acid but two terminal galactose residues [55]. The glycosylated murine J-chain mutant with an Asn48 (corresponding to Asn49 of human J-chain) to Ala substitution in human IgA1 has reduced dimer assembly [56]. The *N*-glycosylation site of the J-chain is distant from any SC–pIgA interaction interface in sIgA, which may be relevant for promoting host and pathogen lectin binding [15,22,25]. Likewise, the glycan attached Asn49 is completely exposed to the surface of the human sIgM molecule without any contact with protein [46].

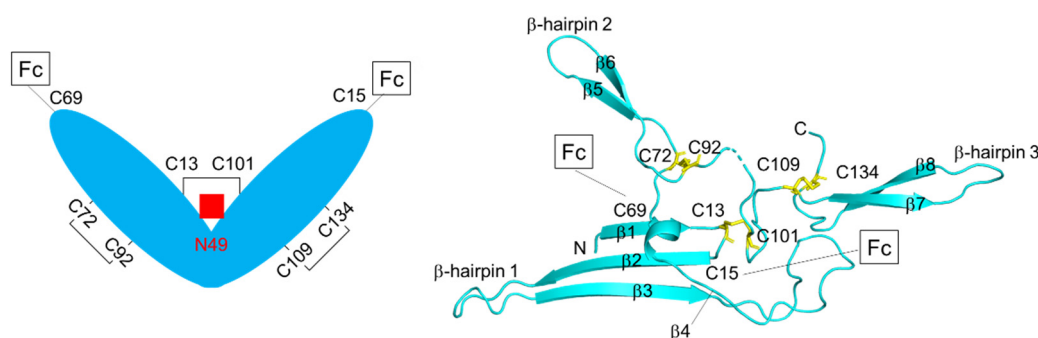


Figure 5. Schematic drawings of human J-chain. Disulfide bonding and *N*-glycosylation site are indicated. 3D structure of human J-chain bound to IgA-Fc is shown on the right (PDB ID: 6UE7). IgA-Fc and SC are omitted for clarity.

5. Structure of Secretory Component

Human pIgR plays a dominant role in mucosal immunity. The extracellular ligand-binding portion (known as SC) of pIgR is proteolytically cleaved and transported into mucosal secretions along with dimeric IgA (dIgA) or pentameric IgM (pIgM) [5]. SCs bind and exclude pathogens as part of the immune response [5,57,58]. Human SC contains

620 amino acids, forming five Ig-like domains named D1–D5 from the N-terminus [59]. There is a short non-immunoglobulin-like sequence between the D5 terminus and the membrane [60]. The three-dimensional structure of SC in a free form has been determined by X-ray crystallography, and the five domains (D1–D5) are organized into a compact, plate-like isosceles triangle (Figure 6). D2–D3 and D4–D5 form two edges, and D1 comes into contact with D2 and D4–D5 to form a third edge [19]. There are seven *N*-glycosylation sites (Asn65, 72, 117, 168, 403, 451, and 481), with fucosylated and sialylated *N*-glycans [61]. The ordered glycans are observed at four *N*-linked glycosylation sites (Asn65, Asn72, Asn168, and Asn481) and are mostly exposed on surfaces of the molecule. [19,60] They help the SC bind to pIg ligands and facilitate interactions between lectin and free SC, in addition to protecting SC from proteolytic degradation [5,22]. Each domain has a basic folded topology consisting of two β -sheets connected by a conserved disulfide bond (Cys22–Cys92 in D1, Cys134–Cys202 in D2, Cys239–Cys307 in D3, Cys353–Cys423 in D4, and Cys468–Cys526 in D5) [19,60,61]. With the determination of the sIgA and sIgM structures, the 3D structure of SC bound to IgA and IgM was also reported. A drastic conformational change of SC is observed in sIgA and sIgM (Figure 6). The D4–D5 side rotates 120° to be colinear with unchanged D2–D3, and D1 is packed on D2–D3 by rotating 84° to allow binding to dIgA and pIgM [21,46]. Noncovalent interactions with three complementary determinants (CDRs) of D1 play an essential role in the assembly of sIgA or sIgM in the presence of the J-chain, and there is a broadly consistent D1 interaction interface in sIgA and sIgM. D2–D4 provide the correct spacing of D1 and D5, thereby assisting interaction with dIgA and pIgM [21,25,46,54]. D5 interacts with Fc through the disulfide bond between Cys468 (SC D5) and Cys311 (IgA Fc2) or Cys414 (IgM Fc2) [62,63].

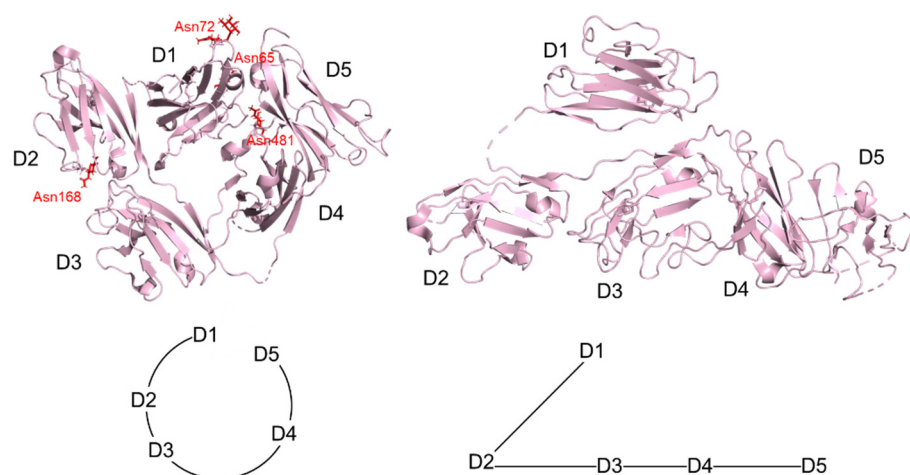


Figure 6. 3D structures of SC in free form (PDB ID: 5D4K, (left)) and SC bound to IgA-Fc dimer and J-chain (PDB ID: 6UE7, (right)). Glycan residues are shown in red with stick representation. On the right panel, IgA-Fc was omitted for clarity.

6. Interaction with Fc Receptors and Others

IgA and IgM Fcs are known to interact with a variety of receptors to mediate multiple effector functions, such as pIgR, $\text{Fc}_{\alpha}/\mu\text{R}$, $\text{Fc}_{\alpha}\text{RI}$, complement receptor, Fc_{μ}R , etc. Under homeostatic conditions, IgA complexed with pIgR inhibits bacterial adherence to the mucosal wall, which functions as the first line of defense of the body. Interactions with pIgR have been discussed in the SC section. Once pathogens enter the bloodstream, serum monomeric IgA initiates the third line of immune defense as a proinflammatory antibody interacting with the IgA-specific receptor $\text{Fc}_{\alpha}\text{RI}$. Here, we elaborate on the interactions with human $\text{Fc}_{\alpha}/\mu\text{R}$ and the IgA-specific receptor $\text{Fc}_{\alpha}\text{RI}$, and IgM with the apoptosis inhibitor of macrophages (AIM). IgA interacts with $\text{Fc}_{\alpha}\text{RI}$ to trigger clearance of IgA-bound aggressive pathogens. Most IgA-dependent immune responses are mediated through $\text{Fc}_{\alpha}\text{RI}$, inducing phagocytosis, antibody-dependent cell-mediated cytotoxicity, respiratory

burst, and cytokine release [64]. Crystal structures of the $\text{Fc}_\alpha\text{RI}$ complex with IgA1 Fc have greatly facilitated our understanding of their interactions with IgA. Like most Ig receptors, $\text{Fc}_\alpha\text{RI}$ is a transmembrane glycoprotein comprising two extracellular Ig-like structural domains (EC1 and EC2), a transmembrane region, and a short cytoplasmic tail. The two extracellular structural domains are folded together at an angle of approximately 90° [23,32,65]. In each extracellular domain, several β -strands are assembled into two β -sheets, where the first β -strand is shared between the two β -sheets and with one strand absent in EC2. Both domains include three short helices, and there is an extra polyproline type-II helix in EC2 [23]. There are six potential *N*-glycosylation sites (Asn44, Asn58, Asn120, Asn156, Asn165, and Asn177) and several *O*-glycosylation sites in free $\text{Fc}_\alpha\text{RI}$. A recent study shows that Asn177 may not be glycosylated [66,67]. IgA monomer and polymer can all bind $\text{Fc}_\alpha\text{RI}$. The crystal structure of the $\text{Fc}_\alpha\text{RI}/\text{Fc}_\alpha$ complex shows that a single Fc dimer binds two $\text{Fc}_\alpha\text{RI}$ receptors. The interaction between $\text{Fc}_\alpha\text{RI}$ and IgA occurs at the $\text{C}_\alpha 2\text{-C}_\alpha 3$ interface, consisting of a central hydrophobic core and two sides of charged residues [23,66,68,69]. Free $\text{Fc}_\alpha\text{RI}$ receptor binds to Fc_α with a conformational change in two loops and a strand in EC1 [23]. Asn58 of $\text{Fc}_\alpha\text{RI}$ is closest to the IgA interaction surface, and deglycosylation at Asn58 results in increased IgA binding [67]. There is an increase in affinity upon desialylation at Asn58, and Asn58 modified with a single GlcNAc residue has the highest receptor affinity [70]. The glycans attached at the other sites exert little or no influence on IgA binding [67,70].

Another novel Fc receptor $\text{Fc}_\alpha/\mu\text{R}$, the only IgM Fc receptor on hematopoietic cells, plays a significant role in triggering IgA- and IgM-mediated immune responses [71–73]. The $\text{Fc}_\alpha/\mu\text{R}$ gene is located adjacent to pIgR on chromosome 1. Amino acid sequence alignment shows that there is a conserved motif in SC D1 that is crucial for interacting with sIgA and pIgM [74,75]. This type-1 transmembrane protein has a unique extracellular loop containing three domains, a short EC1, an Ig variable region-like EC2 that shares 43% homology with SC D1, and a stalk-like EC3 [76]. Studies using an antibody against $\text{Fc}_\alpha/\mu\text{R}$ and 3D homology modeling suggest the presence of a conserved peptide sequence (also present in SC D1) that interacts with IgA or IgM [73,77,78]. Like pIgR, $\text{Fc}_\alpha/\mu\text{R}$ has three CDR-like loops in EC2, and the CDR1-like loop lies exactly at the position of the conserved peptide sequence (TIHCHYAPSSVNRHQRYW). Substitution experiments indicate that the CDR1- and CDR2-like loops together play a more essential role than the CDR3-like loop in binding to IgA and IgM, where positively charged Arg31 and the hydrophobic side chain of Val29 of the CDR1-like loop and Asn54-Gln55 of the CDR2-like loop contribute to ligand binding, while the CDR3-like loop assists in stabilizing the structure. $\text{Fc}_\alpha/\mu\text{R}$ has a higher affinity for IgM than IgA and only binds to IgM and IgA polymers [78–80]. There are two potential *N*-glycosylation sites at Asn167 and Asn276, but the function of putative *N*-glycans in binding to IgA and IgM is unclear [74,81].

Apoptosis inhibitor of macrophages (AIM) is a member of a scavenger receptor cysteine-rich (SRCR) superfamily and is expressed on the surface of macrophages [82]. Recent studies show that the pentameric IgM is a transporter for the effector protein AIM and that the trapping by pIgM inactivates AIM and increases its level in the blood by decreasing renal excretion [83,84]. AIM is released from an AIM–IgM complex to inhibit the apoptosis of thymocytes, especially during acute kidney injury, and this enhances the clearance of excess fat, bacteria, cancer cells, and dead cell debris [85,86]. sIgM is able to bind to the complement receptor and $\text{Fc}_\alpha/\mu\text{R}$ on antigen-presenting cells, including macrophages and follicular dendritic cells (FDC) [87]. AIM-containing IgM-antigen complexes are ligated to the FDC surface by complement receptors. In contrast, cells lacking AIM bind to $\text{Fc}_\alpha/\mu\text{R}$ and are processed and present on MHC class II after internalization [88].

Single-particle negative-stain EM of a pIgM–AIM complex has shown how pIgM associates with AIM [47]. There are three conserved SRCR domains in the AIM molecule. SRCR2 and SRCR3 are essential for the formation of the pIgM–AIM complex, especially Cys194 of SRCR2. SRCR1 does not appear to bind pIgM according to a homology-based structural model and mutational analysis. AIM assumes a broad bean-like structure, located

in a 50° gap in pIgM with the J-chain. The Cys194 of SRCR2 forms an intermolecular disulfide bond with the Cys414 of the Fc-C_μ3 domain at one edge, and the positively charged amino acid cluster (H294, K298, R300, K301, K340) of SRCR3 interacts with the negatively charged cluster of the Fc-C_μ4 domain on the opposite edge [47,89,90]. There are three potential *N*-glycosylation sites (Asn99 of SRCR1, Asn229 of SRCR2, and Asn316 of SRCR3) in murine AIM and these *N*-glycans affect the secretion and lipolytic functions. It is unclear whether the *N*-glycans play a role in IgM interactions [91]. Potential *N*-glycosylation sites of human AIM do not appear to possess any glycans.

7. Therapeutic Potential of IgA and IgM

Although IgA and IgM play an essential role in human mucosal immunity, conventional vaccinations usually do not induce mucosal immunity unless administered to the mucosal surface. The progress in determining their structure and interaction with receptors suggests that IgA and IgM-based immunotherapy is an important field for the development of vaccinations and therapeutics. More than 90 therapeutic IgG antibody products have FDA approval, whereas almost no IgA and IgM antibodies have been tested in humans [92]. The superiority of IgA over IgG for recruiting polymorphonuclear cells and the development of bispecific antibodies (BsAb) have opened up prospects for IgA antibody applications [93–95]. For instance, anti-HER2 × Fc_αRI (against both HER2 and Fc_αRI) effectively clears breast cancer cells through neutrophil accumulation, but anti-HER2 × Fc_γRI does not [96]. Another BsAb, anti-HLA II × Fc_αRI is also a powerful candidate in recruiting polymorphonuclear cells against human B cell malignancies [97]. In addition, bispecific IgM with ten or twelve binding sites potentially allows very high affinity binding to difficult or rare tumor antigens, enabling selective contact with T cells resulting in tumor cell death. Anti-CD20 × CD3 IgM is currently in clinical trials against refractory or resistant non-Hodgkin's lymphoma [98,99].

While there are many possible advantages of IgA and IgM in antibody therapy, there are several issues that need to be overcome. For example, how does IgA mediate both pro- and anti-inflammatory functions via Fc_αRI in order to exert a therapeutic effect. The short half-life makes use of IgA potentially expensive, and the need for the high frequency of administration is inconvenient for patients. Another issue is the efficiency of expression, production, purification, and complete assembly of recombinant IgA and IgM monoclonal antibodies with appropriate homogeneity. A more critical limitation is the lack of suitable animal models, one example being the differences in the polymerization state of serum IgA and the lack of Fc_αRI in the mouse. Many of these issues are now being addressed. For instance, modification of terminal *N*-glycans successfully lengthened the half-life of asialoglycoprotein receptor-mediated clearance [100,101]. Systems for increasing IgA expression and rational assembly are being gradually developed [33,101,102]. Successful establishment of human CD89 and IgA transgenic mice now enables *in vivo* studies of IgA [103,104].

The recently resolved three-dimensional structures of IgM Fc pentamers and IgA Fc multimers have provided us with an excellent base to help understand and modify these complex macromolecules. We hope that this review provides some ideas for the engineering of bispecific IgA and IgM antibodies and the development of more effective therapeutics.

Author Contributions: Conceptualization, Y.Y.; writing—original draft preparation, S.P.; writing—review and editing, S.P., N.M. and Y.Y.; visualization, N.M.; supervision, Y.Y. All authors have read and agreed to the published version of the manuscript.

Funding: This work was supported in part by JSPS KAKENHI Grant Number 19H03362.

Institutional Review Board Statement: Not applicable.

Informed Consent Statement: Not applicable.

Acknowledgments: S.P. is a recipient of the special scholarship from Tohoku Medical and Pharmaceutical University and the scholarship from the Tohoku Kaihatsu Memorial Foundation.

Conflicts of Interest: The authors declare no conflict of interest.

References

- Macpherson, A.J.; Gatto, D.; Sainsbury, E.; Harriman, G.R.; Hengartner, H.; Zinkernagel, R.M. A Primitive T Cell-Independent Mechanism of Intestinal Mucosal IgA Responses to Commensal Bacteria. *Science* **2000**, *288*, 2222–2226. [\[CrossRef\]](#)
- Bakema, J.E.; Van Egmond, M. Immunoglobulin A: A next generation of therapeutic antibodies? In *mAbs*; Taylor & Francis: Abingdon, UK, 2011; Volume 3, pp. 352–361.
- De Sousa-Pereira, P.; Woof, J.M. IgA: Structure, Function, and Developability. *Antibodies* **2019**, *8*, 57. [\[CrossRef\]](#)
- Michaud, E.; Mastrandrea, C.; Rochereau, N.; Paul, S. Human Secretory IgM: An Elusive Player in Mucosal Immunity. *Trends Immunol.* **2020**, *41*, 141–156. [\[CrossRef\]](#) [\[PubMed\]](#)
- Kaetzel, C.S. The polymeric immunoglobulin receptor: Bridging innate and adaptive immune responses at mucosal surfaces. *Immunol. Rev.* **2005**, *206*, 83–99. [\[CrossRef\]](#)
- Mestecky, J.; Russell, M.; Jackson, S.; Brown, T.A. The human IgA system a reassessment. *Clin. Immunol. Immunopathol.* **1986**, *41*, 105–114. [\[CrossRef\]](#)
- Yoo, E.M.; Morrison, S.L. IgA: An immune glycoprotein. *Clin. Immunol.* **2005**, *116*, 3–10. [\[CrossRef\]](#)
- Leusen, J.H. IgA as therapeutic antibody. *Mol. Immunol.* **2015**, *68*, 35–39. [\[CrossRef\]](#) [\[PubMed\]](#)
- Brandtzaeg, P. Role of J chain and secretory component in receptor-mediated glandular and hepatic transport of immunoglobulins in man. *Scand. J. Immunol.* **2010**, *22*, 111–146. [\[CrossRef\]](#)
- Putnam, F.W.; Liu, Y.S.; Low, T.L. Primary structure of a human IgA1 immunoglobulin. IV. Streptococcal IgA1 protease, digestion, Fab and Fc fragments, and the complete amino acid sequence of the alpha 1 heavy chain. *J. Biol. Chem.* **1979**, *254*, 2865–2874. [\[CrossRef\]](#)
- Sørensen, V.; Sundvold, V.; Michaelsen, T.E.; Sandlie, I. Polymerization of IgA and IgM: Roles of Cys309/Cys414 and the secretory tailpiece. *J. Immunol.* **1999**, *162*, 3448–3455. [\[PubMed\]](#)
- Woof, J.M.; Russell, M.W. Structure and function relationships in IgA. *Mucosal Immunol.* **2011**, *4*, 590–597. [\[CrossRef\]](#)
- Chintalacharuvu, K.R.; Raines, M.; Morrison, S.L. Divergence of human alpha-chain constant region gene sequences. A novel recombinant alpha 2 gene. *J. Immunol.* **1994**, *152*, 5299–5304.
- Chintalacharuvu, K.R.; Morrison, S.L. Residues critical for H-L disulfide bond formation in human IgA1 and IgA2. *J. Immunol.* **1996**, *157*, 3443–3449. [\[PubMed\]](#)
- Toraño, A.; Putnam, F.W. Complete amino acid sequence of the α 2 heavy chain of a human IgA2 immunoglobulin of the A2m(2) allotype. *Proc. Natl. Acad. Sci. USA* **1978**, *75*, 966–969. [\[CrossRef\]](#) [\[PubMed\]](#)
- Toraño, A.; Tsuzukida, Y.; Liu, Y.; Putnam, F.W. Location and Structural Significance of the Oligosaccharides in Human IgA1 and IgA2 Immunoglobulins. *Proc. Natl. Acad. Sci. USA* **1977**, *74*, 2301–2305. [\[CrossRef\]](#) [\[PubMed\]](#)
- Chintalacharuvu, K.R.; Yu, L.J.; Bhola, N.; Kobayashi, K.; Fernandez, C.Z.; Morrison, S.L. Cysteine Residues Required for the Attachment of the Light Chain in Human IgA2. *J. Immunol.* **2002**, *169*, 5072–5077. [\[CrossRef\]](#)
- Norderhaug, I.N.; Johansen, F.E.; Schjerven, H.; Brandtzaeg, P. Regulation of the formation and external transport of secretory immunoglobulins. *Crit. Rev. Immunol.* **1999**, *19*, 481–508.
- Stadtmueller, B.M.; Huey-Tubman, K.E.; Lopez, C.J.; Yang, Z.; Hubbell, W.L.; Bjorkman, P.J. The structure and dynamics of secretory component and its interactions with polymeric immunoglobulins. *eLife* **2016**, *5*, e10640. [\[CrossRef\]](#)
- Dourmashkin, R.R.; Virella, G.; Parkhouse, R.M. Electron microscopy of human and mouse myeloma serum IgA. *J. Mol. Biol.* **1971**, *56*, 207–208. [\[CrossRef\]](#)
- Kumar, N.; Arthur, C.; Ciferri, C.; Matsumoto, M.L. Structure of the secretory immunoglobulin A core. *Science* **2020**, *368*, 1008–1014. [\[CrossRef\]](#)
- Wang, Y.; Wang, G.; Li, Y.; Zhu, Q.; Shen, H.; Gao, N.; Xiao, J. Structural insights into secretory immunoglobulin A and its interaction with a pneumococcal adhesin. *Cell Res.* **2020**, *30*, 602–609. [\[CrossRef\]](#) [\[PubMed\]](#)
- Herr, A.B.; Ballister, E.; Bjorkman, P.J. Insights into IgA-mediated immune responses from the crystal structures of human Fc α RI and its complex with IgA1-Fc. *Nature* **2003**, *423*, 614–620. [\[CrossRef\]](#) [\[PubMed\]](#)
- Ramslund, P.A.; Willoughby, N.; Trist, H.M.; Farrugia, W.; Hogarth, P.M.; Fraser, J.D.; Wines, B.D. Structural basis for evasion of IgA immunity by *Staphylococcus aureus* revealed in the complex of SSL7 with Fc of human IgA1. *Proc. Natl. Acad. Sci. USA* **2007**, *104*, 15051–15056. [\[CrossRef\]](#) [\[PubMed\]](#)
- Kumar Bharathkar, S.; Parker, B.W.; Malyutin, A.G.; Haloi, N.; Huey-Tubman, K.E.; Tajkhorshid, E.; Stadtmueller, B.M. The structures of secretory and dimeric immunoglobulin A. *eLife* **2020**, *9*, e56098. [\[CrossRef\]](#)
- Kawamura, S.; Saitou, N.; Ueda, S. Concerted evolution of the primate immunoglobulin alpha-gene through gene conversion. *J. Biol. Chem.* **1992**, *267*, 7359–7367. [\[CrossRef\]](#)
- Royle, L.; Roos, A.; Harvey, D.J.; Wormald, M.R.; van Gijlswijk-Janssen, D.; Redwan, E.R.M.; Wilson, I.A.; Doha, M.R.; Dwek, R.A.; Rudd, P.M. Secretory IgA N- and O-glycans provide a link between the innate and adaptive immune systems. *J. Biol. Chem.* **2003**, *278*, 20140–20153. [\[CrossRef\]](#)

28. Field, M.C.; Amatayakul-Chantler, S.; Rademacher, T.W.; Rudd, P.M.; Dwek, R.A. Structural analysis of the N-glycans from human immunoglobulin A1: Comparison of normal human serum immunoglobulin A1 with that isolated from patients with rheumatoid arthritis. *Biochem. J.* **1994**, *299 Pt 1*, 261–275. [\[CrossRef\]](#)
29. Hui, G.K.; Wright, D.W.; Vennard, O.L.; Rayner, L.E.; Pang, M.; Yeo, S.C.; Gor, J.; Molyneux, K.; Barratt, J.; Perkins, S.J. The solution structures of native and patient monomeric human IgA1 reveal asymmetric extended structures: Implications for function and IgAN disease. *Biochem. J.* **2015**, *471*, 167–185. [\[CrossRef\]](#)
30. Maurer, M.A.; Meyer, L.; Bianchi, M.; Turner, H.L.; Le, N.P.L.; Steck, M.; Wyrzucki, A.; Orlowski, V.; Ward, A.B.; Crispin, M.; et al. Glycosylation of Human IgA Directly Inhibits Influenza A and Other Sialic-Acid-Binding Viruses. *Cell Rep.* **2018**, *23*, 90–99. [\[CrossRef\]](#)
31. Mattu, T.S.; Pleass, R.; Willis, A.C.; Kilian, M.; Wormald, M.R.; Lellouch, A.C.; Rudd, P.M.; Woof, J.M.; Dwek, R.A. The Glycosylation and Structure of Human Serum IgA1, Fab, and Fc Regions and the Role of N-Glycosylation on Fc α Receptor Interactions. *J. Biol. Chem.* **1998**, *273*, 2260–2272. [\[CrossRef\]](#) [\[PubMed\]](#)
32. Woof, J.M.; Burton, D.R. Human antibody-Fc receptor interactions illuminated by crystal structures. *Nat. Rev. Immunol.* **2004**, *4*, 89–99. [\[CrossRef\]](#)
33. Lombana, T.N.; Rajan, S.; Zorn, J.A.; Mandikian, D.; Chen, E.C.; Estevez, A.; Yip, V.; Bravo, D.D.; Phung, W.; Farahi, F.; et al. Production, characterization, and in vivo half-life extension of polymeric IgA molecules in mice. *mAbs* **2019**, *11*, 1122–1138. [\[CrossRef\]](#)
34. Zhang, S.; Cao, X.; Liu, C.; Li, W.; Lu, H. N-glycopeptide Signatures of IgA₂ in Serum from Patients with Hepatitis B Virus-related Liver Diseases. *Mol. Cell. Proteom.* **2019**, *18*, 2262–2272. [\[CrossRef\]](#)
35. Yoo, E.M.; Li, J.Y.; Wims, L.A.; Goldberg, D.; Morrison, S.L. Differences in N-glycan structures found on recombinant IgA1 and IgA2 produced in murine myeloma and CHO cell lines. *mAbs* **2010**, *2*, 320–334. [\[CrossRef\]](#) [\[PubMed\]](#)
36. Steffen, U.; Koeleman, C.A.; Sokolova, M.V.; Bang, H.; Kleyer, A.; Rech, J.; Unterweger, H.; Schicht, M.; Garreis, F.; Hahn, J. IgA subclasses have different effector functions associated with distinct glycosylation profiles. *Nat. Commun.* **2020**, *11*, 120. [\[CrossRef\]](#) [\[PubMed\]](#)
37. Grönwall, C.; Vas, J.; Silverman, G.J. Protective Roles of Natural IgM Antibodies. *Front. Immunol.* **2012**, *3*, 66. [\[CrossRef\]](#) [\[PubMed\]](#)
38. Eskeland, T.; Christensen, T. IgM Molecules with and without J Chain in Serum and after Purification, Studied by Ultracentrifugation, Electrophoresis, and Electron Microscopy. *Scand. J. Immunol.* **1975**, *4*, 217–228. [\[CrossRef\]](#) [\[PubMed\]](#)
39. Dolder, F. Occurrence, isolation and interchain bridges of natural 7-S immunoglobulin M in human serum. *Biochim. Biophys. Acta* **1971**, *236*, 675–685.
40. Davis, A.C.; Roux, K.H.; Pursey, J.; Shulman, M.J. Intermolecular disulfide bonding in IgM: Effects of replacing cysteine residues in the μ heavy chain. *EMBO J.* **1989**, *8*, 2519–2526. [\[CrossRef\]](#)
41. Pasalic, D.; Weber, B.; Giannone, C.; Anelli, T.; Müller, R.; Fagioli, C.; Felkl, M.; John, C.; Mossuto, M.F.; Becker, C.F.W.; et al. A peptide extension dictates IgM assembly. *Proc. Natl. Acad. Sci. USA* **2017**, *114*, E8575–E8584. [\[CrossRef\]](#)
42. Keyt, B.A.; Baliga, R.; Sinclair, A.M.; Carroll, S.F.; Peterson, M.S. Structure, Function, and Therapeutic Use of IgM Antibodies. *Antibodies* **2020**, *9*, 53. [\[CrossRef\]](#)
43. Gall, W.E.; Edelman, G.M. The covalent structure of a human γ G-immunoglobulin. X. Intrachain disulfide bonds. *Biochemistry* **1970**, *9*, 3188–3196. [\[CrossRef\]](#) [\[PubMed\]](#)
44. Feinstein, A.; Munn, E. Conformation of the free and antigen-bound IgM antibody molecules. *Nature* **1969**, *224*, 1307–1309. [\[CrossRef\]](#)
45. Davis, A.C.; Roux, K.H.; Shulman, M.J. On the structure of polymeric IgM. *Eur. J. Immunol.* **1988**, *18*, 1001–1008. [\[CrossRef\]](#)
46. Li, Y.; Wang, G.; Li, N.; Wang, Y.; Zhu, Q.; Chu, H.; Wu, W.; Tan, Y.; Yu, F.; Su, X.D.; et al. Structural insights into immunoglobulin M. *Science* **2020**, *367*, 1014–1017. [\[CrossRef\]](#)
47. Hiramoto, E.; Tsutsumi, A.; Suzuki, R.; Matsuoka, S.; Arai, S.; Kikkawa, M.; Miyazaki, T. The IgM pentamer is an asymmetric pentagon with an open groove that binds the AIM protein. *Sci. Adv.* **2018**, *4*, eaau1199. [\[CrossRef\]](#) [\[PubMed\]](#)
48. Colucci, M.; Stöckmann, H.; Butera, A.; Masotti, A.; Baldassarre, A.; Giorda, E.; Petrini, S.; Rudd, P.M.; Sitia, R.; Emma, F. Sialylation of N-linked glycans influences the immunomodulatory effects of IgM on T cells. *J. Immunol.* **2015**, *194*, 151–157. [\[CrossRef\]](#) [\[PubMed\]](#)
49. Muraoka, S.; Shulman, M.J. Structural requirements for IgM assembly and cytolytic activity. Effects of mutations in the oligosaccharide acceptor site at Asn402. *J. Immunol.* **1989**, *142*, 695–701.
50. Moh, E.S.; Lin, C.; Thaysen-Andersen, M.; Packer, N.H. Site-Specific N-Glycosylation of Recombinant Pentameric and Hexameric Human IgM. *Am. Soc. Mass Spectrom.* **2016**, *27*, 1443–1455. [\[CrossRef\]](#)
51. Mestecky, J.Z.J.; Zikan, J.; Butler, W.T. Immunoglobulin M and Secretory Immunoglobulin A: Presence of a Common Polypeptide Chain Different from Light Chains. *Science* **1971**, *171*, 1163–1165. [\[CrossRef\]](#)
52. Weinheimer, P.F.; Mestecky, J.; Acton, R.T. Species distribution of J chain. *J. Immunol.* **1971**, *107*, 1211. [\[PubMed\]](#)
53. Frutiger, S.; Hughes, G.J.; Paquet, N.; Lüthy, R.; Jaton, J.C. Disulfide bond assignment in human J chain and its covalent pairing with immunoglobulin M. *Biochemistry* **1992**, *31*, 12643–12647. [\[CrossRef\]](#)
54. Kumar, N.; Arthur, C.P.; Ciferri, C.; Matsumoto, M.L. Structure of the human secretory immunoglobulin M core. *Structure* **2021**, *29*, 564–571. [\[CrossRef\]](#)
55. Baenziger, J.U. Structure of the oligosaccharide of human J chain. *J. Biol. Chem.* **1979**, *254*, 4063–4071. [\[CrossRef\]](#)

56. Krugmann, S.; Pleass, R.J.; Atkin, J.D.; Woof, J.M. Structural requirements for assembly of dimeric IgA probed by site-directed mutagenesis of J chain and a cysteine residue of the α -chain CH2 domain. *J. Immunol.* **1997**, *159*, 244–249.
57. Brandtzaeg, P.; Prydz, H. Direct evidence for an integrated function of J chain and secretory component in epithelial transport of immunoglobulins. *Nature* **1984**, *311*, 71–73. [[CrossRef](#)] [[PubMed](#)]
58. Mostov, K.E.; Friedlander, M.; Blobel, G. The receptor for transepithelial transport of IgA and IgM contains multiple immunoglobulin-like domains. *Nature* **1984**, *308*, 37–43. [[CrossRef](#)]
59. Frutiger, S.; Hughes, G.J.; Hanly, W.C.; Kingzette, M.; Jaton, J.C. The amino-terminal domain of rabbit secretory component is responsible for noncovalent binding to immunoglobulin A dimers. *J. Biol. Chem.* **1986**, *261*, 16673–16681. [[CrossRef](#)]
60. Hamburger, A.E.; West, A.P.; Bjorkman, P.J. Crystal Structure of a Polymeric Immunoglobulin Binding Fragment of the Human Polymeric Immunoglobulin Receptor. *Structure* **2004**, *12*, 1925–1935. [[CrossRef](#)]
61. Hughes, G.J.; Reason, A.J.; Savoy, L.A.; Jaton, J.C.; Frutiger-Hughes, S. Carbohydrate moieties in human secretory component. *Biochim. Biophys. Acta-Protein Struct. Mol. Enzymol.* **1999**, *1434*, 86–93. [[CrossRef](#)]
62. Coyne, R.S.; Siebrecht, M.; Peitsch, M.C.; Casanova, J.E. Mutational analysis of polymeric immunoglobulin receptor/ligand interactions. Evidence for the involvement of multiple complementarity determining region (CDR)-like loops in receptor domain I. *J. Biol. Chem.* **1994**, *269*, 31620–31625. [[CrossRef](#)]
63. Longet, S.; Miled, S.; Lötscher, M.; Miescher, S.M.; Zuercher, A.W.; Corthésy, B. Human plasma-derived polymeric IgA and IgM antibodies associate with secretory component to yield biologically active secretory-like antibodies. *J. Biol. Chem.* **2013**, *288*, 4085–4094. [[CrossRef](#)] [[PubMed](#)]
64. Monteiro, R.; Kubagawa, H.; Cooper, M.D. Cellular distribution, regulation, and biochemical nature of an Fc α receptor in humans. *J. Exp. Med.* **1990**, *171*, 597–613. [[CrossRef](#)] [[PubMed](#)]
65. Aleyd, E.; Heineke, M.H.; Egmond, M.V. The era of the immunoglobulin A Fc receptor FcRI; its function and potential as target in disease. *Immunol. Rev.* **2015**, *268*, 123–138. [[CrossRef](#)]
66. Egmond, M.V.; Bakema, J.E.; Woof, J.M. *Fc Receptors in Mucosal Immunology*; Academic Press: Cambridge, MA, USA, 2015.
67. Xue, J.; Zhu, L.; Zhang, W.; Zhao, Q. Deglycosylation of Fc α R at N58 increases its binding to IgA. *Glycobiology* **2010**, *20*, 905–915. [[CrossRef](#)] [[PubMed](#)]
68. Wines, B.D.; Sardjono, C.T.; Trist, H.M.; Lay, C.S.; Hogarth, P.M. The interaction of Fc α RI with IgA and its implications for ligand binding by immunoreceptors of the leukocyte receptor cluster. *J. Immunol.* **2001**, *166*, 1781–1789. [[CrossRef](#)]
69. Herr, A.B.; White, C.L.; Milburn, C.; Wu, C.; Bjorkman, P.J. Bivalent Binding of IgA1 to Fc α RI Suggests a Mechanism for Cytokine Activation of IgA Phagocytosis. *J. Mol. Biol.* **2003**, *327*, 645–657. [[CrossRef](#)]
70. Göritz, K.; Turupcu, A.; Maresch, D.; Novak, J.; Strasser, R. Distinct Fc α receptor N-glycans modulate the binding affinity to immunoglobulin A (IgA) antibodies. *J. Biol. Chem.* **2019**, *294*, 13995–14008. [[CrossRef](#)] [[PubMed](#)]
71. Sakamoto, N.; Shibuya, K.; Shimizu, Y.; Yotsumoto, K.; Miyabayashi, T.; Sakano, S.; Tsuji, T.; Nakayama, E.; Nakauchi, H.; Shibuya, A. A novel Fc receptor for IgA and IgM is expressed on both hematopoietic and non-hematopoietic tissues. *Eur. J. Immunol.* **2015**, *31*, 1310–1316. [[CrossRef](#)]
72. Kinet, J.-P.; Launay, P. Fc α / μ R: Single member or first born in the family? *Nat. Immunol.* **2000**, *31*, 1310–1316. [[CrossRef](#)]
73. Cho, Y.; Usui, K.; Honda, S.I.; Tahara-Hanaoka, S.; Shibuya, K.; Shibuya, A. Molecular characteristics of IgA and IgM Fc binding to the Fc α / μ R. *Biochem. Biophys. Res. Commun.* **2006**, *345*, 474–478. [[CrossRef](#)] [[PubMed](#)]
74. Shibuya, A.; Sakamoto, N.; Shimizu, Y.; Shibuya, K.; Osawa, M.; Hiroyama, T.; Eyre, H.J.; Sutherland, G.R.; Endo, Y.; Fujita, T. Fc α / μ receptor mediates endocytosis of IgM-coated microbes. *Nat. Immunol.* **2000**, *1*, 441–446. [[CrossRef](#)]
75. Shimizu, Y.; Honda, S.I.; Yotsumoto, K.; Tahara-Hanaoka, S.; Eyre, H.J.; Sutherland, G.R.; Endo, Y.; Shibuya, K.; Koyama, A.; Nakauchi, H. Fc α / μ receptor is a single gene-family member closely related to polymeric immunoglobulin receptor encoded on Chromosome 1. *Immunogenetics* **2001**, *53*, 709–711. [[CrossRef](#)] [[PubMed](#)]
76. Raghavan, M.; Bjorkman, P. Fc Receptors and Their interactions with immunoglobulins. *Annu. Rev. Cell Dev. Biol.* **1996**, *12*, 181. [[CrossRef](#)]
77. Konstantin, A.; Lorenza, B.; Jürgen, K.; Torsten, S. The SWISS-MODEL workspace: A web-based environment for protein structure homology modelling. *Bioinformatics* **2006**, *22*, 195–201.
78. Yang, X.; Zhao, Q.; Zhu, L.; Zhang, W. The three complementarity-determining region-like loops in the second extracellular domain of human Fc alpha/mu receptor contribute to its binding of IgA and IgM. *Immunobiology* **2013**, *218*, 798–809. [[CrossRef](#)]
79. Cho, Y.; Honda, S.; Yoshizawa, Y.; Takagaki, K.; Usui, K.; Shibuya, A. Requirement of the cytoplasmic portion for dimer formation of Fc α / μ receptor expressed on cell surface. *Mol. Immunol.* **2010**, *47*, 878–882. [[CrossRef](#)]
80. Yoo, E.M.; Trinh, K.R.; Lim, H.; Wims, L.A.; Morrison, S.L. Characterization of IgA and IgM binding and internalization by surface-expressed human Fc α / μ receptor. *Mol. Immunol.* **2011**, *48*, 1818–1826. [[CrossRef](#)]
81. Kikuno, K.; Kang, D.W.; Tahara, K.; Torii, I.; Kubagawa, H.; Ho, K.; Baudino, L.; Nishizaki, N.; Shibuya, A.; Kubagawa, H. Unusual biochemical features and follicular dendritic cell expression of human Fc α / μ receptor. *Eur. J. Immunol.* **2007**, *37*, 3540–3550. [[CrossRef](#)] [[PubMed](#)]
82. Resnick, D.; Pearson, A.; Krieger, M. The SRCR superfamily: A family reminiscent of the Ig superfamily. *Trends Biochem. Sci.* **1994**, *19*, 5–8. [[CrossRef](#)]

83. Arai, S.; Maehara, N.; Iwamura, Y.; Honda, S.I.; Nakashima, K.; Kai, T.; Ogishi, M.; Morita, K.; Kurokawa, J.; Mori, M. Obesity-Associated Autoantibody Production Requires AIM to Retain the Immunoglobulin M Immune Complex on Follicular Dendritic Cells. *Cell Rep.* **2013**, *3*, 1187–1198. [CrossRef]
84. Kai, T.; Tomoko, Y.; Satoko, A.; Toru, M.; Aguila, M.B. Stabilization and Augmentation of Circulating AIM in Mice by Synthesized IgM-Fc. *PLoS ONE* **2014**, *9*, e97037. [CrossRef] [PubMed]
85. Miyazaki, T.; Yamazaki, T.; Sugisawa, R.; Gershwin, M.E.; Arai, S. AIM associated with the IgM pentamer: Attackers on stand-by at aircraft carrier. *Cell. Mol. Immunol.* **2018**, *15*, 563–574. [CrossRef] [PubMed]
86. Gong, S.; Ruprecht, R.M. Immunoglobulin M: An Ancient Antiviral Weapon—Rediscovered. *Front. Immunol.* **2020**, *11*, 1943. [CrossRef]
87. Colombo, M.J.; Abraham, D.; Shibuya, A.; Alugupalli, K.R. B1b lymphocyte-derived antibodies control *Borrelia hermsii* independent of Fc α / μ receptor and in the absence of host cell contact. *Immunol. Res.* **2011**, *51*, 249–256. [CrossRef]
88. Blandino, R.; Baumgarth, N. Secreted IgM: New tricks for an old molecule. *J. Leukoc. Biol.* **2019**, *106*, 1021–1034. [CrossRef] [PubMed]
89. Miyazaki, T.; Hirokami, Y.; Matsushashi, N.; Takatsuka, H.; Naito, M. Increased Susceptibility of Thymocytes to Apoptosis in Mice Lacking AIM, a Novel Murine Macrophage-derived Soluble Factor Belonging to the Scavenger Receptor Cysteine-rich Domain Superfamily. *J. Exp. Med.* **1999**, *189*, 413–422. [CrossRef] [PubMed]
90. Chappell, P.; Garner, L.; Yan, J.; Metcalfe, C.; Hatherley, D.; Johnson, S.; Robinson, C.; Lea, S.; Brown, M. Structures of CD6 and Its Ligand CD166 Give Insight into Their Interaction. *Structure* **2015**, *23*, 1426–1436. [CrossRef] [PubMed]
91. Mori, M.; Kimura, H.; Iwamura, Y.; Arai, S.; Miyazaki, T. Modification of N-glycosylation modulates the secretion and lipolytic function of apoptosis inhibitor of macrophage (AIM). *FEBS Lett.* **2012**, *586*, 3569–3574. [CrossRef] [PubMed]
92. Drugs@FDA: FDA-Approved Drugs. Available online: <https://www.accessdata.fda.gov/scripts/cder/daf/> (accessed on 11 October 2020).
93. Brandsma, A.M.; Bondza, S.; Evers, M.; Koutstaal, R.; Broeke, T.T. Potent Fc Receptor Signaling by IgA Leads to Superior Killing of Cancer Cells by Neutrophils Compared to IgG. *Front. Immunol.* **2019**, *10*, 704. [CrossRef]
94. Niels, H.; Marjolein, V.E. Monoclonal antibody-mediated killing of tumor cells by neutrophils. *Eur. J. Clin. Investig.* **2018**, *48*, e12962.
95. Steen, L.; Tuk, C.W.; Bakema, J.E.; Kooij, G.; Reijerkerk, A.; Vidarsson, G.; Bouma, G.; Kraal, G.; Vries, H.; Beelen, R. Immunoglobulin A: Fc α RI interactions induce neutrophil migration through release of leukotriene B4. *Gastroenterology* **2009**, *137*, 2018–2029. [CrossRef]
96. Otten, M.A.; Rudolph, E.; Dechant, M.; Tuk, C.W.; Reijmers, R.M.; Beelen, R.; Van, D.; Egmond, M.V. Immature Neutrophils Mediate Tumor Cell Killing via IgA but Not IgG Fc Receptors. *J. Immunol.* **2005**, *174*, 5472–5480. [CrossRef] [PubMed]
97. Guettinger, Y.; Barbin, K.; Peipp, M.; Bruenke, J.; Dechant, M.; Horner, H.; Thierschmidt, D.; Valerius, T.; Repp, R.; Fey, G.H. A recombinant bispecific single-chain fragment variable specific for HLA class II and Fc α RI (CD89) recruits polymorphonuclear neutrophils for efficient lysis of malignant B lymphoid cells. *J. Immunol.* **2010**, *184*, 1210–1217. [CrossRef] [PubMed]
98. Baliga, R.; Li, K.; Manlusoc, M.; Hinton, P.; Keyt, B. High Avidity IgM-Based CD20 \times CD3 Bispecific Antibody (IGM-2323) for Enhanced T-Cell Dependent Killing with Minimal Cytokine Release. *Blood* **2019**, *134* (Suppl. S1), 1574. [CrossRef]
99. A Safety and Pharmacokinetic Study of IGM-2323 in Subjects with Relapsed/Refractory Non-Hodgkin Lymphoma. Available online: <https://clinicaltrials.gov/ct2/show/NCT04082936> (accessed on 11 October 2020).
100. Lohse, S.; Meyer, S.; Meulenbroek, L.; Jansen, J.; Nederend, M.; Kretschmer, A.; Klausz, K.; Moginger, U.; Derer, S.; Rosner, T. An Anti-EGFR IgA That Displays Improved Pharmacokinetics and Myeloid Effector Cell Engagement In Vivo. *Cancer Res.* **2016**, *76*, 403–417. [CrossRef]
101. Rouwendal, G.J.; Van, M.M.; Meyer, S.; Reiding, K.R.; Schouten, J.; De, R.G.; Egging, D.F.; Leusen, J.H.; Boross, P.; Wuhler, M. A comparison of anti-HER2 IgA and IgG1 in vivo efficacy is facilitated by high N-glycan sialylation of the IgA. In *mAbs*; Taylor & Francis: Abingdon, UK, 2016; Volume 8, pp. 74–86.
102. Valasek, C.C.F.; Hensel, F.; Ye, P.; Conner, M.A.; Ultee, M.E. Production and Purification of a PER.C6-Expressed IgM Antibody Therapeutic—BioProcess—BioProcess International. *BioProcess Int.* **2011**, *9*, 28–37.
103. Launay, P.; Grossetête, B.; Arcos-Fajardo, M.; Gaudin, E.; Torres, S.P.; Beaudoin, L.; Patey-Mariaud, D.; Lehuen, A.; Monteiro, R.C. Fc α Receptor (CD89) Mediates the Development of Immunoglobulin A (IgA) Nephropathy (Berger's Disease): Evidence for Pathogenic Soluble Receptor–IgA Complexes in Patients and CD89 Transgenic Mice. *J. Exp. Med.* **2000**, *191*, 1999–2010. [CrossRef]
104. Duchez, S.; Amin, R.; Cogné, N.; Delpy, L.; Sirac, C.; Pascal, V.; Corthésy, B.; Cogné, M. Premature replacement of μ with α immunoglobulin chains impairs lymphopoiesis and mucosal homing but promotes plasma cell maturation. *Proc. Natl. Acad. Sci. USA* **2010**, *107*, 3064–3069. [CrossRef]

Article

Ribitol in Solution Is an Equilibrium of Asymmetric Conformations

Shiho Ohno ¹, Noriyoshi Manabe ¹, Takumi Yamaguchi ² , Jun Uzawa ³ and Yoshiki Yamaguchi ^{1,3,*} 
¹ Division of Structural Glycobiology, Institute of Molecular Biomembrane and Glycobiology, Tohoku Medical and Pharmaceutical University, 4-4-1 Komatsushima, Aoba-ku, Sendai 981-8558, Miyagi, Japan; s.ohno@tohoku-mpu.ac.jp (S.O.); manabe@tohoku-mpu.ac.jp (N.M.)

² School of Materials Science, Japan Advanced Institute of Science and Technology, 1-1 Asahidai, Nomi 923-1292, Ishikawa, Japan; takumi@jaist.ac.jp

³ Structural Glycobiology Team, RIKEN (The Institute of Physical and Chemical Research), 2-1 Hirosawa, Wako 351-0198, Saitama, Japan; uzawa_fe79@ck9.so-net.ne.jp

* Correspondence: yyoshiki@tohoku-mpu.ac.jp; Tel.: +81-22-727-0208

Abstract: Ribitol (C₅H₁₂O₅), an acyclic sugar alcohol, is present on mammalian α -dystroglycan as a component of O-mannose glycan. In this study, we examine the conformation and dynamics of ribitol by database analysis, experiments, and computational methods. Database analysis reveals that the anti-conformation (180°) is populated at the C3–C4 dihedral angle, while the gauche conformation ($\pm 60^\circ$) is seen at the C2–C3 dihedral angle. Such conformational asymmetry was born out in a solid-state ¹³C-NMR spectrum of crystalline ribitol, where C1 and C5 signals are unequal. On the other hand, solution ¹³C-NMR has identical chemical shifts for C1 and C5. NMR ³J coupling constants and OH exchange rates suggest that ribitol is an equilibrium of conformations, under the influence of hydrogen bonds and/or steric hinderance. Molecular dynamics (MD) simulations allowed us to discuss such a chemically symmetric molecule, pinpointing the presence of asymmetric conformations evidenced by the presence of correlations between C2–C3 and C3–C4 dihedral angles. These findings provide a basis for understanding the dynamic structure of ribitol and the function of ribitol-binding enzymes.

Keywords: ribitol; conformation; dynamics; NMR; MD simulation; hydrogen bond



Citation: Ohno, S.; Manabe, N.; Yamaguchi, T.; Uzawa, J.; Yamaguchi, Y. Ribitol in Solution Is an Equilibrium of Asymmetric Conformations. *Molecules* **2021**, *26*, 5471. <https://doi.org/10.3390/molecules26185471>

Academic Editor: Hideyuki Takeuchi

Received: 9 August 2021

Accepted: 6 September 2021

Published: 8 September 2021

Publisher's Note: MDPI stays neutral with regard to jurisdictional claims in published maps and institutional affiliations.



Copyright: © 2021 by the authors. Licensee MDPI, Basel, Switzerland. This article is an open access article distributed under the terms and conditions of the Creative Commons Attribution (CC BY) license (<https://creativecommons.org/licenses/by/4.0/>).

1. Introduction

Ribitol (C₅H₁₂O₅) is an acyclic sugar alcohol and a component of teichoic acid found in Gram-positive bacteria [1] (Figure 1). Ribitol is also found in riboflavin (vitamin B2) and flavin mononucleotide (riboflavin 5'-phosphate). Ribitol phosphate (D-ribitol 5-phosphate) is a component of O-mannose glycans on mammalian α -dystroglycan [2]. A genetic deficiency of ribitol phosphate transferase leads to muscular dystrophy, highlighting the essential role of ribitol phosphate in the development of skeletal muscle [3]. Laminin is known to interact with ribitol-containing O-mannose glycans, and the ribitol residues are likely acting as a hinge in bridging laminin and α -dystroglycan. Hence, the structure and dynamics of ribitol are now receiving much attention. However, compared with the cyclic hemiacetal sugars, our knowledge of the structural properties and dynamics of such an acyclic sugar alcohol is rather limited.

Jeffrey et al. investigated the crystal structures of nine alditols, including ribitol [4]. In the crystalline state, the carbon chain of alditols tends to adopt an extended, planar zigzag conformation when the configurations at alternate carbons are different (e.g., C_n and C_{n+2} will be D and L or L and D). When the configurations of alternate carbons are the same (D and D or L and L), the C_n-O and C_{n+2}-O bonds align in parallel. This arrangement causes steric hindrance such that the carbon chain changes its conformation to bent and non-planar. Ribitol adopts the same configuration at C2 and C4 (D and D), and the steric

hindrance brought by O2 and O4 is avoided by rotating the C2–C3 or C3–C4 bonds by 120° . In fact, the crystal structure of ribitol adopts a bent conformation, avoiding the steric hindrance induced by a stretched planar zigzag structure. Likewise, the ribitol moiety of riboflavin exhibits a bent conformation in crystals [5,6].

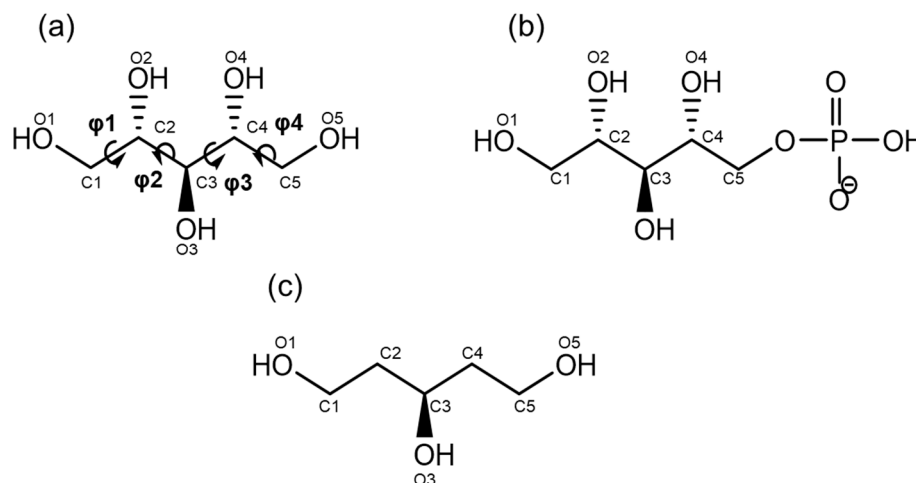


Figure 1. Chemical structures of the compounds examined in this study. (a) Ribitol, (b) ribitol phosphate (D-ribitol 5-phosphate is analyzed in this study, which is the form found in nature), and (c) 1,3,5-pentanol (reference compound). Carbon and oxygen numbering is indicated in the figure. The main-chain dihedral angles are defined as ϕ_1 (O1–C1–C2–C3), ϕ_2 (C1–C2–C3–C4), ϕ_3 (C2–C3–C4–C5), and ϕ_4 (C3–C4–C5–O5) throughout this manuscript.

Hawkes et al. performed solution NMR analysis to determine the structure of ribitol based on $^3J(\text{H,H})$ values [7]. Ribitol equilibrates between a twist at C2–C3 and one at C3–C4, removing the O2/O4 interaction in the planar chain form. It should be noted that $^3J(\text{H2,H3})$ and $^3J(\text{H3,H4})$ of ribitol are indistinguishable in solution NMR. The relationship between C2–C3 and C3–C4 torsion angles is not definitive solely from solution NMR analysis.

Garrett and Serianni synthesized ^{13}C -labeled sugar alcohols, including D-[1- ^{13}C] ribitol, for NMR analysis [8]. $^3J(\text{C1,C4})$ is 1.7 Hz, which is intermediate between ≈ 1.3 Hz (gauche conformations) and ≈ 2.3 Hz (anti conformation), indicating that the C2–C3 or C3–C4 linkage is a mixture of extended and bent forms. Franks et al. found that the $^3J(\text{H,H})$ values are significantly different in water and organic solvents, suggesting that hydration and hydrogen bonding affect the conformation of ribitol [9].

Klein et al. performed MD and Monte Carlo (MC) simulations for the tetrasaccharide-ribitol unit in teichoic acid [9]. They found that the GalNAc-ribitol linkage is more flexible than other glycosidic linkages, but the ribitol chain itself is not completely flexible. Hatcher et al. parameterized the CHARMM force field for acyclic sugar alcohols and performed MD calculations for sugar alcohols, including ribitol [10]. Other than these, there are few studies on the conformational dynamics of ribitol.

Our present study aims to build on previous knowledge on the conformation of ribitol and to deepen our understanding of static and dynamic structures of ribitol through database analysis, experimental NMR analysis, and MD simulation.

2. Results and Discussion

2.1. Database Analysis of Ribitol and Ribitol Phosphate

Crystal structures of oligosaccharides bound to proteins provide good insight into the more stable conformations of each glycosidic linkage [11]. Following this notion, we extracted the conformation(s) of ribitol and ribitol phosphate from the Cambridge Crystallographic Data Centre (CCDC) and the Protein Data Bank (PDB), in total, six ribitol and four ribitol-phosphate structures (Figure 2).

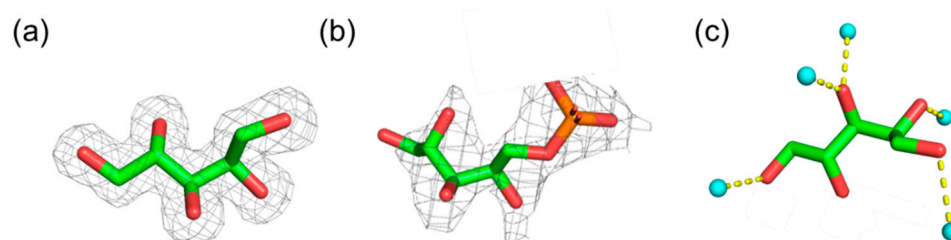


Figure 2. Representative 3D structure of ribitol and ribitol phosphate extracted from the database. (a) Crystal structure of ribitol (PDB ID: 5IAI). (b) Ribitol phosphate (PDB ID: 6H4F). (c) Ribitol interacting with water molecules (PDB ID: 4A0S). The structures are shown in stick representation. In (a,b), the electron density map is depicted in gray mesh contoured at 2.0 σ level. Proteins are omitted for clarity. In (c), water molecules hydrogen bonded with ribitol are shown in cyan sphere.

The dihedral angles of the carbon main chain and the C1–C5 distance of extracted structures are listed in Table 1. Although the data are limited, one can examine the stable conformations for each dihedral angle. In each structure, the dihedral angles suggest staggered conformations. Except for one example (6H4M), the four dihedral angles ($\varphi 1$ – $\varphi 4$) do not all simultaneously assume anti-conformations; some prefer bent conformations.

Table 1. Main chain dihedral angles ($^{\circ}$), C1–C5 distance (\AA), and resolution (\AA) of ribitol and ribitol phosphate extracted from the CCDC and the PDB. NA; not available.

CCDC Deposition Number/DB ID	$\varphi 1$ (O1–C1–C2–C3)	$\varphi 2$ (C1–C2–C3–C4)	$\varphi 3$ (C2–C3–C4–C5)	$\varphi 4$ (C3–C4–C5–O5)	C1–C5 Distance	Resolution	Reference
ribitol							
1249410	171	−62	−172	71	4.5	–	[12]
662559	171	−61	−171	73	4.6	–	[13]
1015979	171	−61	−170	73	4.6	–	[14]
5IAI	173	166	60	170	4.5	1.6	NA
4Q0S	−176	−62	−167	176	4.5	1.9	[15]
4F2D	−150	−174	77	−147	4.5	2.3	NA
Ribitol phosphate							
6H4F	149	94	83	156	4.4	2.2	[16]
6H4M	131	−136	−143	−158	5.0	2.7	[16]
6HNQ	166	160	69	155	4.6	2.4	[16]
6KAM	−75	164	96	−168	4.8	2.5	[17]

When $\varphi 2$ (C1–C2–C3–C4) is in the anti-conformation, $\varphi 3$ (C2–C3–C4–C5) adopts gauche and vice versa. These results indicate that $\varphi 2$ and $\varphi 3$ correlate with each other. C1–C5 distances were also calculated to ascertain the degree of carbon chain stretch. The C1–C5 distance of the fully extended ribitol measured 5.0 \AA . The average value of the C1–C5 distance of 10 extracted ribitol and ribitol phosphate structures is 4.6 \AA , suggesting that ribitol and ribitol phosphate are not completely extended, possibly to avoid the continuous anti-conformations that induce O2/O4 repulsion. In high-resolution structures of ribitol (PDB ID: 5IAI and 4Q0S), hydrogen bonding with surrounding water molecules is observed (Figure 2c). This suggests that intermolecular interaction with water molecules may be involved in the various conformations of ribitol. It seems that the phosphorylation of ribitol does not significantly change the ribitol conformation, although it needs further detailed study. In this paper, we mainly focus on ribitol.

2.2. NMR Analysis

2.2.1. Solid-State ^{13}C -NMR Analysis of Crystalline Ribitol

We can conclude from the database analysis that stable conformations of ribitol are likely asymmetric. To investigate the conformation of crystalline ribitol from another aspect, solid-state ^{13}C -NMR was performed. When the conformation of ribitol is asymmetric, carbon signals will be observed separately in the NMR spectra. Indeed, a ^{13}C CP-MAS NMR spectrum of crystalline ribitol shows four separate signals (Figure 3a). By comparison with the solution ^{13}C -NMR spectrum of ribitol (Figure 3b), partial assignments of ^{13}C

signals were possible for 72 and 73 ppm to C2/C3/C4 and the peaks at 60 and 62 ppm to C1/C5. Interestingly, C1/C5 shows two separate peaks. This observation may indicate that C1 and C5 of ribitol are in different microenvironments. As seen above, ribitols deposited in CCDC have an asymmetric structure (Table 1). It is plausible that ribitol has an asymmetric structure in the solid state as well, which gives different chemical shifts. C2/C3/C4 signals appear around the same frequency; therefore, interpretation here is impossible without a complete assignment.

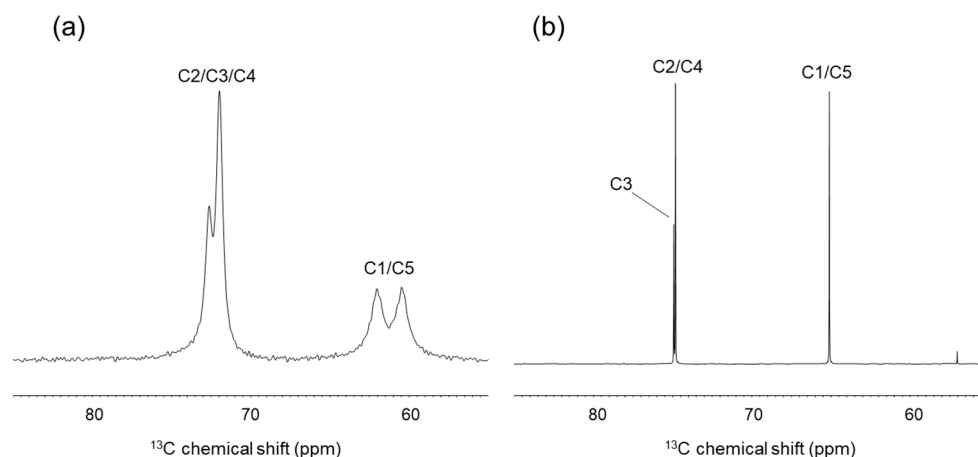


Figure 3. Comparison of solid-state and solution ^{13}C -NMR spectra of ribitol. (a) Solid-state ^{13}C CP-MAS -NMR spectrum of crystalline ribitol. (b) Solution ^{13}C -NMR spectrum of ribitol dissolved in D_2O .

In contrast, the solution ^{13}C -NMR of ribitol showed that C1 and C5, C2 and C4 have the same chemical shifts (Figure 3b). These results suggest that ribitol transits rapidly in solution between stable asymmetric conformations, giving rise to averaged signals.

2.2.2. Solution NMR Analysis of Ribitol Based on Coupling Constant

Then, the dihedral angle of the ribitol main chain was analyzed from the coupling constants obtained by solution NMR. We initially tried to obtain $^3J(\text{H,H})$ from the splitting of the signals, assuming a first-order approximation. However, the assumption was not valid due to strong coupling in ribitol, even at the ^1H observation frequency of 600 MHz. Therefore, 3J values were estimated by comparing simulated and experimental spectra iteratively. To improve the accuracy, 1D- ^1H NMR measurements were performed at the ^1H observation frequencies of 270, 400, and 600 MHz, and the iterative comparison was done at each frequency (Figure 4). $^3J(\text{C,H})$ was estimated from the HR-HMBC method [18]. The observed chemical shifts and coupling constants are summarized in Table 2.

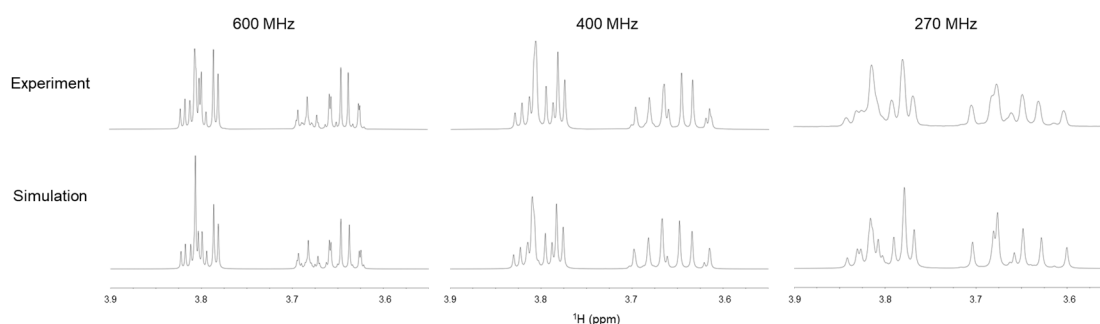


Figure 4. Solution ^1H -NMR spectra of ribitol (**upper**) at ^1H observation frequencies of 600 (**left**), 400 (**middle**), and 270 MHz (**right**). Simulated NMR spectra at each ^1H frequency are shown in the lower panel.

Table 2. ^1H and ^{13}C chemical shift and coupling constant of ribitol determined in this study.

Chemical Shift (ppm)	
H1R(<i>pro-R</i>)	3.79
H1S(<i>pro-S</i>)	3.64
H2	3.81
H3	3.68
C1	65.1
C2	74.8
C3	74.9
Coupling constant (Hz)	
$^3J(\text{H1R}, \text{H2})(\textit{pro-R})$	3.00
$^3J(\text{H1S}, \text{H2})(\textit{pro-S})$	7.20
$^3J(\text{H2}, \text{H3})$	6.50
$^2J(\text{H1R}, \text{H1S})$	−12.70
$^3J(\text{C1}, \text{H3})$	3.8 *
$^3J(\text{C3}, \text{H1S})$	2.9 *

* $^3J(\text{C}, \text{H})$ may include errors due to the presence of strong $^3J(\text{H}, \text{H})$ coupling.

Chemical shifts and $^2,3J(\text{H}, \text{H})$ coupling constants are in substantial agreement with those of previous studies [7,8,10,19]. $^3J(\text{C1}, \text{H3})$ was measured as 3.8 Hz in this study, similar to a previous report (3.7 Hz) [8]. Then, these coupling constants are used for estimating the distribution of each conformer using the Haasnoot equation, which includes a set of empirical constants [20]. Regarding the O1–C1 dihedral angle ($\varphi_1 = \text{O1–C1–C2–C3}$), the population of three conformers ($\varphi_1 = 180^\circ$, -60° , and $+60^\circ$) was calculated using $^3J(\text{H1R}, \text{H2})(\textit{pro-R})$ and $^3J(\text{H1S}, \text{H2})(\textit{pro-S})$ with reference to the method of Hawkes [7]. The φ_1 ratio was estimated as $180^\circ:-60^\circ:+60^\circ = 64:36:0$. This closely conforms to the result of Hawkes [7]. For the C1–C2 dihedral angle φ_2 ($\varphi_2 = \text{C1–C2–C3–C4}$), the conformations can be estimated from $^3J(\text{H2}, \text{H3})$ and $^3J(\text{C1}, \text{H3})$. The population of each φ_2 conformation was calculated as $180^\circ:-60^\circ:+60^\circ = 2:46:52$. These data suggest the presence of a rapid transition (>10 Hz in terms of coupling constant) around the C1–C2 axis and a relatively small population of the anti-conformation. It should be noted that φ_1 and φ_4 or φ_2 and φ_3 cannot be discussed separately because their NMR signals (e.g., H1 and H5, H2 and H4) overlap in solution.

2.2.3. NMR Analysis of Hydroxy Protons

Franks et al. found that the $^3J(\text{H}, \text{H})$ values of ribitol differ significantly in water and organic solvents [19], and this suggests that hydration and hydrogen bonding affect the conformation of ribitol. In this study, we analyzed the hydroxyl group of ribitol by directly observing the hydroxyl proton by ^1H -NMR. The assignments of OH signals are shown in Figure 5. At 0°C , two sharp peaks are observed at 5.9 ppm and 5.8 ppm, and these correspond to OH3 and OH2/OH4 (Figure 5a). The OH3 signal gives a relatively sharp peak at 0°C , suggesting that OH3 is stabilized by hydrogen bonding. To validate the exchange of the hydroxyl proton, the temperature coefficient (ppb K^{-1}) was estimated as 11 ppb K^{-1} for ribitol OH3. According to Sandström et al., the temperature coefficient is greater than 11 ppb K^{-1} when the OH proton is fully hydrated [8]. This suggests that OH3 is mostly exposed to solvent, but some transient hydrogen bond may exist. The exchange rate constant of OH3 was also estimated from 2D EXSY. From the build-up curve of exchange peak volume, it was estimated as $k_{\text{ex}} = 193 \text{ s}^{-1}$. To estimate the effect of an intramolecular hydrogen bond on the temperature coefficient and OH exchange rate, the same experiment was performed using the model compound 1,3,5-pentanol (Figure 1), which does not have hydroxyl groups at the 2 and 4 positions. 1,3,5-Pentanol gives a broad OH peak around 5.7 ppm at 0°C . This peak can be assigned to OH1/OH3/OH5, and the peak almost disappears at 25°C (Figure 5b). We reasoned that this is due to the lack of a hydrogen bond, and hence, OH3 shows faster proton exchange.

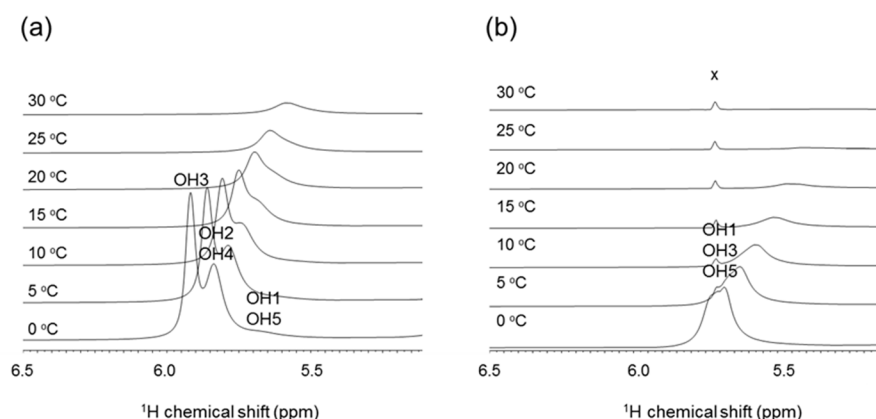


Figure 5. Part of 1D- ^1H -NMR (OH region) spectra of ribitol and 1,3,5-pentanol measured at 0, 5, 10, 15, 20, 25, and 30 °C in 10 mM sodium acetate buffer, pH 6.0 ($\text{H}_2\text{O}:\text{D}_2\text{O} = 1:1$). (a) Ribitol. (b) 1,3,5-Pentanol. x = impurity.

For comparison, the temperature coefficient of 1,3,5-pentanol was calculated as 13 ppb K^{-1} for OH1/3/5. Similarly, the exchange rate of OH1/3/5 was estimated from EXSY to be $k_{\text{ex}} = 650 \text{ s}^{-1}$. These observations suggest that ribitol OH3 tends to form water-mediated or intramolecular hydrogen bonds.

2.3. MD Simulations

Distribution of Main Chain Dihedral Angles

Since solution NMR does not distinguish between $^3J(\text{H2},\text{H3})$ and $^3J(\text{H3},\text{H4})$, MD simulations were performed to shed light on the dihedral angles of φ_2 and φ_3 separately. We used three ribitol coordinates in PDB (PDB ID: 5IAI, 4Q0S, 4F2D) as an initial structure (Supplementary Table S1). Independent MD simulations (referred to as Run #1, #2, and #3, respectively) were performed for 100 ns for each initial structure. The MD simulation results are essentially the same; therefore, the following discussion is based on the results of Runs #1–#3. Figure 6 shows the results of MD simulations of ribitol (left, Run #1) and 1,3,5-pentanol (right) for each dihedral angle φ_1 to φ_4 . The MD simulation results of Run #2 and #3 are shown in Supplementary Figure S1.

Table 3. Comparison of calculated and experimental coupling constants of ribitol. Calculated J values are obtained from the average of three independent MD simulations (mean \pm SD).

	Calculated J Value (Hz)	Experimental J Value (Hz)
$^3J(\text{H1R},\text{H2})(\text{pro-R})$	3.11 ± 0.05	3.00
$^3J(\text{H1S},\text{H2})(\text{pro-S})$	7.57 ± 1.02	7.20
$^3J(\text{H2},\text{H3})$	6.41 ± 0.09	6.50
$^3J(\text{C1},\text{H3})$	4.20 ± 0.36	3.9
$^3J(\text{C3},\text{H1S})$	2.67 ± 0.64	3.1

It seems that φ_2 and φ_3 tend to share the same dihedral angle, i.e., $(\varphi_2, \varphi_3) = (+60^\circ, +60^\circ)$ or $(-60^\circ, -60^\circ)$ during the MD trajectory. This differs from the database analysis, in which (φ_2, φ_3) mostly adopts (anti, gauche) or (gauche, anti). This discrepancy may come from the intermolecular contacts in the crystal lattice. The combination of φ_2 and φ_3 $(+60^\circ, +60^\circ)$ or $(-60^\circ, -60^\circ)$ can avoid steric hindrance between O2 and O4, and this arrangement seems reasonable.

MD simulations of 1,3,5-pentanol were also performed to investigate the role of OH2 and OH4 in ribitol (Figure 5, right). In 1,3,5-pentanol, φ_1 and φ_4 assume all three conformations $(180^\circ, +60^\circ, -60^\circ)$ almost equally (Supplementary Table S2). φ_2 and φ_3 also assume all three conformations, but -60° is slightly less populated for φ_2 and $+60^\circ$ for φ_3 . Overall, transitions are frequent among conformers in 1,3,5-pentanol, while they are less so in ribitol. These results suggest that the presence of OH groups at positions 2 and 4 affects the frequency of conformational transitions. It is likely that this is because ribitol

OH2 and OH4 form water-mediated or intramolecular hydrogen bonds that restructure the molecule.

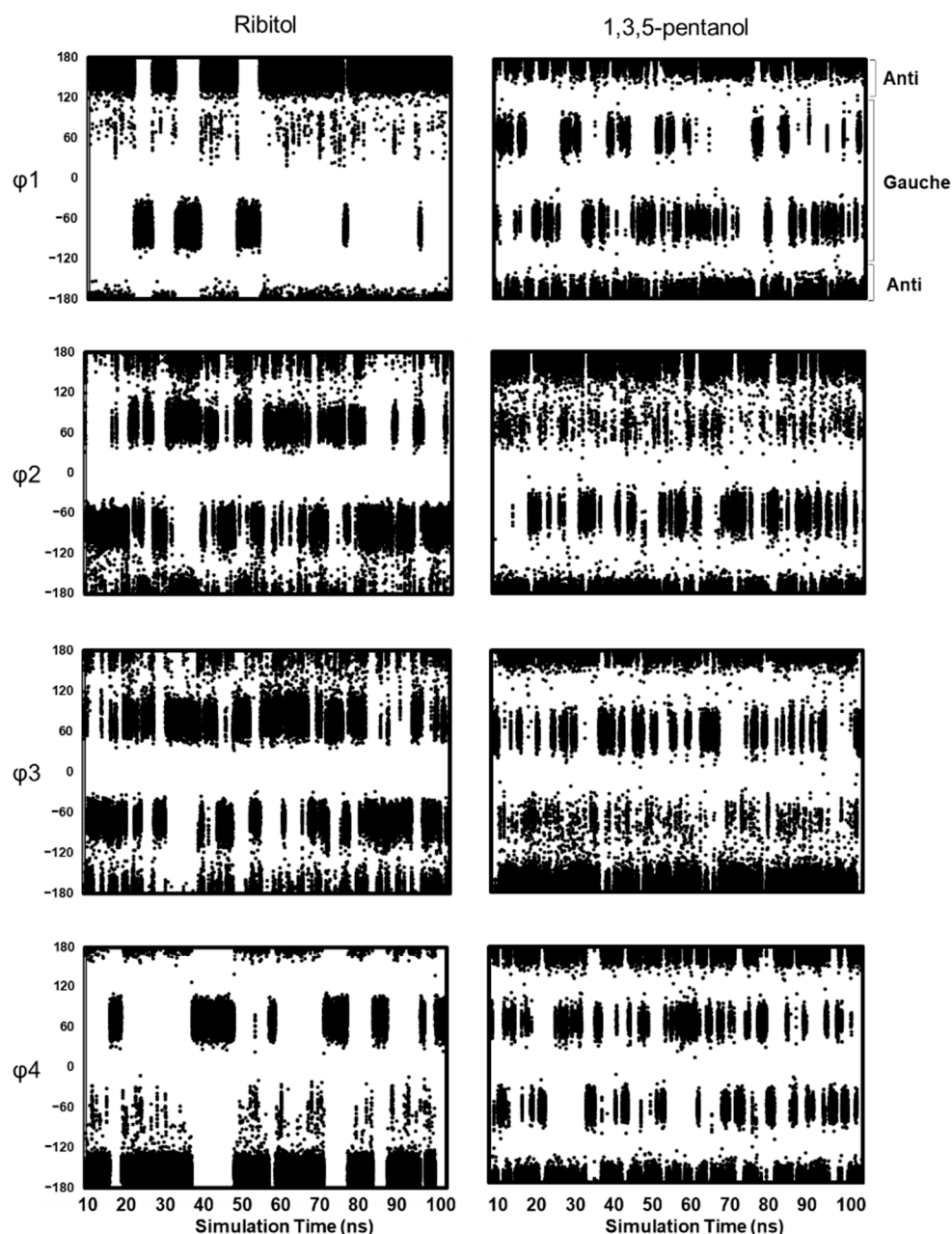


Figure 6. Dihedral angle distribution of ribitol (left, Run#1) and 1,3,5-pentanol (right) in MD simulations. The results of each dihedral angle are shown after 10 ns. The dihedral angles are defined as ϕ_1 (O1–C1–C2–C3), ϕ_2 (C1–C2–C3–C4), ϕ_3 (C2–C3–C4–C5), and ϕ_4 (C3–C4–C5–O5). ϕ_1 and ϕ_4 of ribitol are mostly distributed in anti (180°) and gauche (-60° for ϕ_1 and $+60^\circ$ for ϕ_4) (Supplementary Table S2). This is consistent with the NMR result, in which the populations of dihedral angle ϕ_1 are estimated as $180^\circ:-60^\circ:60^\circ = 64:36:0$. For ϕ_2 and ϕ_3 of ribitol, gauche conformations (-60° and $+60^\circ$) are dominant, but the anti-conformation is also populated. This is consistent with the NMR result ($180^\circ:-60^\circ:+60^\circ = 2:46:52$). To validate the MD results quantitatively, $^3J(\text{H,H})$ and $^3J(\text{C,H})$ are calculated from the population of anti and gauche conformations, and the calculated J values are compared with experimental values (Table 3). The calculated J values are mostly consistent with the experimental values, suggesting that MD simulation quantitatively reflects the energy level of each conformer based on the Boltzmann distribution.

3. Materials and Methods

3.1. Database Analysis of Ribitol and Ribitol Phosphate

Three-dimensional (3D) crystal structures of ribitol and ribitol phosphate (resolution less than 2.7 Å) were extracted from the Cambridge Crystallographic Data Centre (CCDC, as of May, 2020) and the Protein Data Bank (PDB, as of April 2020). Coordinates of ribitol phosphate were extracted that had at least one terminal CH₂OH group. When analyzing tandem ribitol phosphate, the terminal ribitol with the CH₂OH group was chosen. The dihedral angles of ribitol and ribitol phosphate are defined as φ_1 (O1–C1–C2–C3), φ_2 (C1–C2–C3–C4), φ_3 (C2–C3–C4–C5), and φ_4 (C3–C4–C5–O5).

3.2. Solution NMR Analysis

Ribitol was purchased from Tokyo Chemical Industry (Tokyo, Japan), and 1,3,5-pentanol was purchased from ChemCruz. Solution NMR analyses were performed using JNM-ECZ600R/S1, JNM-ECZ400S/L1 and EX270 spectrometers (JEOL, Tokyo, Japan). The probe temperature was set from 273 to 303 K. A sample (18–30 mg) was dissolved in 650 μ L of D₂O for signal assignment or 10 mM sodium acetate buffer, pH 6.0 (H₂O:D₂O = 1:1) for detection of OH chemical shifts. ¹H and ¹³C chemical shifts were reportedly related to the internal standard of 4,4-dimethyl-4-silapentane-1-sulfonic acid (DSS, 0 ppm). NMR chemical shifts of ribitol were assigned by analyzing 1D-¹H, 1D-¹³C, 2D-DQF-COSY, NOESY, TOCSY, and ¹H-¹³C HSQC spectra. NMR chemical shifts of ribitol phosphate were assigned by analyzing 1D-¹H, 1D-¹³C, 2D-¹H-¹³C HSQC, and 2D-¹H-¹³C HMBC spectra. Stereospecific assignment of *pro-R* and *pro-S* protons in ribitol was conducted with the aid of 1D-¹H-NMR spectral simulation by Mnova 14.1.1 (Mestrelab Research, Santiago, Spain). Due to the presence of a second-order term, the ³J(H,H) and ²J(H,H) coupling constants of ribitol were obtained by iterative comparison of simulated NMR spectra with observed NMR spectra obtained at ¹H observation frequencies of 270, 400, and 600 MHz. ³J(C,H) coupling constants were obtained from HR-HMBC spectra [18]. A scaling factor (*n*) of 25 was used, and the digital resolutions for f1 (¹³C) and f2 (¹H) were 4.4 and 0.7 Hz/point, respectively. The conversion from coupling constant ³J(H,H) to dihedral angle was done using the Haasnoot equation, which includes a correction for electronegativity of substituents and the orientation of each substituent relative to the coupled protons [20]. ³J(C,H) is also applied to an empirical prediction equation [21,22]. The exchange rate of hydroxyl protons with water was calculated from 2D chemical exchange spectroscopy [23,24]. Mixing times of 3 to 24 ms with increments of 3 ms were used. The exchange rate constant was calculated from the initial build-up rate of the diagonal peak volume over the exchange cross-peak. The temperature coefficient (ppb K^{−1}) of hydroxyl protons in ribitol and 1,3,5-pentanol was measured by collecting a series of 1D-¹H-NMR spectra at different temperatures (273, 278, 283, 288, 293, 298, and 303 K). NMR data processing was performed using Delta5. 3. 1 (JEOL, Tokyo, Japan), and NMR spectral analyses were performed using Mnova.

3.3. Solid-State ¹³C-CP-MAS NMR

¹³C CP-MAS spectra of crystalline ribitol (Tokyo Chemical Industry, Tokyo, Japan) were obtained using a Bruker Avance III 500 spectrometer at a ¹H frequency of 500 MHz. A VPn probe (4 mm) was used at the spinning rate of 15,000 Hz or 8000 Hz with a spectral width of 300 ppm or 200 ppm, respectively. The data point was set to 2k. ¹³C chemical shifts were referenced to carboxyl carbon of glycine (176.03 ppm).

3.4. MD Simulation

MD simulations were performed using Discovery Studio 2019 [25]. The coordinates of ribitol (PDB ID: 5IAI, 4Q0S and 4F2D) were used as the initial structure (Supplementary Table S1), and the three simulations were performed independently. CHARMM36 was assigned as the force field [10]. Hydrogens were generated using the “Add Hydrogens” protocol in Discovery Studio. The simulation time was set to 100 ns. An explicit periodic boundary was used as

the solvation model. An orthorhombic cell shape was used in the explicit periodic boundary solvation model. The minimum distance from the periodic boundary was set to 7.0 Å. For each ribitol coordinate, 182–184 water molecules were explicitly placed based on the protocol in Discovery Studio 2019. CHARMM36 was optimized using the TIP3P water model [26], which was used as the force field template. Explicit waters were 190 for 1,3,5-pentanol. Minimization of the initial coordinate was done in two steps. The first step is to eliminate distortion of the entire structure with the steepest descent algorithm. In the second step, minimization was performed with the adopted basis Newton–Raphson (NR) algorithm. Heating was done at 500 K. After equilibration, the time step was set to 2 fs, and production was done under *NPT* ensemble. MD simulations were also performed for 1,3,5-pentanol under the same protocol. The initial structure of 1,3,5-pentanol is a zigzag form with each dihedral angle of the carbon main chain being 180°.

4. Conclusions

Until the present study, it has been assumed that the C-C bonds of alditols are rather unstructured, and the molecule exhibits little or no stable folded structure. Here, NMR and MD simulation of ribitol reveal that ribitol is a dynamic conformational equilibrium of staggered conformations. Then, ribitol, is rather structured compared with model compound 1,3,5-pentanol. Conformational asymmetry may prevail in ribitol due to repulsion between OH2 and OH4 and to transient weak hydrogen bonds involving OH3. These findings provide a basis for understanding the dynamic structure of ribitol and the function of ribitol-related enzymes involved in ribitol biosynthesis and glycan chain elongation.

Supplementary Materials: The following are available online, Figure S1: Dihedral angle distribution of ribitol in MD simulations Run #2 and #3, Table S1: The initial XYZ coordinates for MD simulations, and Table S2: The population (%) of dihedral angles in MD simulations of ribitol (Runs #1–#3) and 1,3,5-pentanol.

Author Contributions: Manuscript conception, writing and original draft preparation, S.O., Y.Y.; NMR analysis, S.O., T.Y., Y.Y.; MD simulations, S.O.; editing, data analysis, and interpretation, S.O., N.M., J.U., Y.Y. All authors have read and agreed to the published version of the manuscript.

Funding: This work was supported in part by grants-in-aid of KAKENHI 19H05648 and 19H03362.

Institutional Review Board Statement: Not applicable.

Informed Consent Statement: Not applicable.

Data Availability Statement: Not applicable.

Acknowledgments: We acknowledge Ohgi Takahashi (Shonan University of Medical Sciences) for technical advices on computational calculations, and Hiroshi Many and Tamao Endo (Tokyo Metropolitan Geriatric Hospital and Institute of Gerontology) and Jun-ichi Tamura (Tottori University) for intriguing discussions and encouragement. We also express our thanks to Tomoyuki Matsuki and Shin-ichi Sato (Tohoku Medical and Pharmaceutical University) for NMR measurements. This work was partly supported by Nanotechnology Platform Program (Molecule and Material Synthesis) of MEXT.

Conflicts of Interest: The authors declare no conflict of interest.

Sample Availability: Samples of the compounds are not available from the authors.

References

1. Brown, S.; Santa Maria, J.P., Jr.; Walker, S. Wall teichoic acids of gram-positive bacteria. *Annu. Rev. Microbiol.* **2013**, *67*, 313–336. [[CrossRef](#)]
2. Kanagawa, M.; Kobayashi, K.; Tajiri, M.; Many, H.; Kuga, A.; Yamaguchi, Y.; Akasaka-Many, K.; Furukawa, J.I.; Mizuno, M.; Kawakami, H.; et al. Identification of a post-translational modification with ribitol-phosphate and its defect in muscular dystrophy. *Cell Rep.* **2016**, *14*, 2209–2223. [[CrossRef](#)] [[PubMed](#)]
3. Endo, T. Mammalian O-mannosyl glycans: Biochemistry and glycopathology. *Proc. Jpn. Acad. Ser. B Phys. Biol. Sci.* **2019**, *95*, 39–51. [[CrossRef](#)] [[PubMed](#)]
4. Jeffrey, G.A.; Kim, H.S. Conformations of the alditols. *Carbohydr. Res.* **1970**, *14*, 207–216. [[CrossRef](#)]

5. Tanaka, N.; Ashida, T.; Sasada, Y.; Kakudo, M. The crystal structure of riboflavin hydrobromide monohydrate. *Bull. Chem. Soc. Jpn.* **1969**, *42*, 1546–1554. [[CrossRef](#)] [[PubMed](#)]
6. Tanaka, N.; Ashida, T.; Sasada, Y.; Kakudo, M. The crystal structure of riboflavin hydrobromide monohydrate. *Bull. Chem. Soc. Jpn.* **1967**, *40*, 1739. [[CrossRef](#)] [[PubMed](#)]
7. Hawkes, G.E.; Lewis, D. ^1H nuclear magnetic resonance spectra and conformations of alditols in deuterium oxide. *J. Chem. Soc. Perk. Trans.* **1984**, 2073–2078. [[CrossRef](#)]
8. Garrett, E.C.; Serianni, A.S. (^{13}C)Alditols: Elimination of magnetic equivalence in ^1H - and ^{13}C -n.m.r. spectra of symmetric compounds through (^{13}C)-substitution. *Carbohydr. Res.* **1990**, *208*, 23–35. [[CrossRef](#)]
9. Klein, R.A.; Hartmann, R.; Egge, H.; Behr, T.; Fischer, W. The aqueous solution structure of the tetrasaccharide-ribitol repeat-unit from the lipoteichoic acid of *Streptococcus pneumoniae* strain R6 determined using a combination of NMR spectroscopy and computer calculations. *Carbohydr. Res.* **1994**, *256*, 189–222. [[CrossRef](#)]
10. Hatcher, E.; Guvench, O.; Mackerell, A.D., Jr. CHARMM additive all-atom force field for acyclic polyalcohols, acyclic carbohydrates and inositol. *J. Chem. Theory Comput.* **2009**, *5*, 1315–1327. [[CrossRef](#)]
11. Imberty, A. Oligosaccharide structures: Theory versus experiment. *Curr. Opin. Struct. Biol.* **1997**, *7*, 617–623. [[CrossRef](#)]
12. Kim, H.S.; Jeffrey, G.A.; Rosenste, R.D. Crystal structure of ribitol. *Acta Crystallogr. Sect. B Struct. Crystallogr. Cryst. Chem.* **1969**, *25*, 2223–2230. [[CrossRef](#)]
13. Madsen, A.O.; Larsen, S. Insight into solid-state entropy from diffraction data. *Angew. Chem. Int. Ed. Engl.* **2007**, *46*, 8609–8613. [[CrossRef](#)] [[PubMed](#)]
14. Madsen, A.O.; Mattson, R.; Larsen, S. Understanding thermodynamic properties at the molecular level: Multiple temperature charge density study of ribitol and xylitol. *J. Phys. Chem. A* **2011**, *115*, 7794–7804. [[CrossRef](#)] [[PubMed](#)]
15. Yoshida, H.; Yoshihara, A.; Teraoka, M.; Terami, Y.; Takata, G.; Izumori, K.; Kamitori, S. X-ray structure of a novel L-ribose isomerase acting on a non-natural sugar L-ribose as its ideal substrate. *FEBS J.* **2014**, *281*, 3150–3164. [[CrossRef](#)] [[PubMed](#)]
16. Gerlach, D.; Guo, Y.; De Castro, C.; Kim, S.H.; Schlatterer, K.; Xu, F.F.; Pereira, C.; Seeberger, P.H.; Ali, S.; Codee, J.; et al. Methicillin-resistant *Staphylococcus aureus* alters cell wall glycosylation to evade immunity. *Nature* **2018**, *563*, 705–709. [[CrossRef](#)] [[PubMed](#)]
17. Kuwabara, N.; Imae, R.; Many, H.; Tanaka, T.; Mizuno, M.; Tsumoto, H.; Kanagawa, M.; Kobayashi, K.; Toda, T.; Senda, T.; et al. Crystal structures of fukutin-related protein (FKRP), a ribitol-phosphate transferase related to muscular dystrophy. *Nat. Commun.* **2020**, *11*, 303. [[CrossRef](#)]
18. Furihata, K.; Tashiro, M.; Seto, H. High resolution-HMBC (HR-HMBC), a new method for measuring heteronuclear long-range coupling constants. *Magn. Reson. Chem.* **2010**, *48*, 179–183. [[CrossRef](#)]
19. Franks, F.; Kay, R.L.; Dadok, J. A nuclear magnetic resonance study of isomeric pentitols in aqueous and non-aqueous solutions. *J. Chem. Soc. Farad. Trans.* **1988**, *84*, 2595–2602. [[CrossRef](#)]
20. Haasnoot, C.A.G.; Deleeuw, F.A.A.M.; Altona, C. The relationship between proton-proton NMR coupling constants and substituent electronegativities. 1. An empirical generalization of the Karplus equation. *Tetrahedron* **1980**, *36*, 2783–2792. [[CrossRef](#)]
21. Palermo, G.; Riccio, R.; Bifulco, G. Effect of electronegative substituents and angular dependence on the heteronuclear spin-spin coupling constant $3J(\text{C-H})$: An empirical prediction equation derived by density functional theory calculations. *J. Org. Chem.* **2010**, *75*, 1982–1991. [[CrossRef](#)]
22. Aydin, R.; Günther, H. ^{13}C , ^1H spin-spin coupling. X—Norbornane: A reinvestigation of the karplus curve for $^3J(^{13}\text{C}, ^1\text{H})$. *Magn. Reson. Chem.* **1990**, *28*, 448–457. [[CrossRef](#)]
23. Dobson, C.M.; Lian, L.Y.; Redfield, C.; Topping, K.D. Measurement of hydrogen-exchange rates using 2D NMR-spectroscopy. *J. Magn. Reson.* **1986**, *69*, 201–209. [[CrossRef](#)]
24. Sandstrom, C.; Baumann, H.; Kenne, L. The use of chemical shifts of hydroxy protons of oligosaccharides as conformational probes for NMR studies in aqueous solution. Evidence for persistent hydrogen bond interaction in branched trisaccharides. *J. Chem. Soc. Perk. Trans.* **1998**, 2385–2393. [[CrossRef](#)]
25. BIOVIA Discovery Studio. *Discovery Studio 2019*; Dassault Systèmes: San Diego, CA, USA, 2019.
26. Jorgensen, W.L.; Chandrasekhar, J.; Madura, J.D.; Impey, R.W.; Klein, M.L. Comparison of simple potential functions for simulating liquid water. *J. Chem. Phys.* **1983**, *79*, 926–935. [[CrossRef](#)]